Mineralogical characterization of South African mine tailings with aim of evaluating their potential for the purposes of Mineral Carbonation

Maxwell Amponsah-Dacosta

A thesis submitted for the degree of **Master of Science** in the

Department of Geological Sciences,

University of Cape Town, South Africa.

2017

DECLARATION

I know the meaning of plagiarism and declare that all the work contained in this thesis, save for that which is properly acknowledged, is my own.

Signed by candidate

Signature removed

Maxwell Amponsah-Dacosta

13 January 2017

ABSTRACT

South Africa is an energy intensive economy which primarily relies on the burning of fossil fuel such as coal. The South African coal energy sector accounts for approximately 420 million metric tonnes of carbon dioxide emitted per annum. With present alarming concerns with regards to the ever-increasing atmospheric carbon dioxide concentrations resulting in global warming and climate change, several mitigation strategies have to be implemented. A majority of Carbon Capture and Storage (CCS) technologies require monitoring from potential leakages, making the process expensive. However, a benign technology exists to permanently store away anthropogenic CO_2 with products obtained instantaneously. This CCS technology is known as Mineral Carbonation. The fundamental procedure is a reaction between (magnesium - calcium - iron) silicates and CO_2 to form carbonates. The products of from the reaction require no monitoring and the fear of leakage of CO_2 is eliminated. Moreover, the carbonates from this technology are useful in the road, agriculture and building industries. The CO_2 storage capacity in mineral carbonation exceeds other CCS techniques.

The South African mineral industry annually produce immense tonnages of ultramafic mine tailings. Due to the generally fine nature of the tailings, no further cost would be incurred in grinding the material. The platinum group metal (PGM), nickel and copper companies are examples of industries that produce massive tonnages of which could serve as potential feedstock for the purposes of mineral carbonation. Recent studies have shown that, the potential feedstock could sequester close of 70% of the annual CO_2 produced at Secunda, South Africa.

A mineralogical investigation into the mineral carbonation potential of mine tailings was conducted using samples from seven mining companies. Four of the mining operations considered (Impala, Rustenburg, Amandelbult and Mogalakwena) are PGM operations mining the Merensky, Upper Group 2 (UG-2) and Platreef. Nkomati was another operation selected for the study, with samples collected from the Main Mineralised Zone (MMZ) and Chromititic Peridotite Mineralized Zone (PCMZ). Tailings material from the dormant O'okiep operation was the seventh, chosen for the study.

To determine the suitability of these tailings for mineral carbonation, the particle size, surface area and mineral for each individual operation was accounted using Malvern, BET analysis, XRF, QXRD and QEMSCAN respectively.

The overall fine-grained nature of the mine tailings was manifested in the particle size distribution results were sizes ranged from d(0.5) = 33.67 (Nkomati) to d(0.5) = 231.45 (Impala). The range in surface area was 1.45 m^2/g (Amandelbult) to 5.89 m^2/g (Nkomati).

A theoretical carbonation capacity ranking scheme was developed where the seven mining companies selected for this study were graded based on their suitability for mineral carbonation. Three distinct factors made up the classification criteria of the ranking scheme. The first was the carbonation capacity. This was determined by the mineralogy, the R_{co2} value and the tonnage of mine waste produced annually. The second major factor was the reactivity (ignoring kinetics) of the tailings. In this case, the particle size distribution and surface area of the respective mine tailings were considered. Thirdly, the distance from the CO_2 (Secunda) source was taken into account as the cost of transporting CO_2 to the mineral carbonation facility should be weighed up. In using these principles, Nkomati was unquestionably ranked first while O'okiep was rated last priority among the seven operations.

The motive behind was to improve upon the theoretical carbonation capacity ranking scheme and in turn examining a variety of South African mine tailings for the purposes of detailed mineral carbonation studies in South Africa.

CONFERENCE PRESENTATIONS

Oral Presentation: *Mineralogical characterization of mine tailings for Mineral Carbonation.*1-5 December 2014. 2nd National Global Change Conference. Port Elizabeth, South Africa.

Oral Presentation: *Mineralogical characterization of South African mine tailings for the purposes of Mineral Carbonation.* 1-5 September 2014. 21st General Meeting of the International Mineralogical Association (IMA), Johannesburg, South Africa.

Poster Presentation: *South African mine tailings for the Mineral Carbonation, an interdisciplinary response to mine closure.*18-22 August 2014. 12th International Mine Water Association Congress (IMWA 2014), Xuzhou, China.

Poster Presentation*: Mineralogical characterization of South African mine tailings for Mineral Carbonation.*17 April 2014. Postgraduate Research Expo. University of Cape Town, South Africa.

Oral Presentation: *Mineralogical characterization of mine tailings for the purposes of Mineral Carbonation.* 07 November 2013. Minerals to Metals (MtM) Research Day, Cape Town, South Africa.

ACKNOWLEDGEMENTS

Successful completion of this research project could not have been made possible without the cooperation of many individuals. I wish to express my profound gratitude to the Almighty God for His care and strength He gave me in order to complete this research project. A big thank you goes to my supervisor Prof David Louis Reid for his guidance and relentless motivation that he offered me during the research work as well as the compilation and preparation of this report.

A special word of appreciation goes to the management and staff of Anglo Platinum, Impala Platinum and Nkomati Mine for the innumerable assistance in sampling of their respective tailings. The department of Chemical Engineering and Geological Sciences at the University of Cape Town provided laboratory assistance in sampling preparation and mineralogical data acquisition. I greatly acknowledge the contributions of each and every staff member of these department. The Julian Baring Scholarship Organisation was my financial backbone and I appreciate their immerse support throughout this project.

I owe a depth of gratitude to my parents, Dr Francis Amponsah-Dacosta and Mrs Cynthia Amponsah-Dacosta. I also wish to express my heartfelt appreciation to my siblings, Edina and David, for the encouragement and moral support during the challenging moments of the project. Finally, a big thank you goes to Ms Euraeffie Oppon for her endless support and motivation, making the impossible seem possible during the toughest moments of this project.

TABLE OF CONTENTS

DECLARATION I

ABSTRACT III

CONFERENCE PRESENTATIONS VI

ACKNOWLEDGEMENTS VIII

TABLE OF CONTENTS X

GLOSSARY XXIV

CHAPTER 1 1

INTRODUCTION 1

1.1. Background and Motivation 1

1.2. Statement of the Research Problem 3

1.3. Significance of Study 3

1.4. Scope of Study 4

1.5. Study Objectives 4

1.6. Expected Outcome 4

1.7. Dissertation Layout 5

CHAPTER 2 6

LITERATURE REVIEW 6

2.1. Introduction 6

2.2. Carbon Capture and Storage (CCS) 6

2.2.1. CO_2 Separation from energy related sources 9

2.2.2. Transportation of CO_2 captured 11

2.2.3. CO_2 Storage 12

2.3. Mineral Carbonation 15

2.3.1. In-Situ mineral carbonation 17

2.3.2. Ex-situ mineral carbonation 17

2.3.3. Natural Mineral Carbonation 19

2.4. Raw Material Availability in South Africa 22
2.4.1. Bushveld Igneous Complex 22
2.4.2. Uitkomst Complex 27
2.4.3. Namaqualand Metamorphic Complex 31
2.5. Mineral Processing 35
2.5.1. Platinum Group Metal (PGM) Processing 36
2.5.2. Nickel 41
2.5.3. Copper 43
2.6. Previous research work on Mineral Carbonation 45
2.7. Effects of CCS by geological storage 46
2.7.1. The Lake Nyos disaster 47
2.7.2. Impacts of geological storage 47
2.8. Summary 49
CHAPTER 3 51
METHODOLOGY 51
3.1. Introduction 51
3.2. Research Approach 51
3.3. Field Sampling 51
3.3.1. Impala 52
3.3.2. Nkomati 56
3.3.3. Amandelbult 62
3.3.4. Other Anglo Platinum plants 62
3.3.5. O'okiep 63
3.4. Sample Preparation 64
3.4.1. Splitting 64
3.4.2. Sieve analysis 71
3.5. X-ray Fluorescence (XRF) 75

3.5.1. Fusion discs 76
3.5.2. Pressed Pellets 77
3.6. Quantitative X-ray Diffraction (QXRD) 79
3.6.1. Micronizing the sample 79
3.6.2. QXRD sample preparation 80
3.7. Malvern Particle Size Analysis 81
3.8. Brunauer Emmett and Teller (BET) Surface Area Analysis 82
3.9. Quantitative Evaluation of Mineral by Scanning Electron Microscopy (QEMSCAN) 84
3.9.1. Routine samples 84
3.9.2. Vertical sections 86
CHAPTER 4 88
RESULTS 88
4.1. Introduction 88
4.2. Characterization of PGM Tailings 88
4.2.1. Impala Platinum 88
4.2.2. Amandelbult Tailings 100
4.2.3. Mogalakwena Tailings 110
4.2.4. Union Section Tailings 118
4.2.5. Rustenburg Tailings 126
4.3. Characterization of Nkomati nickel tailings 135
4.3.1. Particle size analysis 135
4.3.2. QXRD and QEMSCAN mineralogy 139
4.4. Characterization of O'okiep tailings 147
4.4.1. Particle size analysis 147
4.4.2. QXRD and QEMSCAN mineralogy 151
4.4.3. XRF major oxide geochemistry 155

CHAPTER 5 158
DISCUSSION 158
5.1. Introduction 158
5.2. Authenticity and Reliability of Sieve Analysis. 158
5.3. Relationship between Particle Size Distribution and Surface Area. 161
5.4. Theoretical CO_2 Specific Sequestration Capacity. 166
5.5. Ranking Scheme Revision 169
5.5.1. Carbonation Capacity 170
5.5.2. Relative Reactivity 171
5.5.3. Distance from CO_2 source 172
CHAPTER 6 178
CONCLUSIONS AND RECOMMENDATIONS 178
6.1. Conclusions 178
6.2. Recommendations 179
6.2.1. Kudu Gas Project 179
6.2.2. Onsite CO_2 Emission 179
6.2.3. Phytomining through Metal Hyper-accumulation 180
CHAPTER 7 181
REFERENCES 181
APPENDICES 202
A. Particle Size Analysis 202
A 1 Screening Exercise 202
A1.1. Impala 202
A1.2. Amandelbult 204
A1.3. Mogalakwena 208
A1.4. Union Section 209
A1.5. Rustenburg 210

A1.6. O'okiep 211
A1.7. Nkomati 213
A2 Particle Size Distribution 220
A2.1. Impala 220
A2.2. Amandelbult 223
A2.3. Mogalakwena 226
A2.4. Union Section 229
A2.5. Rustenburg 232
A2.6. O'okiep 235
A2.7. Nkomati 238
A3. BET Surface Area 241
A3.1. Impala 241
A3.2. Amandelbult 242
A3.3. Mogalakwena 243
A3.4. Union Section 244
A3.5. Rustenburg (Waterval) 245
A3.6. O'okiep 246
A3.7. Nkomati 247
B. Mineralogical Analysis 248
B1. XRF Data 248
B1.1. Impala 248
B1.2. Amandelbult 249
B1.3. Mogalakwena 250
B1.4. Union Section 251
B1.5. Rustenburg (Waterval) 252
B1.6. O'okiep 253
B1.7. Nkomati 254

C. Calculations 255
C 1 BET Surface Area Calculations 255
C1.1. Impala 257
C1.2. Amandelbult 257
C1.3. Mogalakwena 258
C1.4. Union Section 258
C1.5. Rustenburg (Waterval) 259
C1.6. O'okiep 260
C1.7. Nkomati 260

LIST OF FIGURES

Figure 2. 1: Total South African CO_2 emission in the year 2004 indicating the proportion of sequestrable sources highlighted in green and non-sequestrable sources in red (modified from Surridge and Cloete, 2009). 8
Figure 2. 2: A schematic diagram showing the types of CO_2 capture systems (adapted from British Petroleum, 2004)..... 10
Figure 2. 3: CCS CO_2 transportation modes (modified from Norisor et al., 2012). ... 11
Figure 2. 4: : A distribution of carbonate rocks on South Africa with the main source of CO_2 (red star), Secunda (modified from Doucet, 2011)..... 13
Figure 2. 5: Underground geological storage options for CO_2 as a climate change mitigation measure (from Priestnall, 2013)..... 14
Figure 2. 6: : A schematic diagram of the ex-situ mineral carbonation process (from Metz et al., 2005)..... 17
Figure 2. 7: Evidence of carbonate formation at New Denmark Colliery (from Ringane 2003)..... 20
Figure 2. 8: Thin sections showing mineral alterations under plane polarized light (PPL) and cross polarized light (XPL). Plagioclase (Plag); Pyroxene (Px); and Carbonated Dolerite (Carb) are seen in the thin section (from Ringane, 2003)..... 21
Figure 2. 9: A stratigraphic column of the Bushveld Complex showing the correlation between the Merensky Reef and its equivalent (Platreef) and the position of the UG-2 Reef (modified after Vermaak, 1995). 24
Figure 2. 10: Southern Africa and Bushveld Complex geological map (top) and conceptual cross-section (bottom), including PGM mines, smelters, refineries and future projects (adapted from Glaister and Mudd, 2010)..... 26
Figure 2. 11: (A) The geological location of the Uitkomst Complex with respect to the Bushveld Complex. (B) An illustration orientation of the Uitkomst Complex (C) a cross-section of the Uitkomst Complex showing locations of the massive and disseminated sulphides (modified from Li et al., 2002)..... 28
Figure 2. 12: An idealised cross-section through the Nkomati nickel deposit showing the MSB, MMZ, BMZ and PCMZ (modified after Mishra et al., 2013). 29
Figure 2. 13: A map of the mine sites with the one of the study areas (O'okiep) on the Koperberg Suite and outcrops of 1 700 individual bodies (after Lombaard et al., 1986). 31

Figure 2. 14: A cross-section of some mine sites on the Koperberg Suite (courtesy of Clifford and Barton, 2012). 34
Figure 2. 15: A flowsheet showing the Merensky ore processing circuit (courtesy: Lebowa Platinum Mine, 2006). 38
Figure 2. 16: A flow diagram showing the UG-2 processing circuit (courtesy: Lebowa Platinum Mine, 2006). 39
Figure 2. 17: A process flowsheet for the for the Mogalakwena operation (Humphries et al., 2006). 40
Figure 2. 18: A simplified flowsheet of the Nkomati crushing circuit (after Cockburn, 2013). 42
Figure 2. 19: A diagram showing the Nkomati ore processing routes to the final step whereby gangue mineral are transported to the Onverwacht tailings dam (courtesy: Cockburn, 2013). 43
Figure 2. 20: : An idealized flowing diagram of the copper processing circuit at a concentrator (Lossin, 2001). 44
Figure 3. 1: : The study area locations (A) Schematic map of the Bushveld Complex where five study areas are located (Cawthorn, 2010). (B) The Namaqualand Metamorphic Complex where O'okiep tailings samples were collected (from Cairncross, 2004). (C) A map of the Uitkomst Complex showing the location of the Nkomati mine (after Cawthorn, 1993)……..52

Figure 3. 2: : Impala Platinum Mine Dam 4 with the two sampling points (distal and proximal) indicated. Courtesy: (Google Earth, 2012). 53
Figure 3. 3: Dam 4 at Implats. A centreline-constructed dam. (a) A spigot method of tailings disposal with perimeter spigots directed towards the centre. (b) Two decant towers situated at the centre of the dam, where tailing water is collect and recycled. 54
Figure 3. 4: Distal sample (IMP-001) collection on Dam 4, Implats. 55
Figure 3. 5: Chromite streaks observed after sampling. An indication to UG-2-Merensky reef blending on site. 55
Figure 3. 6: Duplicate sample collection point of final plant tails from the MMZ plant at Nkomati mine. 56
Figure 3. 7: A map of the mine layout (Google Earth, March 2014). 57

Figure 3. 8: A map of the Nkomati mine showing proximity of the Onverwacht tailing dam (bottom of the map) from the mining operation (Google Earth, 2014). 57
Figure 3. 9: A map of the Onverwacht tailings site showing the position of the dam wall which makes up the proximal end of the tailings facility where coarse material is allowed to settle (Good Earth, 2014). 58
Figure 3. 10: One of the ten cyclones along the dam wall depositing coarse material. 59
Figure 3. 11: A hose line pumping the finer material to the distal end of the dam. ... 59
Figure 3. 12: Sample collection close to Cyclone 4 on the Onverwacht dam where sample NK-CNC/4 was collected. 60
Figure 3. 13: Proximal coarse fraction sampling (NK-PCMZ/CDC) on the co- disposal site..... 61
Figure 3. 14: Sampling of finer material (NK-PCMZ/CDF) from the co-disposal slime pond. 61
Figure 3. 15: Sampling site (Dam 1), Amandelbult Section historic tailings facility. Drill grid superimposed on a Google Earth image (Lekgau, 2012). 62
Figure 3. 16: OKP-1, a brown material collect at the top of the tailings dam. 63
Figure 3. 17: The nature of the O'okiep dam sample (OKP-2). 64
Figure 3. 18: An open-bin riffle splitter..... 66
Figure 3. 19: A ten-cup rotary splitter with a hopper, a vibrating feeder and a rotating table encapsulating the cups. 67
Figure 3. 20: A Retsch rotary sample divider with a funnel-shaped hopper and glass jars. 69
Figure 3. 21: A Microscal suspension sampler. 70
Figure 3. 22: A wet sieving apparatus with a bucket underneath the sieve to collect undersize particles in water solution..... 72
Figure 3. 23: A pressure filter. 73
Figure 3. 24: A Retsch AS 200 Shaker..... 74
Figure 3. 25: Crucible casted in Pt-Au ware using a Classie Fluxy gas burner instrument. 76
Figure 3. 26: 3.26: A 30 ton press L-30. 77
Figure 3. 27: A finished product of a pressed pellet ready for XRF analysis. 78
Figure 3. 28: A fusion machine stationed at the Department of Geological Sciences, University of Cape Town. 78

Figure 3. 29: A Glen Creston McCrone Micronizing Mill at the Centre for Minerals Research laboratory, University of Cape Town. 80
Figure 3. 30: A sample in solution emptied into the sample dispersion unit of a Malvern Mastersizer 2000 at the Department of Chemical Engineering, University of Cape Town. 82
Figure 3. 31: An automated BET surface area equipment. (a) Micromeritics Flow Prep 060, (b) Micromeritics Tristar 3000 and (c) liquid N2 coolant Dewar depicting the Isothermal Jacket method of maintaining the cold/warm volume ratio in the sample tube (adapted from Phadi, 2012). 83
Figure 3. 32: A vacuum chamber used to release trapped air from the sample-graphite mixture. 85
Figure 4. 1: Screening tests for IMP/001. 90
Figure 4. 2: Screen results for IMP/003. 90
Figure 4. 3: A graph comparing the averages of the two Impala samples. 91
Figure 4. 4: Average sieving results plotted against cumulative percentage for Impala. 92
Figure 4. 5: Malvern particle size distribution graph of the Impala IMP/001 (green) and IMP/003 (orange) PGM tailings samples. 92
Figure 4. 6: Multi-point BET plot for calculating the specific surface area for Impala (IMP/001). 93
Figure 4. 7: Bulk mineralogical composition of Impala (IMP/001) tailings sample as determined by QXRD. 95
Figure 4. 8: A bar chart showing QEMSCAN results for Impala (IMP/001) tailings sample. 97
Figure 4. 9: Major oxide composition of size fractions in IMP/001. 98
Figure 4. 10: Major oxide composition of size fractions in IMP/003. 99
Figure 4. 11: A scatter plot showing the correlation of measured and calculated bulk for both Impala samples. 99
Figure 4. 12: Screening test results for AMB/101. 101
Figure 4. 13: Average sieving results plotted against cumulative percentage for Amandelbult. 102
Figure 4. 14: Malvern particle size distribution curves for Amandelbult tailings samples. 102

Figure 4. 15: Multi-point BET plot used to determine the specific surface area for S/4-TD44. 103
Figure 4. 16: Amandelbult (AMB/101) bulk mineral identification determined by QXRD. 105
Figure 4. 17: QEMSCAN results for Amandelbult (AMB/101) tailings. 107
Figure 4. 18: Major oxide composition of size fractions in AMB/101. 108
Figure 4. 19: Major oxide composition of size fractions in Amandelbult dam tailings. 109
Figure 4. 20: The relationship between measured and calculated bulk for AMB/101. 109
Figure 4. 21: Mogalakwena (MPL/101) screening results. 111
Figure 4. 22: Average sieving results plotted against cumulative percentage for Mogalakwena. 111
Figure 4. 23: Malvern particle size distribution results for MPL/101 112
Figure 4. 24: Mogalakwena multi-point BET plot used to determine the specific surface area. 112
Figure 4. 25: QXRD results for MPL/101. 114
Figure 4. 26: Results from QEMSCAN for MPL/101. 116
Figure 4. 27: Major oxide composition of size fractions in MPL/101. 117
Figure 4. 28: The relationship between measured and calculated bulk for MPL/101. 117
Figure 4. 29: Particle size distribution results from UST/201 screening tests. 118
Figure 4. 30: Average sieving results plotted against cumulative percentage for Union Section. 119
Figure 4. 31: Malvern particle size distribution curve for UST/201. 119
Figure 4. 32: Multi-point BET plot to determine the specific surface area of UST/201. 120
Figure 4. 33: QXRD analysis results for Union Section tailings sample. 122
Figure 4. 34: QEMSCAN analytical results for UST/201. 124
Figure 4. 35: Major oxide composition of size fractions in UST/201. 125
Figure 4. 36: Relationship between the measure bulk and calculated bulk for UST/201. 126
Figure 4. 37: WRT/101 screening test results plots. 127

Figure 4. 38: Average sieving results plotted against cumulative percentage for Rustenburg (Waterval). 127
Figure 4. 39: Size distribution curve for WRT/101 obtained by Malvern analysis. .. 128
Figure 4. 40: Multi-point BET plot used to determine the specific surface area for WRT/101. 129
Figure 4. 41: QXRD data for WRT/101..... 131
Figure 4. 42: QEMSCAN results for WRT/101. 133
Figure 4. 43: Major oxide composition of size fractions in WRT/101. 134
Figure 4. 44: Relationship between measured and calculated bulk for WRT/101. 134
Figure 4. 45: NK-MMZ/PT plant tail screening results including the calculated average. 136
Figure 4. 46: NK-PCMZ/PT screening results including the calculated average. ... 136
Figure 4. 47: A graph comparing the averages of the two Nkomati samples. 137
Figure 4. 48: Average sieving results plotted against cumulative percentage for Nkomati. 138
Figure 4. 49: Malvern size distribution curve results the two Nkomati samples..... 138
Figure 4. 50: Multi-point BET plot to determine the specific surface area for NK-PCMZ/PT. 139
Figure 4. 51: QXRD results for Nkomati MMZ sample. 141
Figure 4. 52: QXRD results for Nkomati PCMZ sample. 142
Figure 4. 53: Nkomati mineralogical analysis determined by QEMSCAN. 144
Figure 4. 54: Major oxide composition of size fractions in NK-MMZ/PT. 145
Figure 4. 55: Major oxide composition of size fractions in NK-PCMZ/PT. 146
Figure 4. 56: Relationship between the measured and calculated bulk for both Nkomati plant tail samples..... 146
Figure 4. 57: O'okiep (OKP-1) screening test results. 148
Figure 4. 58: O'okiep (OKP-2) screening test results. 148
Figure 4. 59: A graph comparing the averages of the two O'okiep samples. 149
Figure 4. 60: Average sieving results plotted against cumulative percentage for O'okiep. 149
Figure 4. 61: Malvern particle size distribution analysis for O'okiep. 150
Figure 4. 62: Multi-point BET plot used to determine the specific surface area for O'okiep (OKP-2). 151
Figure 4. 63: O'okiep (OKP-2) QXRD results. 153

Figure 4. 64: QEMSCAN results for OKP-1 and OKP-2. 155
Figure 4. 65: Major oxide composition of size fractions in OKP-1. 156
Figure 4. 66: Major oxide composition of size fractions in OKP-2. 156
Figure 4. 67: Relationship between measured and calculated bulk for O'okiep. 157
Figure 5. 1 A bar graph representing the average quantity of material retained on the finest size fraction <25 µm for the various tailings samples……...161
Figure 5. 2: A combined particle size distribution of the seven mines in this study. 162
Figure 5. 3: The specific surface area for samples in the study. 163
Figure 5.4: The specific surface area for samples in the study. 163
Figure 5. 5: Particle size distribution of the BRPM, Northam, Impala and Lonmin Merensky PGM mine tailings (Vogeli, 2012). 164
Figure 5. 6: A map showing the distance from Secunda to the tailings sites. 170

LIST OF TABLES

Table 2. 1: A collection of rock and mineral types suitable for mineral carbonation (updated from Sipilä et al., 2008). 16
Table 2. 2: Major minerals of the Bushveld Complex and their composition (after Schouwstra et al., 2000)..... 23
Table 4. 1: Screening test results for Impala samples IMP/001 and IMP003…….. .89
Table 4. 2: Particle size distribution analysis indicating average particle size for Impala samples at percentiles 10, 50 and 90. 93
Table 4. 3: QXRD results for Impala (IMP/001), with the sum of mafic, sulphide and alterations mineral highlighted. 94
Table 4. 4: QEMSCAN results for Impala (IMP/001). The selected size fraction (-150/+106 µm). 96
Table 4. 5: Screening test results for Amandelbult (AMB/101). 101
Table 4. 6: Particle size distribution analysis indicating average particle size for Amandelbult samples at percentiles 10, 50 and 90. 103
Table 4. 7: QXRD results for Amandelbult (AMB/101), with the sum of mafic, sulphide and alteration mineral highlighted. 104
Table 4. 8: QEMSCAN results for Amandelbult (AMB/101). The selected size fraction (-150/+106 µm)..... 106
Table 4. 9: Screening test results for MPL/101. 110
Table 4. 10: QXRD results for Mogalakwena, with the sum of mafic, sulphide and alterations mineral highlighted. 113
Table 4. 11: QEMSCAN results for Mogalakwena. The selected size fraction (-75/+53 µm). 115
Table 4. 12: Tabulated screenings results for Union Section tailings sample..... 118
Table 4. 13: QXRD results for Union Section, with the sum of primary igneous mineral, sulphide and alterations minerals highlighted. 121
Table 4. 14: Union Section's -106/+75 µm mineral distribution determined by QEMSCAN. 123
Table 4. 15: Rustenburg (Waterval) sieving test results. 126
Table 4. 16: QXRD results for Rustenburg, with the sum of mafic, sulphide and alterations mineral highlighted. 130
Table 4. 17: QEMSCAN results for Rustenburg (Waterval). 132

Table 4. 18: 135
Table 4. 19: Nkomati plant tailings Malvern data. 139
Table 4. 20: QXRD results for Nkomati, with the sum of primary igneous, sulphide and alterations mineral highlighted. 140
Table 4. 21: QEMSCAN results for Nkomati PCMZ and MMZ samples. 143
Table 4. 22: As demonstrated in Figure 4.57, test B looked to have retained more sample than tests A and C for fractions 38, 53 and 75 µm. Tests A and C produced fairly similar results. 147
Table 4. 23: Particle size distribution analysis indicating average particle size for O'okiep samples at percentiles 10, 50 and 90. 150
Table 4. 24: QXRD results for O'okiep (OKP-2), with the sum of mafic, sulphide and alterations mineral highlighted. 152
Table 4. 25: QEMSCAN results for O'okiep tailings samples. 154
Table 5. 1: Sieving data of the finest size fraction (<25 µm) for samples in this study……160
Table 5. 2: A complication of specific surface area for respective mine tailings samples. 162
Table 5. 3: Particle size distribution analysis indicating average particle size at 10, 50 and 90 volume % for the seven mining operations. 163
Table 5. 4: Particle size distribution analysis indicating average particle size at 10, 50 and 90 volume % (from Vogeli, 2012). 164
Table 5. 5: BET Surface area analysis of tailings samples (Vogeli, 2012). 165
Table 5. 6: Minerals and their R_{CO2} values. Modified from (Lackner et al., 1995)... 166
Table 5. 7: Mineral deposits and their R_{CO2} values modified from (Gerdemann et al., 2007). 167
Table 5. 8: The carbonation potential (R_{co2}) for the mining operations in this study. 168
Table 5. 9: Annual tonnage of ore milled for the respective mining operations (Anglo American Plc Report, 2013; Cockburn. G, 2013; Impala Annual Report, 2013; Metorex limited Annual Report, 2003; Vogeli et al., 2011; Vogeli 2012). 171
Table 5. 10: A layout of values for the respective variables of the ranking scheme. 172

Table 5. 11: A series of rankings based on individual factors of the theoretical carbonation ranking scheme. 173
Table 5. 12: A overall ranking order based on the average of the rankings from Table 5.11. 174
Table 5. 13: A full updated ranking scheme comparing the two ranking methods used in the study (where T = Tonnage; R = R-value; P = Particle Size; S = Surface Area and D = Distance from CO_2)..... 176
Table A. 1: Wet screening analysis results for IMP/001……..……...202
Table A. 2: Dry screening analysis results for IMP/001. 202
Table A. 3: IMP/001 results for screening analysis which involves dry screening following a wet screening exercise. 203
Table A. 4: Wet screening results for Impala sample IMP/003 203
Table A. 5: IMP/003 dry screening results. 203
Table A. 6: A combined wet and dry screen test results for IMP/003. 204
Table A. 7: Wet screening analysis results for AMB/101. 204
Table A. 8: Dry screening results for Amandelbult sample, AMB/101. 204
Table A. 9: Combined wet and dry screening test results for AMB/101. 205
Table A. 10: Amandelbult (S/4-TD44) wet screening results. 205
Table A. 11: Dry screening results for S/4-TD44. 205
Table A. 12: Results for a combined screening exercise for S/4-TD44. 206
Table A. 13: Results for S/4-TD83 wet screening analysis. 206
Table A. 14: S/4-TD83 dry screening results. 206
Table A. 15: S/4-TD83 combined screening analysis results. 207
Table A. 16: Wet screening results for S3/TD43. 207
Table A. 17: Results for S3/TD43 dry screening analysis. 207
Table A. 18: Combined screening results for S3/TD43. 208
Table A. 19: MPL/101 wet screening results. 208
Table A. 20: Dry screening results for MPL/101. 208
Table A. 21: MPL/101 combined wet and dry screening results. 209
Table A. 22: Union Section (UST/201) wet screening results. 209
Table A. 23: Dry screening results for UST/201. 209
Table A. 24: Combined wet-dry screening results for UST/201. 210
Table A. 25: WRT/101 wet screening results. 210

Table A. 26: Dry screening results for WRT/101. 210
Table A. 27: A combined wet-dry screening result for WRT/101. 211
Table A. 28: Wet screening results for OKP-1. 211
Table A. 29: OKP-1 dry screening results. 211
Table A. 30: Table A 30: Combined screening results for OKP-1. 212
Table A. 31: OKP-2 wet screening results. 212
Table A. 32: A 32: Dry screening results for OKP-2. 212
Table A. 33: A combined screening analysis results for OKP-2. 213
Table A. 34: Wet screening results for NK-PCMZ/PT 213
Table A. 35: Dry screening results for NK-PCMZ/PT. 213
Table A. 36: Combined screening results for NK-PCMZ/PT 214
Table A. 37: Wet screening results for NK-MMZ/PT 214
Table A. 38: Dry screening results for NK-MMZ/PT. 214
Table A. 39: NK-MMZ/PT combined wet-dry screening results. 215
Table A. 40: Wet screening results for NK-CNF. 215
Table A. 41: Dry screening results for NK-CNF. 215
Table A. 42: NK-CNF results for a combined wet-dry screening. 216
Table A. 43: Wet screening results for NK-CNC. 216
Table A. 44: Dry screening results for NK-CNC. 216
Table A. 45: NK-CNC results for combined wet-dry screening. 217
Table A. 46: NK-PCMZ/CDF wet screening results. 217
Table A. 47: NK-PCMZ/CDF dry screening results. 217
Table A. 48: Combined wet-dry screening results for NK-PCMZ/CDF. 218
Table A. 49: Wet screening results for NK-PCMZ/CDC. 218
Table A. 50: Dry screening results for NK-PCMZ/CNC. 218
Table A. 51: NK-PCMZ/CNC results for combined wet-dry screening analysis. 219
Table A. 52: Malvern particle size distribution results for Impala. 220
Table A. 53: Malvern particle size distribution results for Amandelbult. 223
Table A. 54: Table A 54: Malvern results for Mogalakwena. 226
Table A. 55: Union Section Malvern particle size distribution results. 229
Table A. 56: Malvern data for Rustenburg tailings sample. 232
Table A. 57: Malvern results for O'okiep. 235
Table A. 58: Nkomati Malvern particle size data. 238
Table A. 59: Impala BET surface area data. 241

Table A. 60: Amandelbult BET surface area data. 242
Table A. 61: Mogalakwena BET surface area data. 243
Table A. 62: Union Section BET surface area data. 244
Table A. 63: Rustenburg (Waterval) BET surface area data. 245
Table A. 64: O'okiep BET surface area data. 246
Table A. 65: Nkomati BET surface area data. 247
Table B. 1: XRF data for Impala tailings…… ……..248
Table B. 2: Amandelbult XRF data. 249
Table B. 3: Mogalakwena XRF data. 250
Table B. 4: Union Section XRF data..... 251
Table B. 5: Rustenburg (Waterval) XRF data. 252
Table B. 6: O'okiep XRF data. 253
Table B. 7: Nkomati XRF data. 254

GLOSSARY

List of abbreviations

BET	Brunauer, Emmett and Teller, (1938) – Surface area analytical technique
BIC	Bushveld Igneous Complex
BMS	Base Metal Sulphide
Ca	Calcium
Ca^{2+}	Free calcium ions in solution
CaO	Calcium-oxide
CCS	Carbon Capture and Storage
CO_2	Carbon dioxide
Disseminated sulphides	Fine sulphide mineral grains that are sparsely distribute throughout the rock
FeO	Ferrous-oxide
GHG	Greenhouse Gasses
Gt	Giga-metric tons
Kt	Thousand tons
MgO	Magnesium-oxide
mt	metric tons
PGE	Platinum Group Element
PGM	Platinum Group Metal
QEMSCAN	Quantitative Evaluation of Mineralogy through Scanning Electron Microscopy – Mineralogical analysis
QXRD	quantitative X-ray Fluorescence spectrometry
RCO_2	Tons of rock required to sequester 1 ton of CO2
UG-2	Upper Group 2 Reef
Wt%	Weight
XRD	X-ray diffraction – Mineralogical analysis technique
XRF	X-ray Fluorescence spectrometry – Element analysis technique

Definition of terms

Accessory mineral	Mineral present in very low quantities and not important in the classification of the rock
Alteration	Change in the original mineral composition of a rock
Felsic	Descriptive of a light-coloured igneous rock rich in high Si and Al minerals such as quartz and feldspar
Sequesterable	Greenhouse gas emissions that have the potential to be stored in order to separate them from the atmosphere
Carbonatable	Minerals that have the potential to be altered to carbonates via natural or engineered processes
Mafic	Igneous rocks have low silica 45 - 52% and typically high iron - magnesium content
Ultramafic	Igneous rocks with less than 45% silica, contain high iron-magnesium content, and consist of 90% mafic minerals

CHAPTER 1

INTRODUCTION

1.1. Background and Motivation

Anthropogenic carbon dioxide (CO_2) is principally emitted from the burning of fossil fuels, such as those used for electric power generation where large point sources emit a continuous increasing amount per year.

Carbon dioxide Capture and Storage (CCS) is considered one of the options for reducing atmospheric emission of CO_2 from human activities as this is seen to be a significant option for climate change mitigation. CCS involves the use of technology, firstly to collect and concentrate the CO_2 produced in energy-related sources, transport it to a suitable storage location, and then store it away from the atmosphere for long periods of time. Two opportunities for CO_2 storage exist for CCS. The first is mineral carbonation and geological storage, which requires converting CO_2 to solid inorganic carbonates, while the second option is the industrial use of CO_2, either directly or as feedstock for production of various carbon-containing chemicals (Jacobs, 2011).

Geological storage, also known as in-situ carbonation, is achieved when CO_2 is infused into stable geological formations. Little or no monitoring is involved and end results are achieved at a very slow rate, implying that the rate of reaction occurs over geological time scale (IPCC, 2002; Baer, 2003; Dooley and Wise, 2003; Huijgen, 2003; Metz et al., 2005). Conversely, mineral storage, an ex-situ carbonation procedure is relatively faster in terms of its reaction rate. It is a well monitored procedure and end results are obtained at a more rapid rate with the aid of certain catalysts (Jacob, 2011; Pronost et al., 2011).

South Africa, a country dependent on coal energy for 93% of its electricity, is an energy-intensive state which generates approximately 400 million tonnes of CO_2 and significant volumes of industrial wastes yearly (Surridge and Cloete, 2009). This study will focus on the suitability of ultramafic - mafic tailings as a mineral storage reservoir where sequestration of CO_2 is based on the reactions between Ca-Mg-Fe silicates

such as olivine, pyroxene and plagioclase, to form carbonate analogues that are relatively inert and benign in surface reservoirs.

Important enabling factors in the reaction viability include mineral species, mineral composition, mineral structure, mineral proportions, grain size distribution, morphology and surface texture. Elucidation of these and other factors can provide an initial guide to the reactability of mineral tailings.

This research builds on an earlier pilot study undertaken by Vogeli et al., (2011), where a necessarily restricted sample of local platinum group metal (PGM) tailings were investigated, with the aim of ranking their potential to absorb CO_2 produced and stored in 95% pure form by the South African synfuels industry. Tailings produced by four PGM mining operations (Norplats, BRPM, Implats and Lonplats) that processed the Merensky Reef, were the focus of the Vogeli et al., (2011) study and it was considered appropriate to extend the study to other major mining operations, such as Anglo Platinum (the world's biggest producer).

The progressively increasing exploitation of the UG-2 chromitite, with its own mineralogical and textural peculiarities, has resulted in historical Merensky tailings becoming blends of the two contrasting products, with the future most probably being dominated by the UG-2. Access to Anglo Platinum operations also afforded the opportunity to sample a third very high tonnage producing resource in the form of the Platreef, which may well dominate this company's platinum group element (PGE) production for years to come.

A fourth Bushveld hosted Ni-Cu-PGE resource is being exploited at an ever increasing scale at Nkomati mine, operated by African Rainbow Minerals (ARM) and Norilsk Nickel Africa. An additional feature of Nkomati tails is their relatively high sulphide in comparison with those produced from the Merensky, UG-2 and Platreef ores. Finally another historically high sulphide bearing tailings dump occurs at the now closed O'okiep copper mine in Namaqualand, Northern Cape Province. Both of these operations were added to the more comprehensive list of sites sampled in this follow up study.

1.2. Statement of the Research Problem

Mine tailings produced by low grade, high tonnage operations are progressively increasing their environmental footprint across South Africa (as well as world-wide). They are often sources of a wide variety of environmental problems such as fine dust dispersal, slope instability, mud slides, and acid rock drainage (ARD), the last a well-known source of pollution of South Africa's increasingly fragile water supply. Traditionally, the approach has been to minimize the generation of acid waters, but it has also been recognized that acid reactions with Ca-Mg-Fe silicate minerals in tailings could render them more conducive to carbonation, since their surfaces become more reactive due to desilication.

Plant feed has been processed through the concentrator with the aim of maximising recovery through milling, screening and flotation, and apart from their responsibly managed disposal, limited attention has been given to their potential for recycling.

1.3. Significance of Study

This study looks to explore a combined solution to atmospheric CO_2 gas build-up and ARD, with Nkomati and O'okiep arguably being the main contributors to ARD due to their high sulphide content in this study. Rocks and mineral tailings produced by a collective number of South Africa's mining companies are composed of silicates, oxides and sulphides that have the potential to be recycled into a variety of innovative schemes designed to reduce their footprint. There is a possibility mineral recovery from historic dams most especially in the case of the PGE industry. South Africa's reputation as one of the leading producers of PGE worldwide consequently makes it one of the largest producers of industrial waste as compared to other mining industries. Coincidentally, this has resulted in the creation of a large number of platinum sampling points with majority located on the Western limb and one PGE sampling site situated on the Northern limb of the Bushveld Complex. Incorporation into building materials, road aggregates, agricultural applications, landfills, manufactured fillers and many other schemes have been proposed, all of which raise issues of technical viability and cost of effectiveness, and also addresses issues relating to the fate of tailings.

1.4. Scope of Study

This study will focus on designated Anglo Platinum operations comprising the Mogalakwena Platinum Mine, Amandelbult Section, Union Section and the Waterval Concentrator Plant. Dam 4 of the Impala Platinum Mine tailings facility will also be part of the scope related to this study. Nkomati Nickel mine's Main Mineralised Zone (MMZ) and Chromititic Peridotite Mineralized Zone (PCMZ) dams as well as historic O'okiep Copper Mine dams will be mineralogically characterized with special emphasis on the following features; mineral composition, particle size distribution and specific surface area. The potential for CO_2 sequestration of these mining operations will also be outlined. Representative samples in the form of mine feed, plant tails and plant samples will be collected with due prominence given to dam samples as dams could be real resources for carbon dioxide sequestration. Tailings dams are mostly made up of a blend of feeds originating from different plants. The variations in dam properties as a result of the mixture, could render them conducive to sequestration process.

1.5. Study Objectives

The objectives of the study are:

1. To improve the existing ranking scheme for mineral carbonation.
2. To examine the viability of the Nkomati and O'okiep dams for the purpose of mineral carbonation.
3. To explore procedures that allow possible recycling of the gangue to be incorporated into the design of the recovery and rehabilitation process.

1.6. Expected Outcome

It is anticipated that the results of this study will provide a platform for future engineering research into the creation of an appropriated mineral carbonation engineered facility. It is proposed to replace the traditional recovery method of milling and flotation with a modified procedure involving a flotation step followed by leaching that enables further PGE recovery and desilication of the gangue. Ultimately this activated gangue is processed through a carbonation circuit to achieve sequestration.

1.7. Dissertation Layout

The thesis will be structured in seven chapters, with contents in each chapters as described below:

Chapter 1 comprises of the introductory section of the thesis and includes the background, scope, significance and research objectives.

Chapter 2 gives the review of literature pertaining to the research. This chapter gives a vivid description of the study areas and the journey of PGM, copper and nickel ore and silicate gangue from several metres below the earth surface to the tailings dam. Carbon capture and storage with particular emphasis on CO_2 and its effect on this planet are reviewed in the section. Preceding pilot study and previous work relating to this study have been covered under this chapter.

Chapter 3 describes the detailed analytical and experimental techniques used in this research. This section provides a comprehensive account of methods, equipment, and techniques employed in the research. In addition, sample types and material used in this study are mentioned in this section.

Chapter 4 depicts the results obtained from the previous chapter. Data from the analytical techniques employed and the results obtained from experiments performed in the third chapter, are presented in the form of charts, graphs, tables and micrographs, providing an uncomplicated approach to data presentation.

Chapter 5 gives a precise interpretation and discussion of results from techniques and experiments performed.

Chapter 6 draws conclusions from the discussion of the results and recommendations for future work.

Chapter 7 provides all the references and the appendices used in this study.

CHAPTER 2

LITERATURE REVIEW

2.1. Introduction

The literature review is structured into five distinctive parts, each tackling different aspects of this research. The first part provides an overview of Carbon Capture and Storage (CCS) and the methods of storage of carbon dioxide, a greenhouse gas thought by some to be exponentially increasing the rate of Climate Change. The second section gives an introduction to the concept of mineral carbonation, highlighting the various technologies, costs and economic potential involved in the carbonation process. The third evaluates the availability of feedstock for mineral carbonation in South Africa with more emphasis on waste products of mining ultramafic to mafic-hosted ore deposits (mine tailings). The fourth section outlines the distinctive mineral processing techniques employed at the mines whose tailings were the subject of the current study. Flow diagrams will be used to explain and assess any variation between the mineral processing techniques in terms of their milling and grinding patterns.

Section five, will looking into the various mineral processing techniques and the nature of tailings generated. A final section is a summary and highlights the state of knowledge that has led to the current study.

2.2. Carbon Capture and Storage (CCS)

CO_2 emissions due to fossil fuel combustion, have been ever-increasing since the 16^{th} century. As the world's population increases, so does the demand for power and energy. A study conducted by Bernstein et al., (2007) indicates that the increase in global average atmospheric CO_2 has increased from 280 ppm in the 1750s to 389 ppm in 2010. The increase in atmospheric CO_2 over the last two and a half centuries has been attributed to two major anthropogenic forcing fluxes with the major being the emission from fossil fuel combustion and industrial processes and the other anthropogenic alteration attributed to land use change (Yamasaki, 2003; Flannery, 2005; Canadell et al., 2007; Shakun et al., 2012).

As reported by the International Energy Agency (2011), if no proactive mitigation action is taken, energy-related CO_2 emissions are likely to be 40-110% higher in 2030

than they were in 2000 (23.5 Gt CO_2 per annum). The latest figures indicate world CO_2 emissions from fuel combustion were 29.4 Gt in 2008. By 2100, atmospheric CO_2 concentrations could reach 540-970 ppm resulting in a global mean temperature rise of 1.8-4°C (Houghton et al., 2001; Solomon et al., 2007). A temperature increase of such enormity would have extreme implications for water and food availability, human health, ecosystems, coastlines and biodiversity which sums up the concept of climate change in the study conducted by Bernstein et al., (2007).

Based on scientific study, it is evident that modern-day emission of CO_2 is primarily from the burning of fossil fuels in large combustion units such as those used for electric power generation. There is a need to effectively manage the large point sources of CO_2 emission from power plants and large industrial processes in order to significantly mitigate climate change. This process forms a fundamental part of the concept of carbon capture and storage (CCS).

A report by the International Panel for Climate Change (2002), considers CCS as an option in the portfolio of mitigation actions for stabilization of atmospheric greenhouse gas concentrations. CCS is a three step process which involves separation of CO_2 from industrial and energy-related sources or from gaseous waste streams, transport to storage locations and long-term isolation from the atmosphere through carbon storage or sequestration (Metz et al., 2005; Cooney, 2012). A fourth step (monitoring) was made know by Heinrich et al., (2004). Once CO_2 is stored away from the atmosphere, it should be monitored. The main purpose of monitoring is to make sure that the sequestration operation is effective, implying that almost all the CO_2 stays out of the atmosphere (Herzog, 2010).

Praetorius and Schumacher (2009), report that CCS is not a new concept. They further state that technologies and practises associated with carbon capture and transport, and some types of carbon sequestration, geologic storage for example, have been in commercial operation within various industries for 10-50 years. CO_2 capture systems are present in coal and natural gas fired power generation, coal gasification facilities and various industrial facilities. The United States for instance, have more than 6200 km of dedicated CO_2 pipelines and the oil industry has been injecting CO_2 into reservoirs to enhance oil recovery (EOR) since the 1970's (Dooley et al., 2009).

CCS is attracting growing interest around the world, particularly in countries where electricity generation and export income are heavily dependent on fossil fuels, such as China, Western Europe, Australia, Canada and the US (van Alphen et al., 2010). Analysis by Metz et al., (2005) indicate that CCS may contribute up to 15-55% of the cumulative global climate change mitigation effort by 2100 and that the inclusion of CCS in a mitigation portfolio could reduce the costs of stabilizing atmospheric CO_2 concentrations by close to 30%.

An in-country inventory of carbon dioxide emissions revealed that of the more that 400 million tonnes of annual carbon dioxide emissions in South Africa as stated in chapter one, approximately 60% was sequestrable (Figure 2.1). Of the sequestrable emissions, about 65% originated from coal fired electricity generating stations (Surridge and Cloete, 2009).

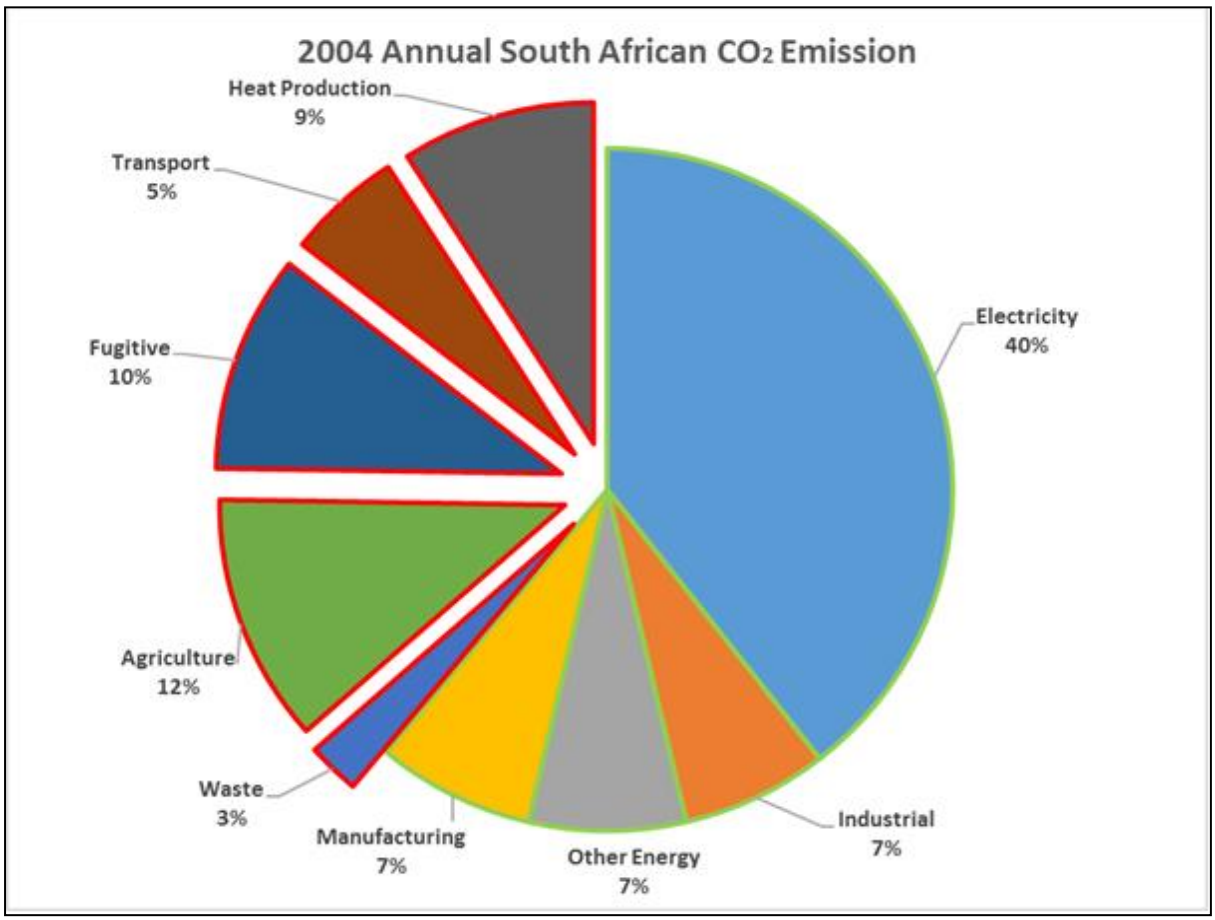

Figure 2. 1: Total South African CO_2 emission in the year 2004 indicating the proportion of sequestrable sources highlighted in green and non-sequestrable sources in red (modified from Surridge and Cloete, 2009).

2.2.1. CO_2 Separation from energy related sources

CO_2 has been captured from industrial process streams for 80 years, although most of the CO_2 that was captured was vented to the atmosphere because there was no incentive or requirement for storage (Kohl and Nielsen, 1997). Presently, capture is generally required to be able to economically transport and store the CO_2 (Rubin, 2003; Herzog, 2010). Metz et al., (2005) gave details of a number of CO_2 separation technologies. Observations made during their study stated that CO_2 may be captured post-combustion, pre-combustion, from oxy-fuel combustion or from industrial process streams. Technologies used in these systems include the separation of CO_2 with sorbents, membranes, cryogenic distillation and chemical-looping with chemical absorption being the most common method used.

2.2.1.1 Post-combustion CO_2 capture

This is the capture of CO_2 from flue gases produced by combustion of fossil fuels and biomass in air. With this type of capture, flue gas is passed through equipment, separating most of the CO_2 instead of the traditional practice of discharging it directly to the atmosphere. The CO_2 is then fed to a storage reservoir and the remaining flue gas is discharged to the atmosphere as shown in Figure 2.2. Post-combustion capture can best be applied to oil, coal and gas power plants (IPCC, 2002; IEA WEO, 2004; IEA CCC, 2005).

2.2.1.2 Oxy-fuel combustion CO_2 capture

In oxy-fuel combustion, nearly pure oxygen is used for combustion instead of air, resulting in a flue gas that is mainly CO_2 and H_2O. If fuel is burnt in pure oxygen, the flame temperature is excessively high, but CO_2 and H_2O-rich flue gas can be recycled to the combustor to moderate this. Oxygen is usually produced by low temperature (cryogenic) air separation and novel techniques to supply oxygen to the fuel, such as membranes and chemical looping cycles are being developed. The power plant systems of reference for oxy-fuel combustion capture systems are the same as those noted above for post-combustion capture systems (IPCC, 2002).

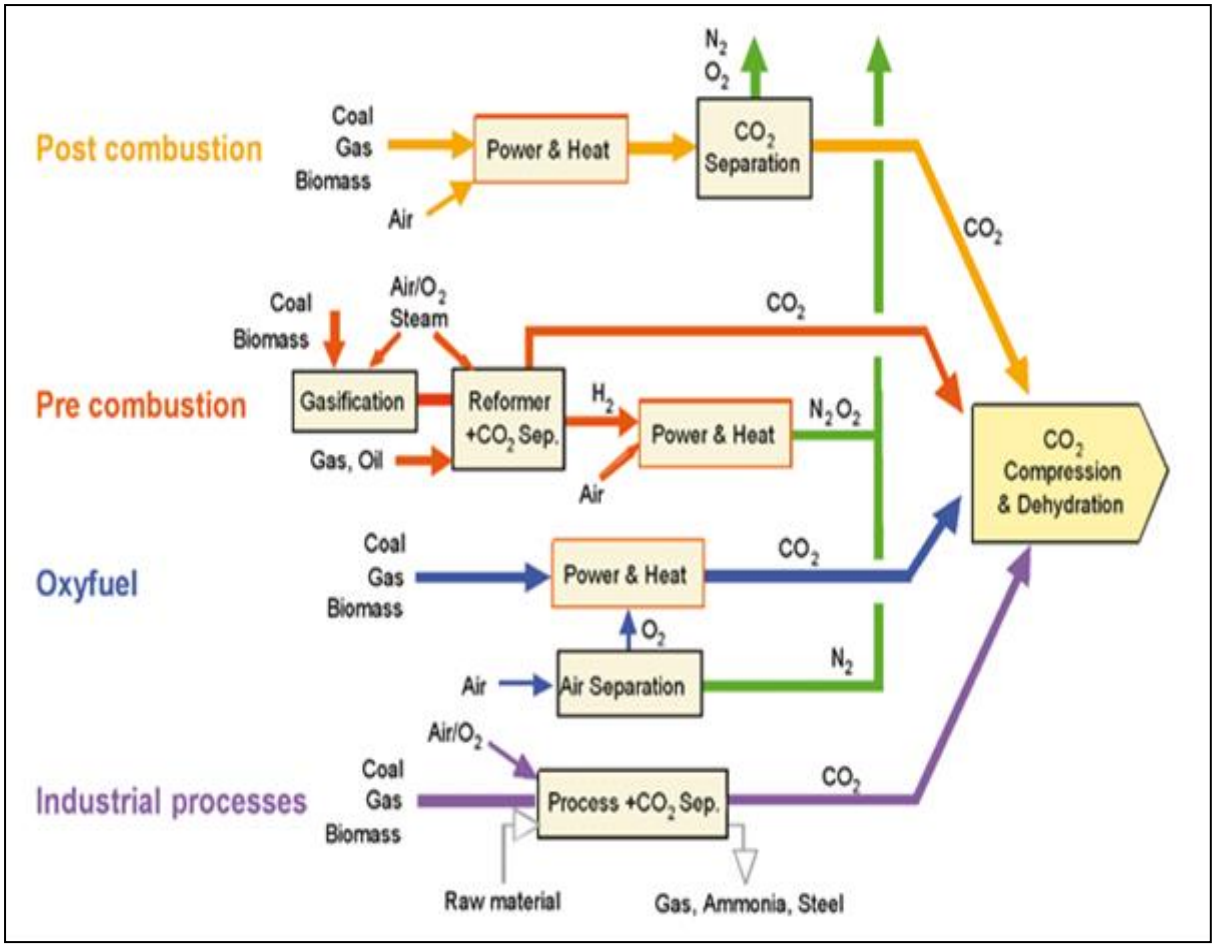

Figure 2. 2: A schematic diagram showing the types of CO_2 capture systems (adapted from British Petroleum, 2004).

2.2.1.3. Pre-combustion CO_2 capture

Pre-combustion capture involves reacting a fuel with oxygen or air or steam to make it a 'synthesis gas (syngas)' or 'fuel gas' composed of carbon monoxide and hydrogen. The carbon monoxide is reacted with steam in a catalytic reactor, called a shift converter, to produce CO_2 and more hydrogen (Figure 2.2). The CO_2 produced from the shift converter is then separated, by a physical or chemical absorption process, resulting in a hydrogen-rich fuel which can be used in many applications, such as boilers, furnaces, gas turbines, engines and fuel cells (IPCC, 2002; Gibbins, et al., 2005;). Reference systems for the application of pre-combustion capture include existing natural gas, oil and coal-based syngas/hydrogen production facilities (Metz et al., 2005).

In South Africa, approximately 30 million tonnes per year of about 95% concentration carbon dioxide is collected and purified by the synthetic fuel industry which includes coal and gas to liquid produced by Sasol and gas to liquid by PetroSA. Approximately

95% pure CO_2 is therefore readily available and merely requires pressurisation before being put to use or before transmission to an injection site (Engelbrecht et al., 2004; Surridge and Cloete, 2009).

2.2.2. Transportation of CO_2 captured

Once CO_2 has been separated and captured as part of CCS, it must be transported to a storage area. Practical modes of overland transport include motor carrier (tankers), rail, and pipeline. The most economic method of transport depends on the locations of capture and storage, distance from source to sink, and the quantities of CO_2 to be transported (Figure 2.3) (Sarv, 2001; Praetorius and Schumacher, 2009; Norisor et al., 2012).

An infrastructure must be developed to move CO_2 from its source to the storage site. Transporting large quantities of CO_2 is most economically achieved with a pipeline (Sarv, 2001). An important technical consideration in the design of CO_2 pipelines is that the CO_2 should remain above its critical pressure. Recompression is often needed for pipelines over 150 km length. However, it may not be needed if a sufficiently large pipe diameter is used (Hattenbach et al., 1999).

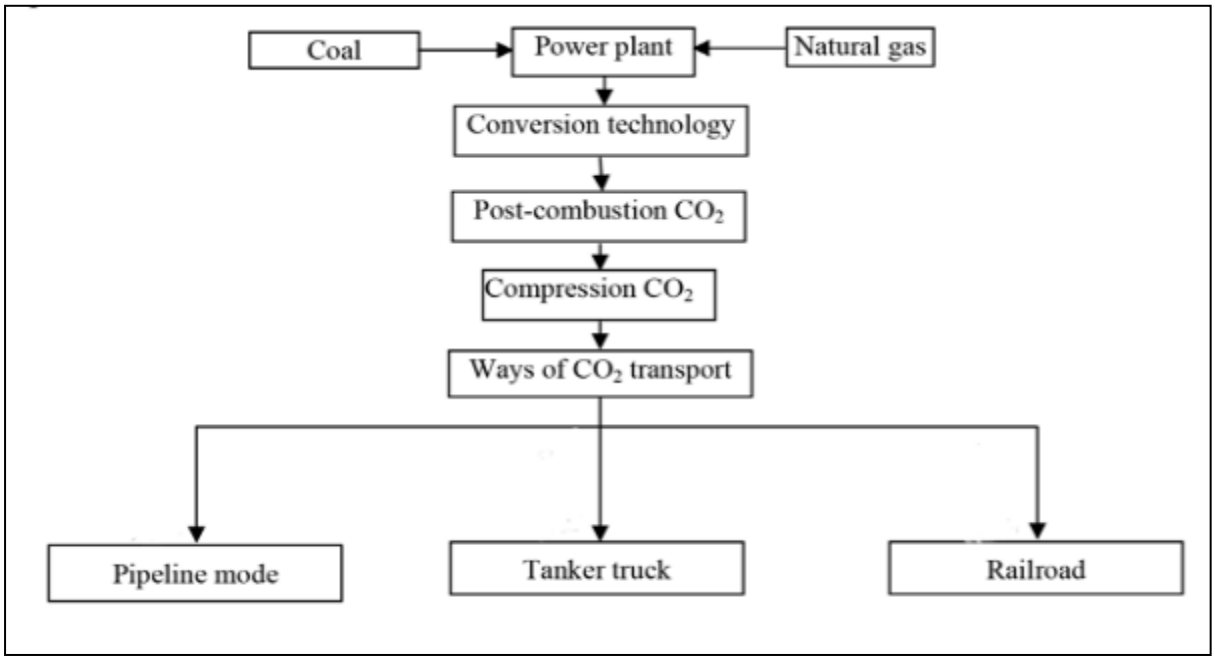

Figure 2. 3: CCS CO_2 transportation modes (modified from Norisor et al., 2012).

Natural gas pipelines are a good analogue to a CO_2 pipeline network for purposes of understanding costs. First, for a given pipeline diameter, the cost of construction per unit distance is generally lower, the longer the pipeline. Second, pipelines built nearer

populated areas tend to be more expensive. Finally, road, highway, river, or channel crossings and marshy or rocky terrain also greatly increase the cost (True, 1990; de Figueiredo et al., 2007).

Seiersten (2001), states that a transportation infrastructure that carries carbon dioxide in large enough quantities to make a significant contribution to climate change mitigation will require a large network of pipelines.

There have been few studies that have addressed the cost of CO_2 transport in detail. However, earlier work by Svensson et al., (2004), identified pipeline transport as the most practical method to move large volumes of CO_2 overland.

As discussed in the above section (2.2), CO_2 has already been separated and presumably captured into metal canisters. The transportation would therefore take a different approach. It would be impractical to re-channel the already captured CO_2 into the pipelines. An appropriate suggestion would be to transport the jars of CO_2 to the storage area by road using trucks.

2.2.3. CO_2 Storage

Storage or sequestration of CO_2 can be accomplished through geological storage, ocean storage, industrial use and mineral sequestration. CO_2 is generally proposed to be injected to depths greater than 800 m, where it is in a super critical state (Matter and Keleman, 2009).

2.2.3.1 Geological storage

The storage of CO_2 within geological formations is regarded as a natural process in the Earth's upper crust. CO_2 derived from biological activity, igneous activity and chemical reactions between rocks and fluids accumulates in the natural subsurface environment as carbonate minerals, in solution or in gaseous or supercritical form, either as a gas mixture or as pure CO_2 (Gunter et al., 1993 ; Korbol and Kaddour, 1994; Holloway, 1997; Cook, 1999 and Bachu and Shaw, 2005). According to Liu and Zhao (1999), the lithosphere acts as an overwhelmingly dominant natural CO_2 sink with 99% of the carbon trapped in the rocks of the Earth's crust. Yuan (1997), further states that these carbonate rocks cover an area of about 22 million km^2 worldwide, with over 90% of rock-forming carbonates consisting of calcite ($CaCO_3$) and dolomite

($CaMg(CO_3)_2$). South African carbonate rocks predominantly consist of dolomite and minor occurrences of limestone (Figure 2.4).

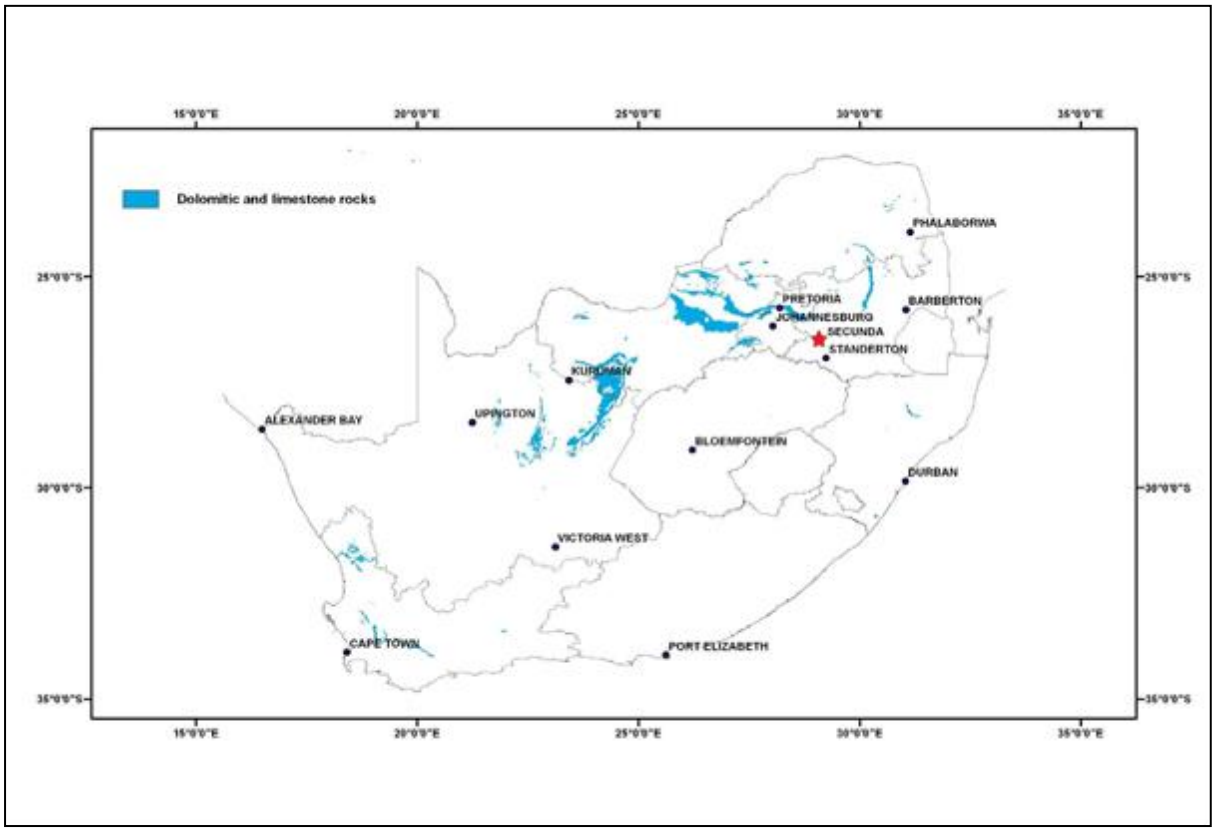

Figure 2. 4: : A distribution of carbonate rocks on South Africa with the main source of CO_2 (red star), Secunda (modified from Doucet, 2011).

As a result of the ever-increasing emission of CO_2, Heinrich et al., (2004) have valid proof that there are opportunities available to store CO_2 in geological formations in a variety of underground geological settings in sedimentary basins, oil fields, depleted gas fields, deep coal seams and saline formations are all possible storage formations as shown in Figure 2.5 by Priestnall (2013). Metz et al., (2005) also concluded that there was available evidence that suggested that there was a technical potential of at least about 2000 Gt CO_2 of storage capacity in geological formations. This is a large number, about two orders of magnitude greater than total annual worldwide CO_2 emissions, indicating the potential of CCS to be a significant CO_2 mitigation strategy.

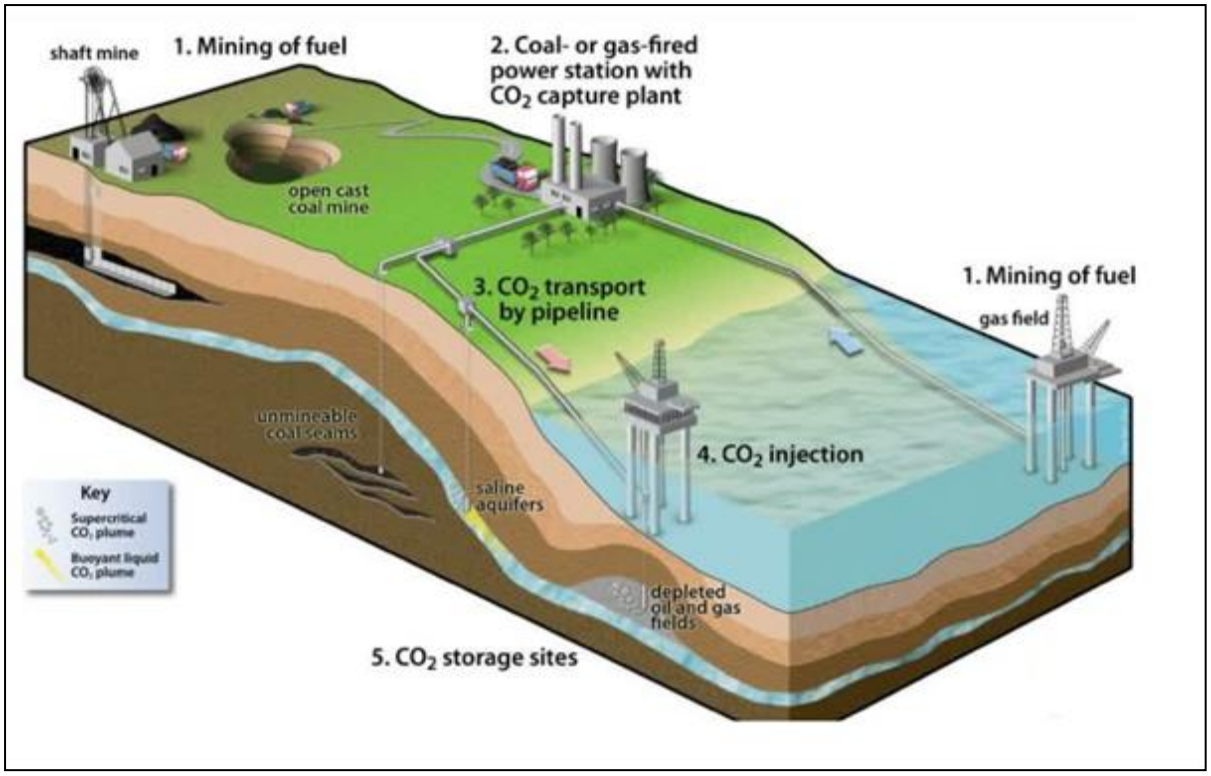

Figure 2. 5: Underground geological storage options for CO_2 as a climate change mitigation measure (from Priestnall, 2013).

A study conducted by Surridge and Cloete (2009) claimed that South Africa should concentrate its efforts on geological storage of CO_2. Their study targeted areas such as the 55m thick Vryheid Formation, located in KwaZulu Natal, which forms part of the coal deposits and made up of carbonaceous shale and sandstone with dull coal seams (Green and Smith, 2012). Other targeted areas included geological formations within the Free State province. A combination of the above mentioned potential storage sites was estimated to store a total of 287 Gt CO_2. It was further argued that South Africa has theoretically four to eleven times more capacity than required for one hundred years of storage of current sequestrable emissions.

2.2.3.2 Ocean storage

The Earth's oceans cover over 70% of the Earth's surface with an average depth of about 3,800 metres; hence, there is no practical physical limit to the amount of anthropogenic CO_2 that could be placed in the ocean. However, the amount that is stored in the ocean on the millennial time scale depends on oceanic equilibration with the atmosphere.

Deductions from ocean modelling suggest that injected CO_2 will be isolated from the atmosphere for several hundreds of years and that the fraction retained tends to be larger with deeper injection. Additional concepts to prolong CO_2 retention include forming solid CO_2 hydrates and liquid CO_2 lakes on the sea floor, and increasing CO_2 solubility by, for example, dissolving mineral carbonates. Over centuries, large scale ocean water mixing can disturb isolation of injected CO_2 and cause leakage to the atmosphere (Akai et al., 2004; Barry et al., 2004).

Experiments show that added CO_2 could harm marine organisms. Effects of elevated CO_2 levels on individual organisms have mostly been studied on time scales up to several months near the ocean surface. Observed phenomena include reduced rates of calcification, reproduction, growth, circulatory oxygen supply and mobility as well as increased mortality over time. In some organisms these effects are seen in response to small additions of CO_2. Immediate mortality is expected close to injection points or CO_2 lakes (Hill et al., 2004).

2.3. Mineral Carbonation

Mineral carbonation was first mentioned as a CO_2 binding concept by Seifritz (1990). A few years later the concept of binding CO_2 in calcium and magnesium carbonate minerals was further investigated in the United States by Dunsmore (1992) and subsequently this process, also known as enhanced natural weathering, was scrutinized in more detail by Lackner and co-workers at Los Alamos National Laboratory (LANL) (Lackner et al., 1995; Goff and Lackner, 1998).

Research around mineral carbonation has accelerated and divided into several different CO_2 sequestration approaches, mainly direct (where the carbonation of the mineral takes place in a single process step) and indirect methods (where calcium or magnesium is first extracted from the mineral and subsequently carbonated). These primarily aim at ex situ processing in a dedicated processing plant (as opposed to *in situ* carbonation by injection of CO_2 into geological formations) (Goff et al., 1997; Dahlin et al., 2000).

Mineral carbonation is the reaction of CO_2 with a metal oxide bearing material to form insoluble but stable carbonates. The most reactive elements are calcium and magnesium as opposed to sodium and potassium. This is because sodium and potassium carbonates are soluble in water. Iron has also been suggested for

carbonation, but as it is a valuable mineral resource sought after for other purposes, it is less suitable for large-scale carbonation implementations (Huijgen and Coman, 2005). Silicate-rich geological materials are the targets of CO_2 sequestration. These include minerals such as talc, pyroxene, plagioclase, olivine, serpentine, chlorite, mica and clays, or rocks containing them (Table 2.1). In addition to the abundant naturally occurring magnesium and calcium containing minerals, there are also industrial solid residues that contain large amounts of Mg, Ca and even Fe.

Table 2. 1: A collection of rock and mineral types suitable for mineral carbonation (updated from Sipilä et al., 2008).

MINERAL/ROCK	FORMULA/COMPOSITION
Dunite	Predominantly Olivine
Basalt	Olivine, pyroxene, plagioclase
Limestone	$CaCO_3$
Eclogite	Garnet, pyroxene, mica
Feldspar	$CaAl_2Si_2O_8$ (Plagioclase Feldspar)
Forsterite	Mg_2SiO_4
Ilmenite	$FeTiO_3$
Listwanite	Carbonated serpentinite
Magnetite	Fe_3O_4
Olivine	$(MgFe)_2\ SiO_4$
Pyroxene	$CaMgSi_2O_6(FeAl)$
Serpentine	$Mg_3Si2O_5(OH)_4$
Serpentinite	serpentine
Talc	$Mg_3Si_4O_{10}\ (OH)_2$
Wollastonite	$CaSiO_3$

Mineral carbonation reactions (such as in Equation 1) are exothermic and occur spontaneously in nature, although on geological time scales (Metz et al., 2005). The challenge is to accelerate carbonation and exploit the heat of reaction with minimal energy and material losses.

$$(Mg, Ca)_xSi_yO_{x+2y} + xCO_2 \rightarrow x(Mg, Ca)CO_3 + ySiO_2 + \text{heat} \qquad [1]$$

2.3.1. In-Situ mineral carbonation

Substantial energy is required to regenerate CO_2 from carbonates. The in-situ carbonation process is closely connected to the geological storage option discussed in Section 2.2.3.1 as it involves the injection of CO_2 into underground reservoirs. The difference is that, in-situ mineral carbonation explicitly aims at producing a reaction with the CO_2 to form carbonates with suitable minerals present rocks such as basalts and peridotites (Kelemen and Matter, 2008; Gislason et al., 2010). The advantages of this route over ex-situ are that mining, transporting and pre-treatment of the minerals as well as the use and recovery of additives are not required (Oelkers et al., 2008). However, it also presents a number of limitations, including the excessive use water for CO_2 injection, and the critical need for impermeable cap rocks. Lackner (2003) introduces another limitation of this process route by stating that that the in-situ method is the most expensive of all methods.

2.3.2. Ex-situ mineral carbonation

On the contrary, the ex-situ process route refers to the original approach to mineral carbonation, which involves the above ground carbonation of natural minerals and industrial alkaline wastes via industrial chemical processes (Figure 2.6). For natural minerals, this scenario includes the mining, crushing and milling of the mineral-bearing ores prior to carbonation (Maroto-Valer et al., 2005; Renforth et al., 2011).

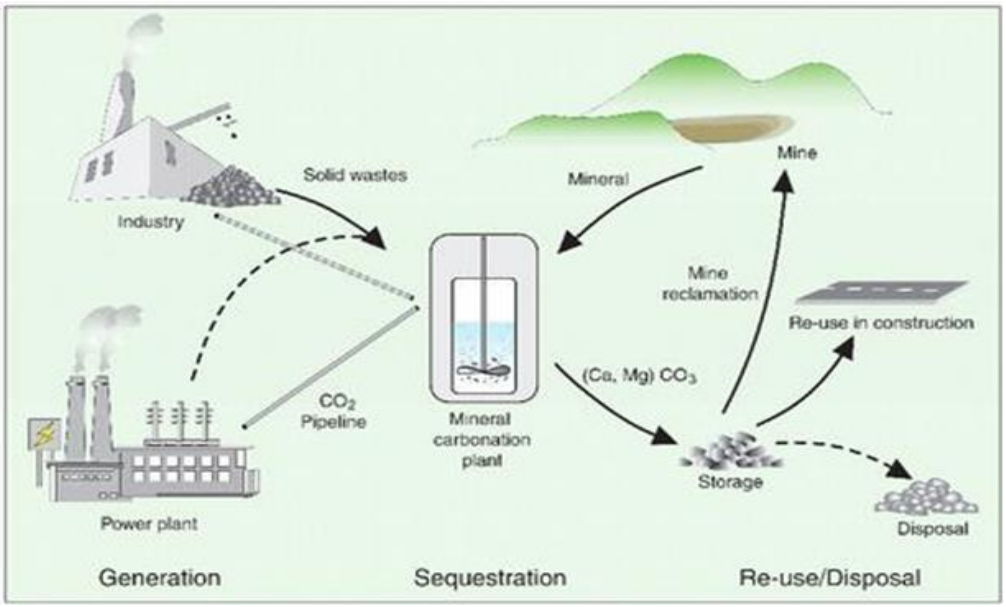

Figure 2. 6: : A schematic diagram of the ex-situ mineral carbonation process (from Metz et al., 2005).

2.3.2.1 Direct carbonation

Gas-solid carbonation

This can be defined as the direct reaction between gaseous CO_2 and solid mineral. It is so far the most uncomplicated mineral carbonation process route. However, the reaction rates are very slow compared to other ex-situ routes (Baciocchi et al., 2009).

Aqueous carbonation

Direct aqueous carbonation involves three coexistent mechanisms in a single reactor. These include (i) aqueous dissolution of CO_2, and (ii) aqueous dissolution of Ca- and Mg-bearing mineral phases, with (iii) precipitation of carbonates. It is generally accepted that silicate dissolution is the rate-limiting step (Huijgen, 2006). For this reason, relentless effort has focused on improving the kinetics of silicate dissolution using a wide range of additives and by varying operating conditions such as temperature, pressure, CO_2 concentration, solid to liquid ratio, and particle size (Baciocchi et al., 2009b).

Researchers have recently investigated this route for the conversion of minerals. For instance forsterite (Kwak et al., 2010), brucite (Zhao et al., 2010) and alkaline wastes such as stainless steel slag, bottom ash (Baciocchi et al., 2009a, 2009b), alkaline paper mill waste and coal-combustion fly ash (Perez-Lopez et al., 2008), waste cement kiln dust (Huntzinger et al., 2009), lignite fly ash (Back et al., 2008) with and without the use of additives.

2.3.2.2. Indirect carbonation

Indirect carbonation is a complex route whereby the overall ex-situ process is divided into two or more steps. For instance, the extraction of Ca and Mg from the feedstock, the dissolution of CO_2 as in the case of aqueous carbonation (Section 2.3.2.1) and the precipitation of carbonate materials take place as separate steps in different reactors (Blencoe et al., 2004; Baldyga et al., 2010).

Indirect gas-solid carbonation

It was initially revealed that direct gas-solid carbonation suffers from poor reaction kinetics. A limitation of such magnitude can possibly be overcome by adopting an indirect staged gas-solid dissolution/carbonation process (Zevenhoven et al., 2006).

Indirect aqueous carbonation

The characteristic of indirect aqueous carbonation is the adoption of two aqueous separate steps for the extraction and the carbonation of Ca and/or Mg respectively. The advantage of this route is that the two steps can be optimized separately, incorporating additional steps if needed. This approach makes use of additives to optimize the operating conditions. A challenge which is generally experienced in this route is the recovery of the additives. However, it improves the feasibility of producing valuable pure materials for further applications (Gerdemann et al., 2007; Lim et al., 2010).

2.3.3. Natural Mineral Carbonation

Natural accumulations of reasonably pure CO_2 are found in a range of geological settings all over the world, more especially in sedimentary basins, faulted areas and in quiescent volcanic structures. Natural mineral carbonation occurs in a number of different types of sedimentary rocks, such as limestone, sandstone and dolomite. A variety of seals (mudstone, shale, salt and anhydrite) are favourable for the natural carbonation process.

Evidence of natural mineral carbonation has been reported in studies by Nwangwe (2009) and Mathivha (2010), who have described dolerite dykes and sills intruding coal seams as a result produced a thermal metamorphic effect in the surrounding coal and were later altered by fluids sourced from the original magma and surrounding country rock sediments in the Highveld and Witbank coalfields of South Africa. Dolerites are extremely abundant throughout South Africa. They are coarser grained in nature, sub-volcanic equivalent of basalts, and rich in divalent cation-bearing minerals such as olivine and pyroxene (Mg-Ca-Fe).

Ringane (2003) examined the dolerite dykes that penetrated the coal seams at New Denmark Colliery. The outcome of the study showed ferrous carbonate formation as a result of the hot doleritic magma reacting with the coal (Figure 2.7).

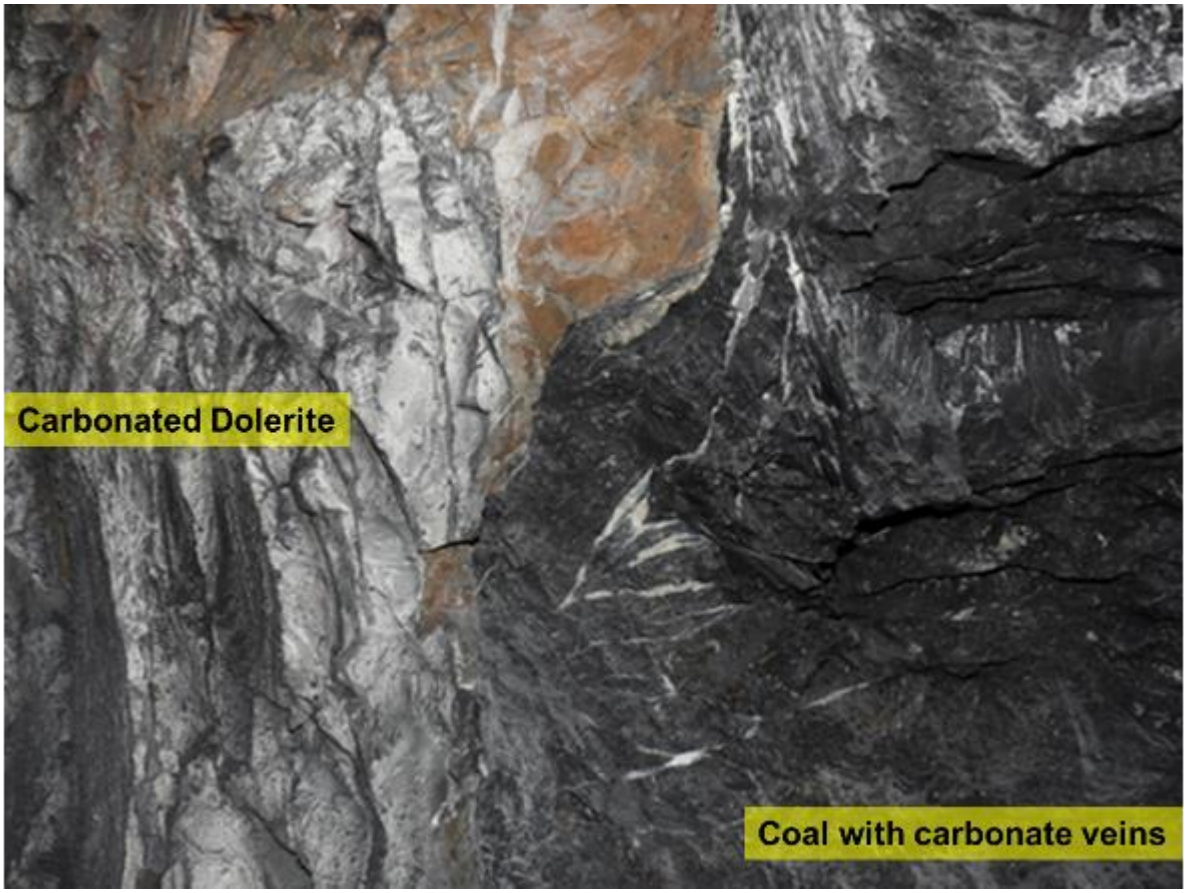

Figure 2. 7: Evidence of carbonate formation at New Denmark Colliery (from Ringane 2003).

Two dolerite samples from Witbank Coalfields and Sasolburg were further examined by du Plessis (2008). Investigation into the 20m Witbank Coalfield sample indicated that biotite was presented and displayed evidence of chloritization with serpentinized olivine. The sample exhibited phenocrysts of olivine, plagioclase and augite pyroxene. A fine groundmass of magnetite, and ilmenite was also evident. Crystallization of the magma was suspected to be rapid as fine grained chilled margins being a main indicator. A 60m thick Sasolburg sample revealed that macrophenocrysts of augite pyroxene and olivine crystal with microphenocryst of plagioclase. Olivine and augite were the main minerals. Slow cooling of magma was believed to have occurred due to the coarse nature of the dolerite.

The replacing carbonates have ternary Ca-Mg-Fe compositions that reflect their hosts, confirming the in situ replacement by fluids migrating into the solidified dolerite. The degree of replacement varies from essentially complete at the contacts but reduces inwards, with dykes wider than about 3m retaining unaltered interiors. The degree of

carbonation in the dyke is dependent on its distance from the contact, as well as the number of joints to allow fluid percolation (Meyer, 2011).

The CO_2 emitted during the reaction with silicates in the dolerite to form the carbonate. The high temperature magmatic intrusions were capable of igniting the coal and presumably generating significant CO_2 in what is essentially a natural fossil fuel conversion process. Some of this CO_2 could have escaped, the extensive carbonate alteration of the adjacent dolerite where it intersected the coal, clearly demonstrates a form of internal self-sequestration. The alteration process appears to be substantial enough for volume pseudomorphic replacement of the dyke from the margins inwards, with the order of preferential carbonation being olivine, followed by pyroxenes and Fe-Ti oxides, and finally feldspar as shown in Figure 2.8. Replacement was complete in narrow dykes (< 1 m) and partial in thicker intrusions, where the degree of alteration dropped towards their interiors. Carbonation was moreover restricted to where the intrusions cut the coal seams (Meyer, 2011).

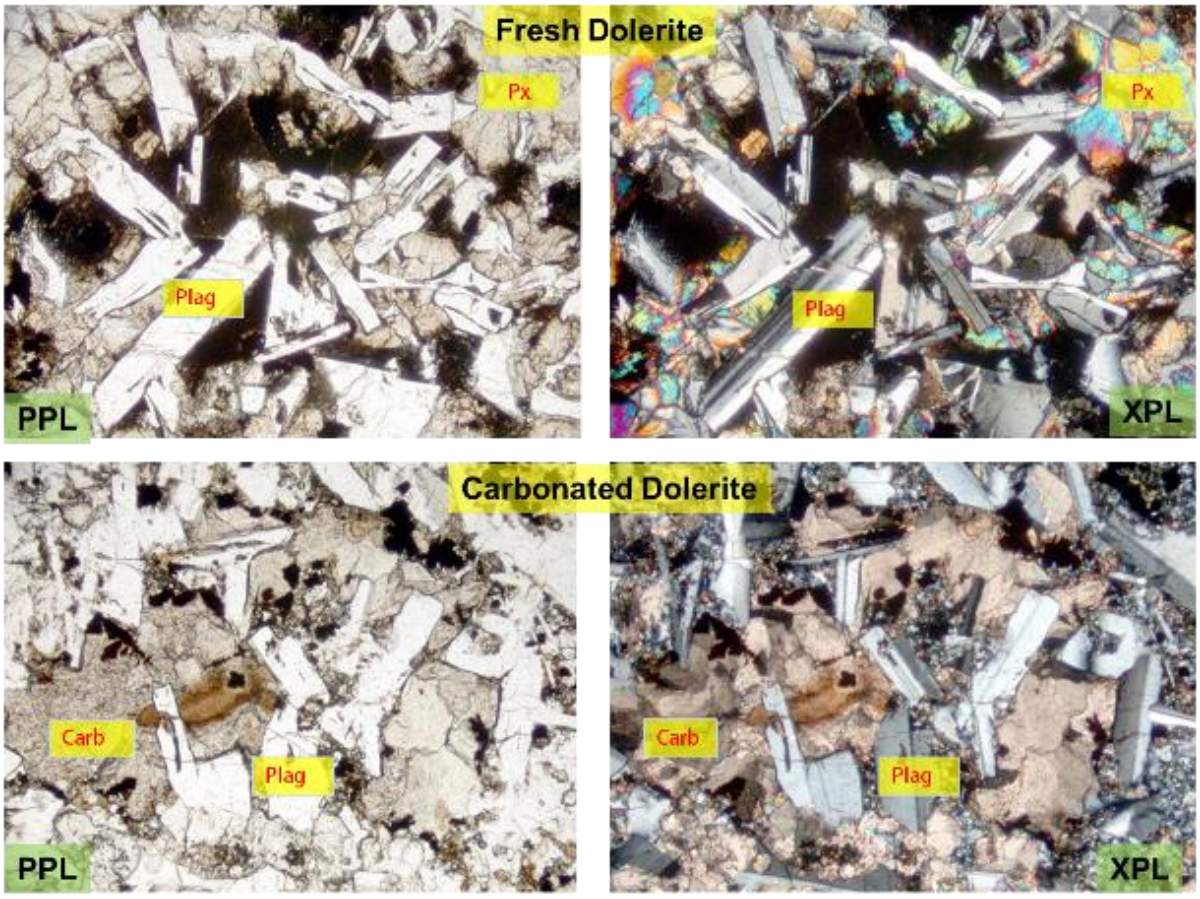

Figure 2. 8: Thin sections showing mineral alterations under plane polarized light (PPL) and cross polarized light (XPL). Plagioclase (Plag); Pyroxene (Px); and Carbonated Dolerite (Carb) are seen in the thin section (from Ringane, 2003).

Investigations into the geochemical factors of this natural carbonation process can give insight into its use in industrial applications. The road pavement and construction industries where 'detrimental carbonation' of the dolerite occurs is a cause for concern as a water-driven action and not the free access to CO_2 creates a powdery loose layered disintegration in dolerite. Repeated wet-dry cycles in construction curing would render the inconsistent to work with (Kleyn and Bergh, 2008).

Even though dolerite dykes are abundant all over the country, they are not massive like their basalt flow equivalents, and therefore are unlikely to be suitable for in situ mineral carbonation. Meyer (2011), lays more emphasis on this unlikelihood by stating that the carbonation process would have to be enhanced by near magmatic temperatures, abundant fluid and prolonged geologic time for dolerite to absorb CO_2 produced by coal metamorphism.

2.4. Raw Material Availability in South Africa

Silicate rocks including mafic and ultramafic rocks contain high amounts of Ca, Mg and Fe and have low Na and K. Ca and Mg are the most abundant alkaline earth metals and, therefore, are generally selected for ex-situ mineral carbonation purposes. South Africa hosts many mafic-ultramafic bodies distributed through the rock record and across the country, which could possibly serve as proposed raw material for mineral carbonation.

2.4.1. Bushveld Igneous Complex

This igneous assemblage forms one of the remarkable geological occurrences in the world. Of particular importance is the Rustenburg Layered Suite (RLS), which intrudes the Transvaal Supergroup in the form of gigantic lopolith (Du Toit, 1954; Eales, 2001).

The RLS is predominantly ultramafic to mafic in composition and sub divisible into several Zones based on the presence of certain cumulus minerals (Cawthorn, 2006). At the base the Lower Zone is composed of olivine and Ca-poor orthopyroxene cumulates (peridotites, harzburgites and pyroxenites), while the overlying Critical Zone contains a transition from ultramafic to mafic rocks containing cumulus plagioclase. Another important feature of the Critical Zone is the development of numerous chromitite seams, which host fabulously rich deposits of Cr, Fe and also sulphide hosted Ni-Cu-PGE (Cawthorn, 1999b). Mining of these rich deposits have ultimately led to vast quantities of waste products (rock dumps and tailings) rich in many of the

minerals mentioned previously as appropriate feedstock for ex-situ mineral carbonation.

The Merensky Reef

This is regarded as a uniform reef type, with large variations occurring in reef thickness and mineralisation. The Merensky Reef is made up of rock forming minerals containing equal amounts of dark iron-magnesium silicate minerals and lighter calcium-aluminium-sodium silicate minerals which are commonly known as feldspathic pyroxenite. This is under and overlain by 5 to 15 mm discontinuous thin layers of chromite concentrations. The total thickness of this package is generally less than 30 cm. This zone, generally known as the Merensky pegmatoid, contains the base metal sulphide grains and associated platinum group minerals. The Merensky Reef has been traced for 300 km around the entire outcrop of the eastern and western limbs of the Bushveld Complex, and to depths of 5 km (Scoates and Freidman, 2008 ; Rose, 2011).

The Merensky Reef is made up of rock-forming minerals that principally contain orthopyroxene (~60 %), plagioclase feldspar (~20 %), clinopyroxene (~15 %), A sporadic distribution of phlogopite (~5 %), with olivine also evident (Table 2.2). There are secondary minerals such as talc, serpentine, chlorite and magnetite occurring extensively within the reef.

Table 2. 2: Major minerals of the Bushveld Complex and their composition (after Schouwstra et al., 2000).

Mineral Group	Mineral	Composition
Pyroxene	Enstatite	Mg, Fe silicate
	Augite	Mg, Fe, Ca silicate
Mica	Biotite	K, Mg, Fe, Al silicate
	Phlogopite	K, Mg, Al silicate
Chlorite	Chlorite	Hydrated Mg, Fe, Al silicate
Clay	Talc	Hydrated Mg silicate
Serpentine	Serpentine	Hydrated Mg, Fe silicate
Spinel	Chromite	Cr, Fe, Mg oxide
Sulphide	Pentlandite	Ni, Fe sulphide
	Chalcopyrite	Cu, Fe sulphide
	Pyrrhotite	Fe mono-sulphide
	Pyrite	Fe di-sulphide

Base metal sulphides found in the Merensky Reef, contain pyrrhotite (~40 %), pentlandite (~30 %), chalcopyrite (~15 %), and trace amounts of millerite (NiS), troilite (FeS), pyrite (FeS_2), and cubanite (Cu_5FeS_4). The major platinum group minerals are cooperite (PtS), braggite [(Pt, Pd, Ni) S], sperrylite ($PtAs_2$) and PGE alloys, although in some areas minerals such as laurite (RuS_2) can be abundant (Cawthorn, 1999b).

The UG-2 Reef

The UG-2 Reef is a platiniferous chromititic layer developed some 20 to 400 metres below the Merensky Reef (Figure 2.9). The chromitite is usually 1 m thick, however, it varies between 0.4 and 2.5 m. Thin chromitite seams of less than 20 cm in thickness appear in both the footwall and, more commonly, in the hanging wall rocks (Naldrett et al., 2012).

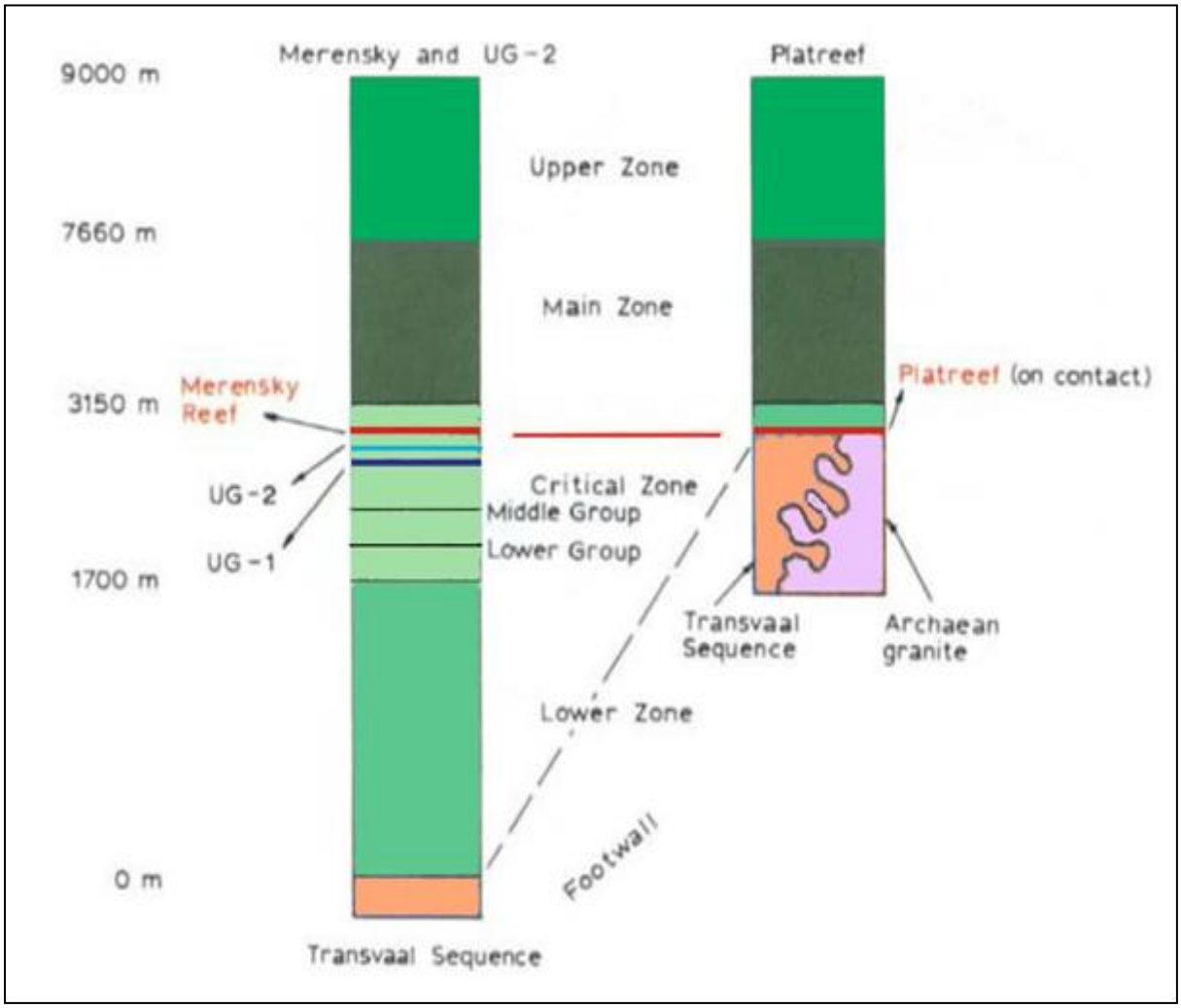

Figure 2. 9: A stratigraphic column of the Bushveld Complex showing the correlation between the Merensky Reef and its equivalent (Platreef) and the position of the UG- 2 Reef (modified after Vermaak, 1995).

(modified after Vermaak, 1995).

The UG-2 consists predominantly of chromite (60 to 90 %) with lesser silicate minerals (5 to 30 % pyroxene, and 1 to 10 % plagioclase). Other minerals such as phlogopite, biotite, ilmenite, rutile and magnetite, and base metal sulphides are present in minor concentrations. Secondary minerals of the UG-2 Reef include quartz, serpentine and talc (Table 2.2). The chromite content of the UG-2 Reef varies between 30 and 35 %, considering that the pure chromitite mineral has an average chromite content of 44 %. The base metal content of a typical UG-2 Reef is approximately 200 to 300 ppm nickel occurring as nickel sulphide and less than 200 ppm copper occurring as copper iron sulphide (Naldrett et al., 2012).

The platinum group minerals present in the UG-2 Reef are highly variable, but generally the UG-2 is characterised by the presence of abundant PGE sulphides (Voordouw et al., 2010), mainly containing laurite, cooperite, and braggite. Most of the platinum group minerals occur in association with the base metal sulphides and silicates. It is only the mineral laurite which exhibits a preferred association with the chromite grains. The major base metal sulphides constitute chalcopyrite, pentlandite and pyrrhotite. The base metal sulphides occur almost entirely within the interstitial silicate and are only very rarely enclosed within the chromite particles. Both the grain size and associations are extremely important as these affect the metallurgical behaviour during subsequent processing (Cawthorn, 1999a).

The Platreef

Located in the northern limb of the Bushveld Complex (Figure 2.10), the Platreef can be found where the Lower and the Critical Zones are known to be poorly developed (McDonald et al., 2005). Bushveld rocks in this vicinity are in contact with the Archaean granite and sediments of the Transvaal Sequence (floor rocks). A unique type of mineralisation has developed, see Figure 2.10. This reef consists of a complex assemblage of pyroxenites, serpentinites and calc-silicates. The different names of these rocks, compared to normal Merensky Reef, is the result of the hot Bushveld magma reacting with the lime-rich floor rocks (Gain and Mostert, 1982; McDonald et al., 2005).

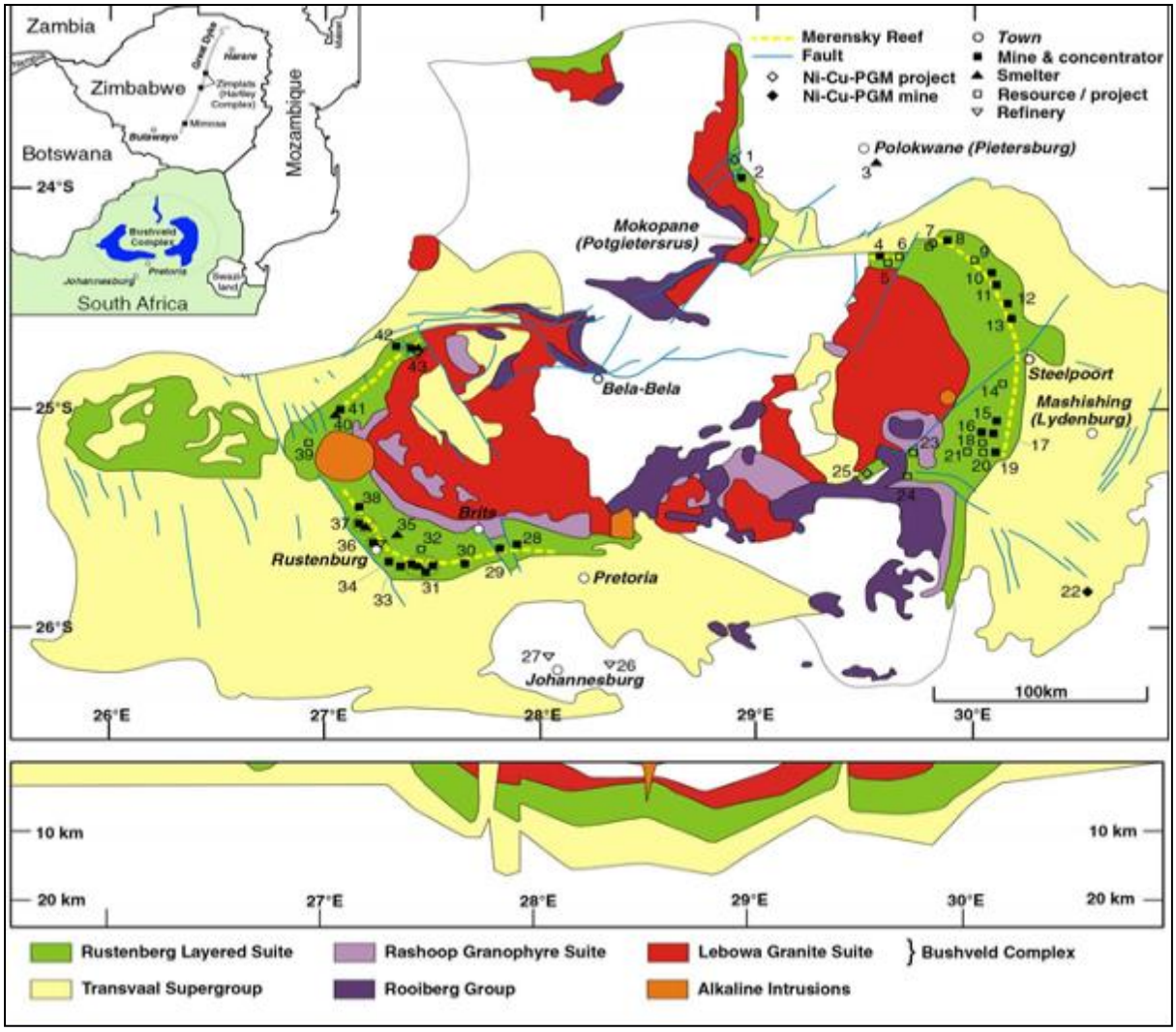

Figure 2. 10: Southern Africa and Bushveld Complex geological map (top) and conceptual cross-section (bottom), including PGM mines, smelters, refineries and future projects (adapted from Glaister and Mudd, 2010).

An exchange of heat and material between the magma and the floor rocks resulted in the formation of abundant lime-rich minerals (calc-silicates) as well as the serpentinisation of the overlying pyroxenites (Kinnaird et al., 2005). Base metal mineralisation and PGE concentrations are found to be highly irregular, both in value as well as in distribution. The mineralisation in places reaches a thickness of up to 40 metres (Howell, 2011).

Although the major platinum group minerals consist of PGE tellurides, platinum arsenides and platinum sulphides, there appears to be a link between the rock type and the type of platinum group minerals: serpentinites are characterised by a relative enrichment in sperrylite, whereas the upper pyroxenites are generally characterised

by more abundant PGE sulphides and alloy. PGE alloys generally dominate mineralisation closer to the floor rocks (van der Merwe, 2008; Howell, 2011).

Common base metal sulphides include pyrrhotite, pentlandite, chalcopyrite and pyrite, and although platinum group minerals frequently occur, enclosed in or on grain boundaries of these base metal sulphides, a high association of PG-minerals with silicate minerals is found in some areas ((Manyeruke, 2003; Kinnaird et al., 2005; Howell, 2011).

2.4.2. Uitkomst Complex

The Uitkomst Complex represents a satellite body of the Bushveld Complex as shown in Figure 2.11 (A), (Naldrett, 1989; Gauert et al., 1995; De Waal and Gauert, 1997; De Waal et al., 2001). It has a strong similarity with the Bushveld Complex, both petrographically and in terms of age (2 025 Ma) investigated by De Waal and Gauert (1997). The Uitkomst Complex is located between the towns of Machadodorp and Barberton in the Great Escarpment area of the Mpumalanga Province of South Africa. . Uitkomst Complex consists of a basal gabbro (6-30 m), lower harzburgite (50-90 m), chromitiferous harzburgite (60 m), main harzburgite (330 m), upper pyroxenite (60 m), and upper gabbronorites (250 m) shown in Figure 2.11 (C). The Uitkomst Complex was discordantly emplaced at the base of the Transvaal Supergroup, forming a trough between the northwest-southeast-striking fracture systems [Figure 2.11 (B)]. The lower part looks tubular, whereas the upper part cut discordantly, funnel-like, over the Malmani dolomite, the Bevets conglomerate and the Timeball Hill shale of the Transvaal Supergroup [Figure 2.11 (B) and (C)]. The tubular body is exposed for 8 km and disappears under an escarpment on Slaaihoek, dipping approximately 4º northwest.

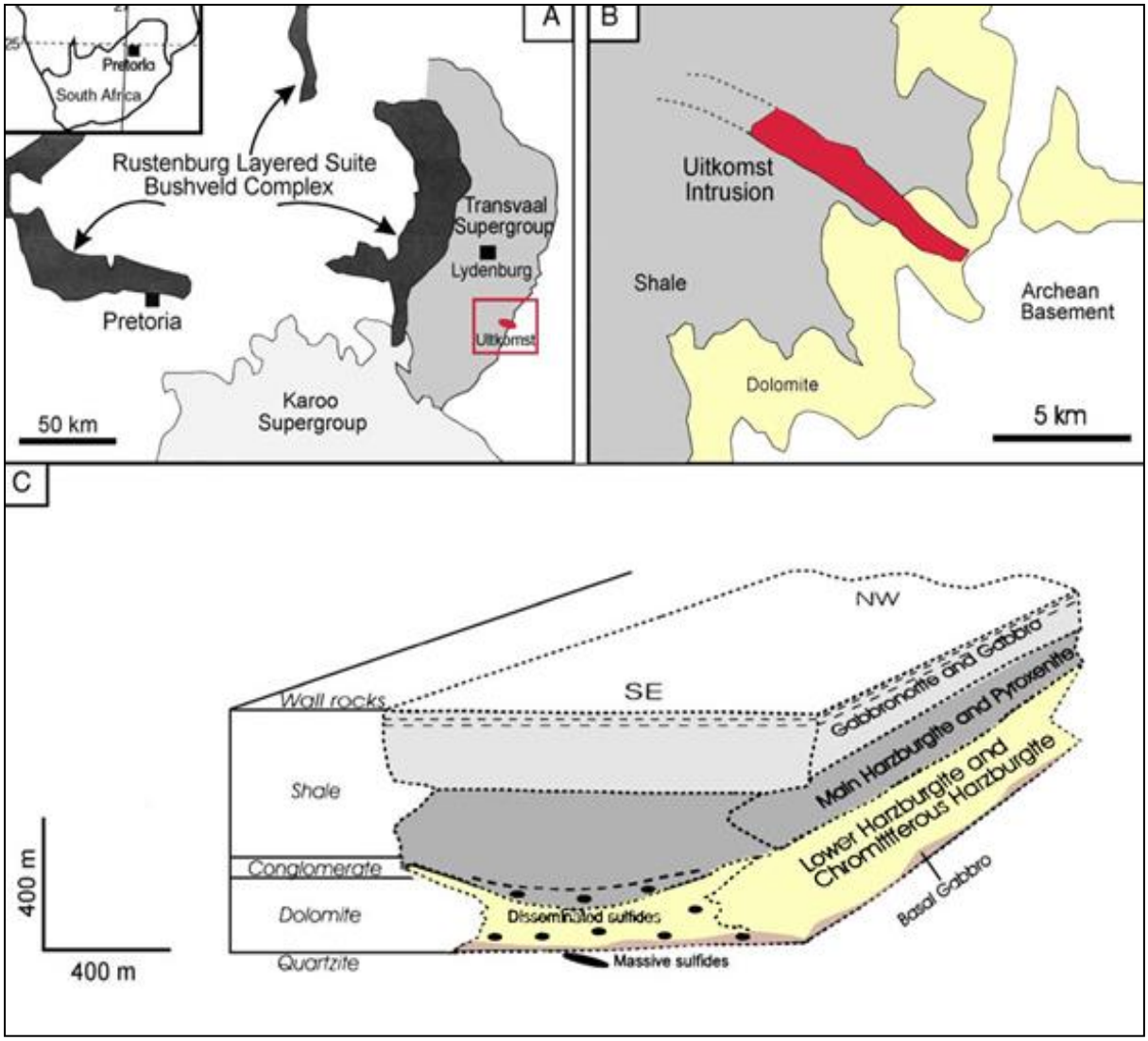

Figure 2. 11: (A) The geological location of the Uitkomst Complex with respect to the Bushveld Complex. (B) An illustration orientation of the Uitkomst Complex (C) a cross-section of the Uitkomst Complex showing locations of the massive and disseminated sulphides (modified from Li et al., 2002).

The Complex consists of a layered suite of ultramafic and mafic rock types formed within a magma conduit (Kenyon et al., 1986; Gauert, 1995), intruded at 2025Ma. Preferential weathering of the mafic rocks has led to the formation of a valley in which erosion has led to the exposure of the lowermost units of the complex on the farm Vaalkop 608JT, with successively high parts of the stratigraphy being exposed westwards of the farm Uitkomst 541JT and Slaaihoek 540JT (Theart and de Nooy, 2001). Disseminated and massive sulphide and chromite ore bodies have been delineated within the lower units of the Complex.

The shallower economically mineralized part of the Main Mineralized Zone of the Complex is now the primary target of the Nkomati Mine. The Massive Sulphide Body

(MSB) was exhausted in the first quarter of 2008. The first two pits were exhausted by 2010.

According to Theart and de Nooy (2001), during the early 1990's re-exploration and major drilling projects were carried out. Three disseminated sulphide mineralized zones were discovered [Figure 2.11 (C)]. These were; the Basal Mineralized Zone (BMZ), Main Mineralized Zone (MMZ) and the Chromititic Pyroxenite Mineralized Zone (PCMZ). A Massive Sulphide Zone (MSB), located at the base of the Uitkomst Complex was also identified (Figure 2.12).

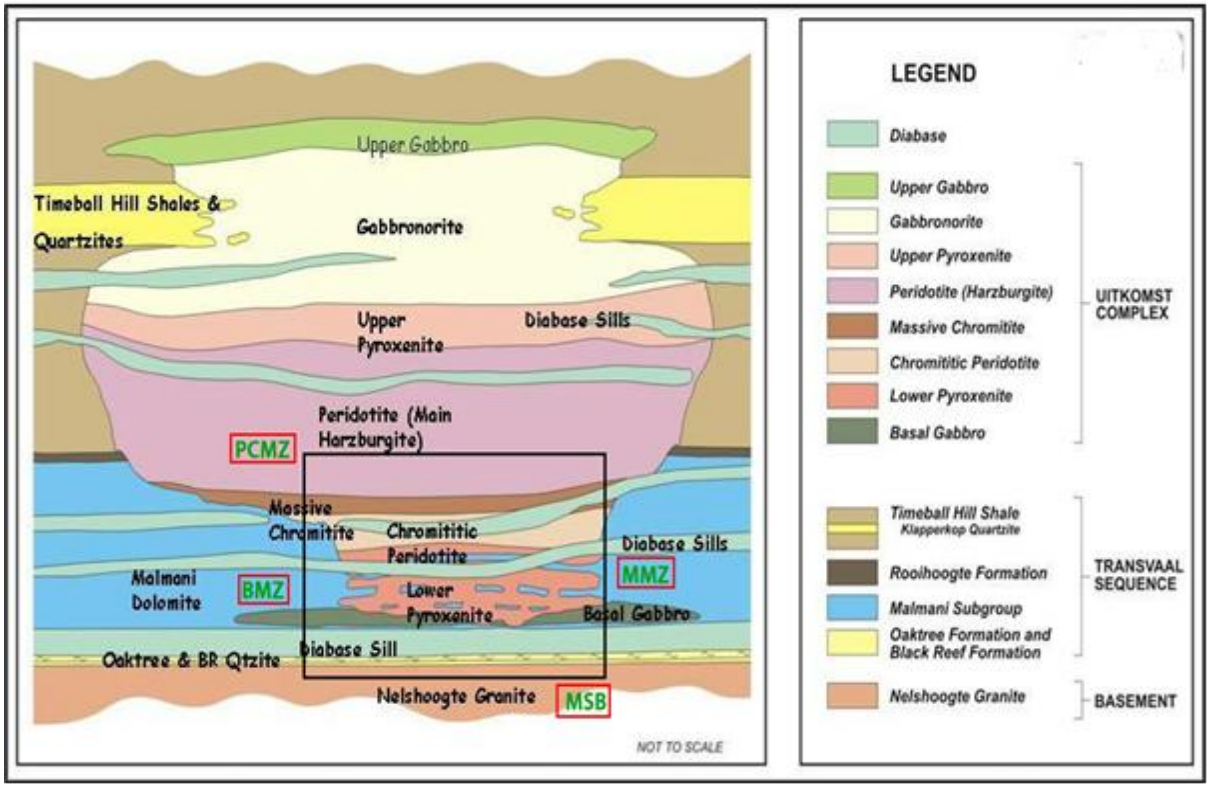

Figure 2. 12: An idealised cross-section through the Nkomati nickel deposit showing the MSB, MMZ, BMZ and PCMZ (modified after Mishra et al., 2013).

In 1995, the Nkomati Joint Venture between Anglo American Corporations and the Anglovaal Group was announced, and a feasibility study was commissioned with the view to explore nickel-copper-cobalt-PGE mineralisation on Slaaihoek and Uitkomst. Their finding were as follows; The PCR ore zone (chromititic pyroxenite/harzburgite), which is not continuous may be up to 20 m thick. The MMZ ore zone (Main Mineralized Zone) in the lower harzburgite is fairly consistent throughout the length of the trough, 300 m wide and between 2-40 m thick (Gauert, 2001). The BMZ ore zone (Basal Mineralised Zone) hosted by the basal gabbro, which is locally developed and varies

in thickness between 1-3.5 m. A high-grade Massive Sulphide Body (MSB) in the quartzite and granite footwall, with an aerial extent of 450 by 250 m and a thickness of between 1 and 25 m (Sharman et al., 2013).

The MMZ is hosted by the lower harzburgite unit and is one of the areas containing economic disseminated sulphide mineralisation. This lower harzburgite is a heterogeneous unit consisting of different ultramafic rocks comprising of poikilitic harzburgite, feldspathic harzburgite, wehrlite (Gauert, 2001).

According to Sarkar et al., (2008) Lherzolite, olivine websterite, are rare amphibolites. Numerous calc-silicate xenoliths occur in the host rock; these xenoliths are also sulphide-containing mostly located close to the contact with the host rock. This leads to variable lithology, textures and metal grades throughout the MMZ). The other areas containing sulphide mineralisation are the Basal Mineralised Zone (BMZ) within the basal gabbronorite unit and the Chromititic Peridotite Mineralised Zone (PCMZ) of the chromitiferous harzburgite (Gauert, 2001). The Massive Sulphide Body (MSB) is hosted by the sedimentary rocks and granite/gneiss below the intrusion (Theart and de Nooy, 2001).

The ore minerals occurring within the Uitkomst Complex are pyrrhotite, pentlandite, chalcopyrite, magnetite, ilmenite, chromite, digenite and pyrite (Table 2.3). Violarite, mackinawite, galena, sphalerite, platinum-group minerals, awaruite, native copper, arsenopyrite, cobaltite and millerite are present in minor amounts (Gauert et al., 1995). Pentlandite is the main host of nickel in the MMZ, with pyrrhotite containing small amounts of nickel in solid solution. Nickel concentrations range in magnetic pyrrhotite from 0.26 – 1.20 wt% and in non-magnetic pyrrhotite 0.55 – 0.90 wt%. The pentlandite is commonly associated with pyrrhotite as flame-like exsolution lamellae but forms granular aggregates enclosed in, or interstitial to, the pyrrhotite as the nickel grade of the ore increases (Gauert et al., 1995).

A hydrothermal activity resulted in extensive alteration of ferromagnesian minerals to amphibole, serpentine, biotite, and talc. Contamination of the ultramafic suite by country rocks accounts for the presence of most of the calcite, dolomite quartz, and plagioclase. Talc content is highly variable within the deposit and irregular (Britz, 2008).

The economic Ni mineralisation is mined at the Nkomati Mine, where initial mining activity was centred on the MSB. More recently, the mining has been focused on the lower grade MMZ and PCMZ ores. Average nickel and copper grades for the MMZ are 0.66-0.68% and 0.22-0.24% respectively (Gauert, 2001).

2.4.3. Namaqualand Metamorphic Complex

Copper has been mined over a period of 150 years in the Okiep District in the Northern Cape Province. The Okiep copper district covers 3 000 km^2 of the Namaqualand region around the town of Springbok and the mining villages of Nababeep, Okiep and Carolusberg. Proven reserves yield a total of 2 113 Mt of copper with almost 89% has already been extracted (Cawthorn and Meyer, 1993; Brandriss et al., 1996; Cairncross, 2004). The O'okiep Copper District is the oldest formal mining area in South Africa, with Springbok Mine being the first in 1852 (Marais et al., 2001). Between 1852 and 2002, the area yielding approximately 2 Mt of copper from 32 mines (Figure 2.13) ranging in ore tonnages from 140,000 t (Tweefontein) to 37 Mt (Koperberg-Carolusberg) of ore (Clifford and Barton, 2012).

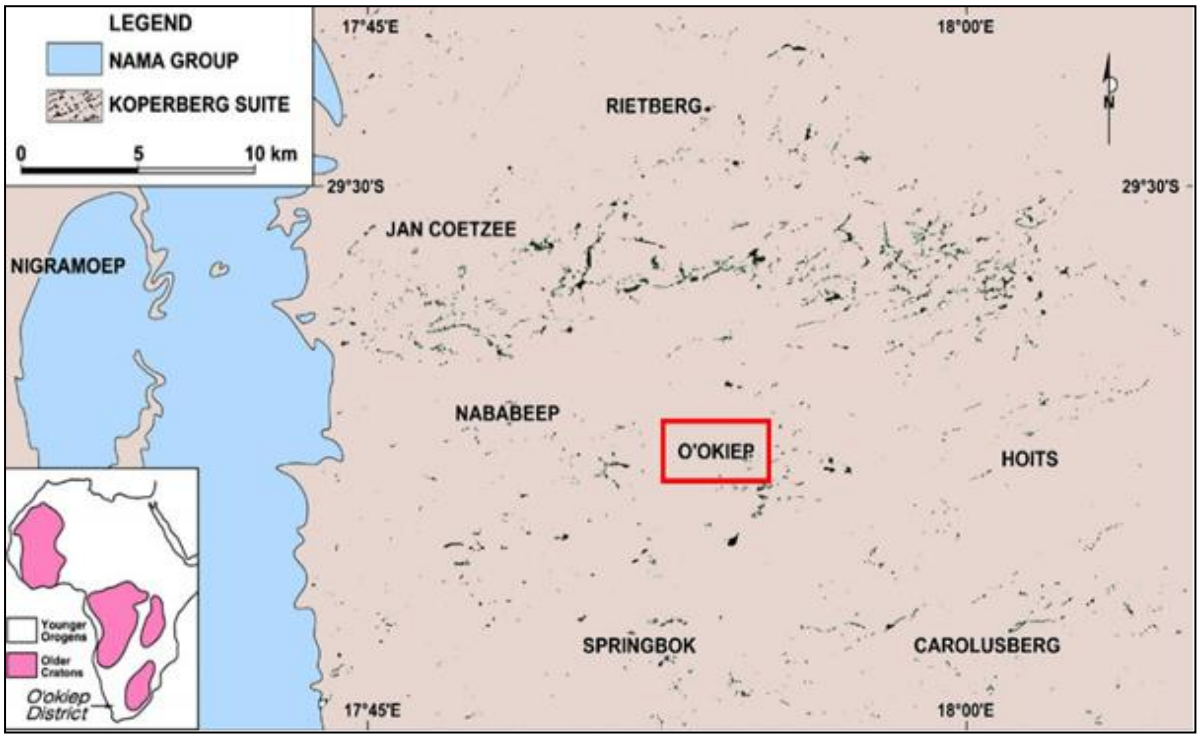

Figure 2. 13: A map of the mine sites with the one of the study areas (O'okiep) on the Koperberg Suite and outcrops of 1 700 individual bodies (after Lombaard et al., 1986).

2.4.3.1 Geological Setting

The O'okiep intrusive rocks include the Koperberg Suite and a number of important granite suites which intrude a basement of crystalline rocks, made up of granite gneiss with remnants of supracrustal rocks. These crystalline rocks were deformed and metamorphosed during the Namaquan Orogeny (late Mesoproterozoic) (Clifford et al., 1981, 2004).

Further research conducted by Clifford et al., (2004) and Robb et al., (1999) proved that several granites, including the Concordia and Kweekfontein Granites, were emplaced around 1200 Ma and were intruded at *ca.* 1030 Ma by the Koperberg Suite.

The Koperberg Suite made up of Cu-bearing sulphide deposits that have been mined for 150 years (Gibson et al., 1996). Virtually, all of the copper occurs in the Koperberg Suite, formerly referred to as "noritoids" (Benedict et al., 1964) or "basic bodies" (Lombaard and Schreuder 1978).

Intrusions of the Koperberg Suite constitute only 0.7% of the outcrop area of the O'okiep District (Lombaard and Schreuder, 1978), but contain all of the primary copper for which the area is famous. Approximately 1700 bodies of the suite are known in the district and they occur either as elongate bodies or irregular pipes that rarely exceed 200m in diameter (Figure 2.13), or as dykes up to 100m in width and generally less than 1 km in length, often associated with "steep structures"(Lombaard et al., 1986; Marais et al., 2001).

Kisters et al., (1994) have claimed that is the disseminated bodies of the Koperberg Suite are detached remnants of intrusions that were boudinaged during late "steep structure" tectonism. These intrusions were coeval with granulite facies metamorphism and ductile deformation (D3) of the country-rock gneiss.

Ougougdal et al., (1996) in their study, discovered three deformational events with varying metamorphism from greenschist facies in the west, through amphibolite, to granulite facies in the east. There are evident steep structures like large scale folds, the refolds the 4-km-thick granite-gneiss succession. Geochemical evidence suggests that magmas of the Koperberg Suite were contaminated by passing through semi-molten crust which was undergoing peak granulite grade metamorphism and deformation at the time of intrusion. They further discovered that the most productive

environment is the contact between the Springbok Quartzite Formation and the Modderfontein Granite as basic bodies intruding this horizon tends to swell out, resulting in massive pipe-like lodes such as that at Carolusberg (Marais et al., 2001).

The sulphides occur as disseminated in the diorite and were generally regarded as having formed by immiscibility. Sulphides could have been formed from late stage hydrothermal fluids. As typical magmatic sulphides are dominated by pyrrhotite with lesser chalcopyrite and Pentlandite. The preponderance of bornite in many of these deposits suggests that there are not simply magmatic sulphide deposits. Two distinct types of mineralisation, namely syngenetic (Carolusberg) type and a Hoit's type in which copper has been remobilised (Raith and Harley, 1998).

Copper mineralisation is hosted in basic to intermediate rock of the intrusive Koperberg Suite which comprise mainly of anorthosite, biotite diorite, pyroxene diorite and pyroxenite, as well as minor glimmerite, shonkinite and orbicular diorite. These are found within the granulite grade gneisses and granites of the Okiep Group, Bushmanland Sub province, Namaqualand Metamorphic Complex. Some composite basic bodies contain two or more mafic varieties. Anorthosite appears to be the oldest member of the suite followed by mafic varieties like leucodiorite, hypersthene diorite (norite) and hypersthenite (Gibson and Walmach, 1992; Van Zwieten, 1996).

The principal rock types of the suite are andesine anorthosite, biotite diorite, and hypersthene-bearing varieties, notably leuconorite, norite, melanorite, and hypersthenite. The suite is subdivided into an earlier series of andesine anorthosite and biotite diorite intruded by hypersthene-bearing rocks (Strauss, 1941; Hamman et al., 1996). Andesine anorthosite, biotite diorite, and hypersthene bearing rocks each constitute about 30–35% of the Koperberg Suite, and Cornelissen (1959) suggested that the average composition of these rocks is hypersthene diorite (leuconorite).

Geological cross-sections of some mined bodies of the Koperberg Suite are shown in Figure 2.14. The earliest members are two-pyroxene rocks that were formerly referred to as hornblende gneiss (Benedict et al., 1964) or two-pyroxene granulite (Clifford et al., 1981) and were grouped with the country rock sequence. However, Strauss (1941) and Van Zyl (1978) respectively called them gabbro and felsic norite and considered them to be part of the Koperberg Suite, a correlation confirmed by the weighted mean $^{207}Pb/^{206}Pb$ age of 1,035±13 Ma for magmatic zircon rims (Clifford et al., 2004).

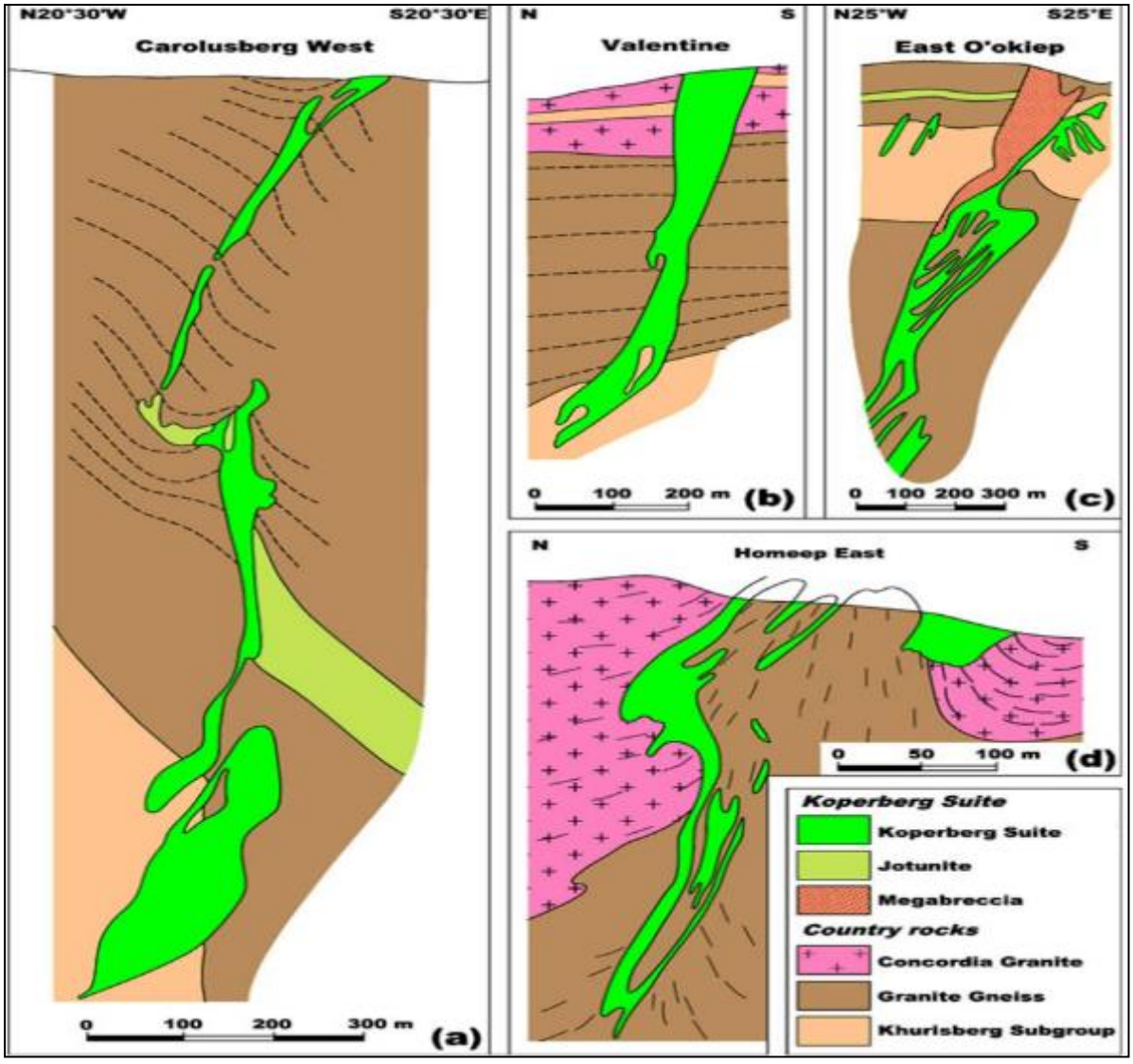

Figure 2. 14: A cross-section of some mine sites on the Koperberg Suite (courtesy of Clifford and Barton, 2012).

2.4.3.2. Mineralogy

The mineralogy of the Koperberg Suite is simple, and the compositions of the minerals record restricted ranges (Conradie and Schoch, 1986; Cawthorn and Meyer, 1993; Brandriss and Cawthorn, 1996). The rocks consist of varying proportions of antiperthitic andesine ($An_{30–50}$), hypersthene ($En_{58–68}$), Ti-rich biotite (MgO/MgO + FeO = 0.59–0.64, up to 5.9% TiO_2), and quartz (Stumpfl et al., 1976). Magnetite, ilmenite, and Cu-sulphides occur in the more mafic rocks, while apatite and zircon are ubiquitous accessories.

The Koperberg Suite exhibits a restricted compositional range of jotunite (a member of the charnockitic rock series equivalent to orthopyroxene monzonorite), andesine

anorthosite, biotite diorite, and leuconorite–norite–hypersthenite. With the exception of biotite diorite, the terminology is consistent with IUGS recommendations on how charnockitic rocks should be named and, as is typical of the anorthosite–charnockite kindred, the plagioclase in the Koperberg anorthosite and leuconorite–norite is andesine. Strauss (1941) emphasized the association of primary copper sulphides with hypersthene-bearing rocks of the Koperberg. Kisters et al., (1994) suggested that hypersthene-bearing parageneses are most prominent in the lower parts of the country rock sequence, while the bulk of anorthosite/diorite bodies occur in higher units, suggesting a buoyancy-controlled ascent.

2.5. Mineral Processing

Mineral processing is usually carried out at the mine site, the plant being referred to as mill or concentrator. The fundamental purpose is to reduce the bulk of the ore which must be transported to and processed by the smelter, by using relatively cheap, low-energy physical methods to separate the valuable minerals from the waste (gangue) minerals (Wills, 1997).

Mineral processing follows mining and prepares ore for the extraction. Despite regulating the size of the ore, it is a practise of physically separating the grains of the valuable minerals from the gangue minerals, to produce and enriched portion, or concentrate, and a discard, or tailing, containing predominantly gangue minerals (Wills and Atkinson, 1991; Wills 1997).

The process of extracting minerals from the ore is categorized by liberation and separation by flotation. Liberation is the process of crushing and grinding the run-of-mine ore as to expose the PGMs contained within. This is typically achieved through a series of crushers and tumbling mills, which operate autogenously or with varying loads of steel balls.

In the flotation circuit, which is broken down into streams through a series of flashing floats, roughers, cleaners, in some cases re-cleaners and scavengers, reagents are added to render the surfaces of the mineral particles sufficiently hydrophobic to enable the valuable minerals to be separated from the waste by froth flotation. The run-of-mine ore grades are typically several g/t, while concentrates are some 100s of g/t (Vermaak, 1995).

Minerals that are unsuccessfully extracted are left in the tail stream and are pumped out to tailings deposition facilities with average tail grades ~0.75 g/t (Fourie, 2008). Ultrafine grinding circuits has significantly improved the liberation and recovery of the valuable minerals, producing finer average grain size in the tailings (Rule, 2009). This property of the tailings is favourable to the carbonation process, as a smaller average grain size results in a high mineral surface area per unit mass, which promotes reactivity.

For the purpose of this study, the mineral processing techniques for three comparative minerals are reviewed, namely; PGMs, nickel and copper. A variability in grinding and milling patterns would strongly influence the particle size distribution and surface area of the gangue minerals. Moreover, dissimilarities in mineral processing techniques would be pivotal in the overall outcome of this study.

2.5.1. Platinum Group Metal (PGM) Processing

The Anglo American Platinum Corporation mining operations on the three reefs (Merensky, UG-2 and Platreef) and Impala Platinum (mining the Merensky, UG-2) utilise froth flotation for recovery of the value minerals to concentrates with the exception of Rustenburg and Amandelbult Merensky Reef operations, where historically, the coarse and dense PGMs (about 30 per cent of the total platinum in the Merensky) are concentrated and removed from the circuit at an early stage by gravity techniques prior to the main flotation banks. This results in a very high-grade stream, which by-passes the smelter stages and is an early feed to the refinery. The remainder of the PGE are recovered by flotation, followed by electric smelting, converting to produce a nickel-copper-PGE matte which, after slow cooling and extraction of the precious metal alloy phases, is sent to the refinery where platinum, palladium, rhodium, ruthenium, iridium, osmium, gold and silver are produced (Merkle and Mckenzie 2002). The mining of PGE ores is through conventional underground or open cut techniques. The elements contained in PGE ores are often reported as ‘4E’ (Pt + Pd + Rh + Au) grades, with osmium extremely rarely reported (3E is Pt + Pd + Au) (Anglo Platinum Limited, 2012).

2.5.1.1 Merensky ore processing

The Merensky ore is crushed at a nominal top-size of 230 mm. The material is mostly delivered via a conveyor belt to the primary mill silo. On route to the silo, a weight

meter is used to provide an integrated reading of the total mass of run-of-mine (ROM) delivers.

Material from the ROM is then fed at a controlled rate into a primary mill which is power motor (Figure 2.15). The milled slurry is screened at 800 µm and the fine fraction is subjected to primary rougher flotation in four stages while the coarse fraction is re-milled. The first concentrate (from smart cells 1 and 2) is transferred to final concentrate, whilst the second concentrate (from smart cells 3 and 4) is pumped to the cleaner flotation circuit (Figure 2.15). The primary rougher flotation tails undergo hydro cyclone classification. Cyclone underflow is fed to the secondary ball mill, while the overflow is fed to the secondary mill discharge sump (Govender and Vukea, 2007).

The second stage milling is conducted in an overflow ball mill in closed circuit with a large diameter hydro-cyclone. The fine fraction of the secondary milled product is subjected to two stages of secondary rougher flotation (first stage is three banks of cells (Figure 2.15) and the second stage is two banks of four cells, with the concentrate being subjected to cleaner flotation, and the tailings transferred to the tertiary milling circuit, after classification.

A final tertiary stage milling is conducted in an overflow ball mill operating in closed circuit with a hydro-cyclone. The fine fraction is subjected to one stage of tertiary rougher flotation in three banks of cells. The concentrate produced is subjected to cleaner flotation, whilst the tailings are classified, thickened thickener, and transferred to the tailings darn by multi-stage pumps (Govender and Vukea, 2007).

The cleaner flotation circuit contains three stages of cleaning and two stages of cleaner scavenging. The first cleaner bank consists of four flotation cells, the second stage consists of four flotation cells and the final cleaners also made up of four stages flotation cells. Cleaner scavenger flotation is conducted in two banks of four tank flotation cells. Cleaner tailings are transferred to the tertiary milling circuit for regrinding as shown in Figure 2.15.

Final concentrate is delivered to the Merensky Concentrator thickener as thickened slurry and stored, prior to pressure filtration, in a filter. Merensky concentrate is then transported to a smelter by road.

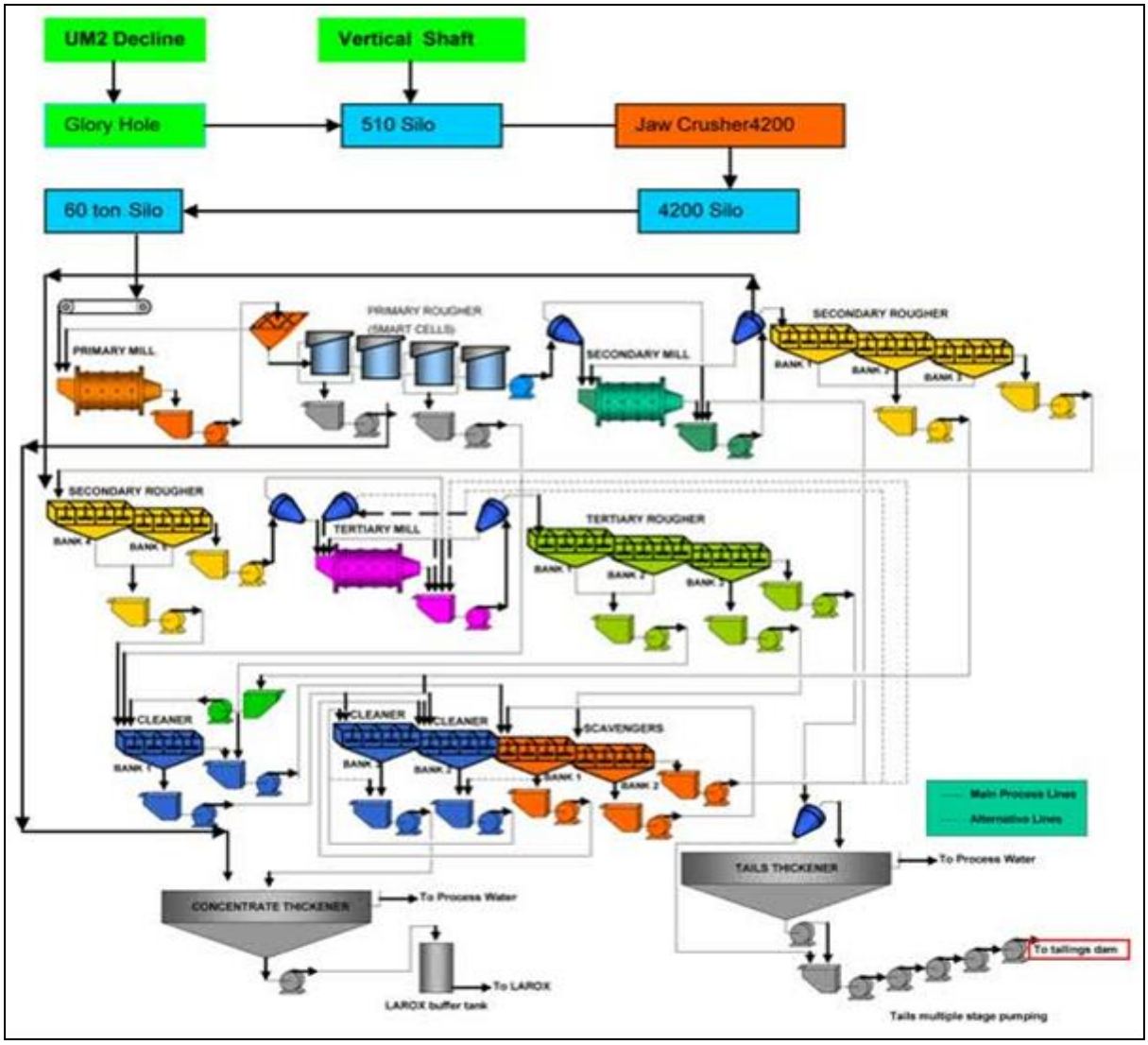

Figure 2. 15: A flowsheet showing the Merensky ore processing circuit (courtesy: Lebowa Platinum Mine, 2006).

2.5.1.2. UG-2 ore processing

In the case of the UG-2 ore, the crushed product is then fed into a surge bin ahead of milling. On route to the mill bin, the mass of the UG-2 ore fed to the plant is recorded using belt weight meter. The belt is also equipped with a magnetic tramp iron removal device.

Primary milling is then employed, with milled products screened and the fines fraction subjected to two stages of primary rougher flotation in six tank cells (Figure 2.16). The first stage concentrate is delivered to final concentrate, while the second stage is transferred to the cleaner circuit. Tailings are classified in two stages with the coarse fraction being re-milled and the fines subjected to secondary (scavenger) flotation (Anglo Platinum Limited, 2012).

Secondary milling is conducted in an overflow ball mill and in open circuit. The milled pulp and the classification overflow are transferred to the secondary flotation circuit, consisting of two stages, and a total of five scavenger flotation cells. The UG-2 concentrate produced is delivered to the cleaner flotation circuit, while the tailings are classified and thickened in a thickener, and transferred to the UG-2 tailings dam.

The rougher concentrates are subjected to four stages of cleaning. The first two stages each consist of two tank cells and the final stage consists of two cells (Figure 2.16). The intermediate concentrate is cleaned in a column cell to reduce the chrome content and increase the PGM content (Bulatovic, 2010). Cleaner tailings are transferred to secondary milling for regrinding as shown in Figure 2.16. Final UG-2 concentrate is then delivered to the UG-2 concentrator thickener, with thickened slurry stored prior to pressure filtration in the common filter (Anglo Platinum Limited, 2012).

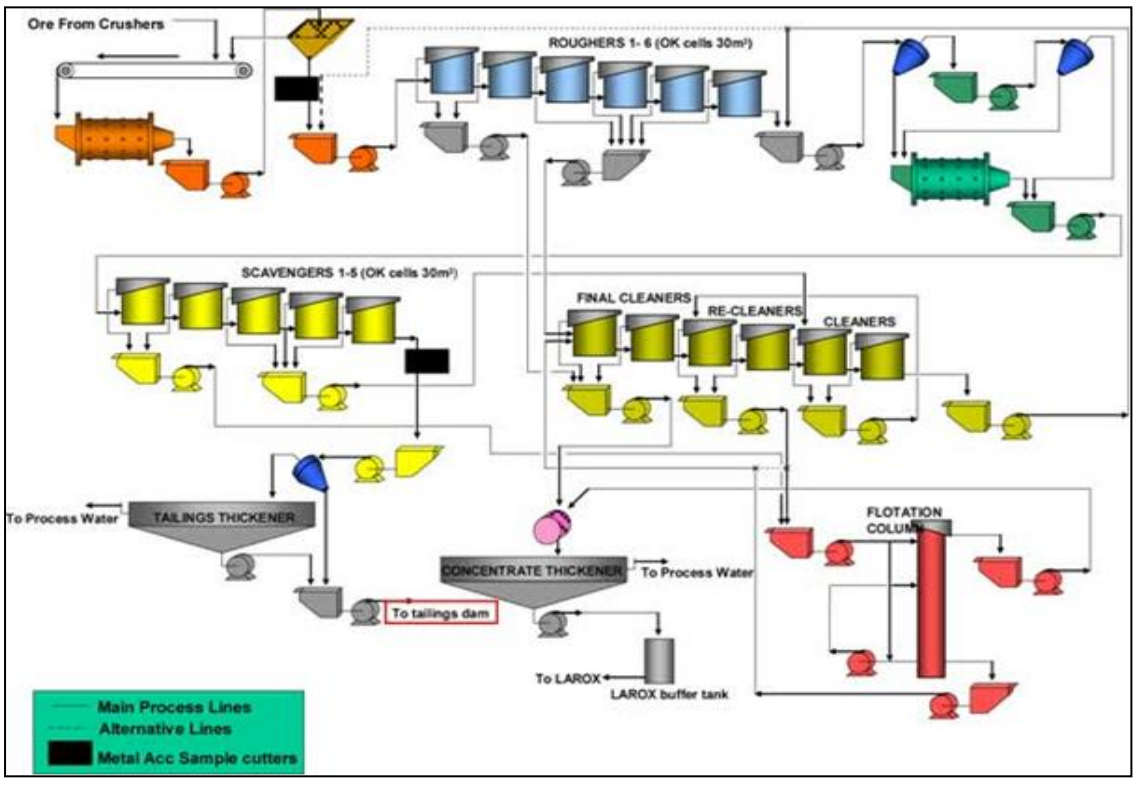

Figure 2. 16: A flow diagram showing the UG-2 processing circuit (courtesy: Lebowa Platinum Mine, 2006).

2.5.1.3. Platreef ore processing

The Platreef ore is processed by Mogalakwena Platinum Mine formally known as PPRust. A multi-stage, mill-float-mill-float (MF2) circuit system is employed. Grinding to achieve a final product size of 80% -75 µm would be required to achieve the required

recovery and grade of concentrates. However, the recent grinding specifications utilize ultra-fine grinding technology, with a target grind of 80%–53 µm showing economic benefit (Humphries et al., 2006).

The circuit comprises vibrating grizzly and primary crusher, delivering products to a conical frame stockpile. The stockpile feeds a secondary crushing circuit in closed circuit (Figure 2.17). The secondary crusher circuit product is stored in silos with live capacity of 15 000 tons. The undersize material is routed to the cyclone feed via the mill discharge sump. This allows flotation size particles to bypass milling directly to flotation. Primary rougher tails are reground in a secondary overflow ball mill (Cole and Ferron, 2002).

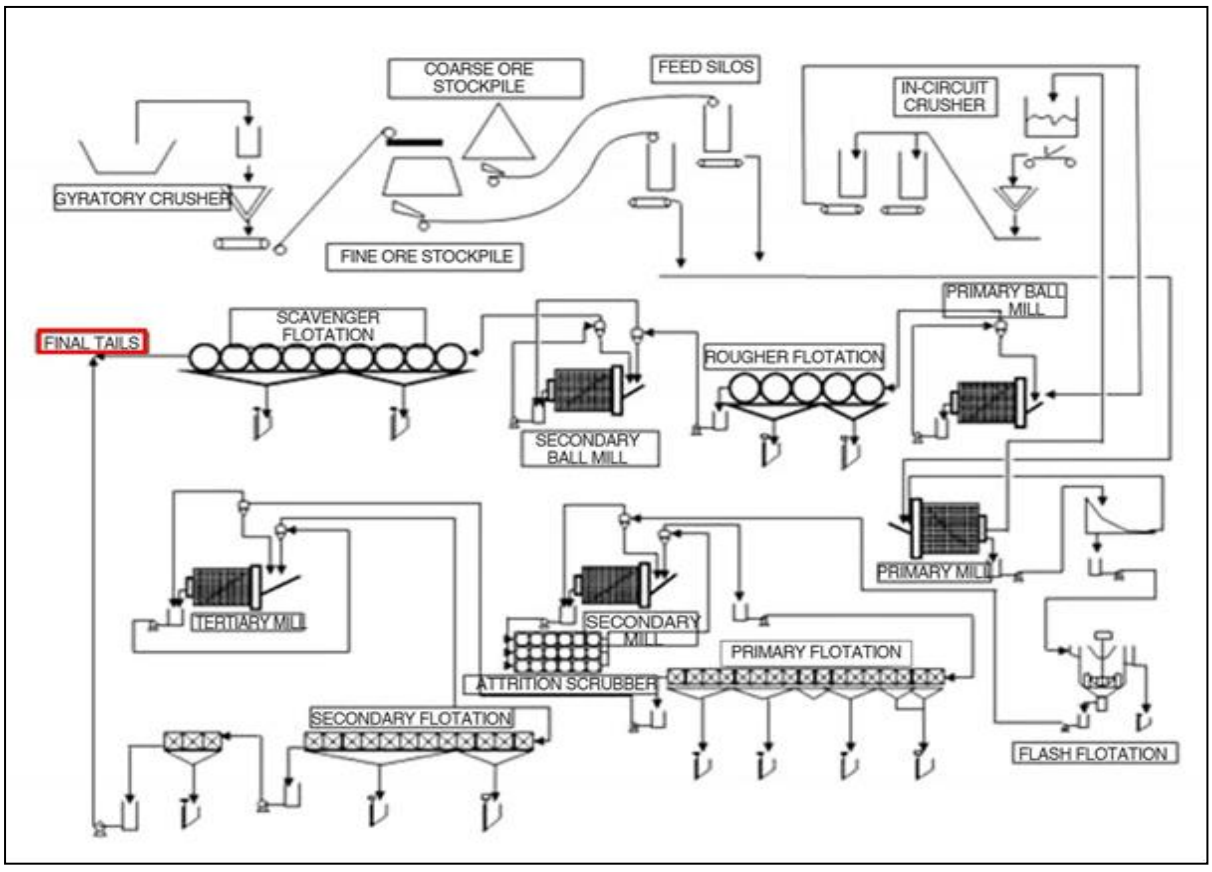

Figure 2. 17: A process flowsheet for the for the Mogalakwena operation (Humphries et al., 2006).

Concentrate cleaning is achieved in a three grade cleaning circuit where mainstream concentrates are fed according to kinetic ranking at the determined point in the circuit. Buffer capacity between mainstream and cleaning flotation is provided by surge tanks (Cole and Ferron, 2002; Humphries et al., 2006).

The final concentrate is thickened and filtered in pressure filters for road dispatch to the group smelters at Polokwane, Mortimer or Waterval. Final tailings are pumped after thickening for deposition on a new tailings impoundment on the lease area. Paste thickening to maximize water use on the project is being evaluated currently (Humphries et al., 2006).

2.5.2. Nickel

Nkomati Nickel JV exploits the Uitkomst deposit in South Africa's Mpumalanga Province, in the mountains between Waterval Boven, Machadodorp, and Badplaas. Nkomati Nickel JV has experienced a phenomenal growth rate over the past few years, from a 10 kt/month operation in 2006 to a 700 kt/month complex in 2013. This growth required the re-engineering of virtually every aspect of the operation, from mining new ore types with new methods, ore preparation and processing, to tailings deposition.

Currently only the MMZ and PCMZ ores are mined. Current open pit ore production is approximately 650 kt/month, approximately 300 kt of which is from the PCMZ and 350 kt from the MMZ. The MMZ is also mined in the underground mining section, producing approximately 50 kt/ month. Board and pillar, and longhole open stoping methods are utilized (Cockburn, 2013).

Nickel is mainly contained within pentlandite, although a significant proportion (as much as 15%) occurs in solid solution within pyrrhotite, and 1-2% within chlorite. Copper occurs almost exclusively within chalcopyrite, with some occurring as bornite (1-2%).

The MMZ in many ways resembles the Merensky Reef, though having substantially lower PGMs but higher base metal sulphides (typically 5-8 %) with traces of PGMs (predominantly merenskyite). The PCMZ resembles the UG-2 Reef, with chrome grades of 7-15% Cr_2O_3. The boundaries of the two ore types are not clearly delineated, making segregation of ore and prevention of cross-contamination challenging (Britz, 2008).

In terms of comminution, Nkomati's MMZ and PCMZ ore types are significantly different. MMZ recoveries are relatively intensive to grind with a target liberation grind

of 67% -75 µm. The target grind specification for the PCMZ ore type is 80% -75 µm, making it extremely sensitive to grind.

Crushing

With the open pit supplying the vast bulk of the ore, a primary gyratory crusher at the pit is selected with transport by overland conveyors to the two plants. Loading and crushing is alternated between the two ore types (MMZ and PCMZ), with crushed ore transported by conveyors approximately 3 km to the respective conical stockpiles locates at the plants (Figure 2.18).

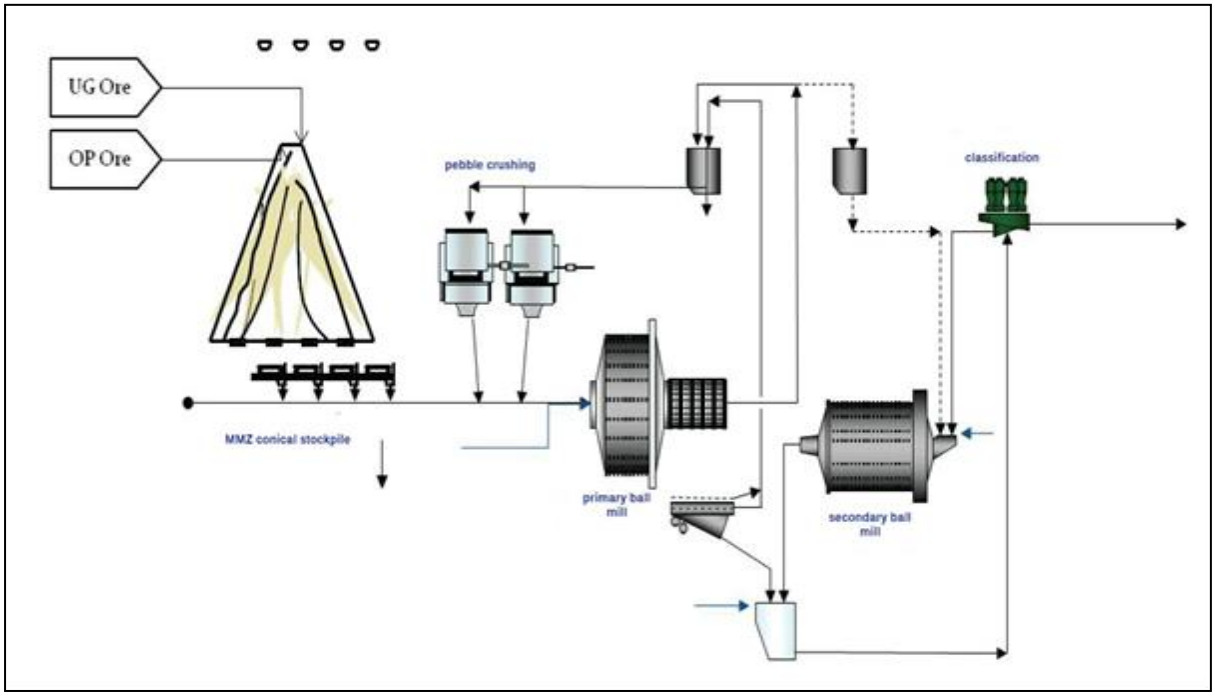

Figure 2. 18: A simplified flowsheet of the Nkomati crushing circuit (after Cockburn, 2013).

Fragmentation pattern improvements within the pit were realized through redesigned drilling patterns, and changes to the blast timing and blast direction. Interestingly, improved fragmentation was achieved at reduced hole spacing and much reduced powder factors. Production hole spacing was increased from 3.0 m x 3.5 m to 3.5 m x 3.5 m, while maintaining the 10.7 m hole depth and 3 m stemming material depth (Van der Merwe, 2012).

Ore liberation

The flow circuit design employed a primary mill in closed circuit with a vibrating screen and pebble crushers. A secondary ball mill in closed circuit with cyclones supplies feed

to the flotation circuit at SG 1.3-1.34, 70% -75 µm at 620 t/h. Cockburn (2013), emphasizes that comminution circuit operating costs are lower on the MMZ plant than the PCMZ.

Ore Separation

The flotation circuit is a relatively standard rougher-cleaner-recleaner configuration (Figure 2.19). The process routes are quite similar that of PGM processing (Section 2.5.1).

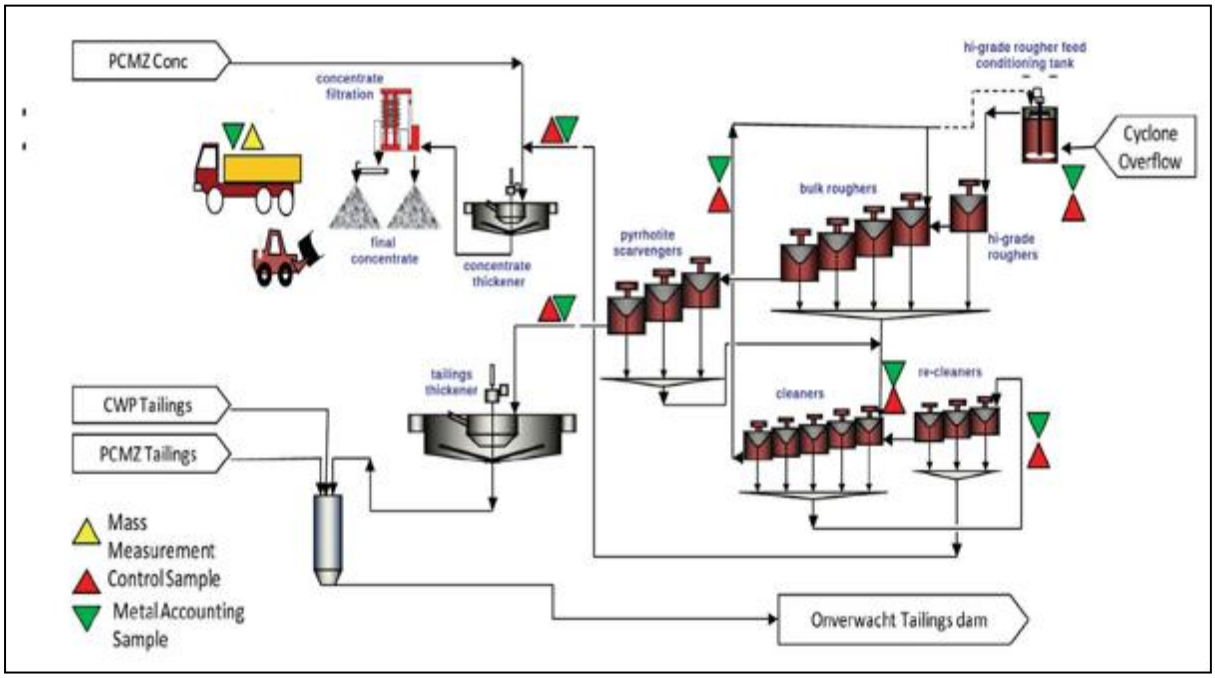

Figure 2. 19: A diagram showing the Nkomati ore processing routes to the final step whereby gangue mineral are transported to the Onverwacht tailings dam (courtesy: Cockburn, 2013).

2.5.3. Copper

Generally, copper extraction follows the sequence illustrated in Figure 2.18. It starts with beneficiation by froth flotation of ore to give copper concentrate. This is followed by a two-stage pyrometallurgical extraction which entails smelting concentrates to matte and converting matte by oxidation to crude copper.

The copper ore coming from the mine (0.5 – 1 % Cu) must be concentrated by beneficiation. The valuable minerals like chalcopyrite are intergrown with gangue. Therefore, in the first step the lumpy ore is crushed and milled into fine particles (< 100 µm) to liberate the individual mineral phases (Thompson, 1991).

Typical equipment for crushing to about 20 cm are gyratory and cone crushers. Then wet grinding in semi-autogenous rod or autogenous ball mills takes place. Size classification takes is performed in cyclones (Figure 2.20).

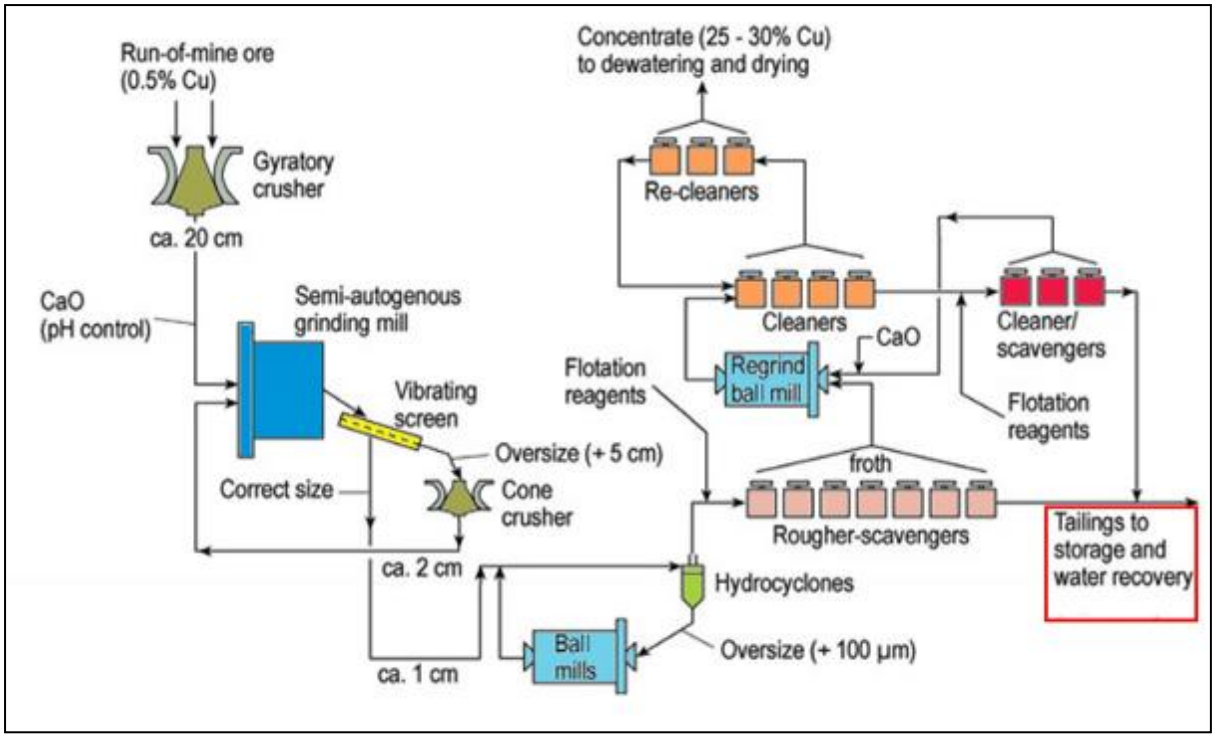

Figure 2. 20: : An idealized flowing diagram of the copper processing circuit at a concentrator (Lossin, 2001).

In the next step of beneficiation, valuable minerals and gangue are separated by froth flotation of the ore pulp, which exploits the different surface properties of the copper ore and the gangue.

The hydrophobic sulphide particles become attached to the air bubbles, which are stirred into the pulp, rise with them to the surface of the pulp, and are skimmed off as a froth of fine concentrate. The hydrophilic gangue minerals remain in the pulp. Organic reagents with sulphur-containing groups at their polar end, such as xanthates, are used as collectors in the flotation process. Additionally, modifiers like hydroxyl ions (pH adjustment) are used to select different sulphide minerals, for example, chalcopyrite and pyrite. Alcohols are used to stabilize the froth (Lossin, 2001).

In the first flotation stage, as much copper as possible is recovered in a rougher concentrate so that as little as possible goes to the tailings (Figure 2.18). To increase the copper recovery rate, often these tailings are leached with sulphuric acid. After

regrinding, the rough concentrate is cleaned in several flotation steps (Beck and Chamart, 1980).

Copper concentrators typically treat up to 100 000 t of ore per day. They are located directly at the mines to achieve low transport costs. The copper recovery efficiency is over 90 %. About 95 % of the ore input goes into the tailings, which are stored in large dams near the mine and are used for water recycling to the flotation stages (Beck and Chamart, 1980; Barbery, 1986).

2.6. Previous research work on Mineral Carbonation

Seifritz (1990) proposed the term mineral carbonation as a CO_2 binding concept. It was not long before Lackner et al., (1995) conducted the first detailed study on mineral carbonation. They made use two types of processes, involving either direct carbonation of minerals at high temperature or processing in aqueous solution. These aim at ex situ processing in a dedicated processing plant as opposed to in situ carbonation by injecting the CO_2 into geological formations

According to (Delgado, 2010), there have been immediate development efforts regarding mineral carbonation since the first detailed study by Lackner et al., (1995). This is fully evidently characterized by patent applications and a trend toward scale-up and demonstration. The availability of large amounts of suitable minerals seems to be the motivation and progress on mineral sequestration is being steadily made and reported by an increasing number of research teams and projects worldwide (Zevenhoven et al., 2011).

As it would be predicted, further mineral carbonation studies emerged following the study by Lackner et al., (1995). A mineral carbonation study of the ultramafic greenstone belts in India was conducted by Mani et al., (2008). The aim of study was to quantify two of the twenty-five main greenstone belts (Kolar and Chitradurga) for their carbon storage capacity taking into consideration the weight percentage of MgO. Pronost et al., (2011) used ultramafic mineral waste for a mineral carbonation study. A microbial approach to mineral carbonation was introduce by Power et al., (2011).

Vogeli et al., (2011) reported an investigation of the potential for mineral carbonation of the Platinum Group Metals' processing tailings in South Africa. While carbonation was possible, the overall conversions were low (3–30 %), predominantly due to the

low Mg extraction levels during the acid leaching step It was concluded that more work is required on Mg extraction from pyroxene materials (Meyer, 2014). However, a study on the optimization of carbonation of magnesium silicate for CO_2 storage was recently performed by Eikeland et al., (2015). Bodenan et al., (2014) evaluated the application of ex situ mineral carbonation technology to ultramafic mining and industrial wastes. They concluded that the region of New Caledonia, France, with local abundances of suitable rocks and industrial wastes, and with significant greenhouse gas emissions, stands out as a strong candidate for application of ex situ mineral carbonation.

Several studies to accelerate the carbonation of mine waste materials are being conducted. Jacobs (2014) quantified the mineral carbonation potential of mine waste material.

Investigation into the carbonation of mine waste from the nickel industry has also begun. Studies by Assima et al., (2014) have been conducted on the aqueous carbonation of nickel mining residues from the waste stream of a Ni-Cu mine pilot plant. The sensitivity of the carbonation reaction to temperature and oxygen content was examined. While successful carbonation was observed, the carbonation rate and yield were both increased and highly dependent upon the presence of brucite and chrysotile, due to the ease of dissolution for Mg production.

Current research is primarily directed towards three main issues: reduction of feed activation energy requirements, improvement of the slow chemical kinetics of the process, and alternative feedstock exploration.

2.7. Effects of CCS by geological storage

As stated by Heinrich et al., (2004), injection of CO_2 into geological formations has been practiced for many years. Geological storage requires injecting the CO_2 into the porous rock of a formation, multiple physical phenomena allow it to remain trapped in the rock. Suitable formations are regarded as those 800 m or more below the surface, so that the increased pressure due to the depth means that the CO_2 is in a dense or supercritical phase.

The rock into which the CO_2 is injected must be porous and able to store the CO_2, and there must be an impermeable “cap” rock, above the formation to ensure that the CO_2 does not rise through the rock layers and escape to the surface. With so many different

physical processes occurring simultaneously, an accurate assessment of leakage potential must take into account the various trapping mechanisms, rock properties, and leakage processes. Literature studies and expert opinion strongly indicate that some leakage may occur but will be very small and will occur far in the future.

CO_2 is benign in very low concentrations, however, the health and safety risks of higher concentrations could prove lethal. Providing long-term control and accountability for the CO_2 is still an open issue. Questions need to be resolved about how to monitor the reservoir once it is closed, and the lengthy duration as in the case of in-situ storage

2.7.1. The Lake Nyos disaster

Volatile gases in the deep interior of the earth are brought to the surface mainly as a result of volcanic activities. In terms of the present-day global carbon cycle, CO_2 discharged from subaerial volcanism and passive CO_2 discharge from the craters or flanks of volcanoes are the major non anthropogenic contributors to atmospheric CO_2.

There are numerous volcanic crater lakes situated along the Cameroonian Volcanic Line. Although no active volcanism is currently found near the lakes. However, magmatic CO_2 is continuously discharged from depth, and is trapped and accumulated in deep waters of the lakes (Kusakabe and Sano, 1992; Evans et al., 1993).

In 1986, this accumulation resulted in a sudden outburst of dissolved gases from Lakes Nyos, causing the gas disasters that claimed the lives of approximately 1 700 people and 3 500 livestock (Sigurdsson et al., 1987). This horrific event overshadowed a smaller but similar event at Lake Monoun on 15 August 1984 which killed 37 people (Sigurdsson et al., 1987). The term “limnic eruption” was coined by J.-C. Sabroux to describe gas outburst from a lake as that of Lake Nyos (Halbwachs et al., 2004).

2.7.2. Impacts of geological storage

The issue of CO_2 leakage is only one among several potential external impacts of CO_2. In other words, leakage links all other CO_2 storage impacts together. For instance, storing CO_2 underground can acidify water in the geological layer under consideration (Riemer et al., 1999; NITG, 2006).

If the geological layers, below which CO_2 is injected, are breached, the groundwater contained in nearby aquifers may acidify, affecting the quality of drinking water if it is

obtained from these sources. The presence of oil, natural gas, and CO_2 trapped in geological formations implies that in sedimentary basins, impermeable cap-rock is available with sufficient quality to confine fluids and gases for long periods of time. Such evidence from natural systems demonstrates that reservoir seals exist that are able to contain fossil fuels and CO_2 underground over time scales of at least millions of years. Still, it is imaginable that CO_2 artificially stored underground gradually dissipates and slowly leaks from its geological storage medium.

Although the hazards involved are likely to be local and temporary, they could nevertheless be pervasive such as the lake Nyos disaster (Section 2.6.1) (Holloway, 2000), Heinrich et al., (2004) stated that it is highly unlikely that massive releases of CO_2 like what occurred at Lake Nyos will occur from geologic storage of CO_2. Pressure excursions should occur only near the injection point and then the CO_2 should diffuse over large areas in the formation. In other words, Lake Nyos tended to concentrate CO_2, while injection into geologic formations will tend to diffuse the CO_2 as it moves away from the injection point. With proper site selection and operation, the chances of a massive release from the formation can be reduced further. The Nyos incident may be regarded as unique and different in many ways from CO_2 artificially stored underground, however, it shows that one in principle has to be wary of the possible consequences of accidental releases of geologically stored CO_2.

Raza (2009) investigated the uncertainty in the location of leaks, leakage amounts, and the start of leakage times. Results of the study showed that the leakage potential is very small, the expected value of the amount of leakage is a small fraction of the total injected volume, and the expected value of the start of leakage is over a thousand years.

A straightforward calculation readily demonstrates that a 0.1%/year CO_2 leakage rate is likely to be more or less acceptable, while a 1%/year rate is probably not. For a storage option with a 1%/year leakage rate, a given quantity of geologically stored CO_2 will have reduced to 37% of that amount after 100 years, whereas 90% of that quantity is still stored underground after a century for a storage medium characterised by a 0.1%/year leakage rate. As climate change is a problem stretching over the forthcoming couple of centuries, one may conclude that in the 1%/year leakage case,

in-situ CCS becomes an ineffective emissions abatement option (Ha-Duong and Keith, 2003).

In considering the livelihood of future generations to come, the issue of CO_2 leakage could possibly be remedied by the ever-beginning mineral sequestration process. It is anticipated that the results of this study will provide a platform for future engineering research into the creation of an appropriated engineered mineral carbonation facility. The proposed facility intends to replace the traditional recovery method of milling and flotation with a modified procedure involving a flotation step followed by leaching that enables further metal recovery and desilication of the gangue. Ultimately this activated gangue would be processed through a carbonation circuit to achieve sequestration.

2.8. Summary

Mineral carbonation is gradually making headway as an important CCS method that could offer an alternative for CO_2 storage in underground formations. This approach offers leakage-free CO_2 storage, with benefit of thermodynamics and energy economy, and very high tonnages of suitable mineral resources that are available worldwide.

Irrespective of the successes with carbonation of residues and promising process ideas for the carbonation of rock material, no concept for carbonation of natural minerals has currently matured into implementation on a large scale as compared with underground sequestration of CO_2. However, recent and current developments and trends indicate rapid changes and stronger support for promising concepts.

At present, both in situ and ex situ mineral carbonation methods are still under development, with indirect processes offering the benefits of faster chemical kinetics and better product quality (Zevenoven et al., 2011).

There are a few challenges in mineral carbonation need to be tackled. These include: (i) overcoming the slow kinetics of mineral–fluid reactions (ii) dealing with the large volume of source material required (iii) reducing the energy consumed to induce reactions and (iv) minimal progress has been made when it comes to the recovery and recycling of additives.

Research into reduction of energy consumption and costs of the process also requires attention for it to be economically viable. Compared with other sequestration options,

mineral carbonation has the advantage of being the longer term option and its theoretically vast capacity (Huijgen and Coman, 2003). Nevertheless the advantages of mineral carbonation as described earlier in this chapter, indicates that CO_2 mineralisation could play a significant role in risk mitigation strategies for CCS activities in South Africa.

Research is currently under way in South Africa to determine the feasibility of CCS. The South African Centre for Carbon Capture and Storage (SACCCS) has begun working towards having a CCS demonstration plant operational in the country by 2020 (IISD Reporting Services., 2009).

There are various potential sites around the country that have been recognized by Doucet (2011). These materials are available in large piles that have already been crushed and milled following mining activities predominantly composed of ultramafic rocks. Engelbrecht et al., (2004) estimated that for a power plant producing 10 000 tonnes of CO_2 per day, approximately 25 000 tonnes/day of this material is required or approximately 9 million tonne per annum.

CHAPTER 3

METHODOLOGY

3.1. Introduction

This chapter summarises the various methods, techniques and equipment used in this study. Sample collection procedure and the criteria for selection of sampling sites are also presented.

3.2. Research Approach

For this project, mine feed, plant and dam tailings were sourced from Anglo Platinum operations on the western and northern limbs of the Bushveld Complex, the active dam at Impala Platinum, two plants processing different ore types at Nkomati Nickel Mine, and a historic tailings dam in the O'okiep copper district of Namaqualand.

Three categories of samples were taken from various sections of the above mentioned mining operations. These comprised mine feed, plant tailings and final tailings, the last collected from various disposal dams. Samples from each category were collected in 20 litre buckets as slurry, and represented about 30kg of material.

3.3. Field Sampling

Samples were tracked depending on the reef types being mined and processed. Only Anglo Platinum processes the three main reefs in the Bushveld complex, namely the Merensky, UG-2 chromite and the base metal sulphide-rich Platreef as discussed in Chapter 2. Some operations combined the Merensky and UG-2 tailings in their respective disposal dams. Figure 3.1 shows the localities distributed across South Africa.

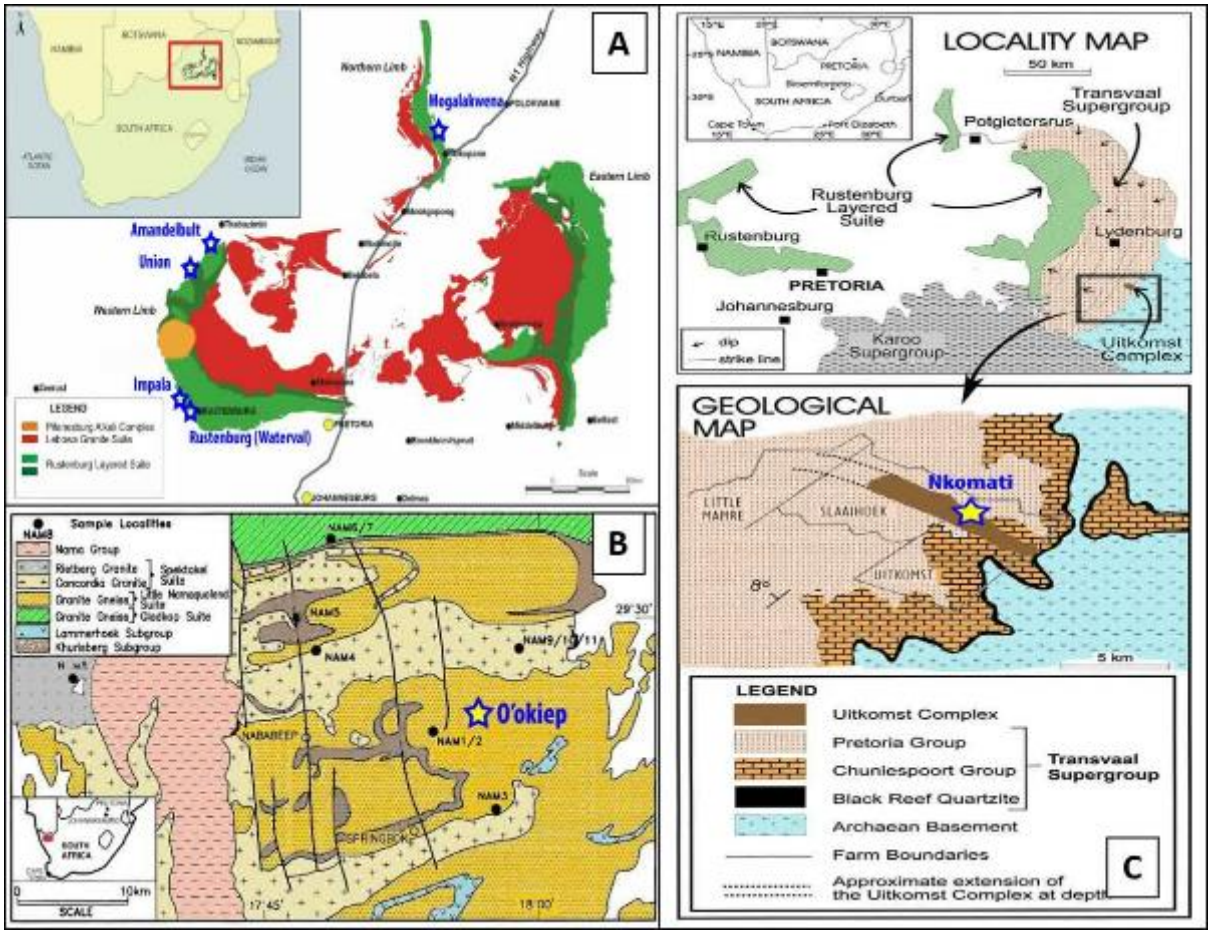

Figure 3. 1: : The study area locations (A) Schematic map of the Bushveld Complex where five study areas are located (Cawthorn, 2010). (B) The Namaqualand Metamorphic Complex where O'okiep tailings samples were collected (from Cairncross, 2004). (C) A map of the Uitkomst Complex showing the location of the Nkomati mine (after Cawthorn, 1993).

3.3.1. Impala

The first set of samples were collected from the Impala Dam 4 (Figure 3.2). It has been active for over 10 years and has an estimated lifespan of about 35 years with a current dimension of 2km x 3km. Dam 4 was constructed using the centreline method, similar to valley dams, where embankments were required to contain the tailings. For a centreline method of dam construction, waste rock are used at later phases of construction (USEPA, 1994).

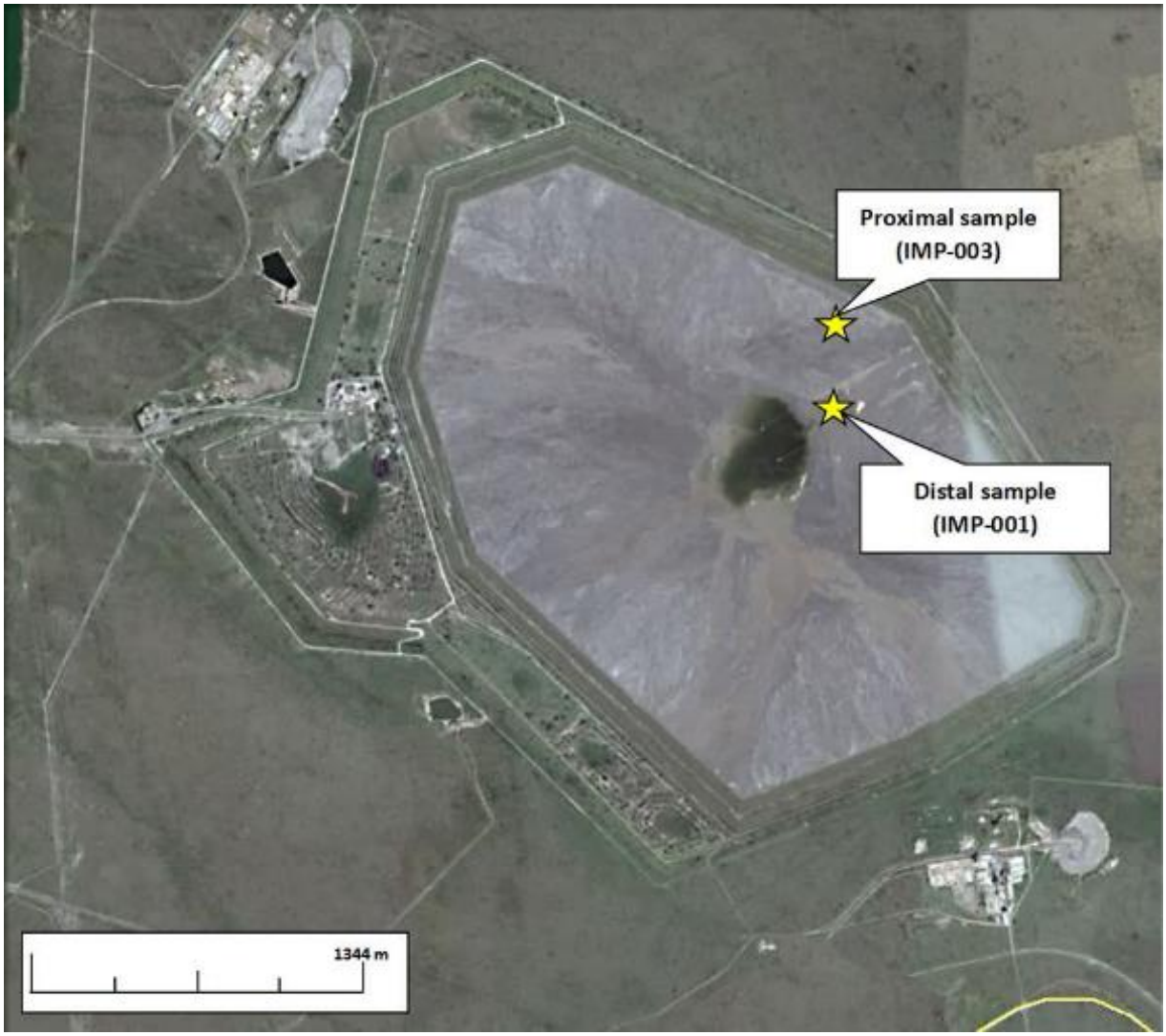

Figure 3. 2: : Impala Platinum Mine Dam 4 with the two sampling points (distal and proximal) indicated. Courtesy: (Google Earth, 2012).

A single impoundment configuration was employed during the construction of the dam with a spigot method of tailings disposal and decant towers (Figure 3.3).

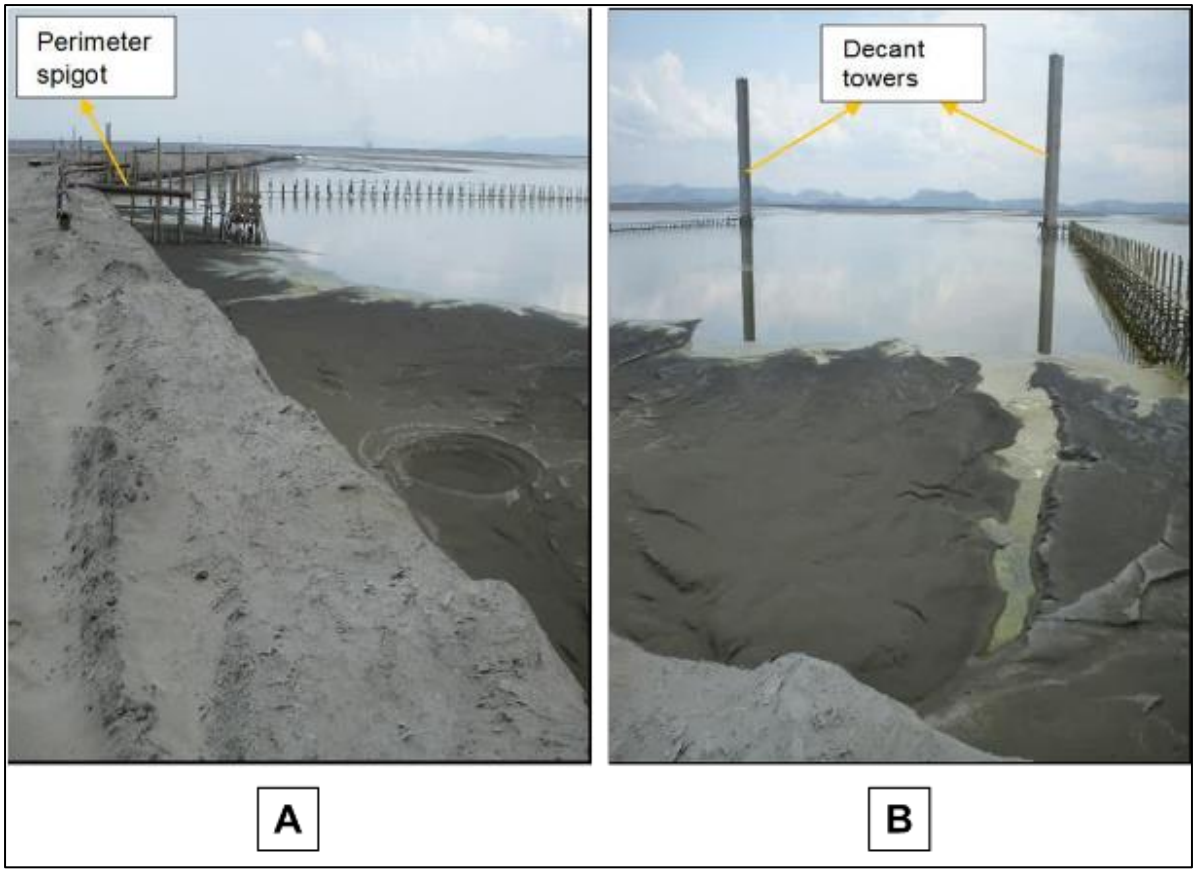

Figure 3. 3: Dam 4 at Implats. A centreline-constructed dam. (a) A spigot method of tailings disposal with perimeter spigots directed towards the centre. (b) Two decant towers situated at the centre of the dam, where tailing water is collect and recycled.

Two samples were collected from the dam surface by digging 50cm deep holes and selecting the lower 30cm (Figures 3.4 and 3.5). A distal sample (IMP-001) was collected towards the centre of the dam furthest from the edge. The second was the proximal sample (IMP-003), collected from near the output spigots at the edge of the dam. It was clear in the field that the distal sample was finer grained than the proximal.

Figure 3. 4: Distal sample (IMP-001) collection on Dam 4, Implats.

Figure 3. 5: Chromite streaks observed after sampling. An indication to UG-2- Merensky reef blending on site.

3.3.2. Nkomati

At the Nkomati mine, sampling was conducted at the two main processing plants that have been installed to handle the ores from the Main Mineralized Zone (MMZ) and Chromititic Peridotite Mineralized Zone (PCMZ). The rougher circuit feed represents the output from the ball mills and thus best approximates the original mine feed or run of mine (MMZ/RF-01). At the other end of the plant circuit the cleaner tails were collected, and represent the residue after the base metal sulphides have been extracted by flotation (i.e. the plant tails). The circuit sample points are designed to provide a duplicate (Figure 3.6), and to enable a longer section of circuit to be collected, both providing better statistical representivity (NK-MMZ/PT, NK-PCMZ/PT).

Figure 3. 6: Duplicate sample collection point of final plant tails from the MMZ plant at Nkomati mine.

Both underground and open cast methods are used for ore extraction with the processing plants in a fairly close proximity to the pits as shown in Figure 3.7. The

Onverwacht disposal dam is situated in a wide valley cut by a tributary of the Nkomati River, about 14km south of the mine (Figure 3.8).

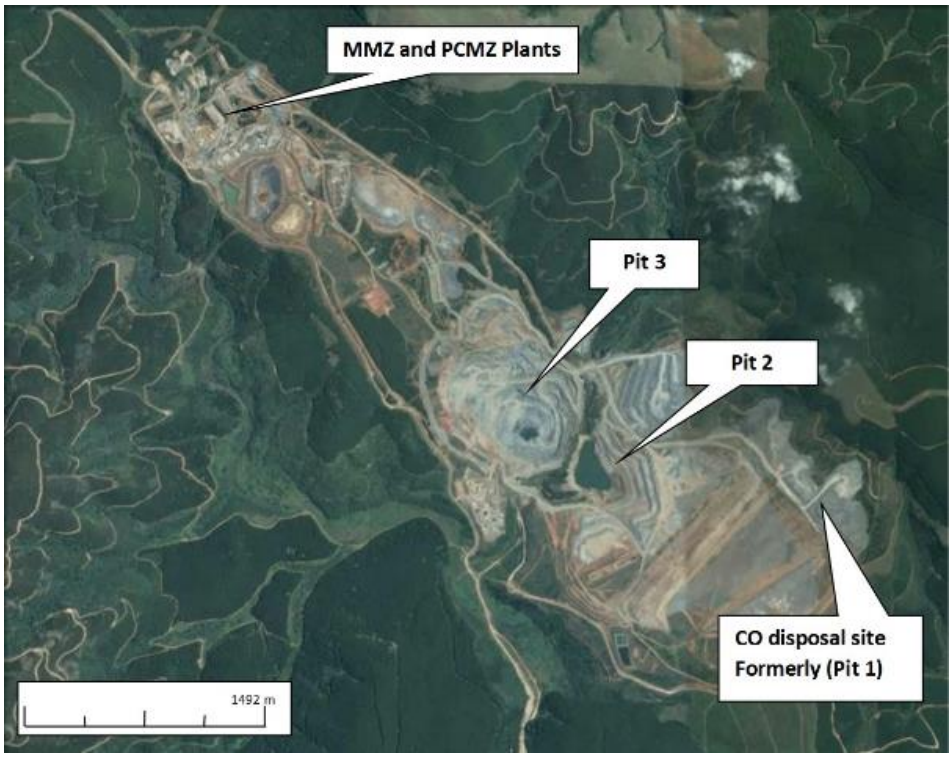

Figure 3. 7: A map of the mine layout (Google Earth, March 2014).

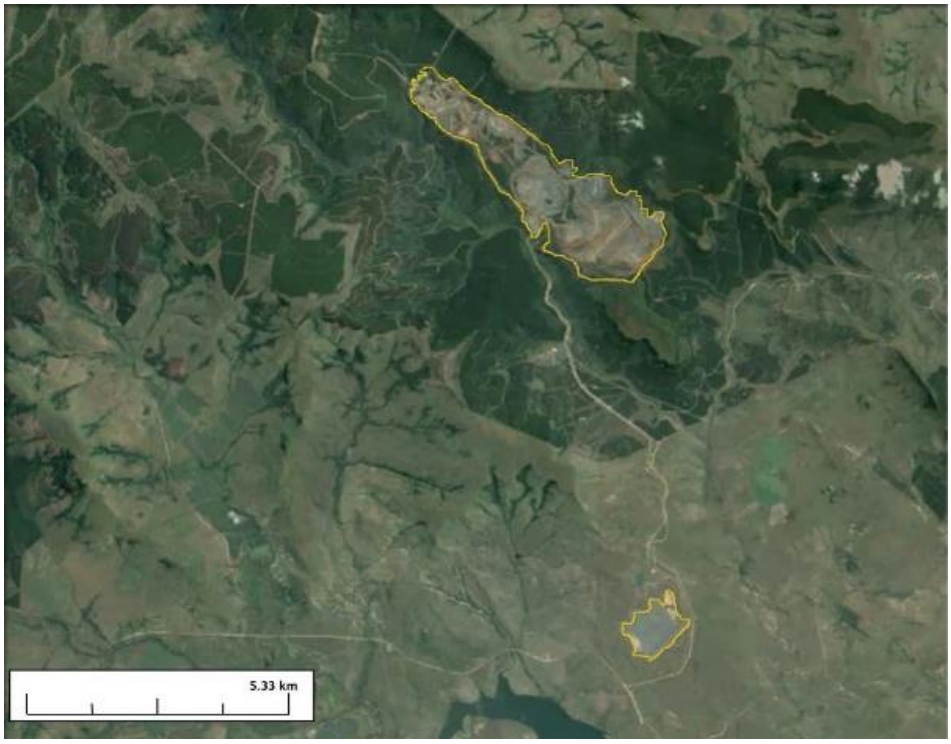

Figure 3. 8: A map of the Nkomati mine showing proximity of the Onverwacht tailing dam (bottom of the map) from the mining operation (Google Earth, 2014).

Tailings from the MMZ plant are pumped through a pipeline and deposited through a distributary system of multiple cyclones spread across the dam wall (Figure 3.9).

Figure 3. 9: A map of the Onverwacht tailings site showing the position of the dam wall which makes up the proximal end of the tailings facility where coarse material is allowed to settle (Good Earth, 2014).

The role of the cyclone (Figure 3.10) is to separate the coarse and fine fractions so that the former builds up proximally, thereby building a steep depositional fan that forms the wall, while the latter is transported via a hose line (Figure 3.11) towards the interior of the dam.

Figure 3. 10: One of the ten cyclones along the dam wall depositing coarse material.

Figure 3. 11: A hose line pumping the finer material to the distal end of the dam.

In this manner the wall heightens and advances downstream with time, while the fines spread in the opposite direction, so that the dam fill migrates upstream. Proximal (coarse) and distal (fine) samples were collected from 4 of the 10 cyclones across the dam wall. The former were taken directly from the outlet spigot of the cyclones (NK-CNC sample series), while the latter (NK-CNF series) were collected near the end of the upstream hoses (Figure 3.12). A somewhat precarious activity given the quicksand consistency of the fines! The coverage enabled the collection of a more representative suite of samples, in the view of the anticipated particle size differentiation developed across the dam during transport and depositional reworking.

Figure 3. 12: Sample collection close to Cyclone 4 on the Onverwacht dam where sample NK-CNC/4 was collected.

Tailings from the PCMZ plant have been stored in another form of dam that started off as an open caste mining pit, located about 3km south-east of the mine (Figure 3.7). Coarse waste rock was initially dumped into the pit after mining ceased, but the considerable voids throughout this material provided a novel means of co-disposing the finer tailings. Entry points of the tailing slurry into the dam where again chosen to collect the proximal coarse fraction (Figure 3.13, sample NK-PCMZ/CDC), while the

pond slime that occupied the interior of the dam represented the finer fraction (Figure 3.14, sample NK-PCMZ/CDF).

Figure 3. 13: Proximal coarse fraction sampling (NK-PCMZ/CDC) on the co- disposal site.

Figure 3. 14: Sampling of finer material (NK-PCMZ/CDF) from the co-disposal slime pond.

3.3.3. Amandelbult

Two categories of tailings sample were collected from the Amandelbult Section of Anglo Platinum. The first represented plant tails collected from the processing circuit in a manner similar to that followed at Nkomati, but by the company's Divisional Metallurgical Lab (DML) situated in Rustenburg, and donated to the current project. The second was also donated from Amandelbult mine directly and formed part of an evaluation of their historic Dam 1 for the purposes of estimating residual PGE grade (Fig. 3.15).

Three buckets each with 30kg sample were collected from the Amandelbult plant by the DML over a period of several weeks (samples AMB/101, AMB/102 and AMB/103). Dam 1 was subjected to a grid sampling pattern where nearly 90 vertical cores were drilled through the ~45m thick tailing sequence. Twelve boreholes were randomly selected from the grid and the top 1 metre interval was split longitudinally and one half donated to the project. Each of the borehole samples donated contained about 6.5 kg of material (S-TD series).

Figure 3. 15: Sampling site (Dam 1), Amandelbult Section historic tailings facility. Drill grid superimposed on a Google Earth image (Lekgau, 2012).

3.3.4. Other Anglo Platinum plants

The DML also collected samples from processing plants that serviced Rustenburg (WRT), Union (UST) Section and Mogalakwena (MPL) mines, only plant tails were

permitted to be sourced. WRT refers to the Waterval plant retrofit circuit tail and represents a dedicated Merensky waste product. Union produces a Merensky – UG-2 blend, while the MPL sample is derived from the Platreef ore zone.

3.3.5. O'okiep

While the main emphasis of the current project was directed at the South African platinum mining industry, the opportunity to visit the now closed O'okiep copper mining district was taken to provide some comparative data, as the overall mineralogy is similar (abundant norites). The historic tailings dam received output from the O'okiep processing plant that was active up to the 1960s, so reflects the less efficient procedures of that period, and perhaps could be a proxy for those contemporary dumps that occur throughout the Bushveld region, which were not accessible. Two samples were collected from O'okiep. OKP-1 was a brown sample suspected to be oxidized matter (Figure 3.16). The other sample was grey in colour and marked OKP-2. The sampling points are shown in Figure 3.17.

Figure 3. 16: OKP-1, a brown material collect at the top of the tailings dam.

Figure 3. 17: The nature of the O'okiep dam sample (OKP-2).

3.4. Sample Preparation

Plant tails and dam samples were prepared for mineral species/phase identification, mineral chemistry analysis, particle size distribution and specific surface area analysis in Chemical Engineering, UCT.

Tailings samples contained moisture and were as a result dried in the open for 72 hours. Frequent tilling was required with the aid of a hand spade to evenly expose the dump samples to room temperature. Although a larger portion of the sample appeared dry within the first 24 hours, some lumps were evident. A laboratory designed rolling pin was used to eliminate the lumps to disaggregate clumped materials.

3.4.1. Splitting

Splitting was the next procedure employed in the sample preparation exercise. This is a vital exercise as sample homogeneity prior to laboratory analyses reduces bias. The acquisition of homogenous samples results in data exhibiting minimal error attributable to sample heterogeneity. Splitting is a method used to divide a sample into several portions or sub-samples and randomly select a portion that is representative of the

whole sample. It apportions the even distribution of constituents within the sample and has to be executed in a very systematic way. For this project, four different splitters were used, the riffle splitter, rotary splitter, rotary divider and the micro-splitter. Each splitter had its own weight capacity and was required to homogeneously split a 30kg tailings sample in order to obtain a 100g sample for the various analytical techniques essential for the project. Four aliquots of 100g were obtained. One aliquot was used for screening, Quantitative Evaluation of Minerals by Scanning Electron Microscopy (QEMSCAN) and X-RAY Fluorescence (XRF) analysis, the second was used for particle size distribution and specific surface area. The third was further split down to 3g for Quantitative X-Ray Diffraction analysis (QXRD). The final homogenous set was held in reserve and used in times of shortage to avoid re-splitting the bulk sample.

3.4.1.1. Riffle splitter

The riffle splitter as shown in Figure 3.18, is made up of a trough-like container (30cm x 150cm x 30cm) with a very narrow base, consisting of a raster of blades to divide the material, with several open chambers at the bottom designed to allow adjacent chambers to permit the material to flow out in two separate directions. Directly at the base are two collecting bins with the same dimensions as the trough, aligned underneath the chambers. The riffle splitter is designed to evenly distribute material to both collectors. Once the sample has been fed into the riffle splitter, both collecting bins should relatively have equal amounts of material. The riffle splitter has a capacity to work with material with a maximum weight of about 20-30kg.

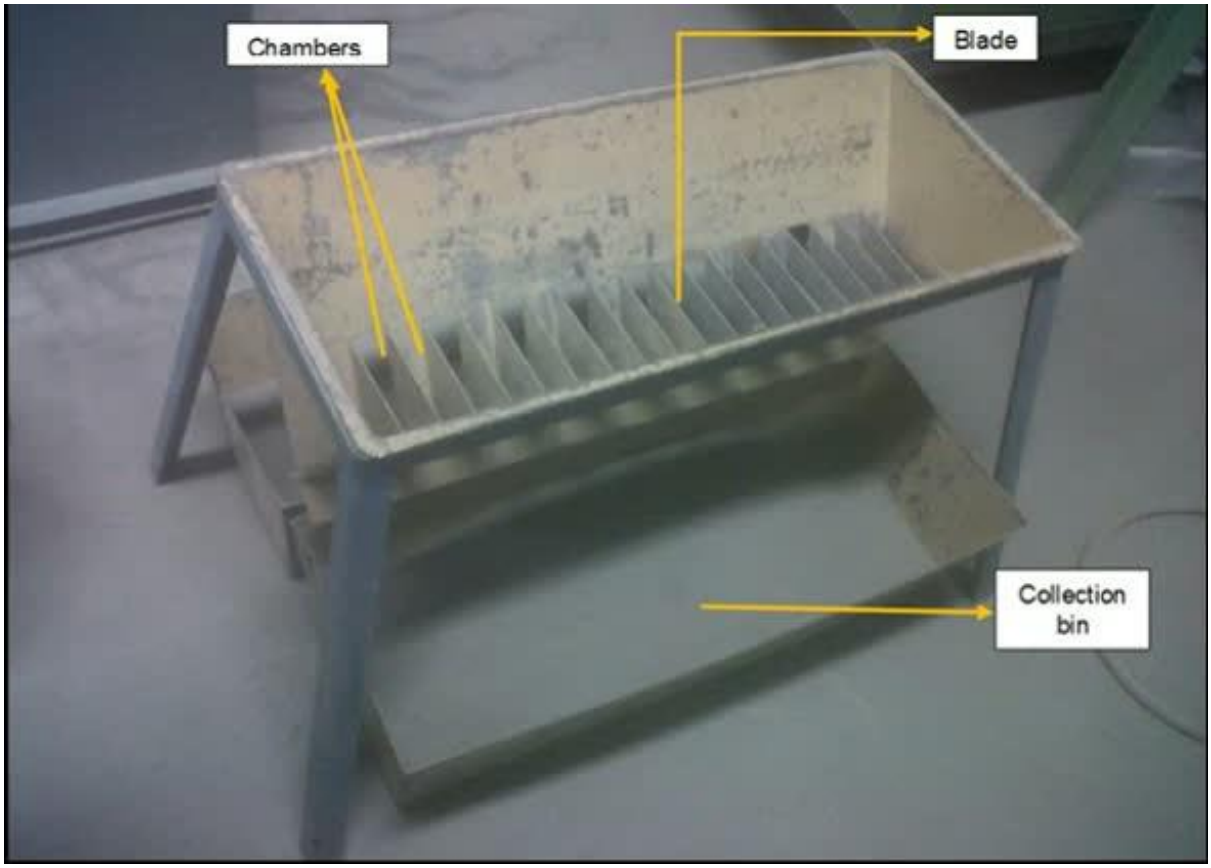

Figure 3. 18: An open-bin riffle splitter.

Each 30kg sample was homogenously split into two 15kg samples. Individual 15kg samples were then split into 7.5kg. The end result of the riffle splitting exercise generated four portions each having approximately 7.5kg of material.

3.4.1.2. Rotary splitter

The rotary splitter, illustrated in Figure 3.19, has a weight capacity of 10kg, implying that samples with a maximum weight of 10kg can be fed into the system instantly. It is of great significance to note that the four fractions of material generated from each collecting trough from the riffle splitter was handled and fed separately into the rotary splitter. Comprising of a hopper, a vibrating feeder and ten cups which rotate on a splitting table, the rotary splitter is more mechanised than the riffle splitter. The rotary splitter is electrically powered to provide constant rotation of the cups on the splitting table as the material is fed into the hopper. It also has a switch to aid in the vibration of the feeder. This vibration allows for a consistent supply of material to the splitting table. The rotation of the cups occurs at a constant rate to distribute the sample evenly among the ten cups.

Figure 3. 19: A ten-cup rotary splitter with a hopper, a vibrating feeder and a rotating table encapsulating the cups.

The rotary splitter was only switched off after all four fractions had been split. Each 7.5kg portion was treated separately, generating approximately 750g of material in individual cups which were bagged independently. A total of 40 bags were produced from the rotary splitting exercise, with individual bags weighing nearly 750g.

In order to avoid bias, one of the forty 750g bags was randomly selected and required further splitting. However, it was impractical to split a 750g sample using a rotary splitter as effective homogeneity could have been somewhat unachievable. A rotary splitting test that was undertaken with a 600g sample, resulted in the uneven distribution of material. This could have been triggered by the speed at which the splitting table rotated and the number of full cycles it attained. It was therefore necessary to use a different type of splitter with a lower weight capacity compared to the rotary splitter.

3.4.1.3. Rotary sample divider

Similar to the rotary splitter, the rotary sample divider (Figure 3.20) also requires electricity to rotate ten glass jars at a constant speed. The rotary divider rotates at a much higher speed of about 78 rotations/min compared to the rotary splitter which is 40 rotations/min. It has a maximum weight capacity of 2.5kg and is much smaller in size, ~¼ the size of the rotary splitter. It has a cone at the top, with a narrow hole that feeds the sample into the rotating jars. The jars are custom designed, notably smaller than the rotary splitter cups and have continuous glass threads around the neck which aid in reliable fastening to prevent breakage or fall of the jars during the spinning action of the sample divider.

The randomly selected 750g bag of material from the rotary splitter was gradually emptied into the funnel-shaped hopper of the sample divider which did not have any vibration mechanism and therefore the hopper was manually tapped regularly to prevent choking.

At the end, each jar had roughly 75g material. With the intention of getting a 100g homogenous split, a marginally complex approach was used. Two jars were randomly selected and bagged separately. The ten jars were emptied and fitted back onto the sample divider. One of the selected bags was split further with each jar containing about 7.5g. Four jars were selected at random, which when combined added up to 30g. The contents from the four jars were added to the remaining 75g sample that was initially chosen adding up to a total of 105g. In some cases, it is practically impossible to achieve an exact 100g split. This is due to the possibility of minimal material loss during the splitting process. However, it is advisable to obtain a split of slightly over 100g.

The process was repeated by selected different 750g bags acquired from the rotary splitter until three more sets of 100g homogenous splits were achieved.

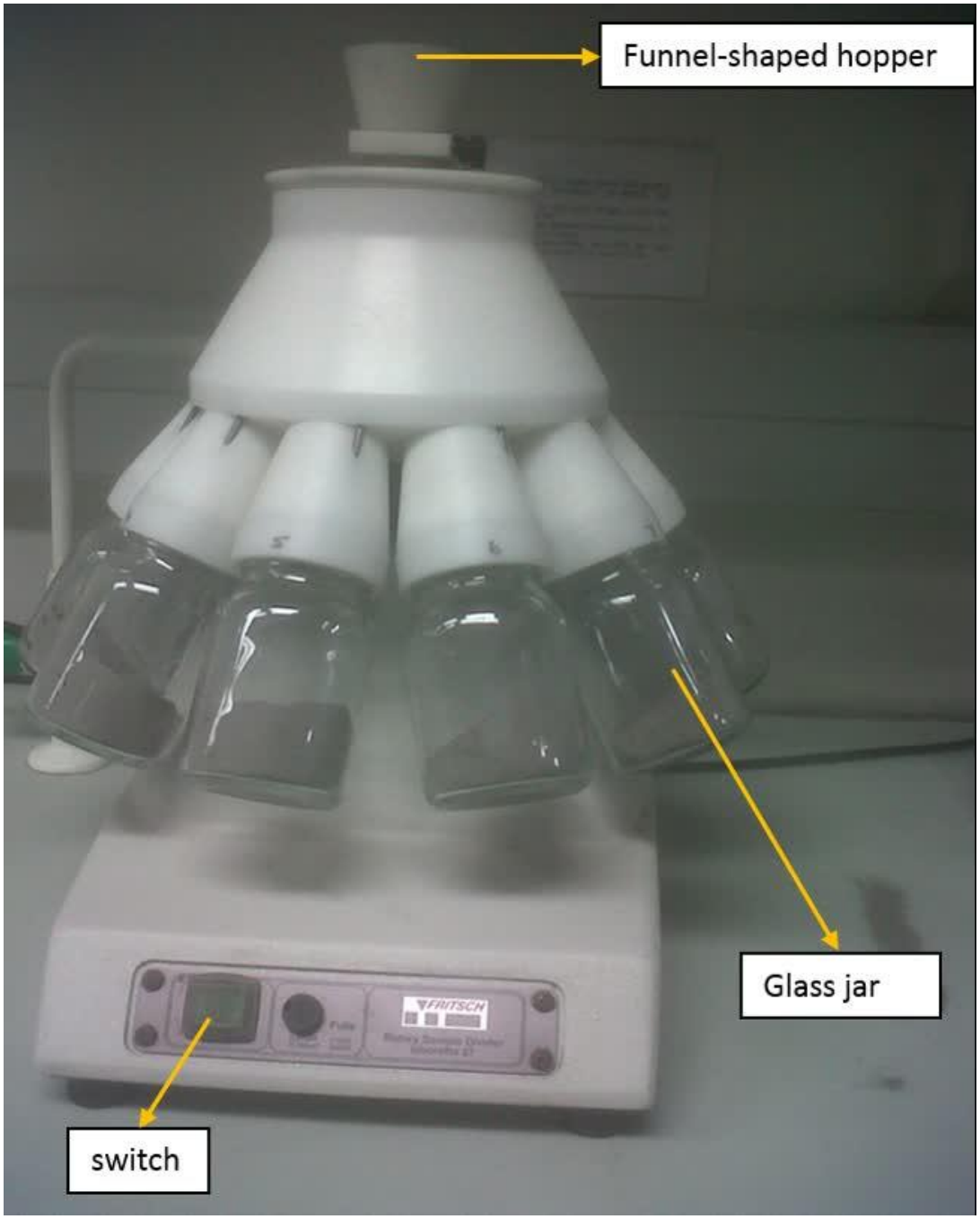

Figure 3. 20: A Retsch rotary sample divider with a funnel-shaped hopper and glass jars.

3.4.1.4. Microscal suspension sampler

This was the final sample splitter employed in this project. The Microscal suspension sampler (Figure 3.21) also known as the rotary micro riffler, can only accommodate a maximum sample feed of 10g.

Figure 3. 21: A Microscal suspension sampler.

Most of the mineralogical analytical techniques used in the project including QEMSCAN, QXRD, and XRF, required samples of about 6-8g or less, making the Microscal suspension sampler the most appropriate splitting device for achieving such quantities of sample. Like the rotary splitter and rotary sample divider, the Microscal suspension sampler is also electrically powered. It is made up of 8 test tubes and a cyclic feeder, vibrating the sample from the feeder into the tubes which rotate at a constant but slow speed of about 30 rotations/min as compared to the two other electricity-operated splitters as discussed previously. Owing to the slow rotating action of the sampler, the Microscal suspension sampler has the advantage of reducing the

risk of any sample loss. Consequently, the Microscal suspension sampler is the most accurate splitter used in this project.

3.4.2. Sieve analysis

Sieve analysis, also known as screening, is the separation of materials on the basis of particle size. The screen sizes were 150 µm, 106 µm, 75 µm, 53 µm, 38 µm and 25 µm.

3.4.2.1. Wet sieving

One of the four 105g homogenous samples was wet sieved to obtain seven size fractions (+150, +106, +75, +53, +38, +25 and -25 µm).

The wet sieving process commenced by adding water to the sample to form a mobile slurry in a laboratory pan. It was then followed by emptying onto the largest screen (+150 µm) which was clamped onto a vibrating apparatus operated with a motor with a bucket underneath to collect the undersized material in an ordinary water solution as illustrated in Figure 3.22.

The vibrating action served two purposes; first and foremost to liberate particles that had adhered to each other and secondly to agitate the particles within the solution so that undersized particles would fall through the sieve. The adhesive property of water was used to collect precipitates that had remained in the pan as the solution was emptied onto the screen to reduce the loss of material.

Running water through a tube, onto the screen at constant pressure was required throughout the process. This was a time consuming procedure and therefore a level of patience had to be exercised in order to effectively filter out undersized particles. Timely observations of water collected with a transparent beaker, as it enter the bucket placed underneath the vibrating frame, was the only indication as to the presence or absence of undersized particles on the sieve. Clear water in the beaker proved that there was an absence of undersize particles while the presence of particles in the beaker signified that the elimination of undersize particle had not been completed thus the procedure has to be continue until the purpose was fulfilled.

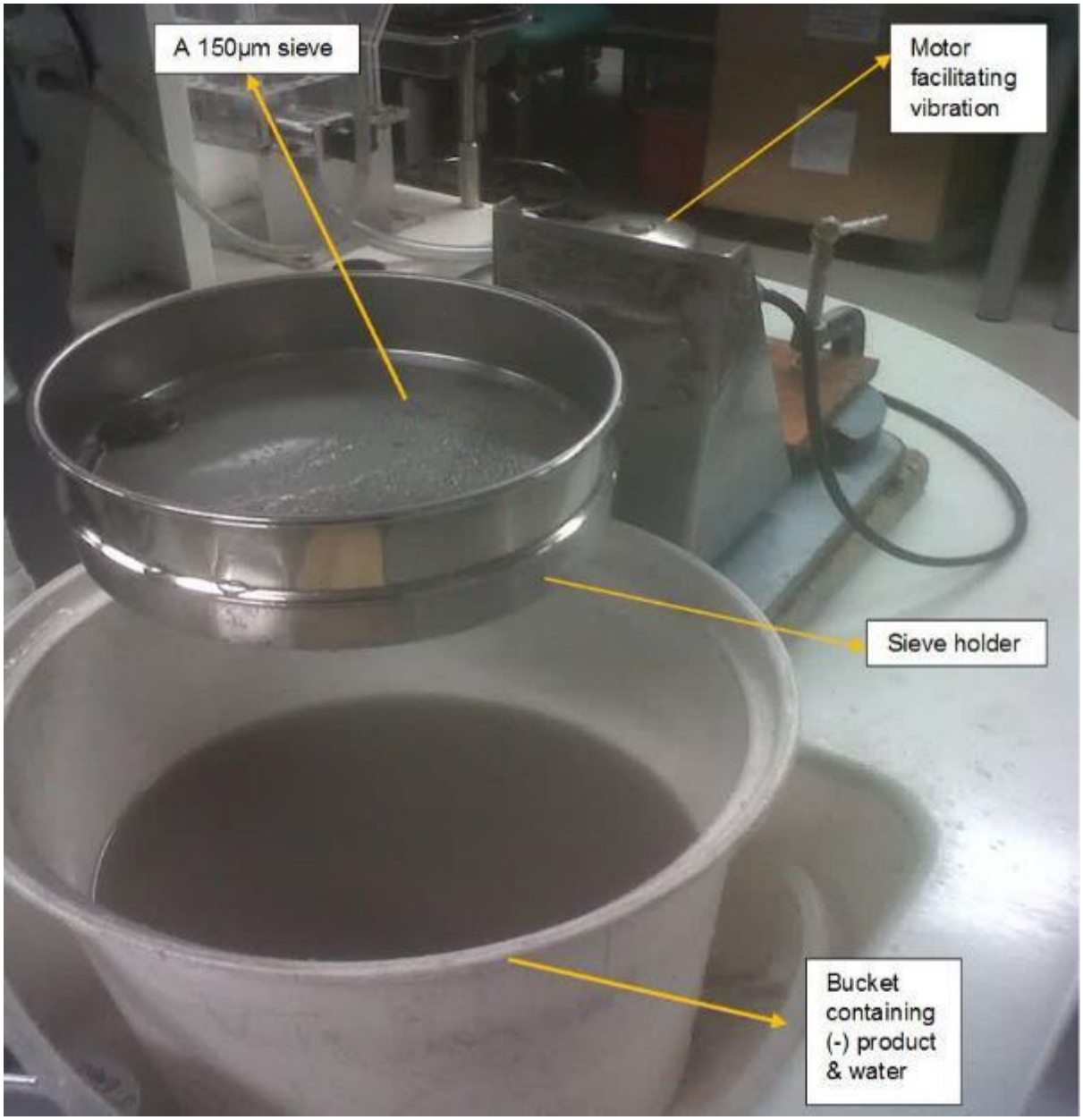

Figure 3. 22: A wet sieving apparatus with a bucket underneath the sieve to collect undersize particles in water solution.

The oversize (+) product that remained on the sieve was collected in water solution, emptied onto a labelled tray and dried under a group of 150watts globes to make the water evaporate from the solution.

The next sieve in the sequence (+106 µm), was clamped onto the vibrating device with an empty bucket placed underneath the apparatus. The bucket containing the undersize (-) products from the 150 µm sieve was gradually emptied onto the new sieve. Precipitates remaining at the base of the bucket were also emptied onto the sieve with the aid of a cup. Running water was then used to liberate any form of

adhesion between particles and allow the undersize particles to filter through the sieve in solution until the water collected beneath the sieve was clear of particles. This procedure was then repeated for all screen sizes.

Undersized (-) products obtained from the 25 µm sieve were not visible to the naked eye. The only evidence that they had been collected was the milky appearance of the water brought about by saturation of the particles in solution. After achieving the (+) products from the 25 µm sieve, there were about five or six 20-litre buckets containing (-) products of the 25 µm sieve in solution.

A pressure filter, shown in Figure 3.23, comprising of a 15-litre steel cylinder and an outlet that decants water and leaves the precipitates behind on a filter paper, was employed. The process of decanting the water was made possible by a gas inlet containing dry air that compressed the water out of the pressure chamber.

The residual material on the filter paper was placed in an oven at 27ºC for a minimum of 6 hours. Once all samples had dried, they were weighed separately and kept in sample containers.

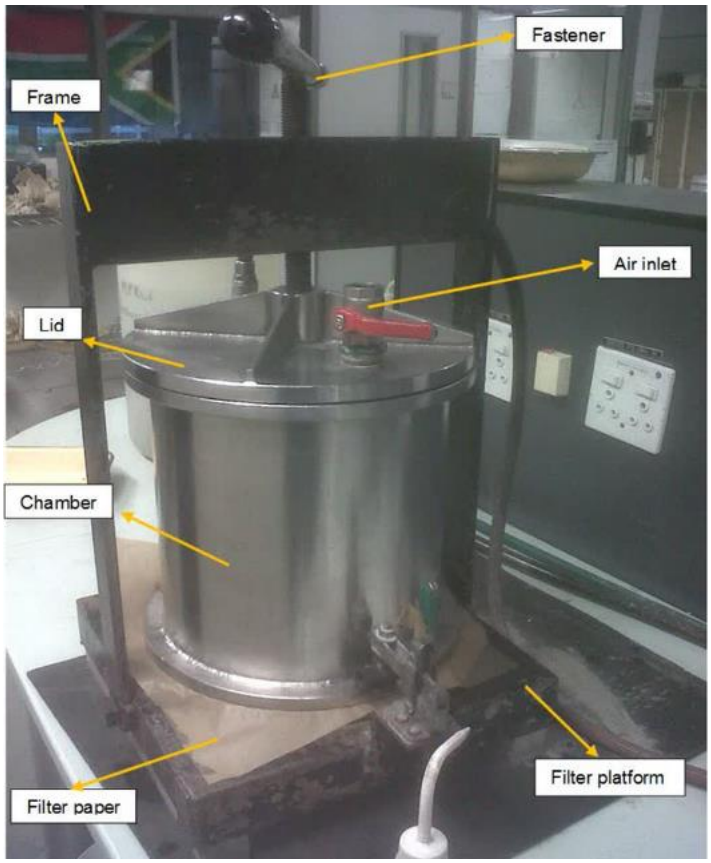

Figure 3. 23: A pressure filter.

3.4.2.2. Dry Sieving

Dry sieving is used to validate the results obtained from wet sieving. The same sequence of the different sizes of sieves used during wet sieving was mounted for the dry sieving procedure. A pan was placed at the end of the stack of sieves which were mounted onto a mechanical shaker as shown in Figure 3.24.

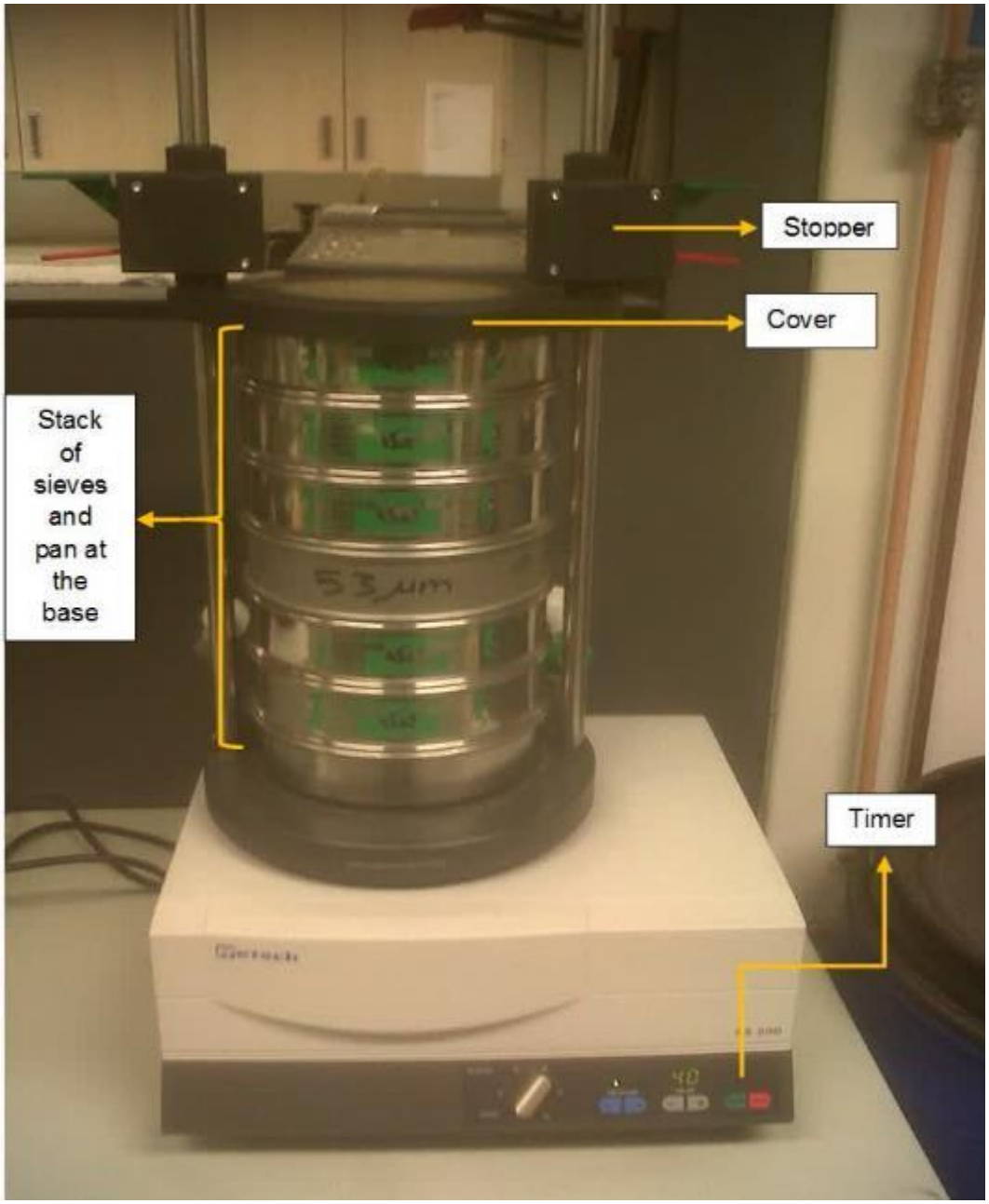

Figure 3. 24: A Retsch AS 200 Shaker.

Size fractions obtained from wet screening were emptied onto corresponding sieves. For instance, the (+) product of the 150 µm sieve was emptied onto the 150 µm sieve, the same applied to all the oversize products with the exception of the 25µmundersize

product. It was emptied into the 25 µm sieve before the dry sieving test commenced. Two rubber balls of 10mm radius were placed onto each sieve as the rubber balls prevented choking of any undersize material on the sieves. The stack of sieves was covered with a specially designed cover and two bolts held the mounted sieves in place.

An amplitude of 60 to induce vibration of the shaker and a sieving time of 60 minutes was used. The shaker makes use of an electromagnetic drive that produces a 3-dimensional throwing motion moving the material equally all over the whole sieving surface. When the shaker is in motion and as the material is equally distributed on the sieve surface, undersize particles that were not identified during the wet sieving procedure are transferred from one sieve to another.

After the 60 minutes sieving time, it was observed that some material settled in the pan, located at the bottom of the sequence. This implied that dry screening was able to achieve more undersize material as compared to wet screening.

The material on each sieve were carefully collected, weighed on a weighing scale and stored in separate well-labelled containers. To ensure that the screening process was effective, the sum of the total amount of product was determine and compared with that of the original sample. Both sieve analyses used in this project allowed for 5% sample loss. Losses higher than this percentage implied that the exercise was inaccurate and had to be re-done.

Further dry sieving tests were conducted with a 100g aliquot from the splitting exercise (Section 3.4.1). A dry sieving process involving the same sieve set up as described above was employed. The difference between this dry sieving test and the one explained above was that, the rudimentary method of starting out with a stack of empty sieves and un-sized material (complete 100g aliquot) was introduced. The un-sized material was dispensed onto the stack of sieves. The sample amplitude and time as explained above was used. The particle size results of the various sieving methods were compared.

3.5. X-ray Fluorescence (XRF)

Bulk and sized tailings were prepared for XRF analysis. Approximately 2g was required for the preparation of fusion discs and 6g for pressed pellets.

3.5.1. Fusion discs

Preparing a fusion disc entails the dissolution or decomposition of a portion of a sample by a flux and fusion into a homogeneous glass entirely eliminating particle size and mineralogical effects. The fusion technique minimises the possibility of high or low specimen dilution for the purpose of decreasing matrix effects. It also eliminates the addition of compounds such as heavy absorbers or internal standards to compensate for matrix effects.

Firstly, clean empty ceramic crucibles are usually stored in an oven at 110ºC. Required crucibles were removed and allowed to cool in a desiccator. 2g of sample powder were weighed into the crucibles and placed back in the oven at 110ºC for at least 4 hours (usually overnight). The loss in weight is ascribed to moisture (H2O-). The crucibles were then placed in a furnace and heated to 950 ºC to record the Loss on Ignition (LOI). 0.7g of the each sample was weighed and the remaining was stored away in case the fusion discs had to be recast.

Exactly 6.000g of flux (lithium borate) was weighed out and added to the 0.700g sample and effectively mixed in a 30ml glass specimen container. The fusion mix was melted at 1200 ºC and cast in Pt-Au ware using a Claisse Fluxy gas burner instrument (Figure 3.25).

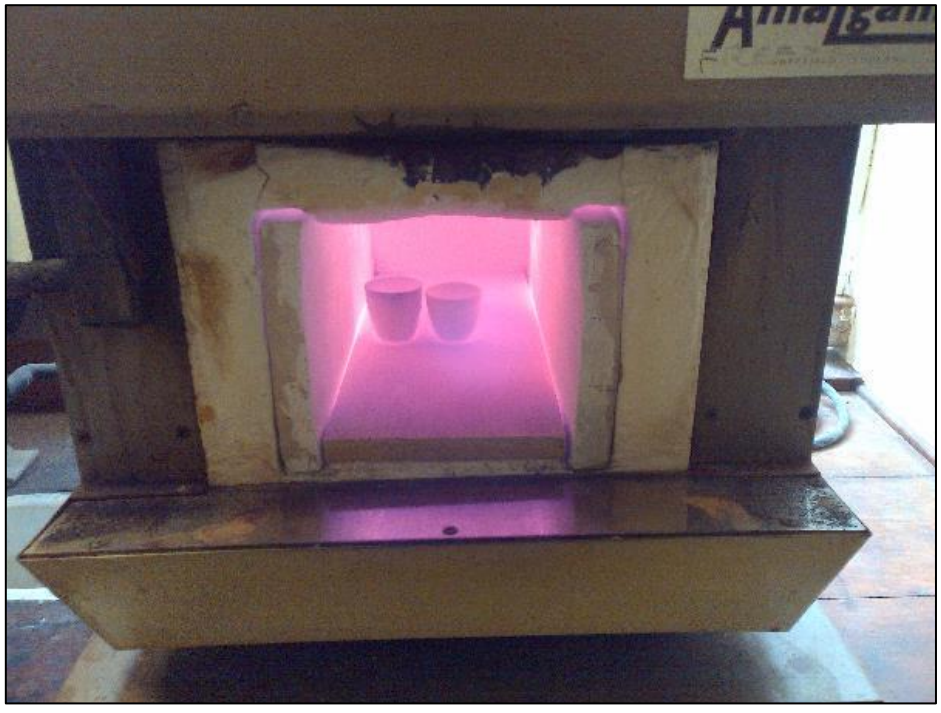

Figure 3. 25: Crucible casted in Pt-Au ware using a Classie Fluxy gas burner instrument.

3.5.2. Pressed Pellets

Practically, sample size particles should be less than about 38 µm. For samples above the required size, an agate mortar was used to grind the samples until a powder sized material had been achieved. About 2 to 3 drops of moviol solution was dropped onto 6g powdered material using a pipette and effectively mixed in a transparent sampling bag. The powder was then compressed with a back of boric acid crystals (Figures 3.26 and 3.27) at 10 tons pressure.

Figure 3. 26: 3.26: A 30 ton press L-30.

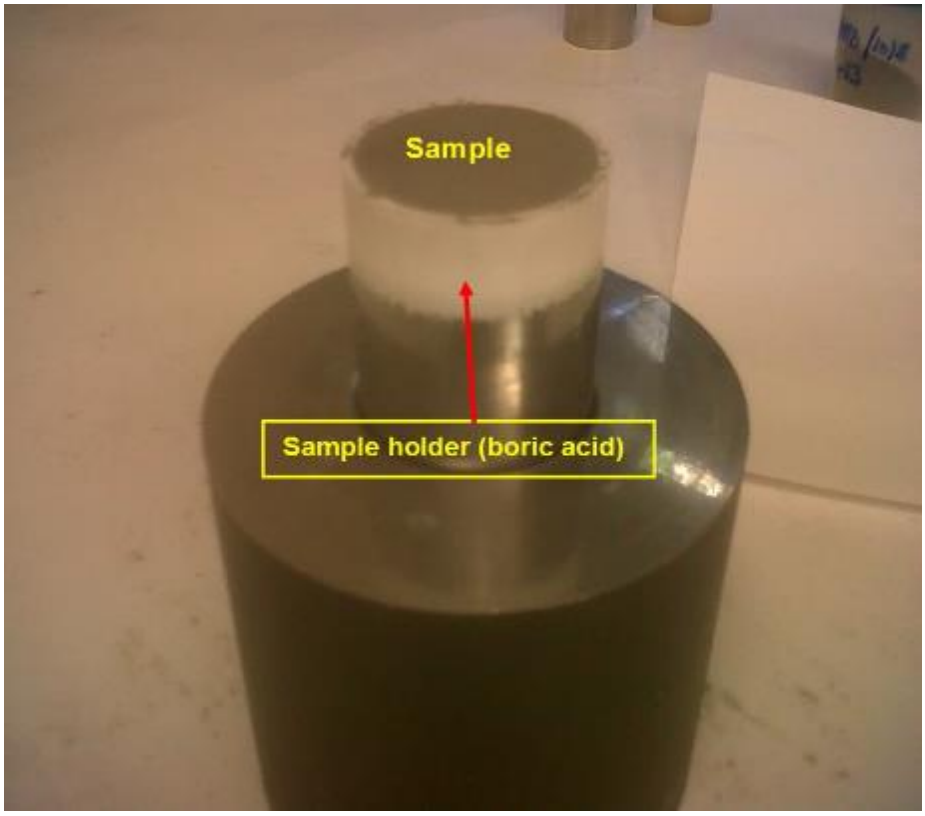

Figure 3. 27: A finished product of a pressed pellet ready for XRF analysis.

Figure 3. 28: A fusion machine stationed at the Department of Geological Sciences, University of Cape Town.

3.6. Quantitative X-ray Diffraction (QXRD)

3.6.1. Micronizing the sample

A bulk samples from each mine site in this study had to be micronized. This is because a grain size of less than 10 micron is required for QXRD analysis. Using a Microscal suspension sampler (Figure 3.21), bulk samples were homogeneously split down to 3g as this was the amount of material require for QXRD analysis. The 3g split sample was then micronized using a Glen Creston McCrone micronizing mill illustrated in Figure 3.29. Both splitting and micronizing exercises were carried out at the Centre for Minerals Research laboratory at the University of Cape Town.

The bench-mounted micronizing mill (Figure 3.29), produced a unique grinding action of the cylinders producing both linear contact blows and planar shearing. A 125 ml polypropylene jar containing 48 corundum grinding pellets in an ordered array was gyrated around a horizontal axis. The sample was emptied into the jar and distributed in-between the pellets. Wet milling was employed to avoid amorphisation during grinding. Ethanol was used as grinding agent for this exercise. Therefore 5ml of ethanol was added to the sample and tightly close to avoid spillage. The polypropylene jar was fitted into the micronizing mill for a period of thirty minutes.

When the micronizing mill had finished grinding the sample, the jar was loosened from the mill and the lid from the jar was replace with a pouring lid with two 6 mm holes. The ground slurry was then poured out through one of the holes and the jar, with the pellets still in place, washed a further two or three times with intermediate shakings using ethanol. This procedure generated a combined pouring and washing together with a clean jar and pellets without having to remove the pellets from the jar.

The slurry generated was recuperated in porcelain cups. More ethanol was used to recover as much as sample as possible. The cups were dried under a fume hood for 24 to 48 hours.

Figure 3. 29: A Glen Creston McCrone Micronizing Mill at the Centre for Minerals Research laboratory, University of Cape Town.

The result was a short grinding time with virtually no sample loss, as well as exceptionally even particle size distribution. There was virtually no chemical degradation of the particles and no disturbance in crystal lattice. Wet grinding in the form of slurry is the preferred method for sample preparation when micronizing. The micronizing mill rapidly reduced samples by a unique vibratory grinding action.

3.6.2. QXRD sample preparation

Roughly 0.5g of sample was needed for QXRD analysis. Side-loading with frosted glass was recommended to fill sample holders. The sample holder was gently tapped while filling, to ensure good packing of the grains. Alternatively, back loading was used.

3.7. Malvern Particle Size Analysis

Particle size analysis was carried out at University of Cape Town's Department of Chemical Engineering by a Malvern Mastersizer 2000. Sample preparation for this type of analysis was simple and less time consuming. The amount of sample required was not fixed and differed from sample to sample. Bulk samples were used in the particle size analysis. A laboratory spatula was used to collect a scoop of each bulk sample. Roughly about 0.5g or less of sample was required for the procedure.

A scoop of sample was poured onto an antistatic pour boat. A surfactant was required to lower the surface tension between the water in the dispersion unit of the Mastersizer and the sample and to avoid dissolution. The surfactant served as a wetting agent as well. Nonidit, a surfactant consisting of non-ionic alkoxylate based linear alcohols was used.

The Malvern Mastersizer 2000 was computer-operated with aid of a Mastersizer software. An analyser tool incorporated in the software controlled the amount of water in the dispersion component of the machine. A gauge gave a visual display of the amount of sample the system could accommodate as the sample in solution was carefully poured into the sample dispersion unit represented in Figure 3.30.

To ensure that good results were achieved, the analytical exercise was performed three times and the average result was selected. Data acquired had to indicate that the weighted residual was less than 1% for results to be classified as valid.

Figure 3. 30: A sample in solution emptied into the sample dispersion unit of a Malvern Mastersizer 2000 at the Department of Chemical Engineering, University of Cape Town.

3.8. Brunauer Emmett and Teller (BET) Surface Area Analysis

The main sample preparation required for BET surface area analysis is degassing the sample. This was performed with a Micromeritics Tristar shown in Figure 3.31 assembled at the University of Cape Town's Department of Chemical Engineering. An appropriate cell size of 9mm for sample was chosen. Using a 5-place analytical balance, the weight of the empty sample cell with fill glass rod was recorded three times and the average calculated. This was recorded as the initial weight.

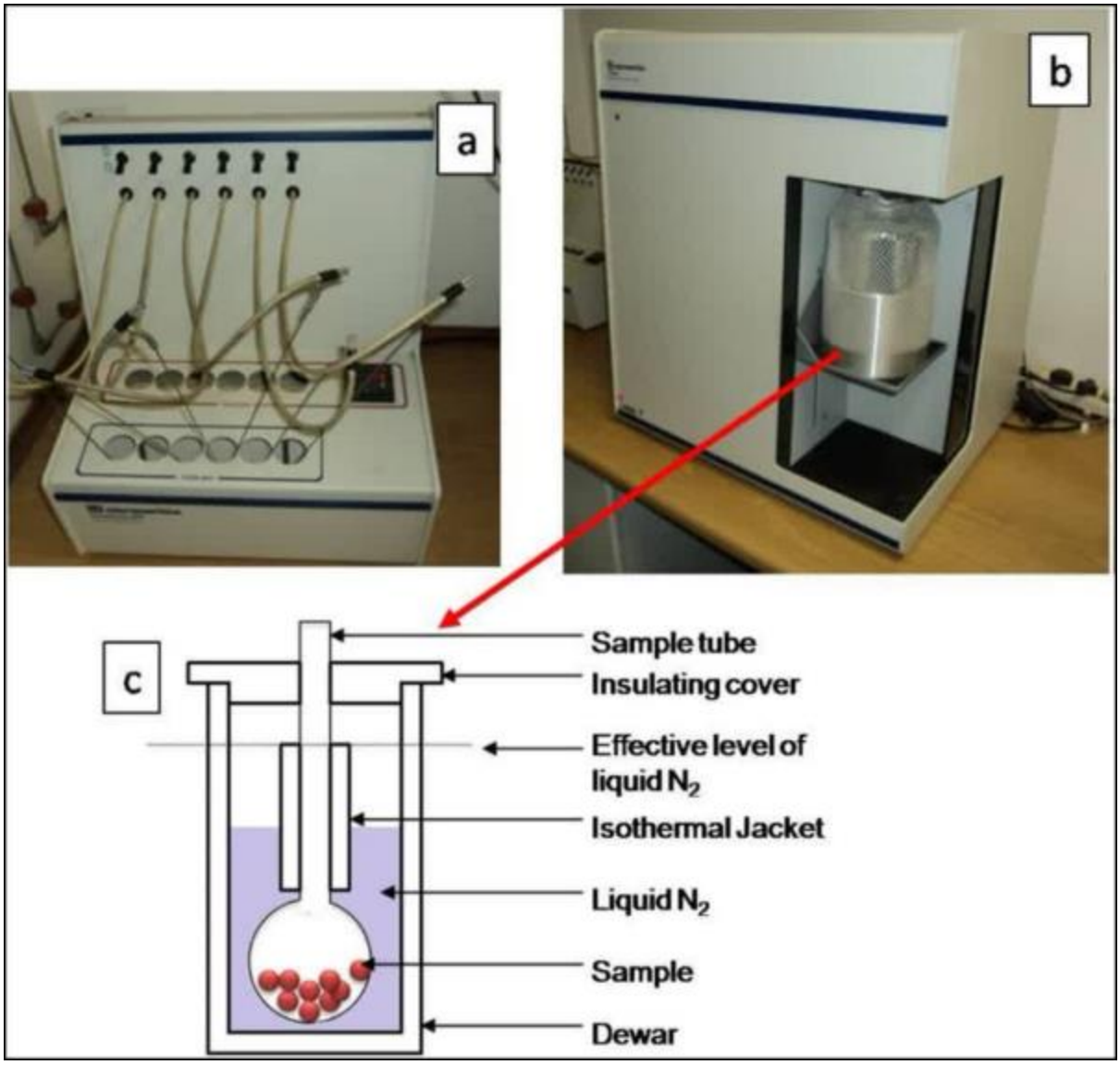

Figure 3. 31: An automated BET surface area equipment. (a) Micromeritics Flow Prep 060, (b) Micromeritics Tristar 3000 and (c) liquid N2 coolant Dewar depicting the Isothermal Jacket method of maintaining the cold/warm volume ratio in the sample tube (adapted from Phadi, 2012).

The fill glass rod was removed and the sample was inserted into the glass cell using a funnel (½ to full volume of the cell was appropriate). The fill glass rod was placed back into the cell. Three measurements were taken for the sample cell with the glass rod and sample. The average was calculated and record as the weight before degassing.

In order to obtain the sample weight, the initial weight was subtracted from the weight before degassing. Put the cell into a heating mantle (pinch mantle to open the mouth) using a clamp to secure cell into mantle. The degassing temperature was set to 90ºC. Degassing took more than 20 hours.

It is recommended that samples should be degassed at the highest temperature to prevent structural changes to the sample. A high temperature will accelerate the degassing process.

The time required to complete degassing procedure, that is complete removal of unwanted vapours and gases adsorbed on the sample surface, can only be accurately determined by conducting a degas test which is built into the AUTOSORB software. As a general guideline however, three hours should be considered a reasonable minimum. IUPAC recommend no less than 16 hours, which can be achieved overnight. Samples that require low temperatures generally require the longest outgas times.

A sample can be considered ready for analysis when the sample passes degas test of no more than 10 µm per minute.

3.9. Quantitative Evaluation of Mineral by Scanning Electron Microscopy (QEMSCAN)

Samples were prepared at the University of Cape Town's Centre for Mineral Research laboratory. Prepared QEMSCAN samples for this study were made up of tailings material mounted on 30 mm - round epoxy plugs. Both routine moulds and vertical sections were prepared for QEMSCAN analyses. Vertical sections were prepared for samples with high chromite content as those containing UG-2 reef types. Cured moulds are cut into <3 mm slices at the Department of Geological Sciences, University of Cape Town.

3.9.1. Routine samples

Samples from the sieving exercise described in Section 3.4.2 were used to prepare samples for QEMSCAN analysis. One size fraction from each sample was used for the analysis. The size fraction selection was based on the mass domination and the size fraction with the highest copper content. About 4g of material, effectively split with the aid of a rotatory splitter (Figure 3.19) was require for sample preparation. Further splitting had to be employed to obtained 1g aliquots for preparing the QEMSCAN blocks. The micro splitter displayed in Figure 3.20 was use to split the 4g sample into 1g aliquots.

Each sample typically required 3 blocks per size fraction. Milled graphite was then added to the sample and mixed with a brush on a screen that was one size fraction

smaller than the sample. Additional mixing of the sample and graphite was required but a sieve one size bigger than the sample was used. The ratio of the sample and graphite was 2:1. Graphite is added to liberate adhesive particles and also to help with electron conductivity.

The addition of the graphite-sample mix into the moulds followed labelling and lubricating of the round shaped moulds. Resin was then added to each mould and carefully mixed into the sample in a figure of eight pattern. Subsequently, the sample moulds were placed into a vacuum chamber displayed in Figure 3.32 for about 5 to 10 minutes and frequently breaking the vacuum. Vacuum impregnation was used to remove entrapped air when encapsulating samples in epoxy. The vacuum pulls air from the mount, displacing it with epoxy, providing complete bonding and support. This maintains sample integrity during abrasive sample preparation, reducing the chances of cracking and delamination.

Figure 3. 32: A vacuum chamber used to release trapped air from the sample-graphite mixture.

Sample moulds were removed from the vacuum chamber and place in the pressure pot overnight to cure. Once the moulds had cured, a printed label and more resin was

added to the back of the mould. This was placed in the oven at 30º C and allowed to cure until evidently dry.

Once the moulds were completely cured, removal the blocks from the moulds for polishing followed. Polishing was done in a series of grinding and polishing steps until a 1 µm polish. The polished blocks are carefully rinsed after gently washing the blocks with soap.

Following the polishing steps, the blocks were placed in an ultrasonic bath for approximately 10 minutes and cleaned further with a generous squirt of ethanol being very careful not to scratch the surface. Sample were dried in the oven at 30º C for a minimum of 1 hour.

An optical microscope was used to check the quality of the final polish ensuring that there were no plucked grains, large differences in relief, cracked or grungy looking grains on the sample surface.

A carbon-coat was applied onto the samples using the Emitech carbon evaporator. The carbon coat was needed to diffuse electrons off the surface of the sample during the QEMSCAN analysis.

3.9.2. Vertical sections

Preparation of vertical section blocks begun with the identical steps of employed in the routine sampling technique of utilising samples from the sieve analysis and effective splitting. The main difference was that samples were split into 4g aliquots and required one block per fraction for vertical sections.

Similarly, milled graphite was added to the sample and mixed on a screen one size fraction smaller than the sample and mined further through a sieve one size bigger than your sample. Unlike the routine technique, the sample to graphite ratio was 1:1.

Special ice cube moulds were used for vertical sections unlike the ordinary round moulds used in the routine procedure. The vacuum chamber process employed in the routine sample preparation described above was also employed for vertical section.

After the moulds were removed from the vacuum chamber, the blocks were cut into < 3 mm thick and mounted into 30 mm round mounts. Typically 3 blocks were made per sample fraction.

The vertical section sample preparation continues from the addition of resin as in the routine sample procedure. An important aspect to be taken into considerations is that, the samples should maintain correct placement in the mounting cups. Carbon-coating of the mounts, employed to diffuse electrons off the surface during analysis is the final step of the vertical section sample preparation.

CHAPTER 4

RESULTS

4.1. Introduction

Results obtained in this study are presented in this chapter. Size analysis involved various screening methods that were augmented by instrumental measurement of particle size by the Malvern technique, which uses optical diffraction to produce volume-equivalent sphere diameters, and surface area by the BET gas absorption method. Unsized (bulk) fractions of each sample were used for Malvern, and BET analysis. Size fractions were subsequently analysed by X-Ray techniques, XRF for major element composition while aliquots of bulk samples were examined QXRD for quantitative mineralogy as explicitly described in section 3.4 of Chapter 3. Finally, selected size fraction splits were investigated by the QEMSCAN instrumental technique, which produces independent estimates of quantitative mineralogy and bulk geochemistry, as well as particle properties. All raw data are tabulated in Appendices A and B, while processed results are tabled and graphically illustrated throughout this chapter.

4.2. Characterization of PGM Tailings

Tailings from the five different PGM operations are presented separately in this section.

4.2.1. Impala Platinum

Deposition of tailings at the Impala site was by means of spigots that formed point sources to numerous very low angle distributary fans that coalesced across the massive dam. Predictably the particle stream separated into a proximal zone which was visibly coarser and heavy mineral enriched (black chromite), while the distal zone collected downslope at the centre of the repository, together with the water. Samples of both distal and proximal material (IMP-001 and IMP-003 respectively) were collected and analysed.

4.2.1.1. Particle size analysis

Three sets of screening tests were performed. The tests were denoted by suffixes A (wet screening only), B (dry screening) and C, a combination of both wet and dry screening as explained in Chapter 2.

The masses (wt %) of material retained in each size fraction for sample IMP-001 are given in Table 4.1 and plotted in Fig. 4.1. Data for Sample IMP-003 are given in Table 4.1 and Fig. 4.2. A general feature of both samples is the progressive drop in relative abundance of the size fractions from coarse to fine. In both samples the most abundant fraction was retained on the 150 µm sieve, while there was little or no <25 µm material. The three different sieve methods did not show any significant deviation for these two size fractions. Ultra-fine material that would have reported to the < 25 µm fraction has probably been lost to the innermost zone of the dam, which was inaccessible due to the accumulated water, and/or lost by wind activity.

Several discrepancies were encountered in the intermediate size fractions (Figs 4.1 and 4.2) and clearly reflect the different responses of the particulate material to the various sieve methods. Dry sieving (B) has been known to sometimes under report the finer fractions, and thus wet sieving (A) has been the traditional remedy, with a combined approach (C) alleged to represent the best of both. While it was anticipated that the proximal sample (IMP-003) would display a coarser particle size, the sieve results do not bear this out, since the distal sample (IMP-001) has consistently higher percentages of the 150, 106 and 75 µm fractions and which yields a greater overall sum (79 % versus 64 %). Clearly the visual perception at the time of sampling may be misleading.

Table 4. 1: Screening test results for Impala samples IMP/001 and IMP003

	IMP-001A	IMP-001B	IMP-001C	IMP-001 (avg)	IMP-003A	IMP-003B	IMP-003C	IMP-003 (avg)
Sieve (µm)	wt%							
<25	0.2	0.03	0.51	0.25	0.001	0.001	0.001	0.00
25	1.23	2.13	1.98	1.78	3.79	0.89	2.07	2.25
38	6.23	4.55	6.15	5.64	19.86	16.51	21.73	19.37
53	16.23	11.27	12.98	13.49	11.29	17.78	13.54	14.20
75	19.61	24.54	22.98	22.38	16.87	16.68	16.47	16.67
106	22.56	22.87	20.87	22.10	16.92	17.68	17.11	17.24
150	33.95	34.62	34.53	34.37	31.27	30.46	29.08	30.27
TOTAL	100	100	100	100	100	100	100	100

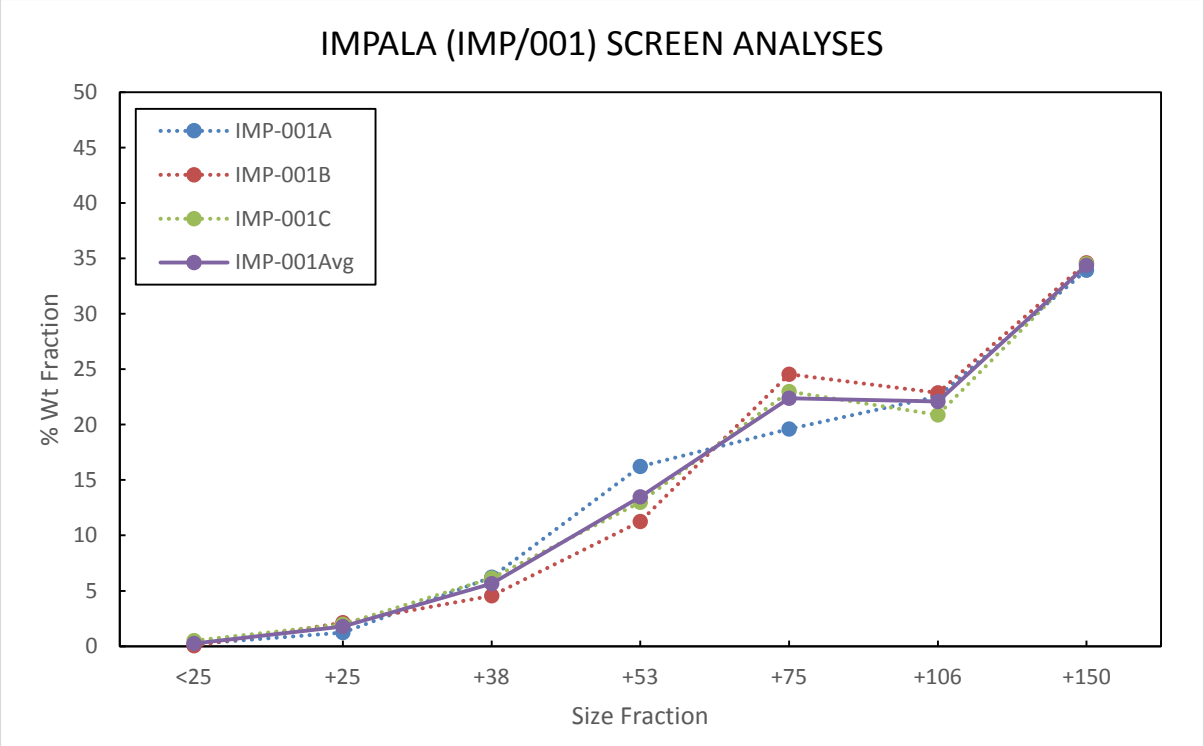

Figure 4. 1: Screening tests for IMP/001.

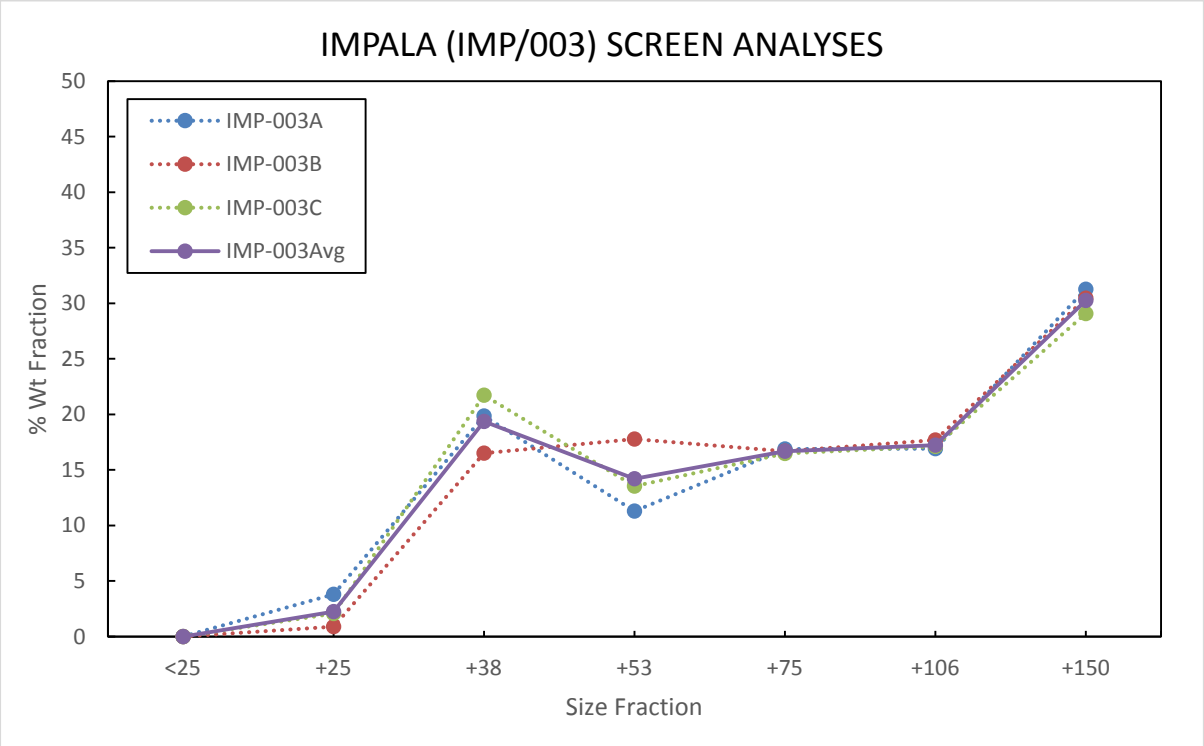

Figure 4. 2: Screen results for IMP/003.

A closer scrutiny confirmed that no significant change in each replicate screening exercise illustrated in Figures 4.1 and 4.2.The averages of the three replicates of

Impala sample IMP/001 and IMP/003, were plotted in order to identify any further differences (Figure 4.3).

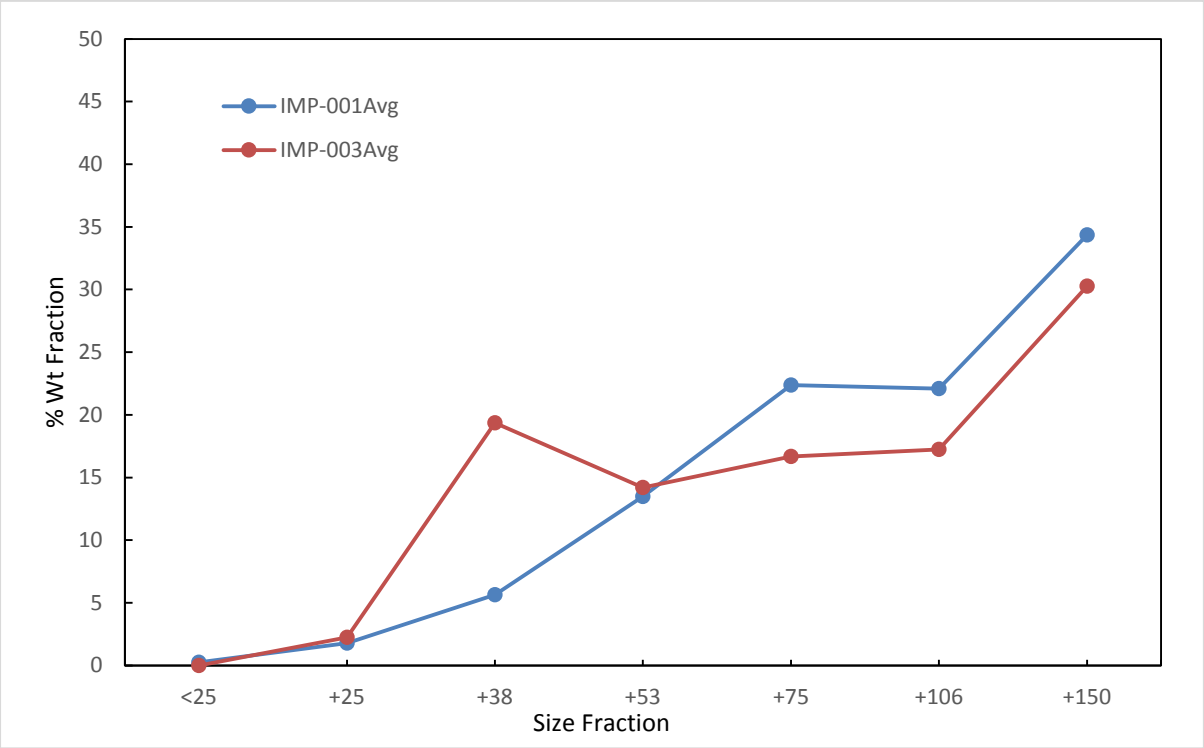

Figure 4. 3: A graph comparing the averages of the two Impala samples.

From Figure 4.3, it was observed that samples IMP/001 and IMP/003 had the same quantity of material retained on size fractions <25, +25 and +53 µm. A vast difference was observed at size fraction +38 µm, where IMP/003 retained significantly way more material than IMP/001. A clear difference of ~15 % was detected the samples. The Coarser fractions (+75, +106 and +150 µm) generally had the most retained material in both samples. However, IMP/001 retained the most samples compared to IMP/003 where an essential 10 % difference was observed between the samples.

Cumulative values were derived from the averages of the replicates of Impala samples IMP/001 and IMP/003 and plotted against the size fractions as shown in Fig. 4.4. This was used to determine any similarities in Malvern results. A full sieve analysis can be found in Appendix A1.1.

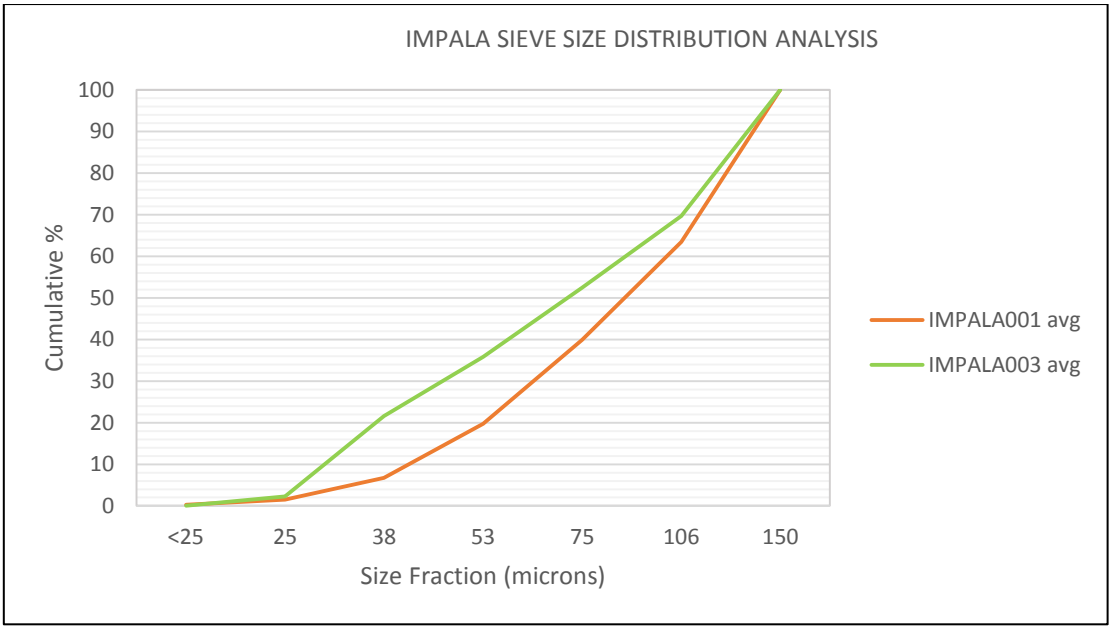

Figure 4. 4: Average sieving results plotted against cumulative percentage for Impala.

Sieve results can be compared with Malvern particle size distribution data (Table 4.2 and Fig. 4.5). Curves for both samples shown in Fig. 4.5 are very similar, with the proximal sample IMP/003 showing a slight coarsening relative to the distal IMP-001 at the 0.5 and 0.9 percentiles. In contrast to the sieve results, the Malvern method does indeed indicate that the proximal sample is marginally coarser, and perhaps confirms the initial visual observation. It is therefore noted that Malvern data may be more representative than sieving.

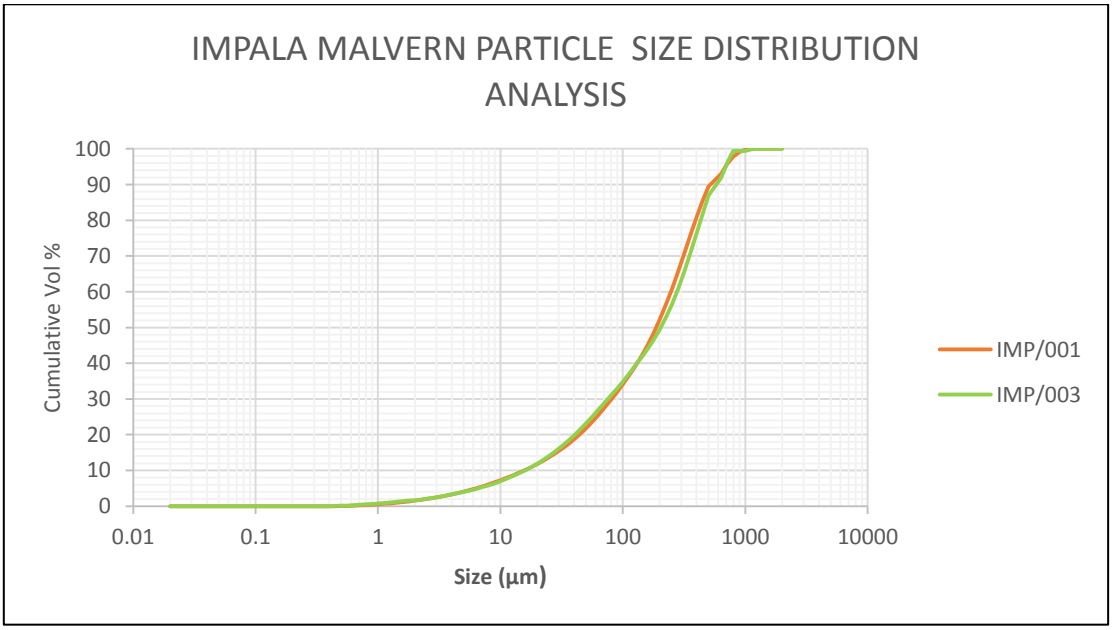

Figure 4. 5: Malvern particle size distribution graph of the Impala IMP/001 (green) and IMP/003 (orange) PGM tailings samples.

Table 4. 2: Particle size distribution analysis indicating average particle size for Impala samples at percentiles 10, 50 and 90.

Tailings Sample	Dv (0.1)(µm)	Dv (0.5)(µm)	Dv(0.9)(µm)
IMP/001	17.542	210.774	573.186
IMP/003	17.852	231.45	591.095

The finer distal sample IMP-001 was further measured for BET analysis and has a specific surface area of 1.810 m^2/g (Fig. 4.6). The BET full table of results and calculation for Impala can be found in Appendix A3.1 and C1.1 respectively.

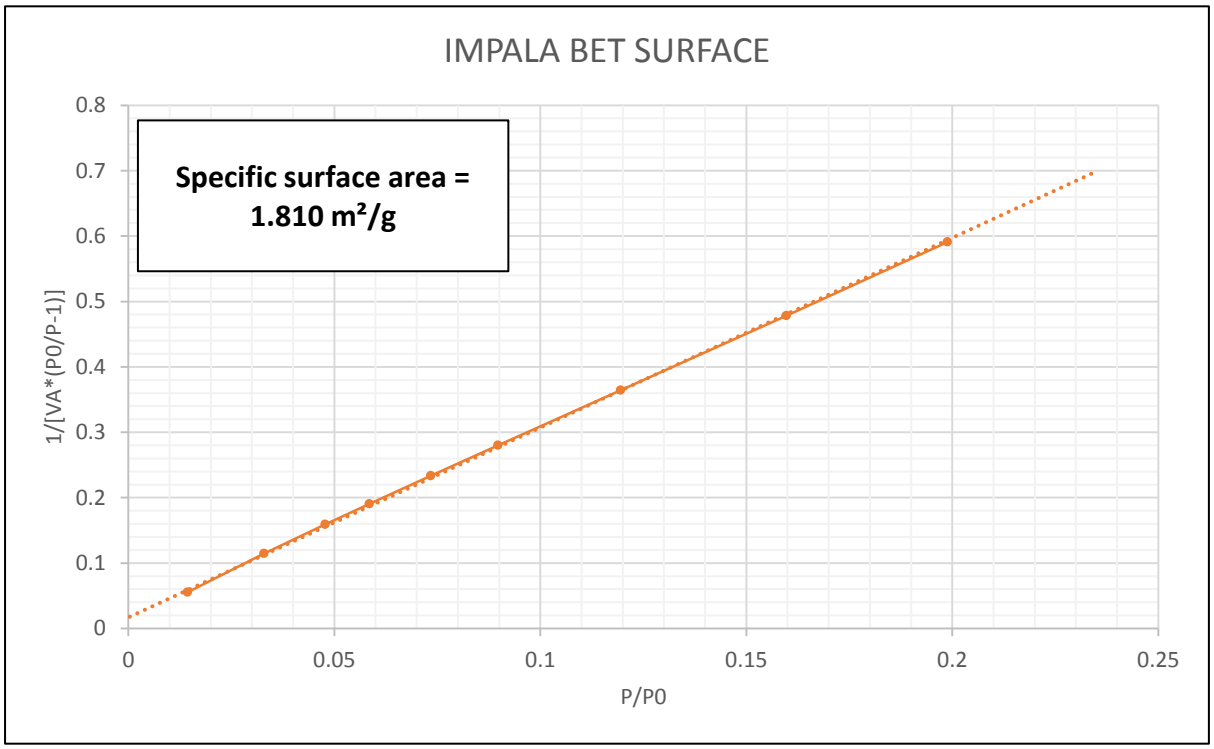

Figure 4. 6: Multi-point BET plot for calculating the specific surface area for Impala (IMP/001).

4.2.1.2. QXRD and QEMSCAN mineralogy for Impala (IMP/001).

Major concentrations of Bytownite (28 %), enstatite (27 %) and chromite (21 %) were detected in the QXRD analysis. From Figure 4.7, a moderate amount of hornblende (8 %) was also identified. Further observations from Figure 4.7 revealed fairly minor concentrations (~3 %) in diopside, talc and epidote, with traces (<1 %) of chalcopyrite, pyrite, pyrrhotite, and pentlandite.

Interestingly, base metal sulphides made up 3.84 % of the Impala sample while there is a little over 60 % mafic minerals and the alteration quite make up 7.50 %.

The mineral assemblage can be grouped into three broad categories: (1) primary igneous (2) sulphide ores and (3) secondary alteration (Table 4.3). The sum of minerals suitable for carbonation reported by QXRD make up 74.81%.

Table 4. 3: QXRD results for Impala (IMP/001), with the sum of mafic, sulphide and alterations mineral highlighted.

IMPALA (IMP/001)		
Lithology	Chemical Composition	%
Chromite	$(Fe, Mg)Cr_2O_4$	21.20
Enstatite*	$MgSiO_3$	26.54
Diopside*	$MgCaSi_2O_6$	3.37
Hornblende*	$Ca_2(Mg, Fe, Al)_5 (Al, Si)_8O_{22}(OH)_2$	7.96
Biotite*	$K(Mg, Fe)_3 (AlSi_3O_{10})(F,OH)_2$	2.18
Bytownite*	$[(Ca, Na)[Al(Al, Si)Si_2O_8]$	27.51
Sum: Primary Igneous		**88.76**
Pyrrhotite	$Fe_{1-x}S$ (x = 0 to 0.2)	1.32
Pentlandite	$(Fe, Ni)_9S_8$	1.08
Chalcopyrite	$CuFeS_2$	0.99
Pyrite	FeS_2	0.45
Sum: Sulphide		**3.84**
Talc*	$Mg_3Si_4O_{10}(OH)_2$	2.88
Lizardite*	$Ni_3(Si_2O_5)(OH)_4$	1.05
Calcite	$CaCO_3$	0.13
Epidote*	$\{Ca_2\}\{Al_2Fe^{3+}\}[O\|OH\|SiO_4\|Si_2O_7]$	3.32
Quartz	SiO_2	0.02
Sum: Alteration		**7.40**
*Carbonatable		74.81
Non carbonatable		25.91

One size fraction (-150/+106 µm) was selected for QEMSCAN analysis. This was based on mass dominance from the screening exercise and highest copper content from XRF analysis.

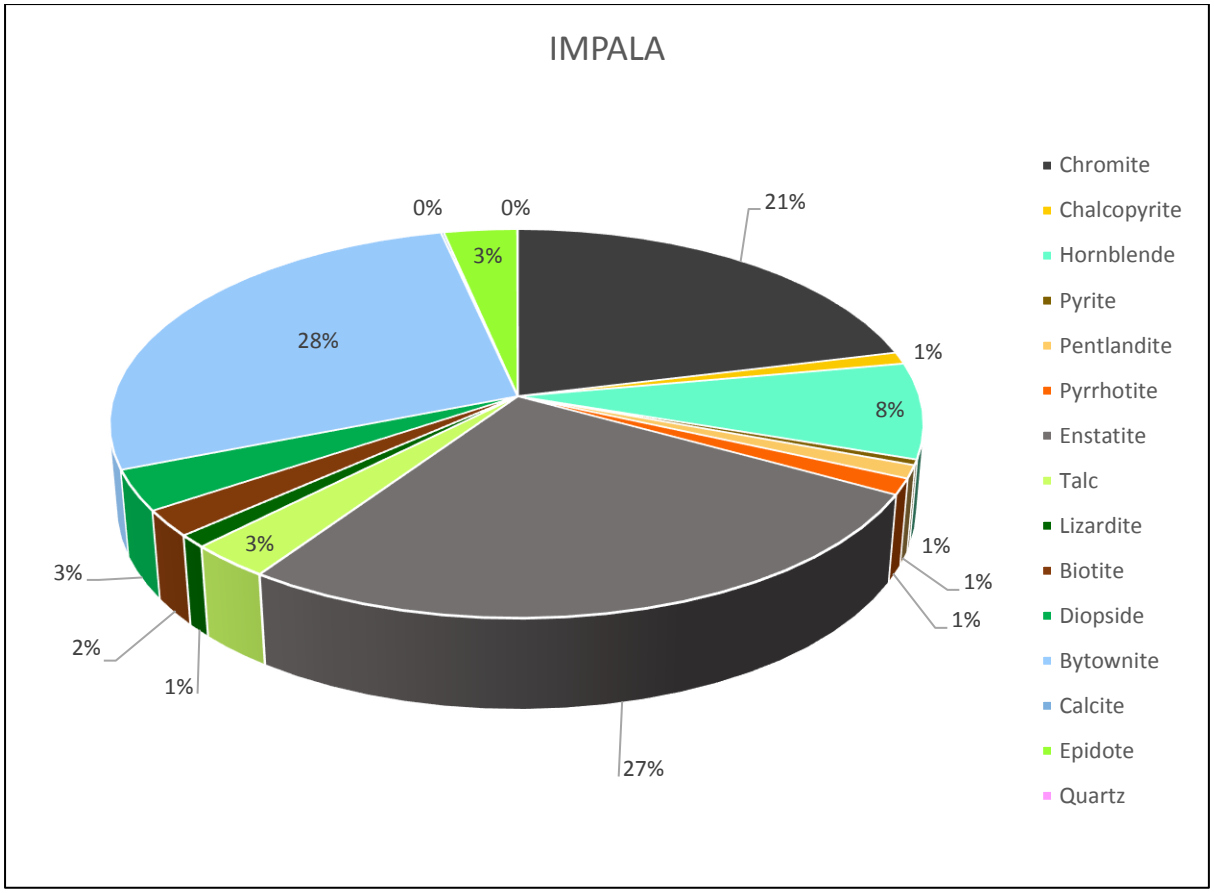

Figure 4. 7: Bulk mineralogical composition of Impala (IMP/001) tailings sample as determined by QXRD.

Orthopyroxene (~35 %), plagioclase (26.47 %) and chromite (19.26 %) recorded higher concentrations for the selected Impala sample (Table 4.4 and Figure 4.8). Alteration minerals highlighted in Table 4.4, made up almost 8 % of the sample. Trace concentrations (<1 %) of base metal sulphide were identified during the QEMSCAN analytical exercise. The major component of the sample was made up of a little over 90 % primary igneous minerals.

The sum of carbonatable minerals was calculated. It was deduced that the total percentage of carbonatable minerals made up 79.50 % of the sample.

From Figure 4.7 and Figure 4.8, it was observed that there was a fairly good correlation between QXRD and QEMSCAN results. Results from both analyses indicate moderately high levels of plagioclase (bytownite), orthopyroxene (enstatite) and chromite.

Table 4. 4: QEMSCAN results for Impala (IMP/001). The selected size fraction (-150/+106 µm).

IMPALA (IMP/001)		
Lithology	Chemical Composition	%
Chromite	$(Fe, Mg)Cr_2O_4$	19.26
Orthopyroxene*	$Mg_2Si_2O_6$	34.47
Clinopyroxene*	$CaMgSi_2O_6$	3.34
Hornblende*	$Ca_2(Mg, Fe, Al)_5 (Al, Si)_8O_{22}(OH)_2$	7.12
Biotite*	$K(Mg, Fe)_3 (AlSi_3O_{10})(F,OH)_2$	0.89
Olivine*	(Mg, Fe)2SiO4	0.50
Plagioclase*	$(Na,Ca)(Si,Al)_4O_8$	26.47
Sum: Primary Igneous		**92.05**
Pyrrhotite	$Fe_{1-x}S$ (x = 0 to 0.2)	0.04
Pentlandite	$(Fe, Ni)_9S_8$	0.03
Chalcopyrite	$CuFeS_2$	0.01
Pyrite	FeS_2	0.15
Sum: Base Metal Sulphide		**0.23**
Talc*	$Mg_3Si_4O_{10}(OH)_2$	1.35
Serpentine*	$Mg_3(Si_2O_5)(OH)_5$	0.22
Chlorite*	$(Mg, Fe)_3(Si, Al)_4O_{10}(OH)_2 \cdot (Mg, Fe)_3(OH)_6$	4.45
Calcite	$CaCO_3$	0.43
Epidote*	$Ca_2Fe_{3+2.25}Al_{0.75}(SiO_4)_3(OH)$	0.69
Quartz	SiO_2	0.58
Sum: Secondary Alteration		**7.72**
*Carbonatable		79.50
Non carbonatable		20.50

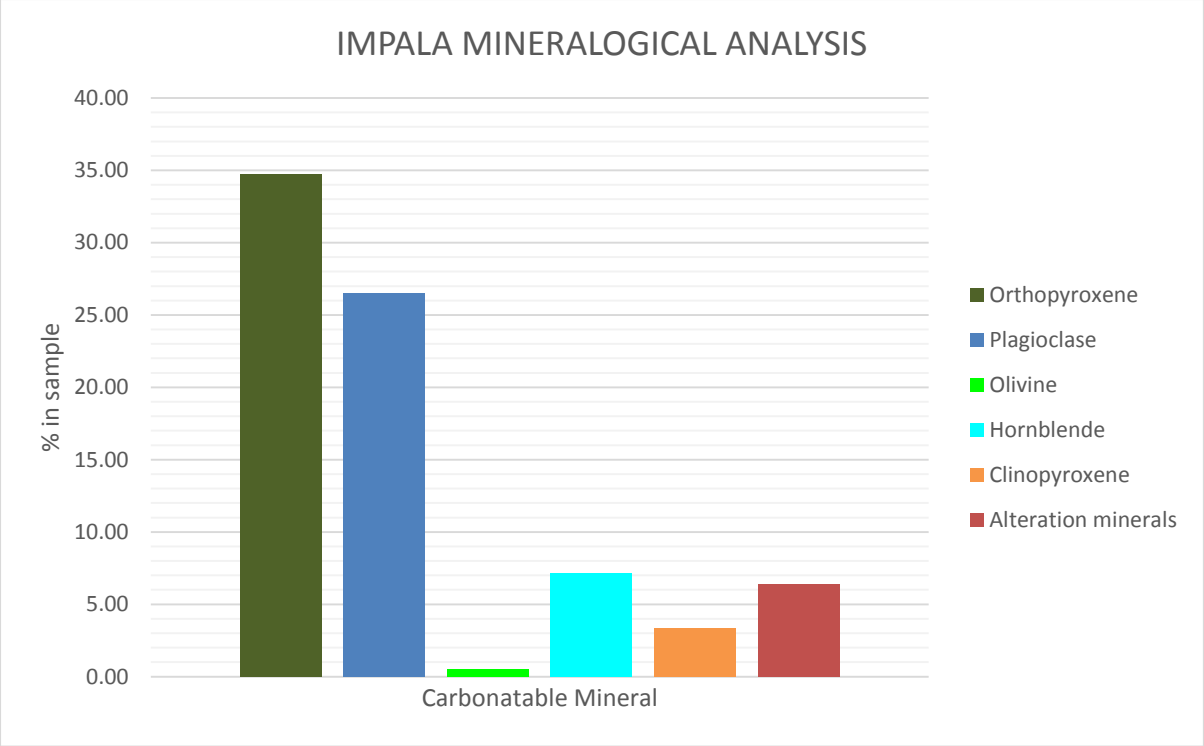

Figure 4. 8: A bar chart showing QEMSCAN results for Impala (IMP/001) tailings sample.

Similarities were observed between QXRD and QEMSCAN results for sample IMP/001. Diopside and Base Metal Sulphides were reported at 3% and <1% respectively in both QXRD and QEMSCAN results. Alteration minerals were also reported in the region of 7% in both sets of results. Chromite according to QXRD results was 21% and 19.26% in QEMSCAN. The sum of carbonatable minerals was 74.81% in QXRD and 79.50% in QEMSCAN.

4.2.1.3. XRF major oxide geochemistry

Both distal (IMP/001) and proximal (IMP/003) samples from the Impala tailings dam were analysed to investigate any mineralogical disparities. Raw XRF data were recalculated to 100 %, assuming total Fe as FeO, on a volatile free basis (H_2O^- and LOI free) before assessment. Major oxides (SiO_2, Cr_2O_3, FeO, MgO, Cao and Al_2O_3) were taken into consideration. From the comprehensive data (Appendix B1.1.), it was observed that analysis performed on the two Impala samples using the XRF technique, displayed fairly dissimilar results.

The specific size fractions pertaining to this study were examined for major oxides within both Impala samples. As presented in Figure 4.9, XRF results for sample IMP/001 revealed unsurprisingly high amounts (>40 %) of SiO_2 for all size fractions.

However, SiO_2 concentrations increase in coarser fractions of IMP/001. MgO (15 %) amounts remained steady within finer fractions but gradually decreased in coarser fractions greater than 75 µm.

IMP/001 generally had higher amounts of Al_2O_3 as compared to CaO. These two major oxides exhibited similar trends in regard to their distribution pattern as shown in Figure 4.9. Concentrations remained steady along finer size fractions and gently increased at the 106 and 150 µm fractions. Moreover, two other oxides (FeO and Cr_2O_3) displayed a distribution trend of their own. There was a typically high concentration of FeO than Cr_2O_3. However, values steadily decreased within finer size fractions and remained fairly constant in material greater than 106 µm as illustrated in Figure 4.9.

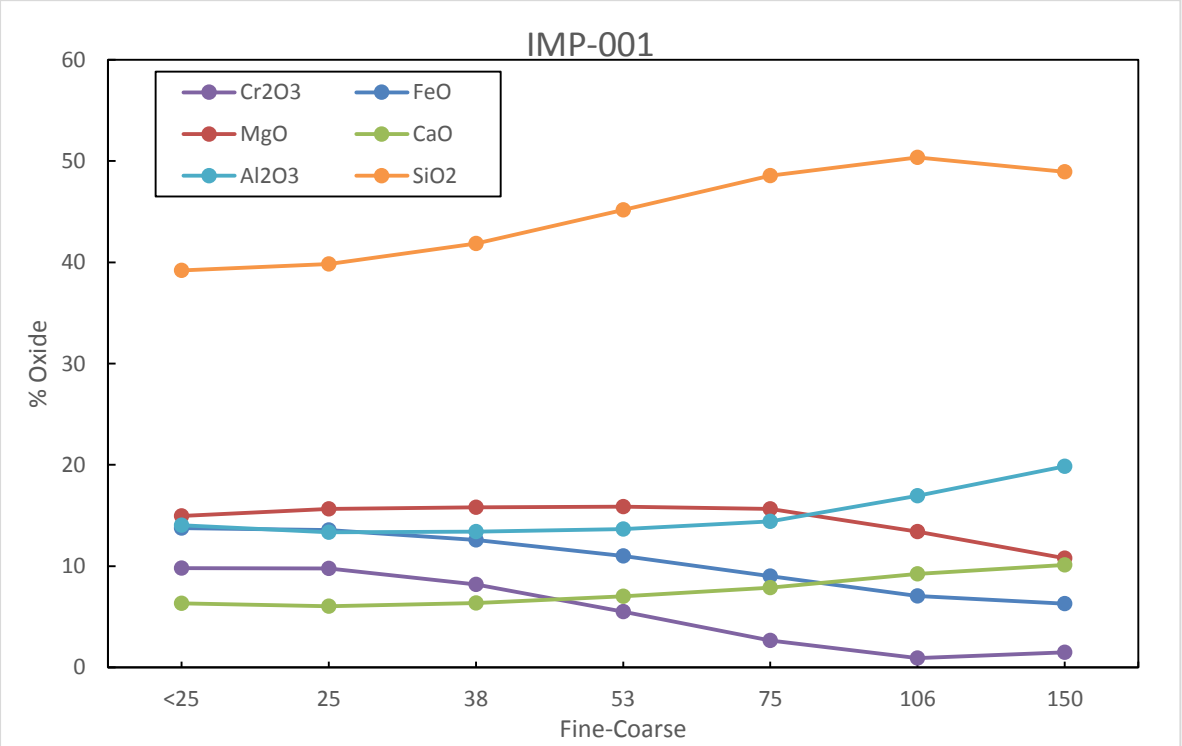

Figure 4. 9: Major oxide composition of size fractions in IMP/001.

Unlike the IMP/001 sample, IMP/003 concentrations in major oxides remained relatively constant across all size fractions as seen in Figure 4.10. Predominately high values of SiO_2 (~35 %) was identified in sample IMP/003. FeO, MgO, Cr_2O_3 and Al_2O_3 followed sequentially with moderate amounts ranging between 12 and 17 %. XRF analysis for CaO proved to be as low as 4 % in sample IMP/003 (Figure 4.10).

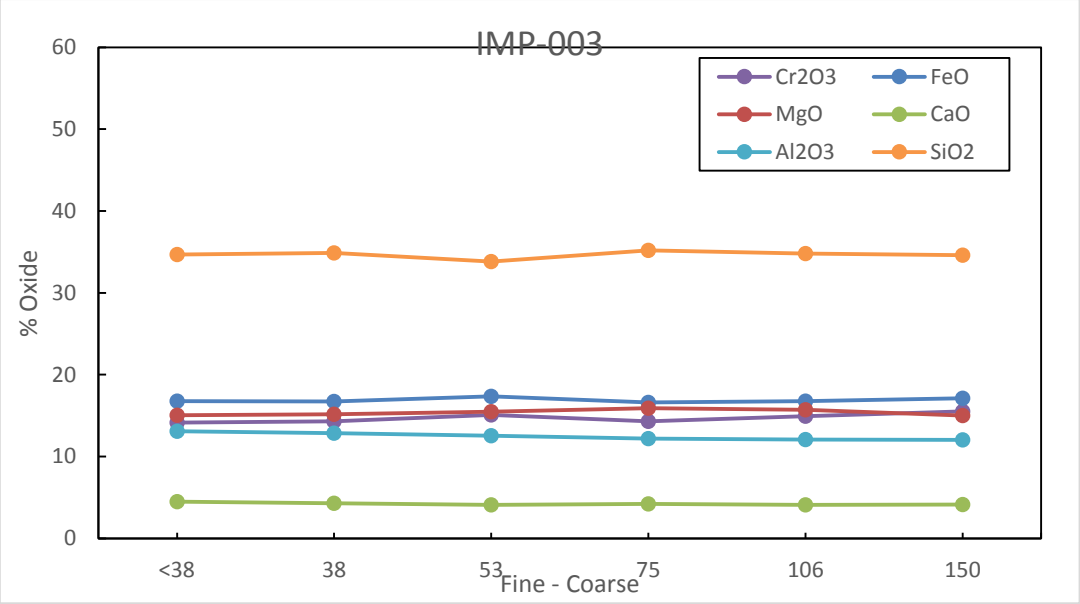

Figure 4. 10: Major oxide composition of size fractions in IMP/003.

A bulk sample spilt not objected to size analysis was analysed for each sample (IMP/001 and IMP/003). This was compared with a calculated bulk from combining the sieve fractions. Each size fraction was calculated as a fraction of the bulk. The fractions from these calculations were used as weighting factors to compute what was essentially an alternative bulk. Discrepancies between the measured and calculated bulk were revealed in Figure 4.11.

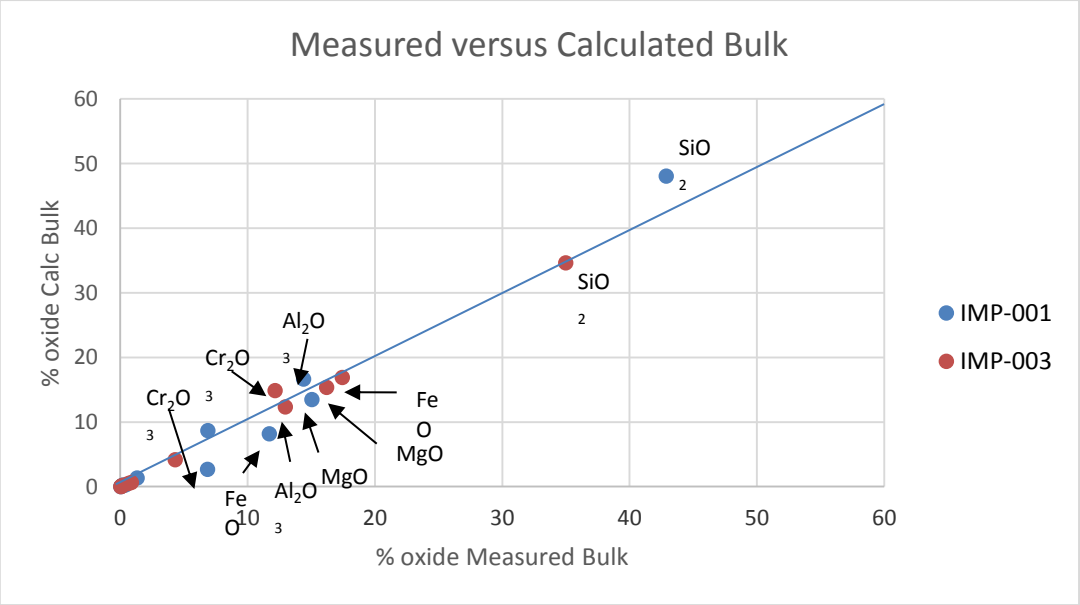

Figure 4. 11: A scatter plot showing the correlation of measured and calculated bulk for both Impala samples.

The relationship between measured and calculated bulk has been presented in Figure 4.11. About a 2 wt% difference for majority of oxides was detected between IMP/001 bulk results. Surprisingly, an approximate difference of 6 wt% was observed measured and calculated bulk for SiO_2. A moderate positive correlation could be said to have occurred between the measured bulk and calculated bulk for IMP/001.

IMP/003 had a very strong positive correlation between the measure and calculated bulk as displayed in Figure 4.11. There were insignificant discrepancies identified. A table of the actual values of the measure and calculated bulk can be seen in Appendix B1.

4.2.2. Amandelbult Tailings

Screening tests were performed on two sets of samples to identify variations in particle size distribution. Plant tail sample (AMB/001) and dam samples denoted by prefix ‘S’, underwent the screening exercise. Samples AMB/001 and S/4-TD44 were further considered for Malvern particles size analysis. BET surface area analysis was performed on the bulk sample with an overall fines particle size observed from the Malvern analysis. This was between bulk samples AMB/010 and S/4-TD44.

Major oxide results from XRF analysis are also presented in this section. Both QXRD and QEMSCAN analyses were performed on one Amandelbult tailings sample.

4.2.2.1 Particle size analysis

Amandelbult screening tests have been tabulated in Table 4.6. Three exercises denoted by suffixes A, B and C were performed. The plant sample (AMB/001) had masses retained staying somewhat steady throughout the size fractions and only varied slightly within the 53 and 38 µm fraction (Figure 4.12). A difference of about 3 % between tests B and C for the 53 µm size fraction was spotted. The same discrepancy was observed for test A in the 38 µm fraction.

Table 4. 5: Screening test results for Amandelbult (AMB/101).

	AMB/101A	AMB/101B	AMB/101C	AMB/101(avg)
Sieve (µm)	wt%			
<25	1.78	1.05	1.08	1.30
+25	7.75	6.23	7.75	7.24
+38	8.96	11.76	11.72	10.81
+53	22.55	24.36	21.22	22.71
+75	22.03	20.19	21.54	21.25
+106	22.64	22.12	22.39	22.39
+150	14.29	14.29	14.29	14.29
Total	100	100	100	100

From Table 4.5 and Figure 4.12, sample AMB/101 appears generally coarse. In the three screening tests, where only about 8 % material report below 38 µm. Very high percentages of the material were retained in the 53, 75 and 106 µm categories.

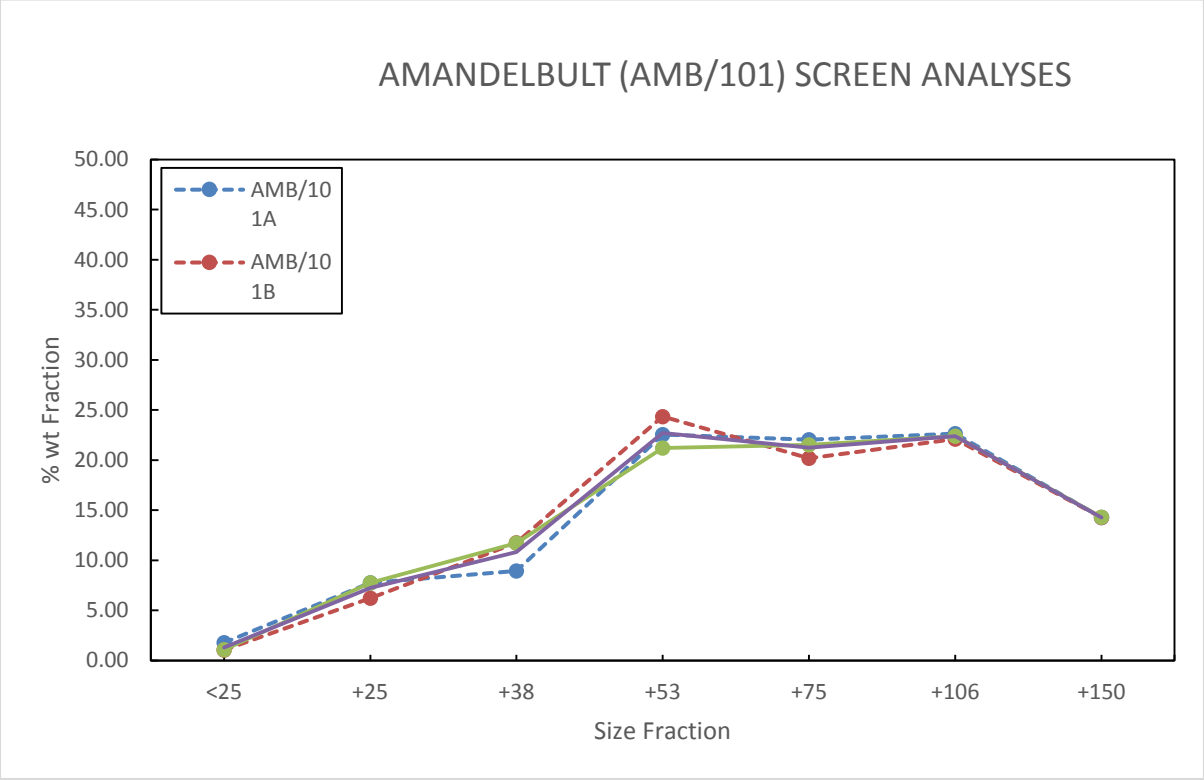

Figure 4. 12: Screening test results for AMB/101.

Cumulative values were derived from the averages of the replicates of Amandelbult sample AMB/101 and plotted against the size fractions as shown in Fig. 4.13. This was compared to the Malvern results in order to identify any similarities or trends. A full sieve analysis can be found in Appendix A1.2.

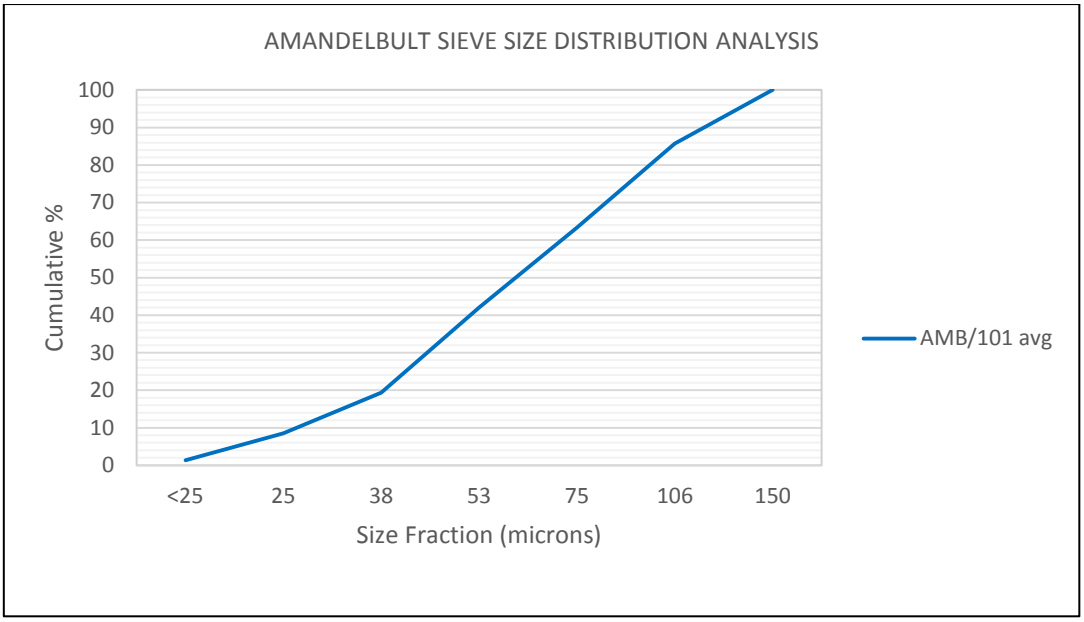

Figure 4. 13: Average sieving results plotted against cumulative percentage for Amandelbult.

A vivid comparison had to be made between the plant and dam tailings in terms of their particle size distribution. Obviously the Malvern technique was seen as a more accurate means to determine the quantity of finest material. Figure 4.14 shows the paticle size distribution curves for plant tail sample AMB/101 and a dam tailings sample S/4-TD44,analyzed to determine their individual particle size distribution. Results between AMB/101 and S/4-TD44 varied distinctively.

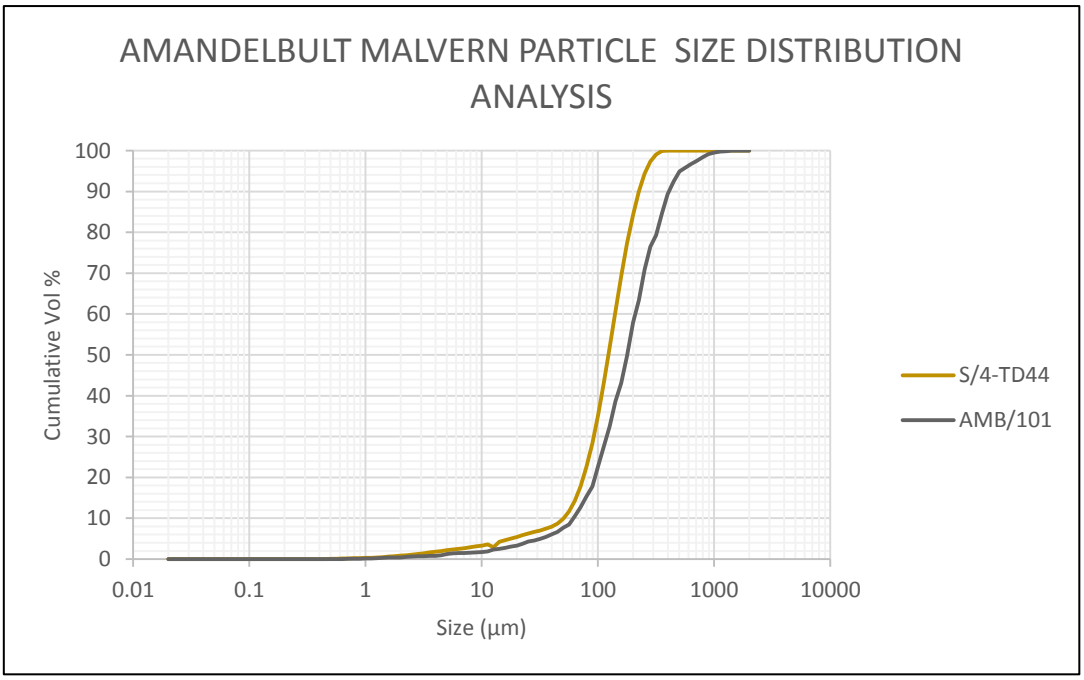

Figure 4. 14: Malvern particle size distribution curves for Amandelbult tailings samples.

Table 4. 6: Particle size distribution analysis indicating average particle size for Amandelbult samples at percentiles 10, 50 and 90.

Tailings Sample	Dv (0.1)(µm)	Dv (0.5)(µm)	Dv (0.9)(µm)
S/4-TD44	56.831	138.178	251.929
AMB/101	62.359	184.626	431.732

S/4-TD44 had the finest particle size distribution at Dv (0.9) = 251.92 µm compared to AMB/101 (431.732 µm) as shown in Table 4.6. A full Malvern data can be seen in Appendix A2.2.

BET analysis was used to determine the specific surface area on sample S/4-TD44 and it was clear that finer particles, having the results a specific surface area contained more of 1.450 m^2/g (Figure 4.15). The full BET results and caculations are presented in Appendices A3.2 and C1.2 respectively.

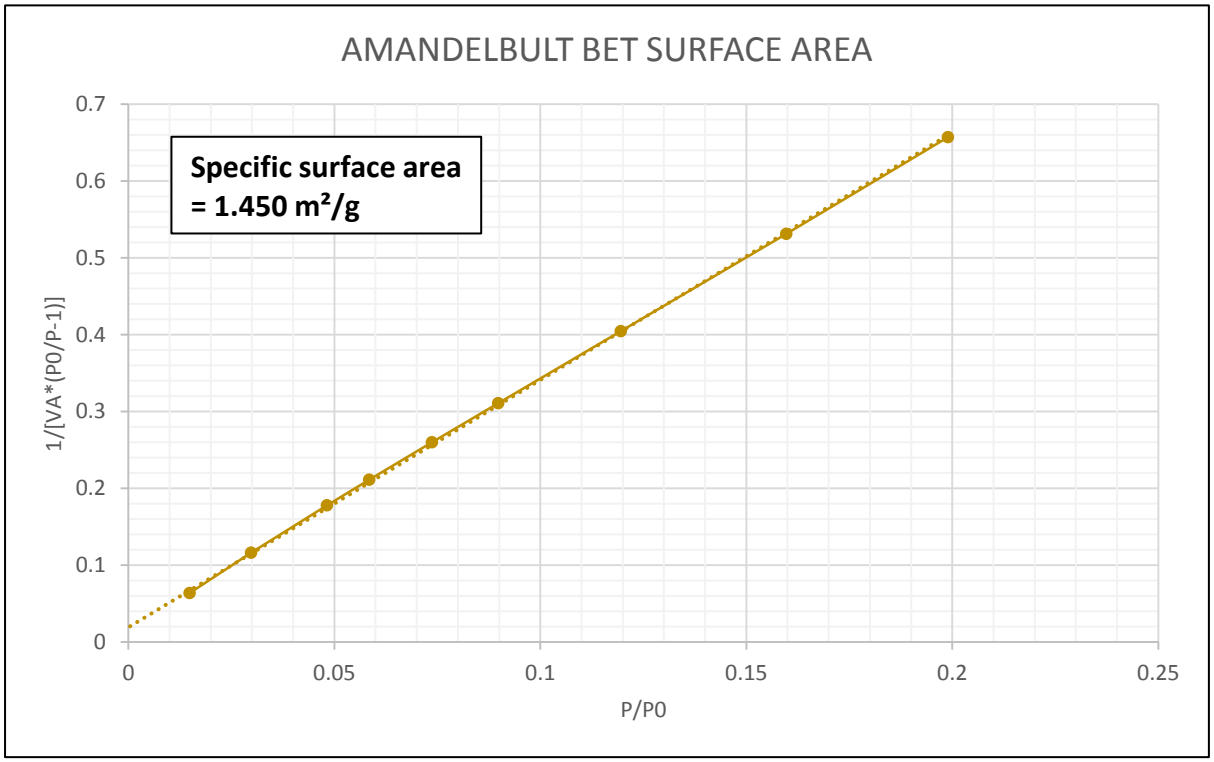

Figure 4. 15: Multi-point BET plot used to determine the specific surface area for S/4-TD44.

4.2.2.2 QXRD and QEMSCAN mineralogy

QXRD analysis proved the Bytownite (30 %) was the most common mineral in the Amandelbult tailings. High enstatite (27 %) amount was also identified. Chromite (16 %) was detected in fairly high quantities. Moreover moderate levels of hornblende at

about 7 % was identified during the QXRD analysis. In general, the mafic component made up about 55 % of the sample. About 5% talc was reported during the analysis. Further analysis also revealed a minimum of 3 % Base Metal Sulphides (BMS) within the sample (Table 4.8 and Figure 4.16).

Table 4. 7: QXRD results for Amandelbult (AMB/101), with the sum of mafic, sulphide and alteration mineral highlighted.

AMANDELBULT		
Lithology	Chemical Composition	%
Chromite	$(Fe, Mg)Cr_2O_4$	16.05
Enstatite*	$MgSiO_3$	26.68
Diopside*	$MgCaSi_2O_6$	3.14
Hornblende*	$Ca_2(Mg, Fe, Al)_5 (Al, Si)_8O_{22}(OH)_2$	7.32
Biotite*	$K(Mg, Fe)_3 (AlSi_3O_{10})(F,OH)_2$	2.51
Bytownite*	$[(Ca, Na)[Al(Al, Si)Si_2O_8]$	30.04
Sum: Primary Igneous		**85.74**
Pyrrhotite	$Fe_{1-x}S$ (x = 0 to 0.2)	1.23
Pentlandite	$(Fe, Ni)_9S_8$	1.00
Chalcopyrite	$CuFeS_2$	0.92
Pyrite	FeS_2	0.42
Sum: Sulphide		**3.57**
Talc*	$Mg_3Si_4O_{10}(OH)_2$	4.46
Lizardite*	$Ni_3(Si_2O_5)(OH)_4$	1.90
Calcite	$CaCO_3$	0.34
Epidote*	$\{Ca_2\}\{Al_2Fe^{3+}\}[O\|OH\|SiO_4\|Si_2O_7]$	3.63
Quartz	SiO_2	0.36
Sum: Alteration		**10.69**
*Carbonatable		79.68
Non carbonatable		20.32

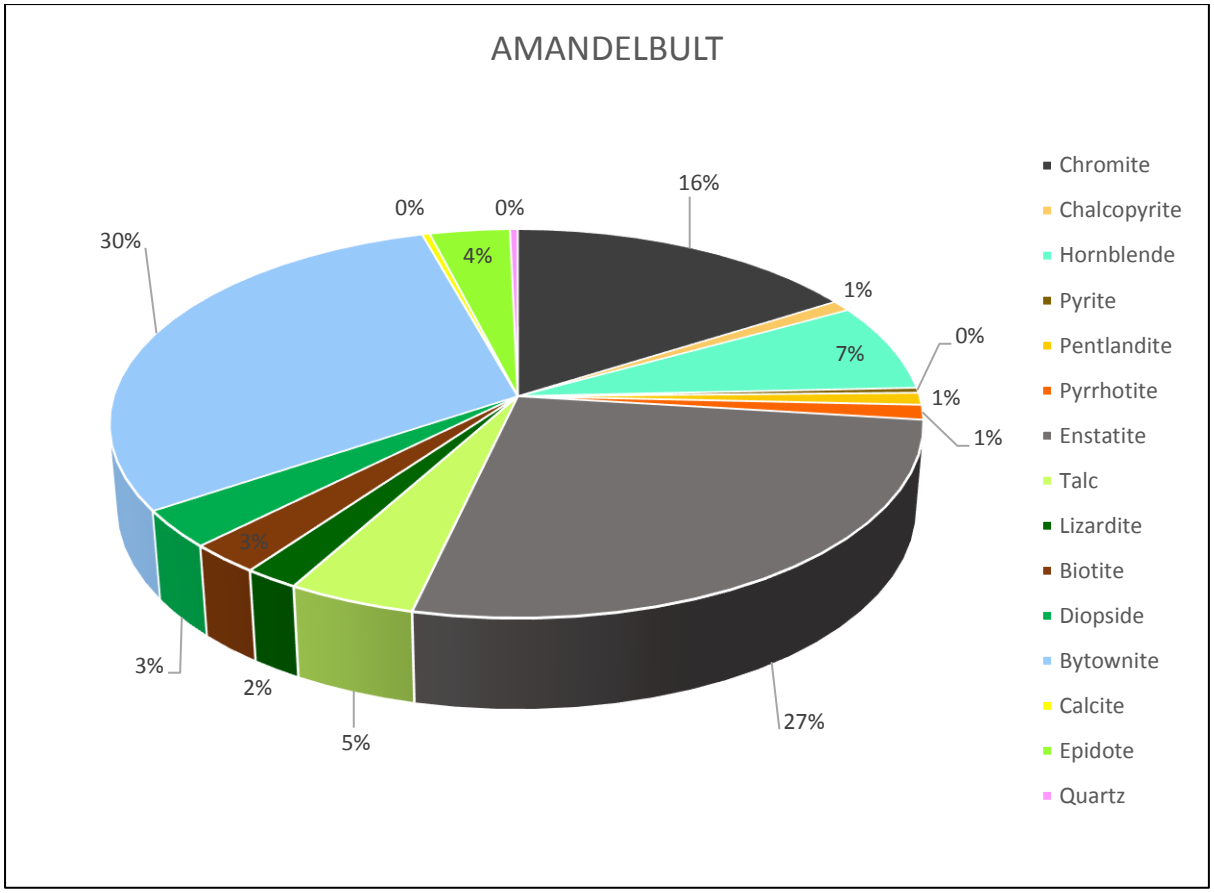

Figure 4. 16: Amandelbult (AMB/101) bulk mineral identification determined by QXRD.

Figure 4.17 displays results of QEMSCAN analysis carried out on Amandelbult tailings. Orthopyroxene (~35 %) was the most abundant mineral. High amounts were recorded for plagioclase (22.32 %) and chromite (26.11 %). The sum of alteration minerals was close to 7 % (Table 4.8). The sum of BMS minerals was below 1 %. Carbonatable minerals made up about 73 % of the entire sample. This value was calculated by simply adding up all carbonatable minerals tabulated in Table 4.8.

Table 4. 8: QEMSCAN results for Amandelbult (AMB/101). The selected size fraction (-150/+106 µm).

AMANDELBULT		
Lithology	Chemical Composition	%
Chromite	$(Fe, Mg)Cr_2O_4$	26.11
Orthopyroxene*	$Mg_2Si_2O_6$	34.47
Clinopyroxene*	$CaMgSi_2O_6$	2.61
Hornblende *	$Ca_2(Mg, Fe, Al)_5 (Al, Si)_8O_{22}(OH)_2$	3.03
Biotite*	$K(Mg, Fe)_3 (AlSi_3O_{10})(F,OH)_2$	0.66
Olivine*	$(Mg, Fe)_2SiO_4$	3.23
Plagioclase*	$(Na,Ca)(Si,Al)_4O_8$	22.32
Sum: Primary Igneous		**92.43**
Pyrrhotite	$Fe_{1-x}S$ (x = 0 to 0.2)	0.08
Pentlandite	$(Fe, Ni)_9S_8$	0.04
Chalcopyrite	$CuFeS_2$	0.05
Pyrite	FeS_2	0.42
Sum: Base Metal Sulphide		**0.59**
Talc*	$Mg_3Si_4O_{10}(OH)_2$	1.68
Serpentine*	$Mg_3(Si_2O_5)(OH)_5$	0.73
Chlorite*	$(Mg, Fe)_3(Si, Al)_4O_{10}(OH)_2 \cdot (Mg, Fe)_3(OH)_6$	3.00
Calcite	$CaCO_3$	0.16
Epidote*	$Ca_2Fe_{3+2.25}Al_{0.75}(SiO_4)_3(OH)$	0.82
Quartz	SiO_2	0.59
Sum: Secondary Alteration		**6.98**
*Carbonatable		72.55
Non carbonatable		27.45

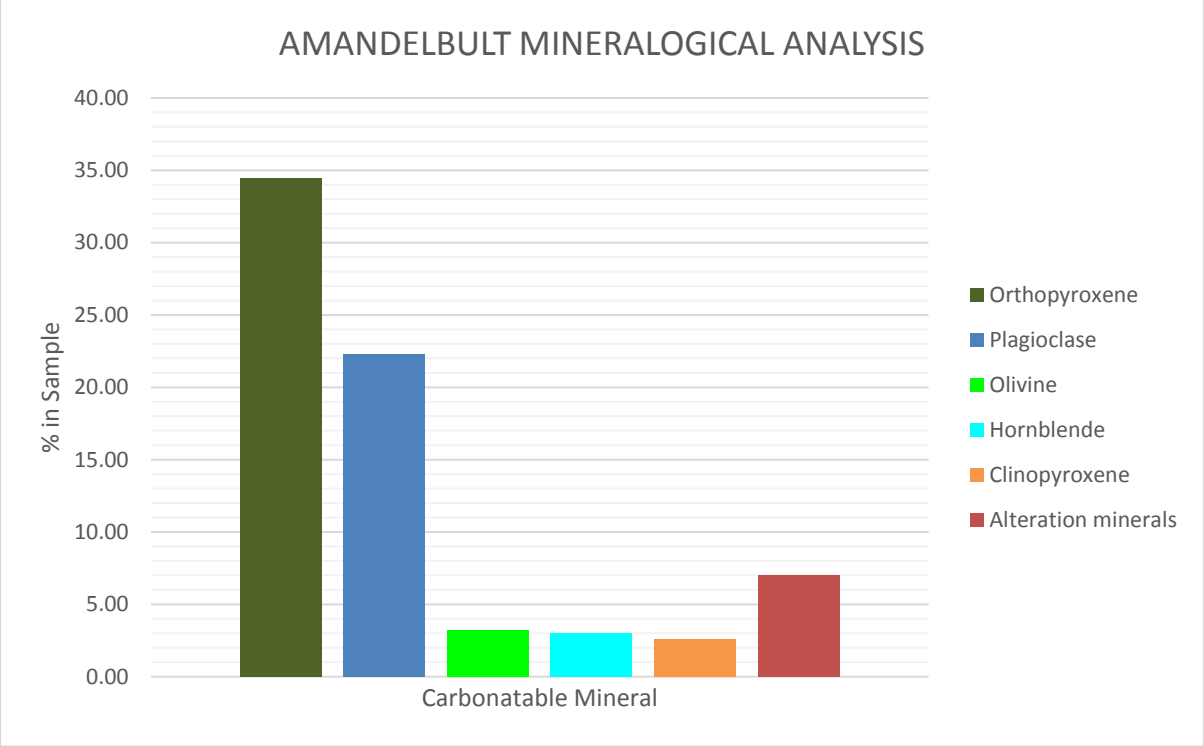

Figure 4. 17: QEMSCAN results for Amandelbult (AMB/101) tailings.

The sum of carbonatable minerals are relatively high in both QXRD and QEMSCAN results shown in Tables 4.7 and 4.8 respectively. QXRD results indicate that carbonatable minerals make up close to 80% compared to QEMSCAN's 72.55%. A fairly high concentration of chromite (26.11%) was identified using the QEMSCAN techniques as opposed to the 16.05% detected by QXRD. Alteration mineral and base metal sulphides detected were generally low in QEMSCAN as compared to QXRD (Table 4.7 and 4.8).

4.2.2.3. XRF major oxide geochemistry

Major oxides examined on Amandelbult samples were also analysed on both sets of single bulk sample as well as fractions of the plant tails (AMB/101) were analysed. Twelve bulk dam samples were also analysed. The relationship between the measured and calculated bulk of the plant tail sample was also establish.

AMB/101 results are displayed on the graph presented in Figure 4.16, and reveal generally high amounts of SiO_2, with about 35 % recorded in the finer fractions and 40 % in the coarsest fraction. MgO, CaO and Cr_2O_3 were fairly constant throughout the size fraction with amounts of 15 %, 5 % and 12 % respectively. Concentrations in FeO gradually decreased towards coarser size fractions (Figure 4.18).

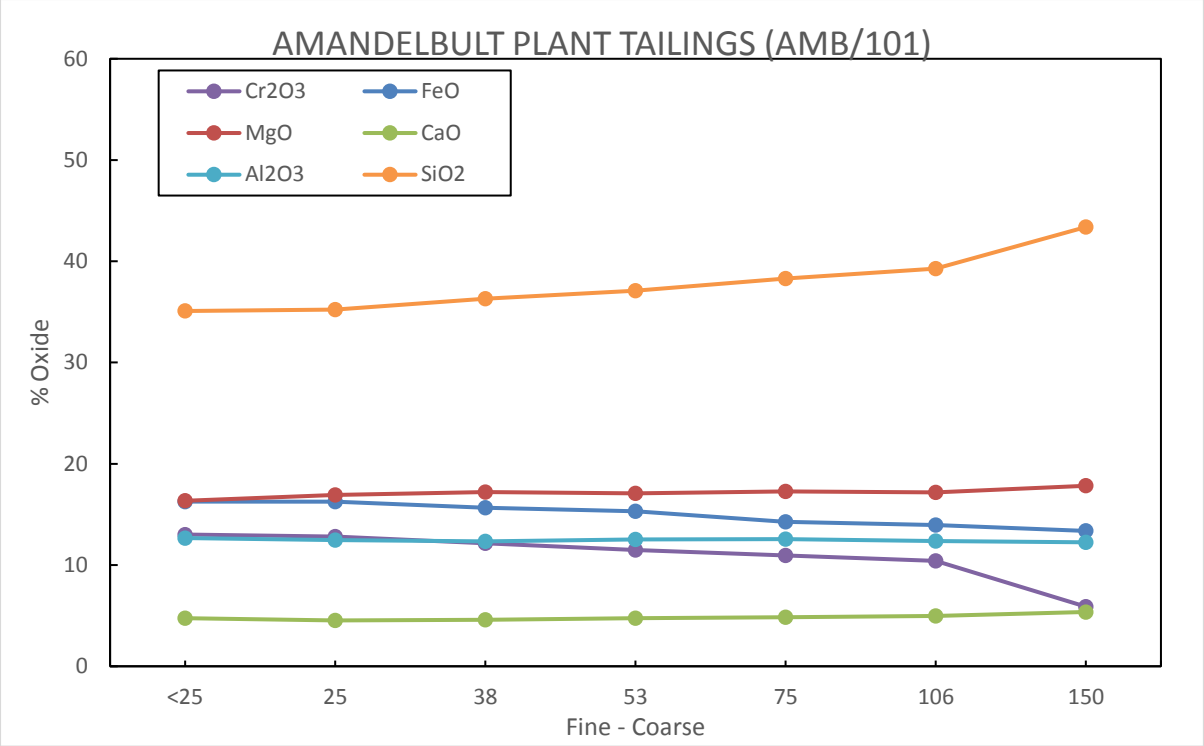

Figure 4. 18: Major oxide composition of size fractions in AMB/101.

Bulk dam tails results revealed observably high SiO_2 amounts. A marked decrease in SiO_2 is observed for samples S/2-TD44 and S/2M-TD44 accompanied by increase in FeO and Cr_2O_3 (Figure 4.19). An average of about 20 % was recorded for FeO in majority of the dam tailings samples. The highest value of Cr_2O_3 was observed in samples S/2-TD44 and S/2M-TD44.

Concentrations recorded in the above mentioned samples were yet higher than SiO_2. Steady levels of MgO and Al_2O_3 were observed in all dam samples. CaO (4 %) detected by XRF was the lowest among the major oxides but also remained constant in all samples (Figure 4.19).

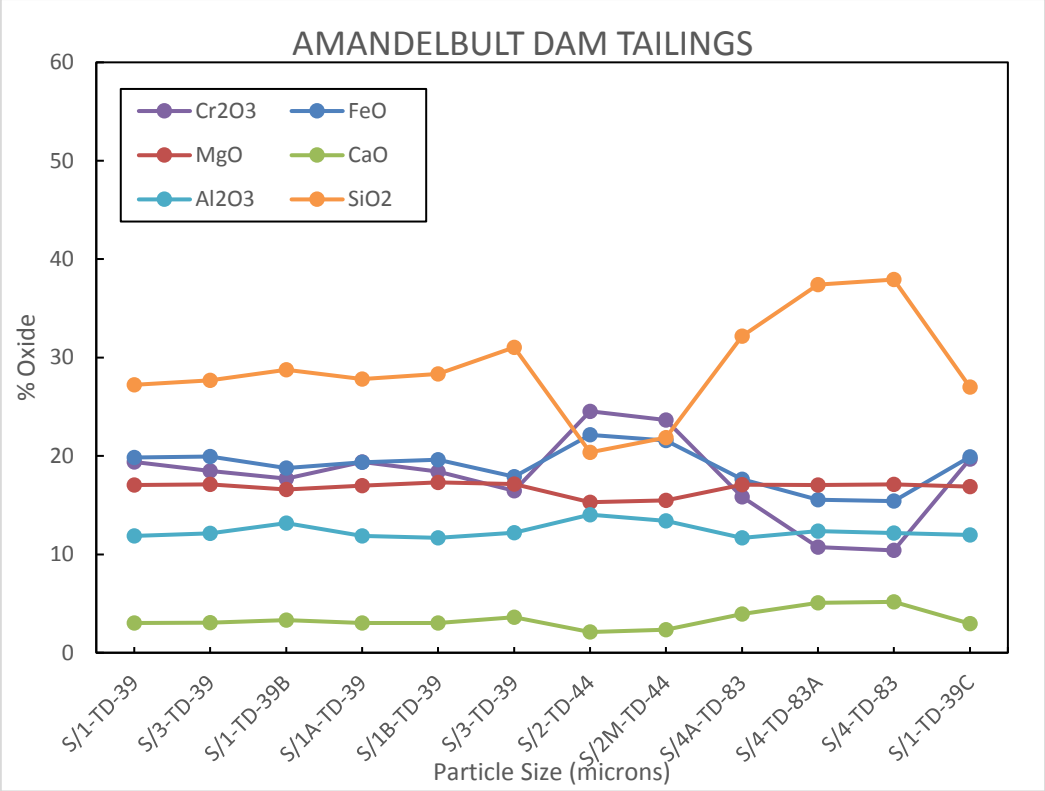

Figure 4. 19: Major oxide composition of size fractions in Amandelbult dam tailings.

A good agreement was observed between the measured and calculated bulk (Figure 4.20).

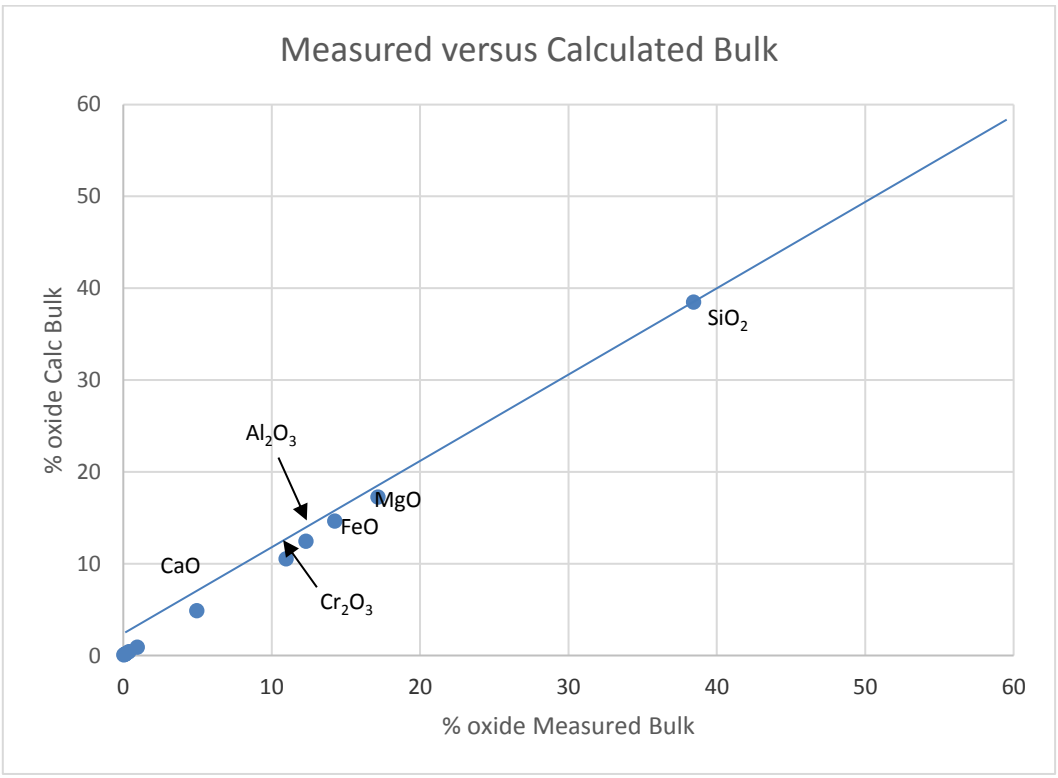

Figure 4. 20: The relationship between measured and calculated bulk for AMB/101.

4.2.3. Mogalakwena Tailings

Only sample (MPL/101) was analysed for particle size distribution, specific surface area and a wide range of mineralogical investigations. During the sample preparation phase, the main property that the Mogalakwena material possessed was its visibly light grey colour and confirms the paucity of mineral such as chromite in the Platreef orebodies. Another property was its smooth texture with no gritty feel. This gave an indication to its generally fine nature in terms of particle size.

4.2.3.1. Particle size analysis

Three sieving tests were performed for MPL /101 using the same procedure employed when handling the Impala and Amandelbult samples. From Table 4.9, a vast majority of the sample was reported below 25 µm. The wet screening test, denoted by MPL/101A recorded 38.25 wt % of sample below 25 µm.

Table 4. 9: Screening test results for MPL/101.

	MPL/101A	MPL/101B	MPL/101C	MPL(avg)
Sieve (µm)	wt%			
<25	38.25	21.47	33.52	31.08
25	12.00	23.39	15.32	16.90
38	14.42	15.99	15.17	15.19
53	15.87	17.30	17.11	16.76
75	10.96	10.70	10.48	10.71
106	4.50	6.87	4.73	5.37
150	3.99	4.29	3.68	3.99
Total	100	100	100	100

The dry screening test (MPL/101B) recorded the highest weight percentage (23.39 %) with the 25 µm size grouping but had the lowest amount of sample compared to the other tests for fraction below 25 µm (Table 4.9). The trend in the particle size distribution seemed unsteady during the dry screening test. On average, about 30 % material was reported to be found in the finest size fraction (Figure 4.21).

Cumulative values were derived from the averages of the replicates of the Mogalakwena sample and plotted against the size fractions as shown in Fig. 4.22. This was used to determine any similarities in Malvern results. A comprehensive version of sieve analysis results are presented in Appendix A1.3.

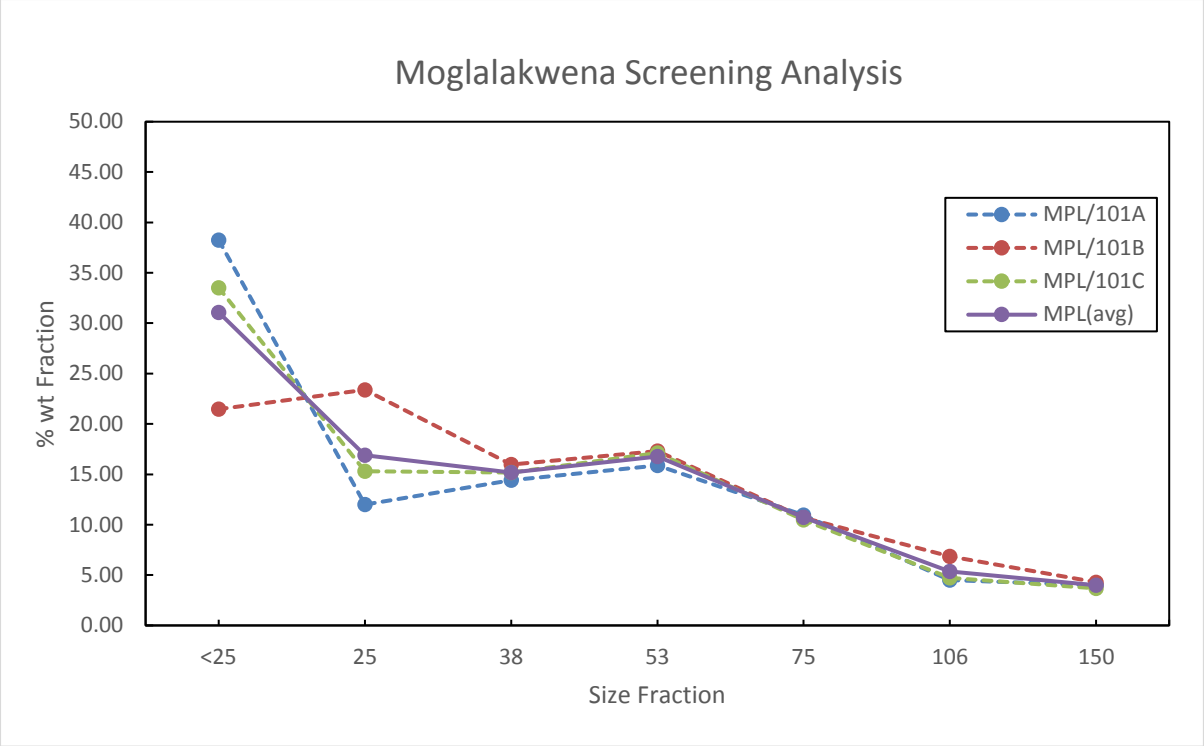

Figure 4. 21: Mogalakwena (MPL/101) screening results.

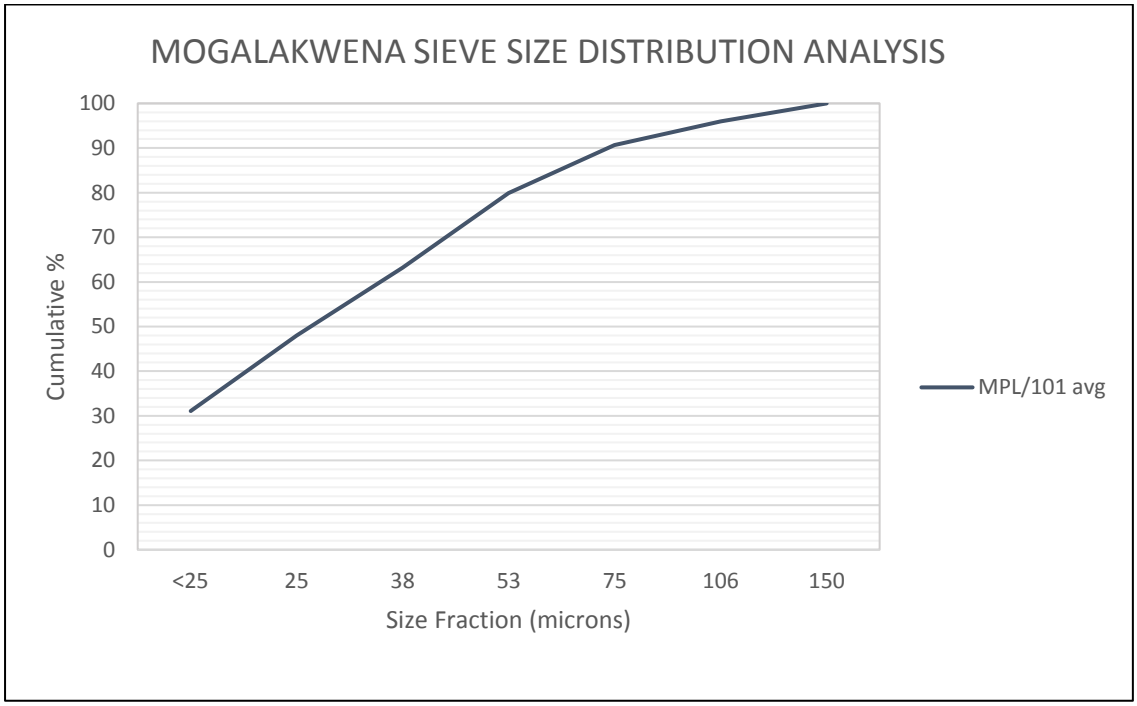

Figure 4. 22: Average sieving results plotted against cumulative percentage for Mogalakwena.

Malvern particle size results (Figure 4.23), showed that the finer particles were reported at Dv 0.9) and the value was 197.39 µm.

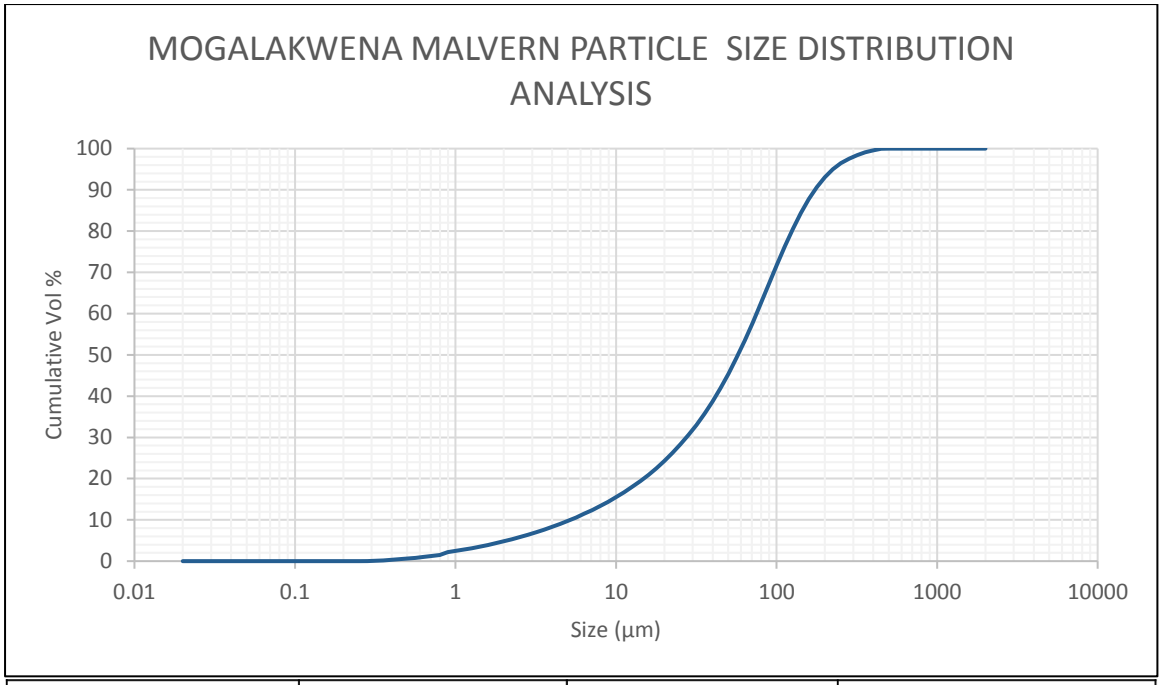

Tailings Sample	Dv (0.1)(µm)	Dv (0.5)(µm)	Dv(0.9)(µm)
MPL/101	5.406	61.028	197.392

Figure 4. 23: Malvern particle size distribution results for MPL/101

The specific surface area for the Mogalakwena tailings saple was 4.625 m^2/g (Figure 4.24). This was generated from the multiploint BET plot in Figure 4.24. Calculations to of the specific durface area can be seen in Appendix C1.3.

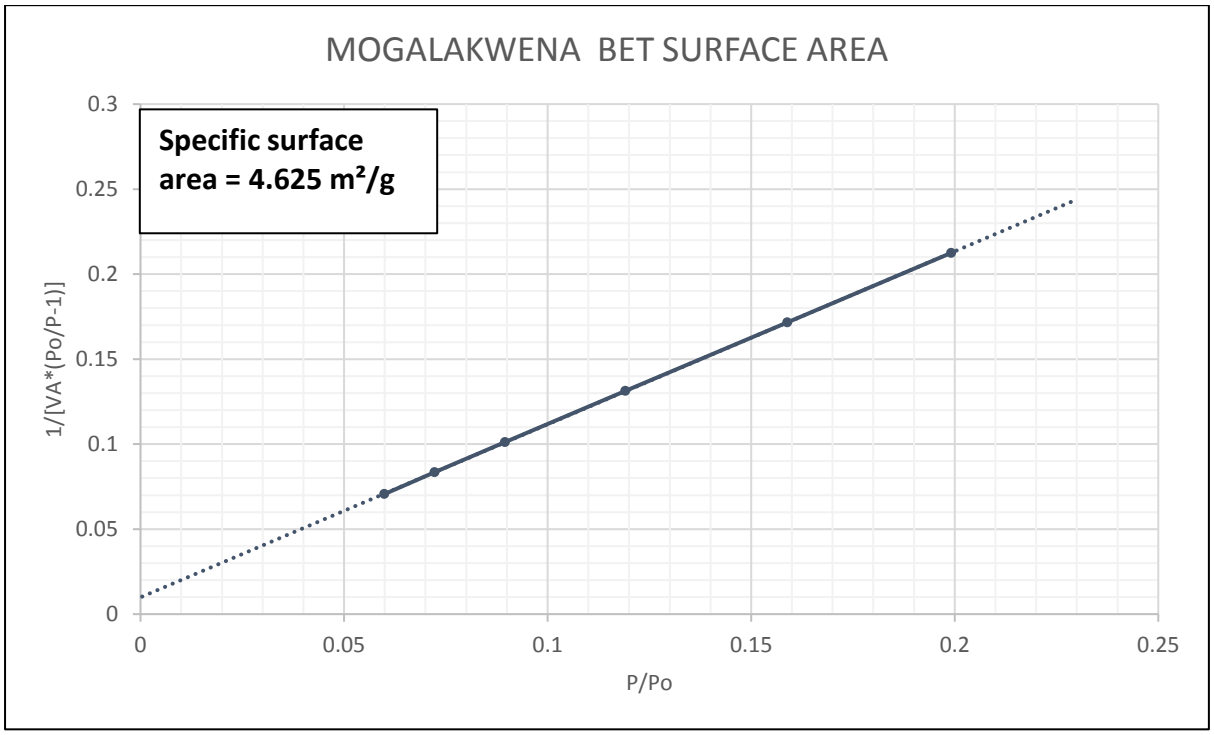

Figure 4. 24: Mogalakwena multi-point BET plot used to determine the specific surface area.

4.2.3.2. QXRD and QEMSCAN mineralogy

An illustration in Figure 4.25 reveals that the most abundant mineral identified during QXRD analysis was bytownite. Enstatite made up about 25 % of minerals detected during the analysis. A high amount of diopside as well as moderate amounts of hornblende and talc were detected (Table 4.10 and Figure 4.25).

From Table 4.10, the sum of mafic material discovered, made up about 55 % of the sample. Base metal sulphides were poorly represented and totalled about 3 % with pyrrhotite and pentlandite each representing slight over 1 %. Alteration minerals amounted to 17 % of the sample.

Table 4. 10: QXRD results for Mogalakwena, with the sum of mafic, sulphide and alterations mineral highlighted.

MOGALAKWENA		
Lithology	Chemical Composition	%
Chromite	$(Fe, Mg)Cr_2O_4$	3.38
Enstatite*	$MgSiO_3$	25.47
Diopside*	$MgCaSi_2O_6$	13.75
Hornblende*	$Ca_2(Mg, Fe, Al)_5 (Al, Si)_8O_{22}(OH)_2$	7.41
Biotite*	$K(Mg, Fe)_3 (AlSi_3O_{10})(F,OH)_2$	4.53
Bytownite*	$[(Ca, Na)[Al(Al, Si)Si_2O_8]$	24.51
Sum: Primary Igneous		**79.05**
Pyrrhotite	$Fe_{1-x}S$ (x = 0 to 0.2)	1.24
Pentlandite	$(Fe, Ni)_9S_8$	1.03
Chalcopyrite	$CuFeS_2$	0.94
Pyrite	FeS_2	0.42
Sum: Sulphide		**3.63**
Talc*	$Mg_3Si_4O_{10}(OH)_2$	7.89
Lizardite*	$Ni_3(Si_2O_5)(OH)_4$	1.67
Calcite	$CaCO_3$	0.90
Epidote*	$\{Ca_2\}\{Al_2Fe^{3+}\}[O\|OH\|SiO_4\|Si_2O_7]$	4.63
Quartz	SiO_2	2.23
Sum: Alteration		**17.32**
*Carbonatable		89.86
Non carbonatable		10.14

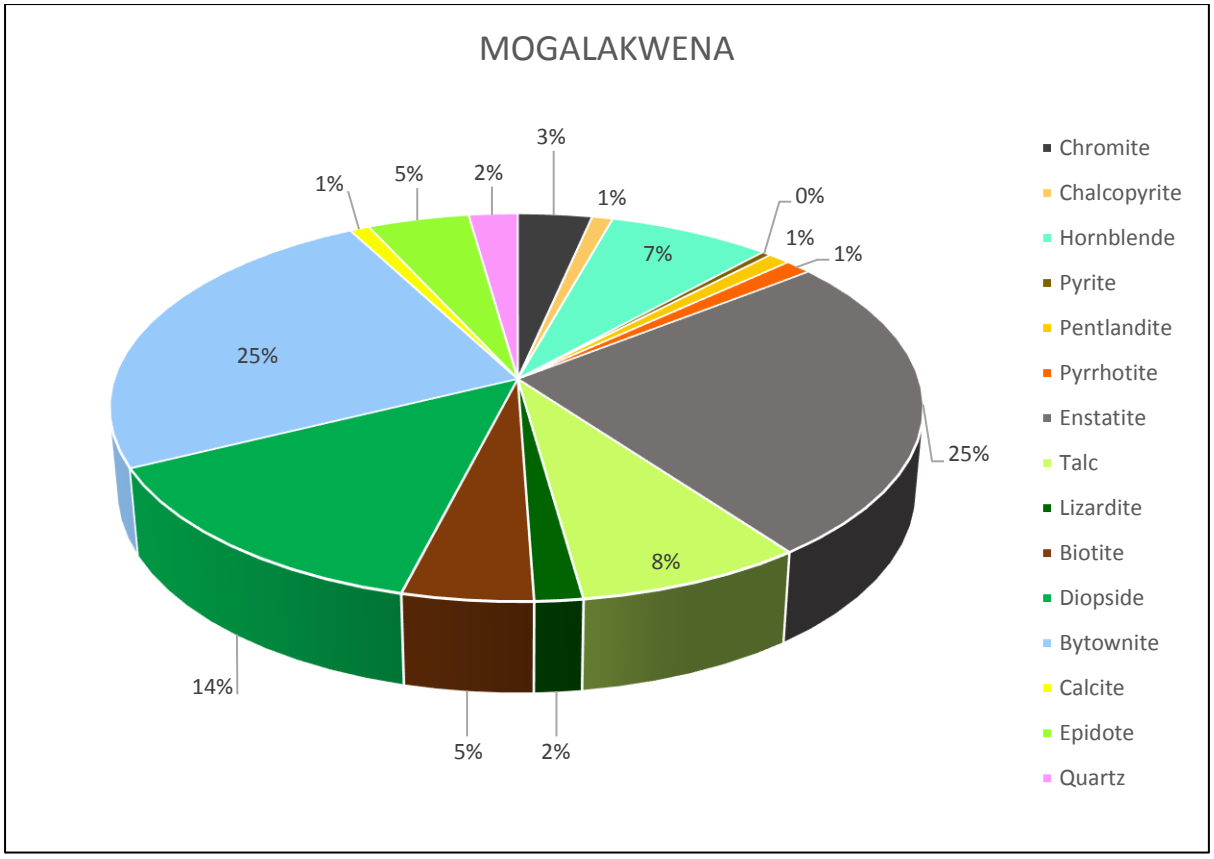

Figure 4. 25: QXRD results for MPL/101.

The -75/+53 µm fraction was selected for QEMSCAN analysis. Results for the analysis confirmed the high presence of orthopyroxenes of more than 40 %. Evidently from Table 4.11 and Figure 4.26, plagioclase and clinopyroxene were also in abundance, with 19 and 13 % detected respectively. A moderate amount of olivine (<5 %) was detected during QEMSCAN analysis.

Table 4.11 shows that the primary igneous minerals amounted to 85 % of the sample. Serpentine, quartz and chlorite made up most of the alteration group of minerals amounting to 14 %. A very low base metal sulphide content of ~1 % in total was detected (Table 4.11). The sum of carbonatable minerals was calculated to make up about 93 % of the Mogalakwena sample.

Table 4. 11: QEMSCAN results for Mogalakwena. The selected size fraction (-75/+53 µm).

MOGALAKWENA		
Lithology	Chemical Composition	%
Chromite	$(Fe, Mg)Cr_2O_4$	1.77
Orthopyroxene*	$Mg_2Si_2O_6$	42.60
Clinopyroxene*	$CaMgSi_2O_6$	14.19
Hornblende *	$Ca_2(Mg, Fe, Al)_5 (Al, Si)_8O_{22}(OH)_2$	3.13
Biotite*	$K(Mg, Fe)_3 (AlSi_3O_{10})(F,OH)_2$	1.12
Olivine*	(Mg, Fe)2SiO4	3.09
Plagioclase*	$(Na,Ca)(Si,Al)_4O_8$	18.98
Sum: Primary Igneous		**84.88**
Pyrrhotite	$Fe_{1-x}S$ (x = 0 to 0.2)	0.13
Pentlandite	$(Fe, Ni)_9S_8$	0.36
Chalcopyrite	$CuFeS_2$	0.51
Pyrite	FeS_2	0.21
Sum: Base Metal Sulphide		**1.21**
Talc*	$Mg_3Si_4O_{10}(OH)_2$	0.59
Serpentine*	$Mg_3(Si_2O_5)(OH)_5$	4.85
Chlorite*	$(Mg, Fe)_3(Si, Al)_4O_{10}(OH)_2 \cdot (Mg, Fe)_3(OH)_6$	3.83
Calcite	$CaCO_3$	1.69
Epidote*	$Ca_2Fe_{3+2.25}Al_{0.75}(SiO_4)_3(OH)$	0.76
Quartz	SiO_2	2.19
Sum: Secondary Alteration		**13.91**
Carbonatable		93.16
Non carbonatable		6.84

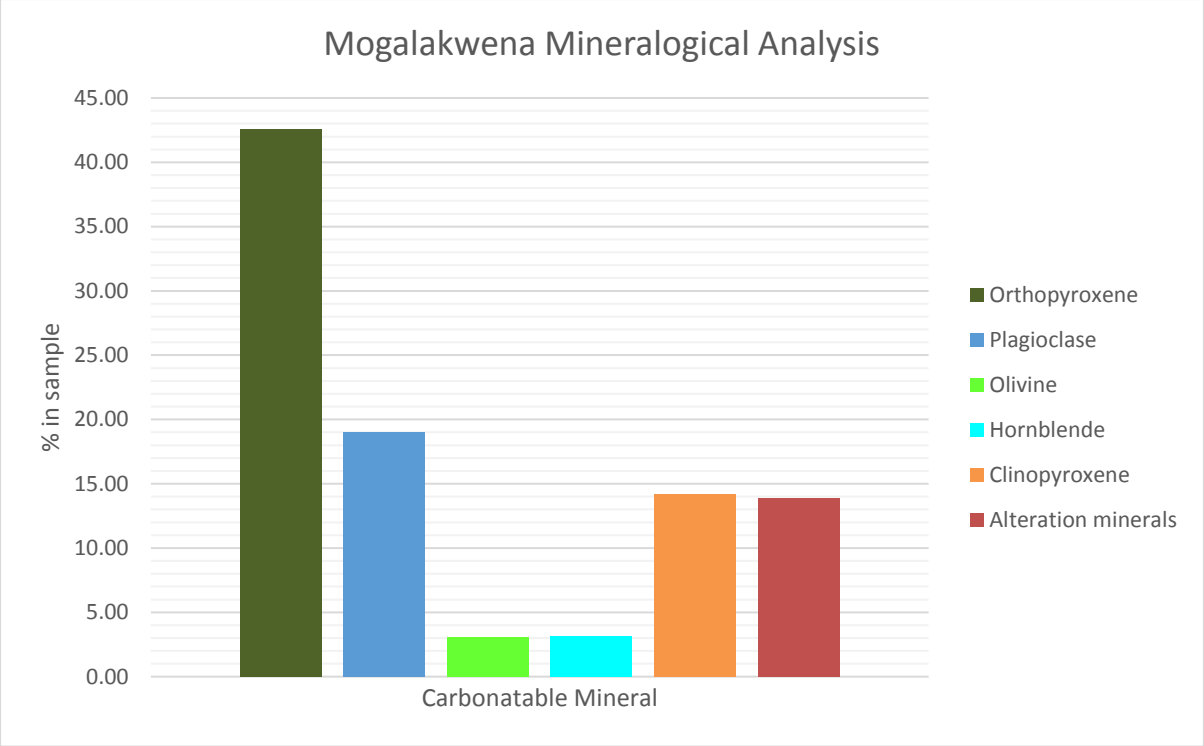

Figure 4. 26: Results from QEMSCAN for MPL/101.

Upon comparing Mogalakwena's MPL/101 QXRD and QEMSCAN results, carbonatable minerals made up 93.16% while QXRD analysis identified 89.86% of carbonatable minerals. Orthopyroxene was high in QEMSCAN (42.60%) compared to QXRD analysis (25.47%). However, a high amount of plagioclase was reported to be in the region of 24.50% in QXRD analysis as opposed to 18.89% in QEMSCAN as shown in Table 4.10 and 4.11. The sum of alteration minerals and based metal sulphides were reported lower in QEMSCAN as compared to results in from QXRD (Table 4.10 and 4.11).

4.2.3.3. XRF major oxide geochemistry

Concentrations of major oxides remained rather constant through the size fractions. As predicted earlier, minute amounts of about (1 %) of Cr_2O_3 was detected. SiO_2 amounts were noticeably the highest within the sample with an average amount of 50 % in all size fractions (Figure 4.27).

A high concentration of MgO (~20 %) was detected in Mogalakwena tailings sample. However, Al_2O_3, FeO and CaO were in moderate amounts between 9 and 11 % (Figure 4.27).

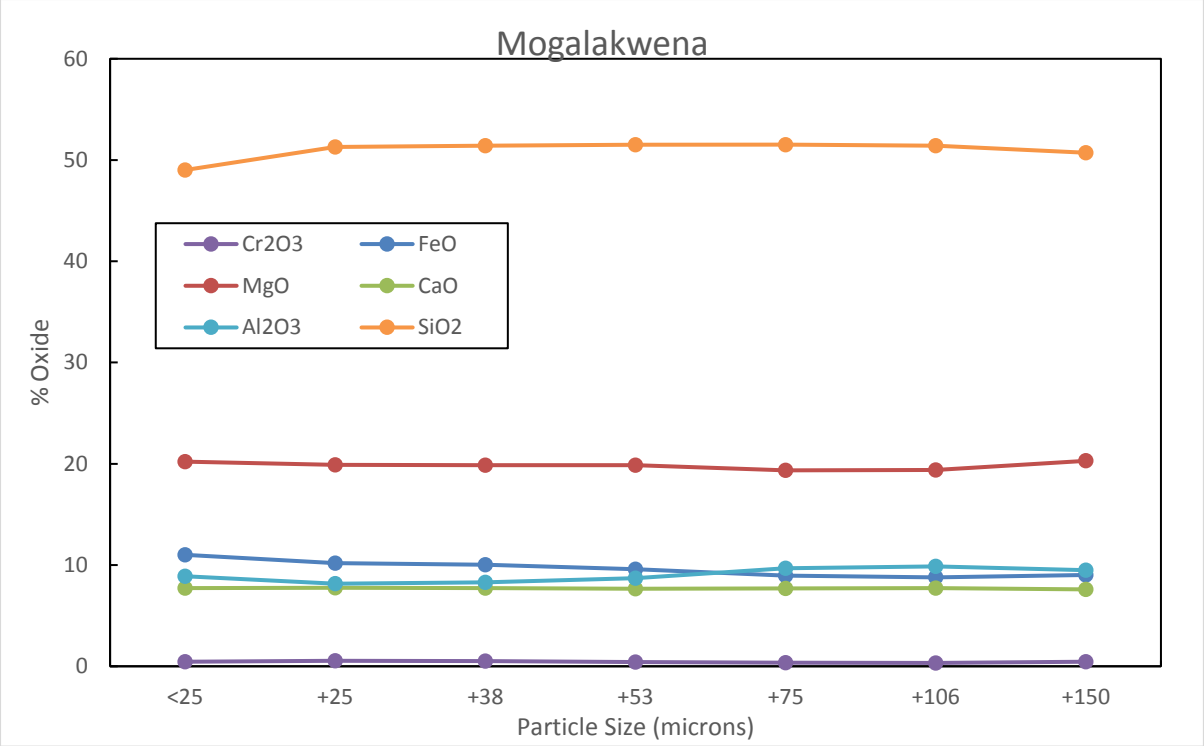

Figure 4. 27: Major oxide composition of size fractions in MPL/101.

The relationship between the bulk is shown in Figure 4.28. However, there were no significant discrepancies.

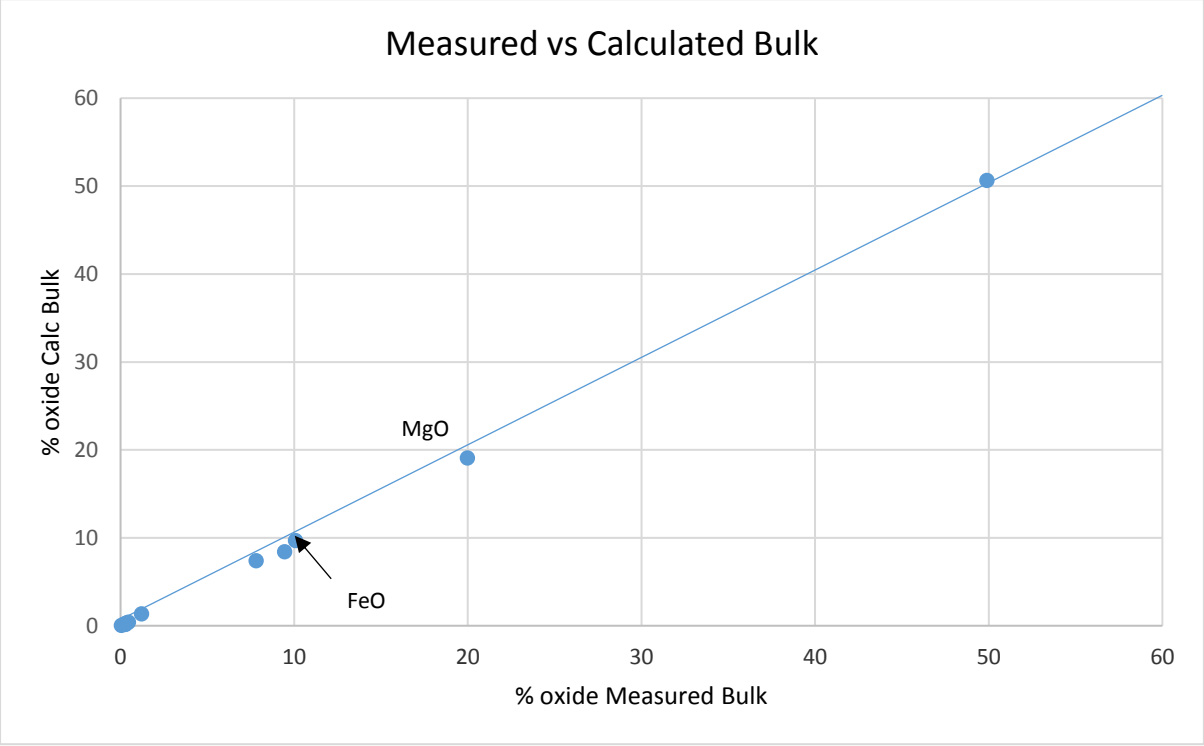

Figure 4. 28: The relationship between measured and calculated bulk for MPL/101.

4.2.4. Union Section Tailings

One plant sample (UST/201) was examined for particle size, surface area and mineralogy.

4.2.4.1. Particle size analysis

As indicated in Chapter 3, a 100g aliquot was used during each screening examination. Table 4.12 displays results for three screening tests for UST/201. The sample appeared to be typically fine with more the 50 % reporting below 38 µm.

Table 4. 12: Tabulated screenings results for Union Section tailings sample.

	UST/201A	UST/201B	UST/201C	UST/201 (avg)
Sieve (µm)	wt%			
<25	2.99	3.66	2.84	3.16
25	6.04	6.88	6.09	6.34
38	12.60	13.28	12.78	12.89
53	15.16	15.52	15.93	15.54
75	14.07	17.40	13.95	15.14
106	8.49	11.40	9.40	9.76
150	40.66	31.87	38.99	37.17
Total	100	100	100	100

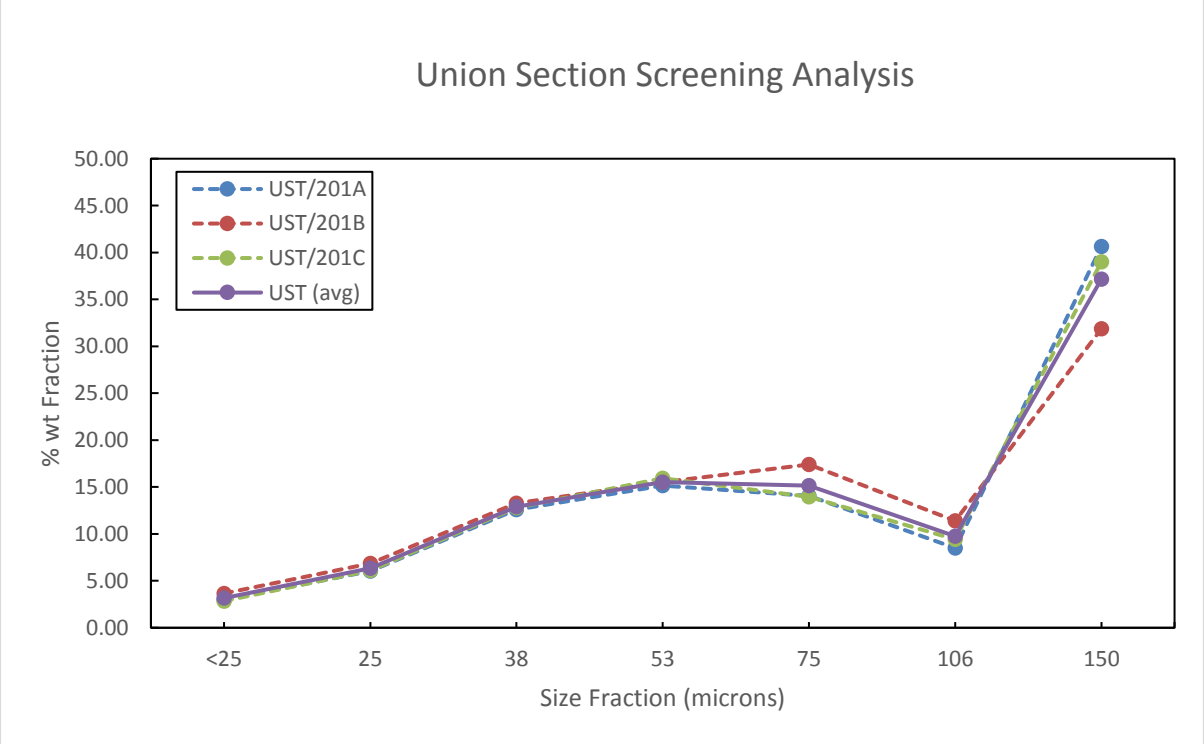

Figure 4. 29: Particle size distribution results from UST/201 screening tests.

Figure 4.30 show a plot of size fraction versus cumulative percentage for the average of the replicates for Union Section sample. This was used to determine any similarities with Malvern results. A full sieve analysis can be found in Appendix A1.4.

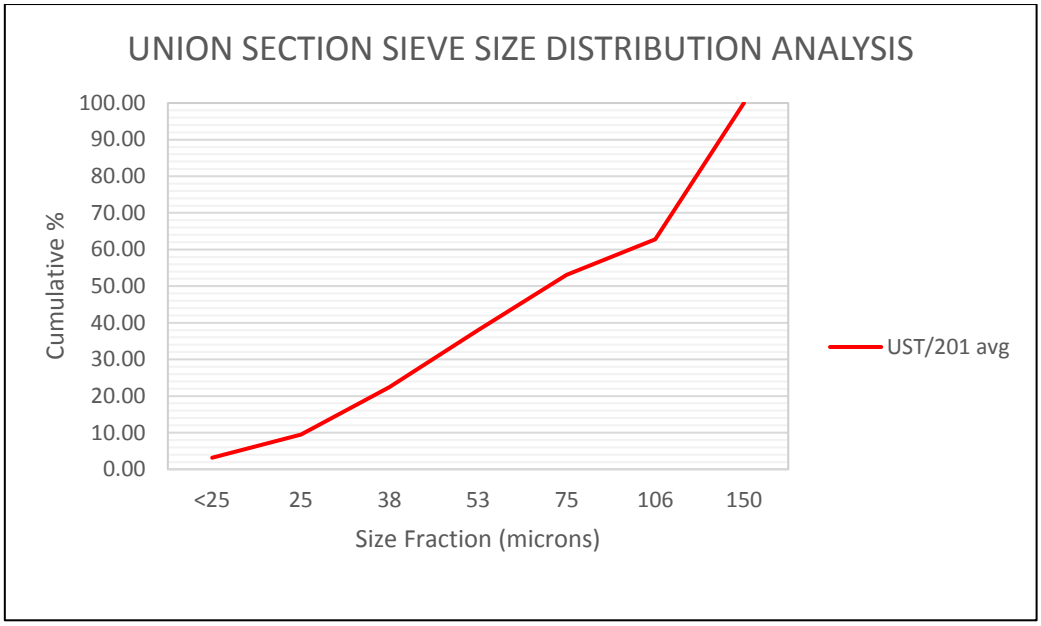

Figure 4. 30: Average sieving results plotted against cumulative percentage for Union Section.

Analysis from Malvern demonstrated a particle size distribution curve in Figure 4.31. The Dv (0.9) value was given as 233.52 µm.

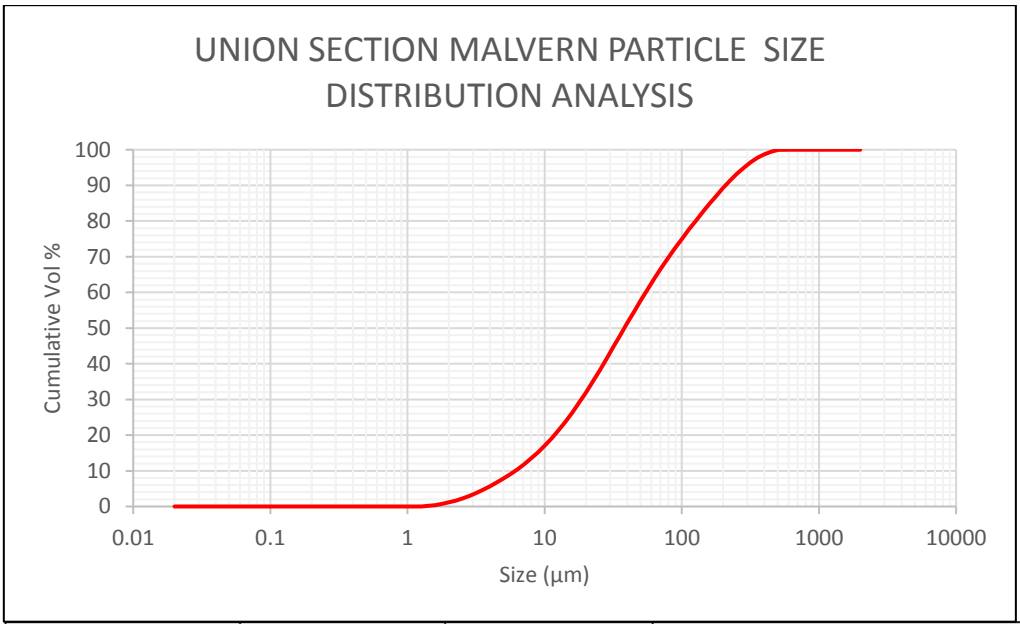

Tailings Sample	Dv (0.1)(µm)	Dv (0.5)(µm)	Dv(0.9)(µm)
UST/201	6.84	42.788	233.523

Figure 4. 31: Malvern particle size distribution curve for UST/201.

Surface area results are presented in Figure 4.32. The Union Section tailings sample recorded a specific surface area of 2.572m^2/g. From the multipoint BET liner graph (Figure 4.32), the slope and intercept was used to calculate the specific surface area. A table presenting the full BET data and calculations are presented in Appendices B3.4 and C1.4 respectively.

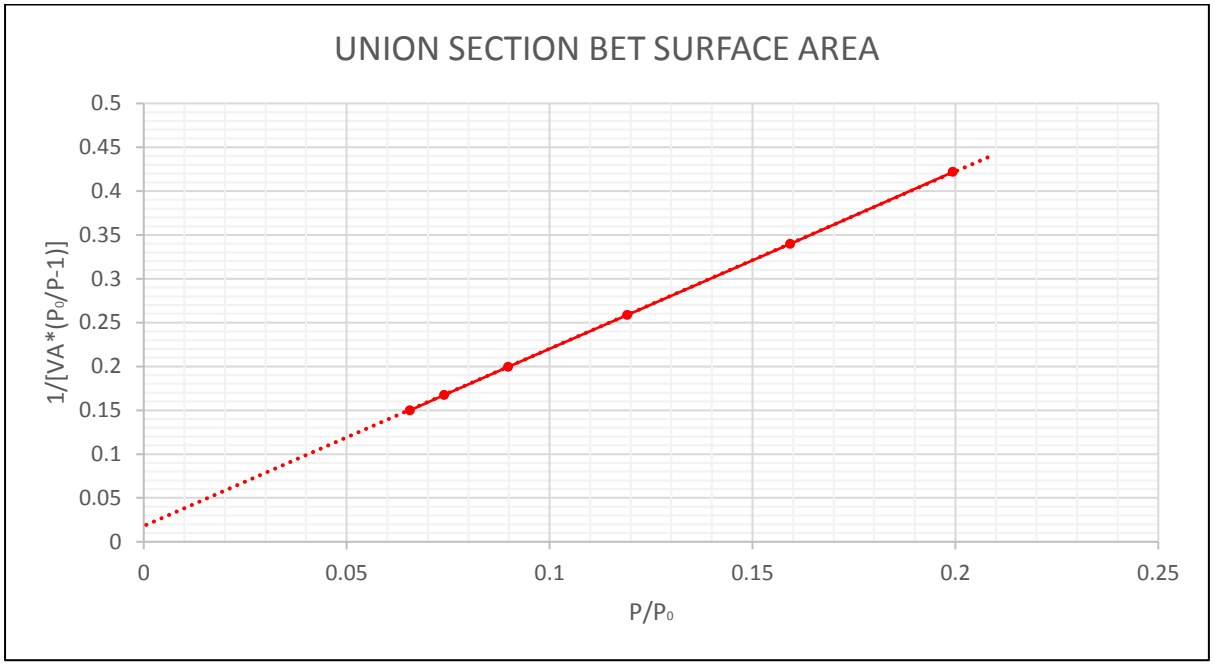

Figure 4. 32: Multi-point BET plot to determine the specific surface area of UST/201.

4.2.4.2. QXRD and QEMSCAN mineralogy

The abundance of chromite (~35 %) was revealed through QXRD analysis displayed in Figure 4.33. Bytownite and enstatite were notably high, making up about 14 % and 23 % respectively. Other evident minerals detected by QXRD included hornblende (9 %), diopside (4 %), epidote (~3 %) and talc (3 %).

Primary igneous minerals made up roughly 89 % of the Union Section tailings sample. Base metal sulphides include pyrrhotite at 1.5 %, pentlandite and chalcopyrite also made up about 1.2 and 1.1 % respectively. The sum of alteration minerals totalled 7 % (Table 4.13).

Table 4. 13: QXRD results for Union Section, with the sum of primary igneous mineral, sulphide and alterations minerals highlighted.

UNION		
Lithology	Chemical Composition	%
Chromite	$(Fe, Mg)Cr_2O_4$	35.79
Enstatite*	$MgSiO_3$	23.42
Diopside*	$MgCaSi_2O_6$	3.69
Hornblende*	$Ca_2(Mg, Fe, Al)_5 (Al, Si)_8O_{22}(OH)_2$	8.80
Biotite*	$K(Mg, Fe)_3 (AlSi_3O_{10})(F,OH)_2$	2.54
Bytownite*	$[(Ca, Na)[Al(Al, Si)Si_2O_8]$	14.43
Sum: Primary Igneous		**88.67**
Pyrrhotite	$Fe_{1-x}S$ (x = 0 to 0.2)	1.46
Pentlandite	$(Fe, Ni)_9S_8$	1.22
Chalcopyrite	$CuFeS_2$	1.10
Pyrite	FeS_2	0.50
Sum: Sulphide		**4.28**
Talc*	$Mg_3Si_4O_{10}(OH)_2$	3.26
Lizardite*	$Ni_3(Si_2O_5)(OH)_4$	1.17
Calcite	$CaCO_3$	0.00
Epidote*	$\{Ca_2\}\{Al_2Fe^{3+}\}[O\|OH\|SiO_4\|Si_2O_7]$	2.55
Quartz	SiO_2	0.07
Sum: Alteration		**7.05**
*Carbonatable		59.86
*Non Carbonatable		40.14

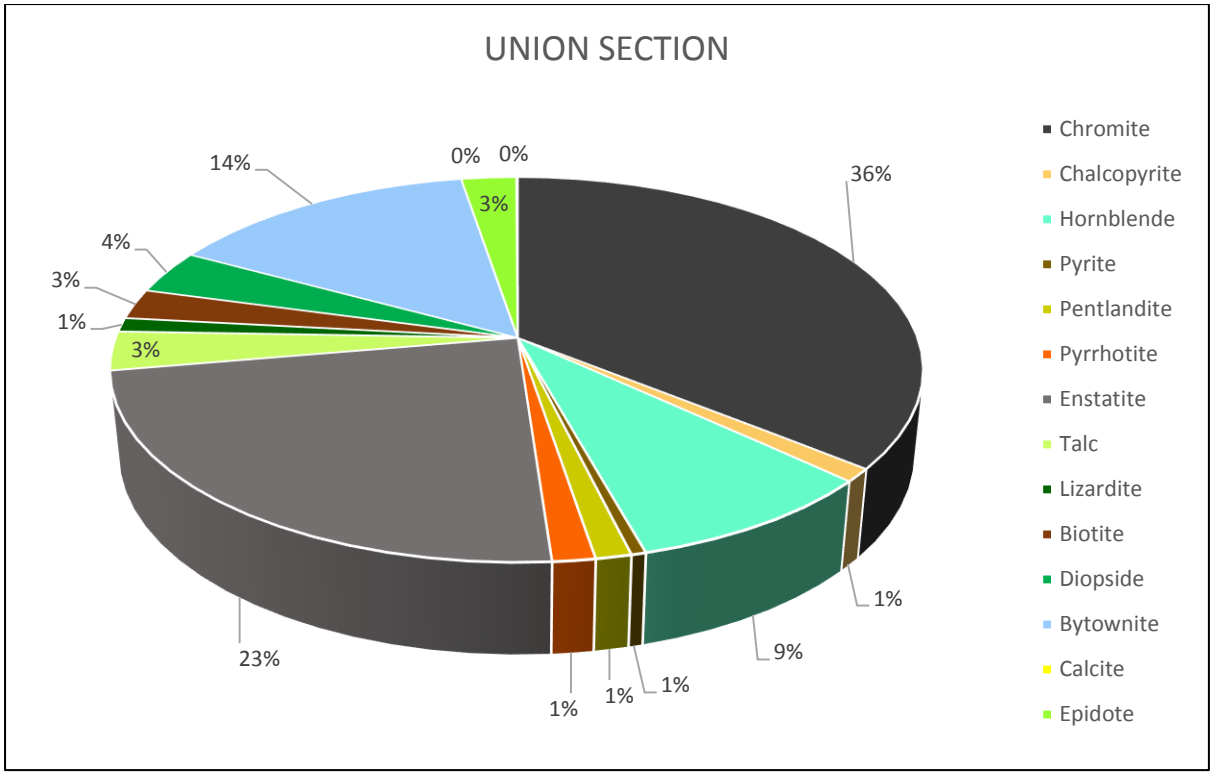

Figure 4. 33: QXRD analysis results for Union Section tailings sample.

The -106/+75 µm size fraction was selected for QEMSCAN analysis. According to the analysis interpreted in Table 4.14 and Figure 4.34, dominant minerals identified were chromite (~52 %) and orthopyroxene (~35 %). Plagioclase was also detected with quantities slightly above 5 %. Other minerals found in much lower amounts (<5 %) were olivine, clinopyroxene, chlorite and talc. From Table 4.14, the sum of base metal sulphides amounted to less than 1 %. A combination of igneous minerals made up about 98 % of the sample with alteration minerals making up less than 2 %. The high presence of chromite could render the Union Section tailings facility disadvantageous to the carbonation exercise.

Table 4. 14: Union Section's -106/+75 µm mineral distribution determined by QEMSCAN.

UNION		
Lithology	Chemical Composition	%
Chromite	$(Fe, Mg)Cr_2O_4$	51.63
Orthopyroxene*	$Mg_2Si_2O_6$	33.99
Clinopyroxene*	$CaMgSi_2O_6$	2.48
Hornblende*	$Ca_2(Mg, Fe, Al)_5 (Al, Si)_8O_{22}(OH)_2$	0.77
Biotite*	$K(Mg, Fe)_3 (AlSi_3O_{10})(F,OH)_2$	0.28
Olivine*	(Mg, Fe)2SiO4	2.16
Plagioclase*	$(Na,Ca)(Si,Al)_4O_8$	6.80
Sum: Primary Igneous		**98.11**
Pyrrhotite	$Fe_{1-x}S$ (x = 0 to 0.2)	0.01
Pentlandite	$(Fe, Ni)_9S_8$	0.01
Chalcopyrite	$CuFeS_2$	0.03
Pyrite	FeS_2	0.09
Sum: Base Metal Sulphide		**0.14**
Talc*	$Mg_3Si_4O_{10}(OH)_2$	0.39
Serpentine*	$Mg_3(Si_2O_5)(OH)_5$	0.61
Chlorite*	$(Mg, Fe)_3(Si, Al)_4O_{10}(OH)_2 \cdot (Mg, Fe)_3(OH)_6$	0.29
Calcite	$CaCO_3$	0.24
Epidote*	$Ca_2Fe_{3+2.25}Al_{0.75}(SiO_4)_3(OH)$	0.02
Quartz	SiO_2	0.20
Sum: Secondary Alteration		**1.75**
*Carbonatable		47.79
Non carbonatable		52.21

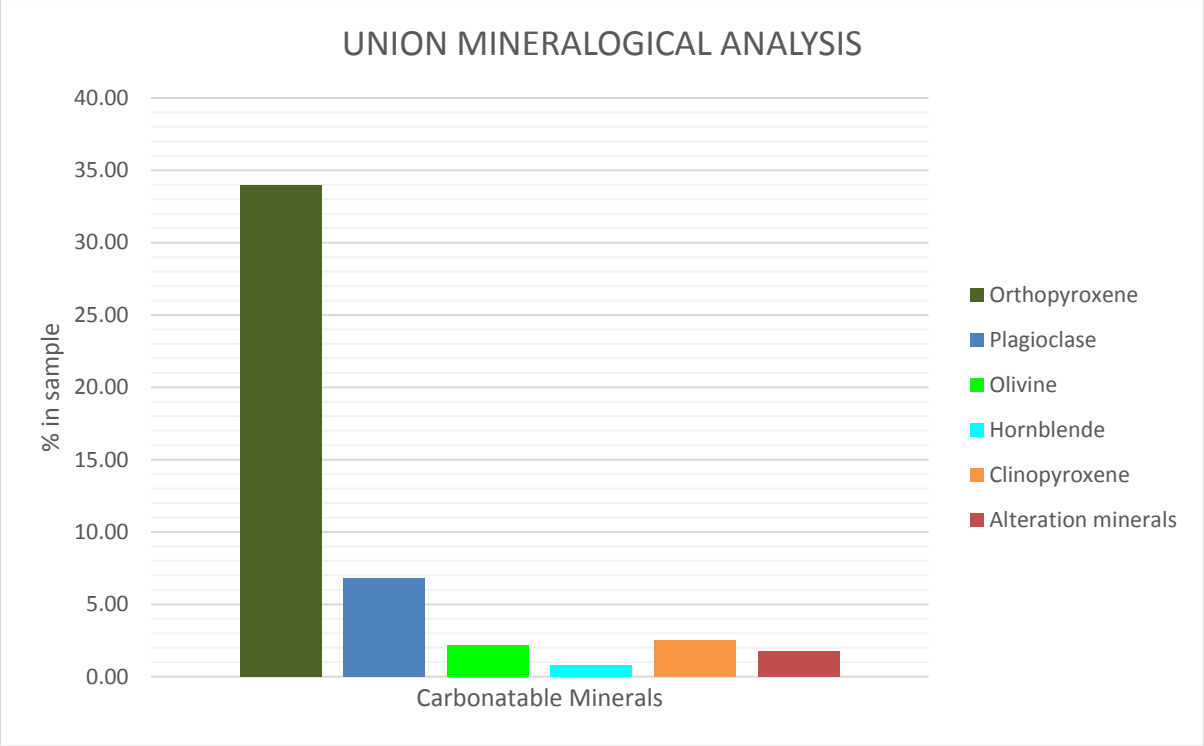

Figure 4. 34: QEMSCAN analytical results for UST/201.

Discrepancies were observed between QXRD and QEMSCAN results for sample UST/201. The most evident difference was seen in chromite values, where QEMCSAN detected more chromite (51.63%) than the 35.79% reported by QXRD. Orthopyroxene was higher in QEMSCAN (33.99%) as opposed to 23.42% from QXRD (Table 4.13 and 4.14).

Plagioclase, hornblende and biotite were observed to have been substantially identified by QXRD as compared to QEMSCAN. Generally, base metal sulphides and alteration minerals had higher values in QXRD compared to results from QEMSCAN. Carbonatable minerals made up 59.86 % of sample UST/201 in the QXRD results while 47.79% of carbonatable minerals was accounted for in the -106/+75 µm size fraction of the UST/201 as shown in Table 4.13 and 4.14.

4.2.4.3. XRF major oxide geochemistry

As presented in Figure 4.35, SiO_2 are as low as 20 % in finer fractions but abruptly increased among particles greater than 53 µm. The most dominant oxide in the finer size fraction Cr_2O_3 with about an average of 20 %. A steep decrease was observed towards coarser (>53 µm) and further reduced to as low as < 10 % in the coarsest size fraction.

An average amount of 20 % was recorded for FeO. This however decreased in material greater than 38 µm. MgO and Al_2O_3 values remained somewhat stable in all size fractions. The lowest oxide detected by XRF was CaO, which made up only 5 % of the Union Section tailings sample (Figure 4.35).

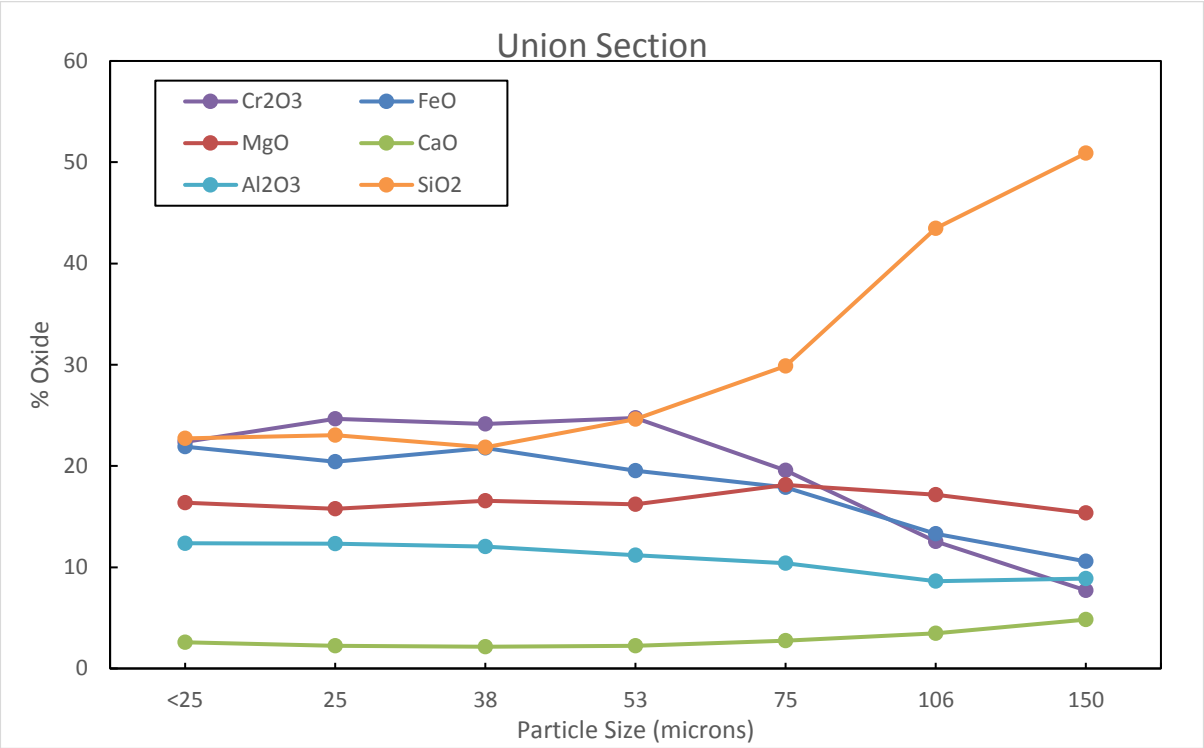

Figure 4. 35: Major oxide composition of size fractions in UST/201.

Based on QXRD and QEMSCAN results (Table 4.13 and 4.14), relatively high concentrations in chromite are observed in the UST/201 sample. Variations in chromite affects Cr_2O_3 and FeO and reduces the SiO_2. Figure 4.35 lays more emphasis on this principle. High amounts of Cr_2O_3 and FeO were observed within size fractions below 53 µm with lower SiO_2 values. As Cr_2O_3 and FeO dropped in coarser fractions, SiO_2 increased.

The relationship between the measured and calculated bulk was determined from Figure 4.36. There were substantial differences between both bulk samples with some oxides positioned marginally further away from the trend line, implying specific values did not necessarily correlate. A moderate correlation was therefore seen between the measured bulk and calculated bulk.

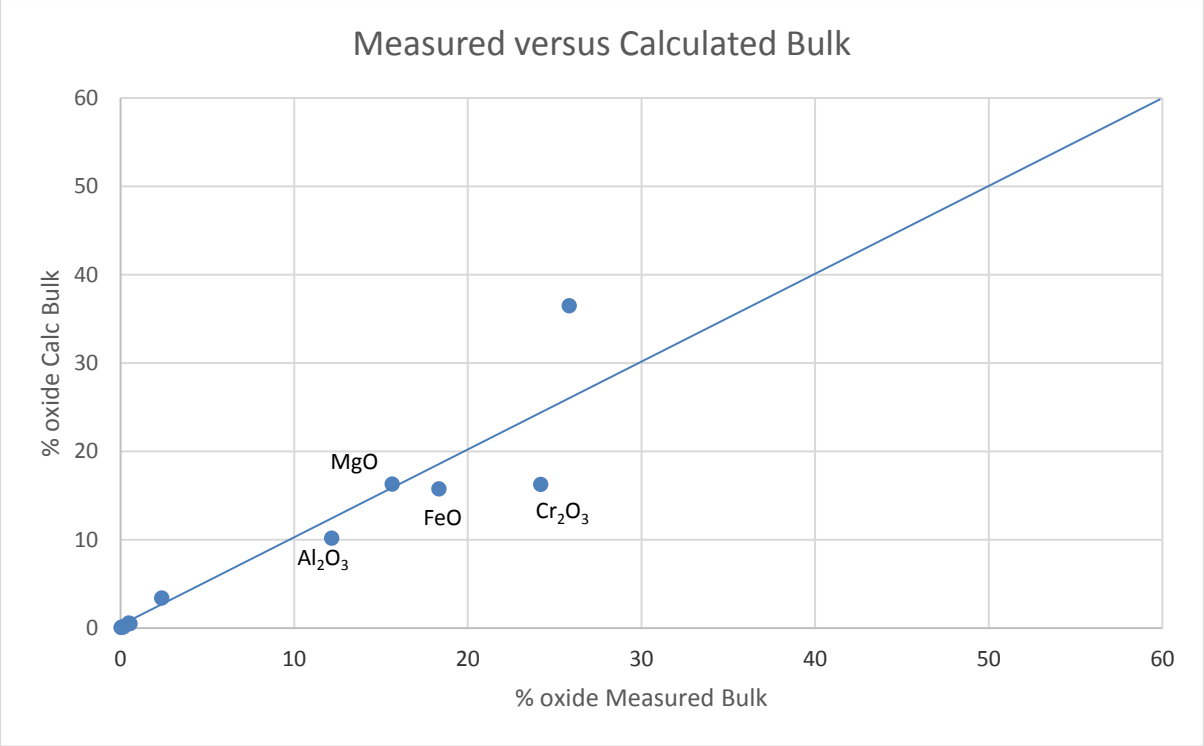

Figure 4. 36: Relationship between the measure bulk and calculated bulk for UST/201.

4.2.5. Rustenburg Tailings

Sample (WRT/101) was the only Rustenburg sample examined for particle size, surface area and mineralogical properties.

4.2.5.1 Particle size analysis

100g aliquots were used during each screening test. Results presented in Table 4.15 demonstrates the typically very fine nature of tailings particles. More than 60 % of the sample is finer than 38 µm.

Table 4. 15: Rustenburg (Waterval) sieving test results.

	WRT-101A	WRT-101B	WRT-101C	WRT-101 (avg)
Sieve (µm)	wt%			
<25	48.67	39.58	44.2	44.15
25	14.33	18.6	16.28	16.40
38	13.47	13.63	14.33	13.81
53	12.35	14.86	12.91	13.37
75	7.08	5.38	7.48	6.65
106	2.68	4.3	3.16	3.38
150	1.42	3.64	1.64	2.23
100	100	100	100	100

Weight fraction is each size range are plotted in Figure 4.37, where all tests A,B and C show the dominance of the finer particles. While variations does occur, there is no consistent bias shown by any of the three sieve techniques.

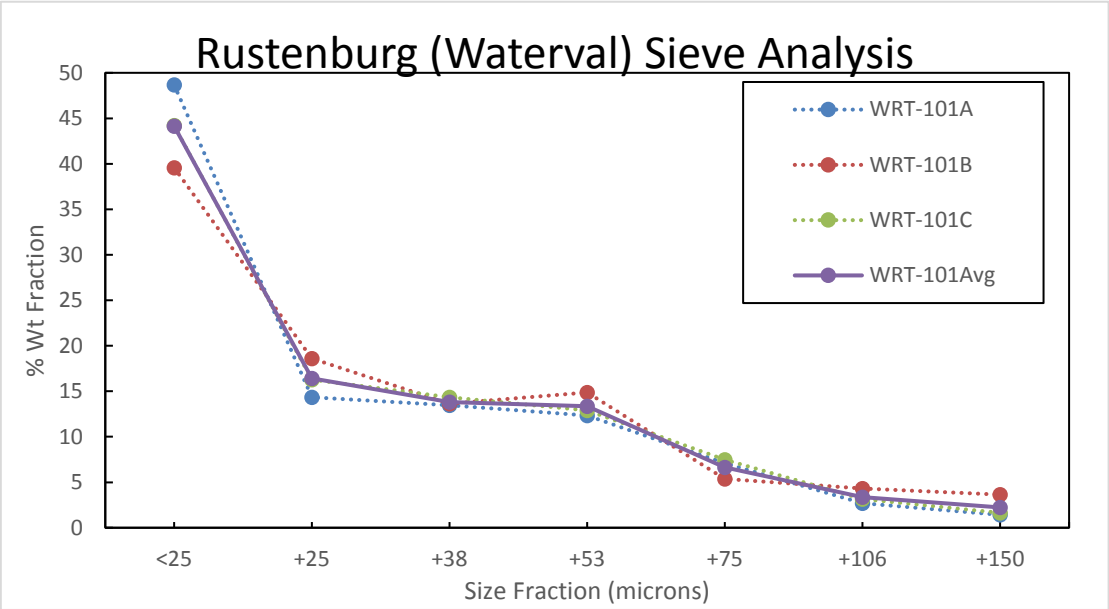

Figure 4. 37: WRT/101 screening test results plots.

The cumulative percentage was calculated from the average of the replicates of Rustenburg sample and plotted against the size fractions as shown in Fig. 4.38. This was used to determine any similarities in Malvern results. A full sieve analysis can be found in Appendix A1.5.

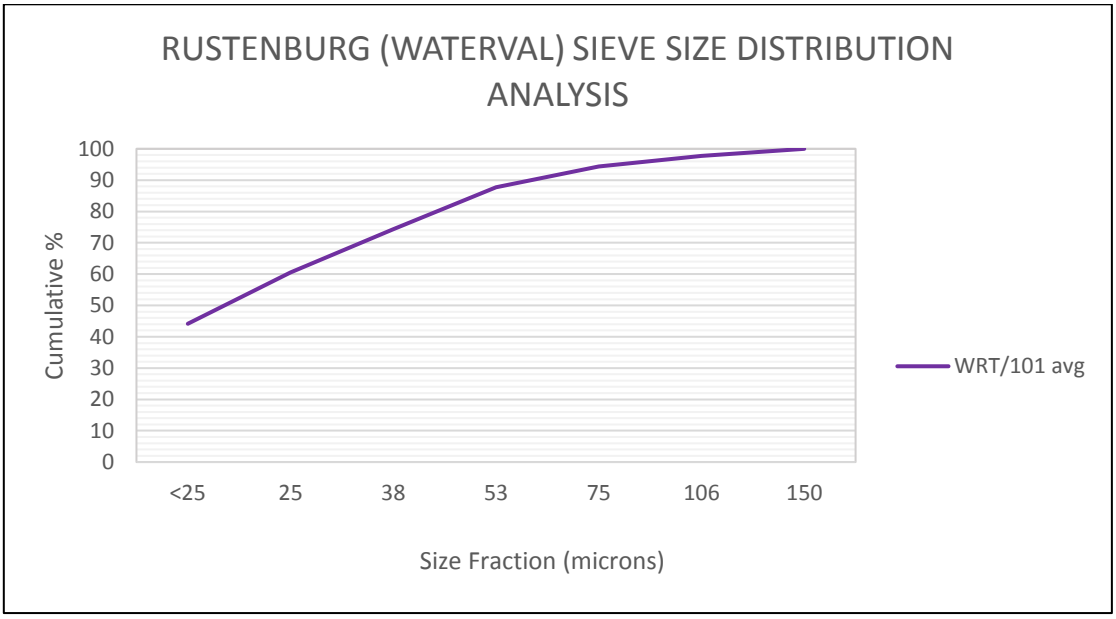

Figure 4. 38: Average sieving results plotted against cumulative percentage for Rustenburg (Waterval).

A Malvern particle size distribution curve was generated as displayed in Figure 4.39. It was observed from the graph that a volume of 90 % was bieleved to be located below 215.182 µm (Figure 4.39).

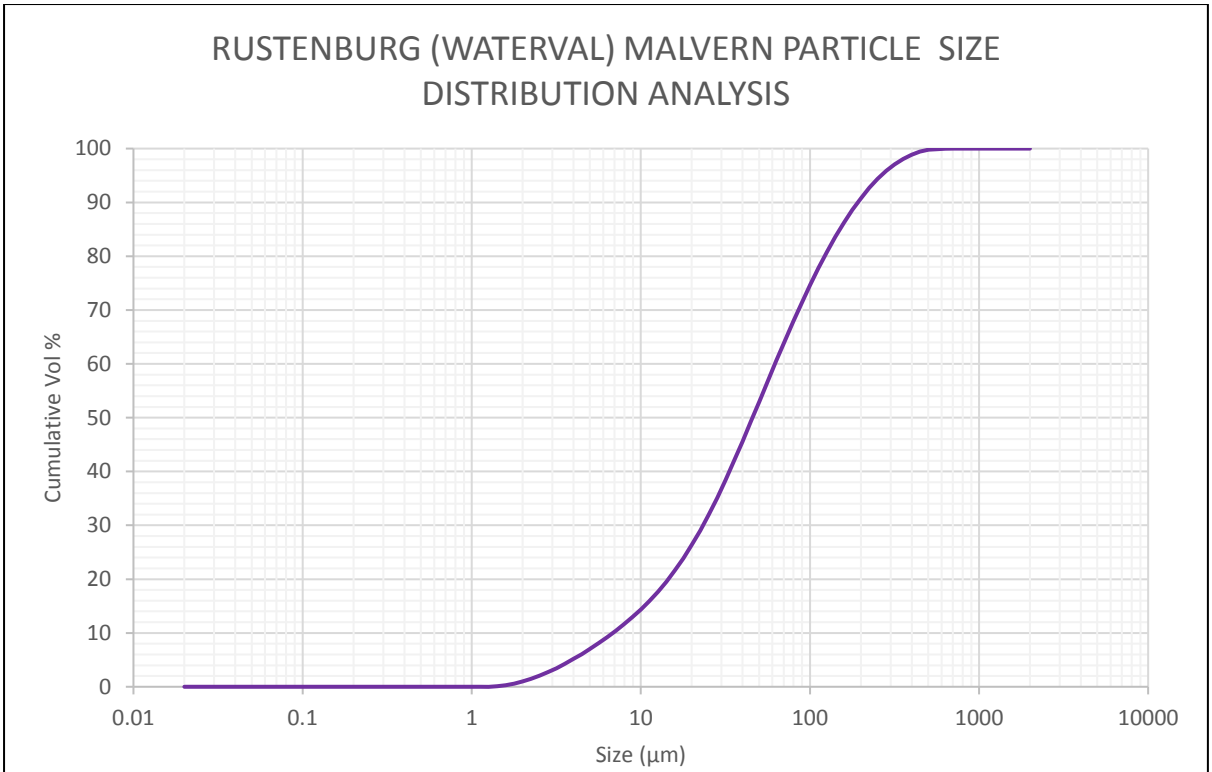

Tailings Sample	Dv (0.1)(µm)	Dv (0.5)(µm)	Dv(0.9)(µm)
WRT/101	7.664	51.376	215.182

Figure 4. 39: Size distribution curve for WRT/101 obtained by Malvern analysis.

The specific surface area for WRT/201 was calculated from the multipoint BET plot (Figure 4.40). The specific surface area for the Rustenburg sample was given as 2.603 m^2/g. The calculation are shown in Appendix C1.5. Variables derived from the Multipoint BET plot are tabulated in Appendix A3.5.

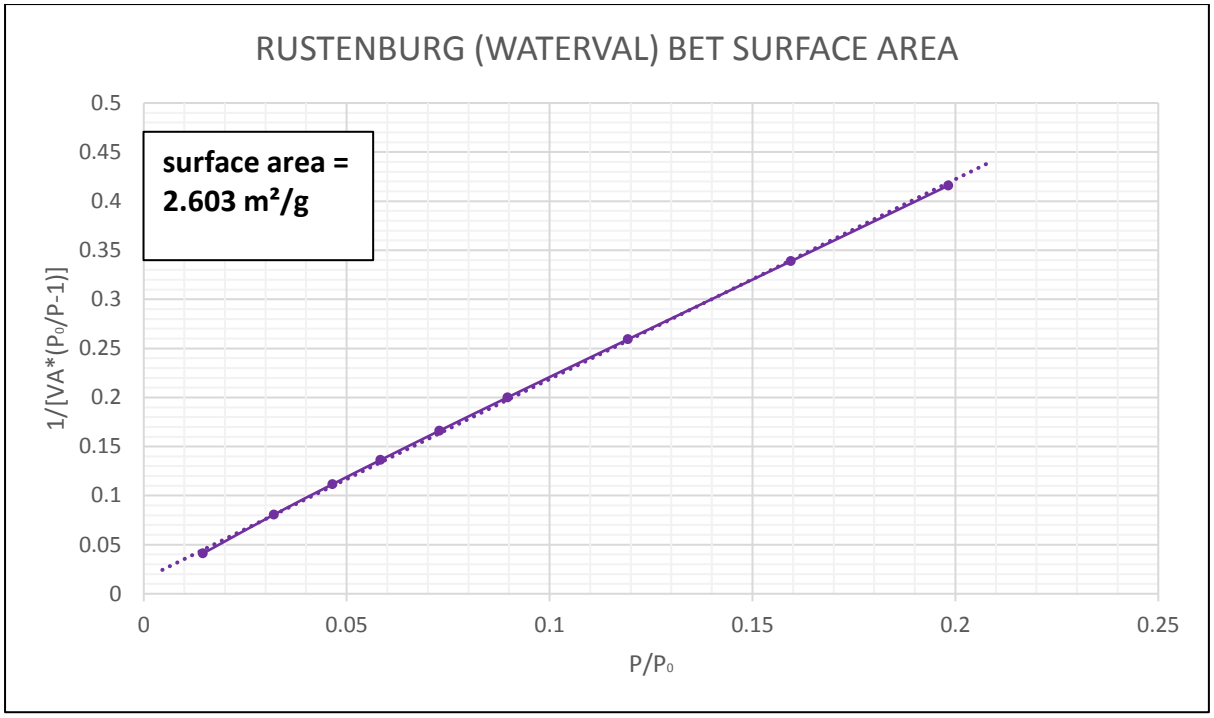

Figure 4. 40: Multi-point BET plot used to determine the specific surface area for WRT/101.

4.2.5.2. QXRD and QEMSCAN mineralogy

QXRD analysis was employed on WRT/101 for mineral identification purposes. Results from the analysis confirmed plagioclase (~46 %) as the most dominant mineral. A high amount of enstatite (25 %) was also detected by QXRD. Chromite made up about 7 % (Figure 4.41).

From Table 4.16, the sum of mafic minerals made up about 43% of the sample. Secondary alteration minerals on the other hand made up 7.5% with talc (~3 %), and epidote (2.4 %) and Lizardite (1.2 %) making minor amounts.

Table 4. 16: QXRD results for Rustenburg, with the sum of mafic, sulphide and alterations mineral highlighted.

RUSTENBURG (WATERVAL)		
Lithology	Chemical Composition	%
Chromite	$(Fe, Mg)Cr_2O_4$	6.70
Enstatite*	$MgSiO_3$	24.69
Diopside*	$MgCaSi_2O_6$	2.79
Hornblende*	$Ca_2(Mg, Fe, Al)_5 (Al, Si)_8O_{22}(OH)_2$	6.80
Biotite*	$K(Mg, Fe)_3 (AlSi_3O_{10})(F,OH)_2$	2.50
Bytownite*	$[(Ca, Na)[Al(Al, Si)Si_2O_8]$	45.85
Sum: Primary Igneous		**89.33**
Pyrrhotite	$Fe_{1-x}S$ (x = 0 to 0.2)	1.13
Pentlandite	$(Fe, Ni)_9S_8$	0.91
Chalcopyrite	$CuFeS_2$	0.84
Pyrite	FeS_2	0.39
Sum: Sulphide		**3.27**
Talc*	$Mg_3Si_4O_{10}(OH)_2$	3.26
Lizardite*	$Ni_3(Si_2O_5)(OH)_4$	1.21
Calcite	$CaCO_3$	0.27
Epidote*	$\{Ca_2\}\{Al_2Fe^{3+}\}[O\|OH\|SiO_4\|Si_2O_7]$	2.41
Quartz	SiO_2	0.25
Sum: Alteration		**7.40**
*Carbonatable		89.51
Non carbonatable		10.49

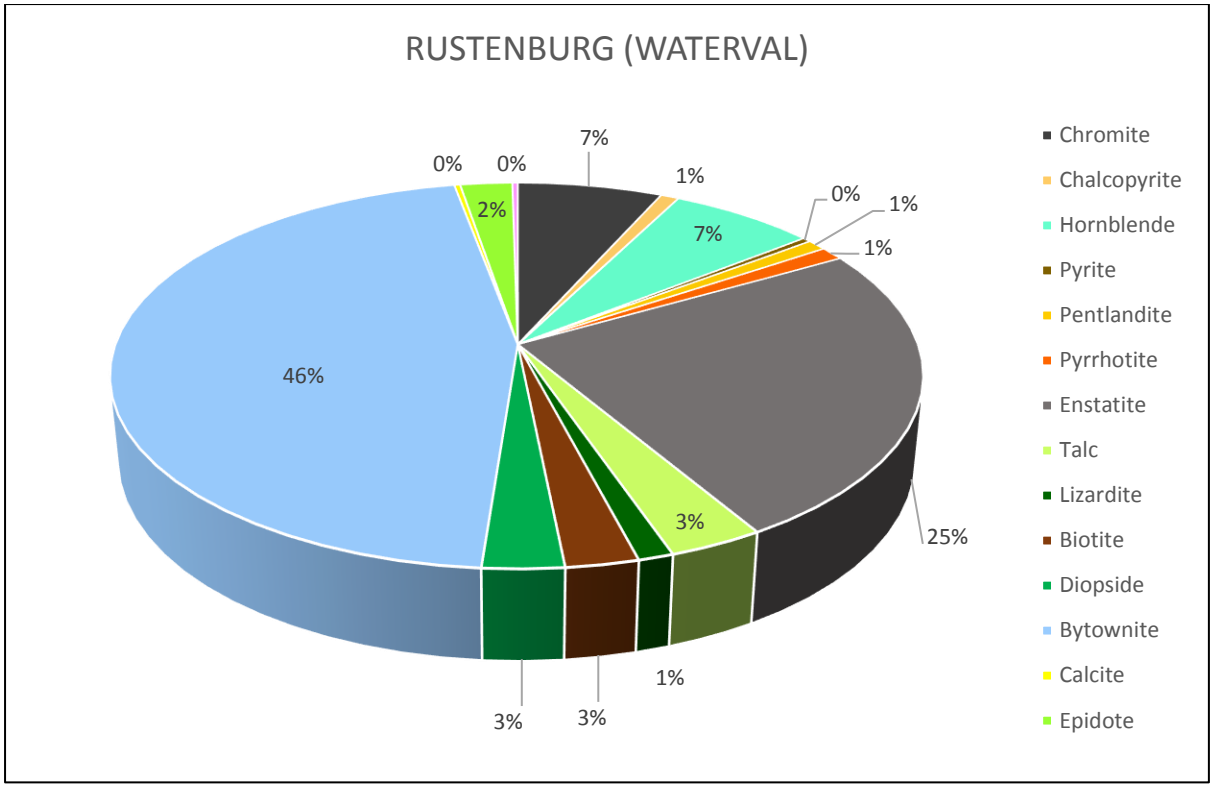

Figure 4. 41: QXRD data for WRT/101.

The -75/+53 µm size fraction was selected for QEMSCAN analysis. Like QXRD, results for QEMSCAN analysis detected plagioclase as the most abundant mineral. Plagioclase concentrations were as high as 39 %. Orthopyroxene (35 %) also recorded a fairly high amounts (Table 4.17). Chromite made up about 14% of the sample. The sum of secondary alteration minerals were less than 4.5% (Figure 4.42). BMS were less than 0.5 % (Table 4.17). The sum of carbonatable minerals amounted to about 84 %.

Table 4. 17: QEMSCAN results for Rustenburg (Waterval).

RUSTENBURG (WATERVAL)		
Lithology	Chemical Composition	%
Chromite	$(Fe, Mg)Cr_2O_4$	14.38
Orthopyroxene*	$Mg_2Si_2O_6$	34.86
Clinopyroxene*	CaMgSi2O6	2.68
Hornblende*	$Ca_2(Mg, Fe, Al)_5 (Al, Si)_8O_{22}(OH)_2$	1.65
Biotite*	$K(Mg, Fe)_3 (AlSi_3O_{10})(F,OH)_2$	0.88
Olivine*	(Mg, Fe)2SiO4	2.04
Plagioclase*	$(Na,Ca)(Si,Al)_4O_8$	38.68
Sum: Primary Igneous		**95.17**
Pyrrhotite	$Fe_{1-x}S$ (x = 0 to 0.2)	0.08
Pentlandite	$(Fe, Ni)_9S_8$	0.01
Chalcopyrite	$CuFeS_2$	0.03
Pyrite	FeS_2	0.34
Sum: Base Metal Sulphide		**0.46**
Talc*	$Mg_3Si_4O_{10}(OH)_2$	1.05
Serpentine*	$Mg_3(Si_2O_5)(OH)_5$	0.57
Chlorite*	$(Mg, Fe)_3(Si, Al)_4O_{10}(OH)_2 \cdot (Mg, Fe)_3(OH)_6$	0.09
Calcite	$CaCO_3$	0.12
Epidote*	$Ca_2Fe_{3+2.25}Al_{0.75}(SiO_4)_3(OH)$	1.69
Quartz	SiO_2	0.85
Sum: Secondary Alteration		**4.37**
Carbonatable		84.19
Non carbonatable		15.81

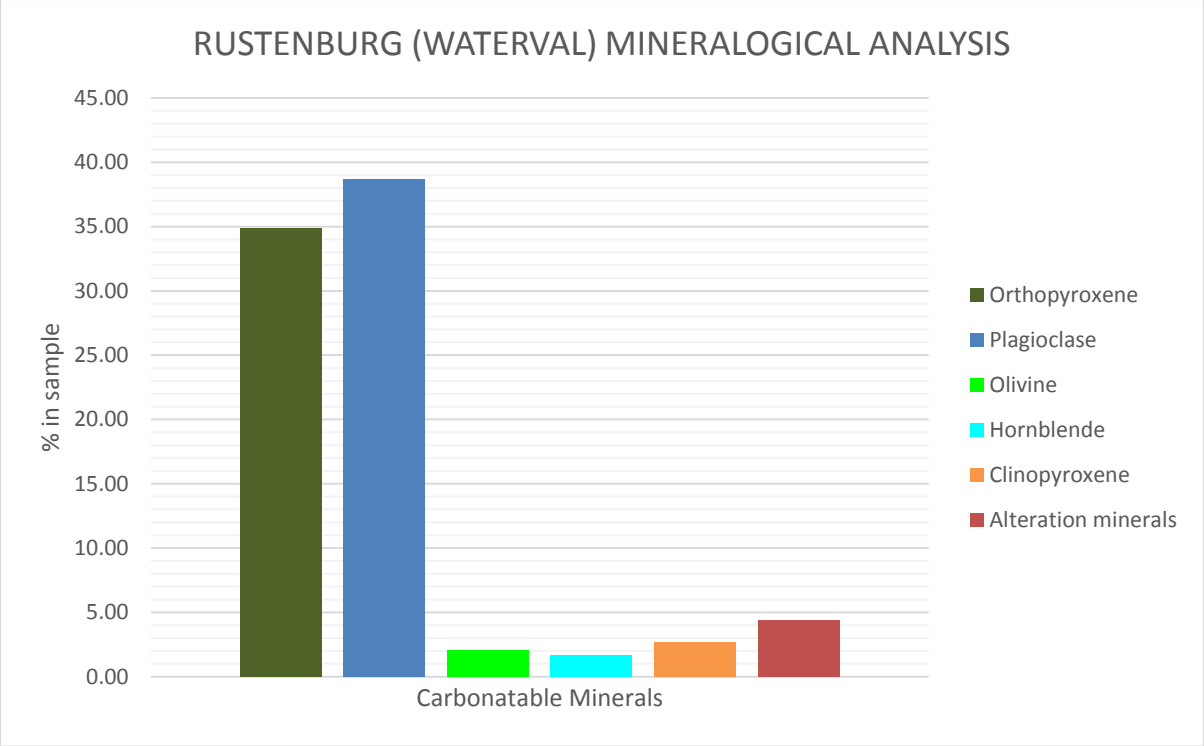

Figure 4. 42: QEMSCAN results for WRT/101.

About a 10% difference was observed between QXRD and QEMSCAN results for orthopyroxene. QXRD identified 24.69% and QEMSCAN 34.86%. Chromite was higher in QEMSCAN (14.38%) as compared to QXRD's 6.70%. QXRD reported about 45% plagioclase whereas QEMSCAN identified 36.68%. Hornblende and biotite were relatively high in QXRD than in QEMSCAN. The sum of base metal sulphides and alteration minerals were fairly high in QXRD than the values reported by QEMSCAN. In terms of the total carbonatable minerals, 89.51% was calculated for QXRD while QEMSCAN reported 84.19%.

4.2.5.3. XRF major oxide geochemistry

The major oxides have been displayed on a graph for each size fraction and presented in Figure 4.43. Evidently from the graph, SiO_2 was in extremely high concentration in all size fractions with an average of about 50 %. SiO_2 concentrations remain steady in finer fractions but slightly increase in fractions greater than 75 µm. Average concentrations for detected for both Al_2O_3 and CaO were 18 and 9% respectively.

However, both oxides followed the same trend as they maintained their masses in finer fractions and gently decreased in fractions greater than 75 µm. FeO (9 %) and Cr_2O_3 (4 %) were both steady in finer fractions but increased in fractions greater than

75 µm. The mass of MgO made up 15 % in most size fractions and only increased gently at in fractions above 106 µm (Figure 4.43).

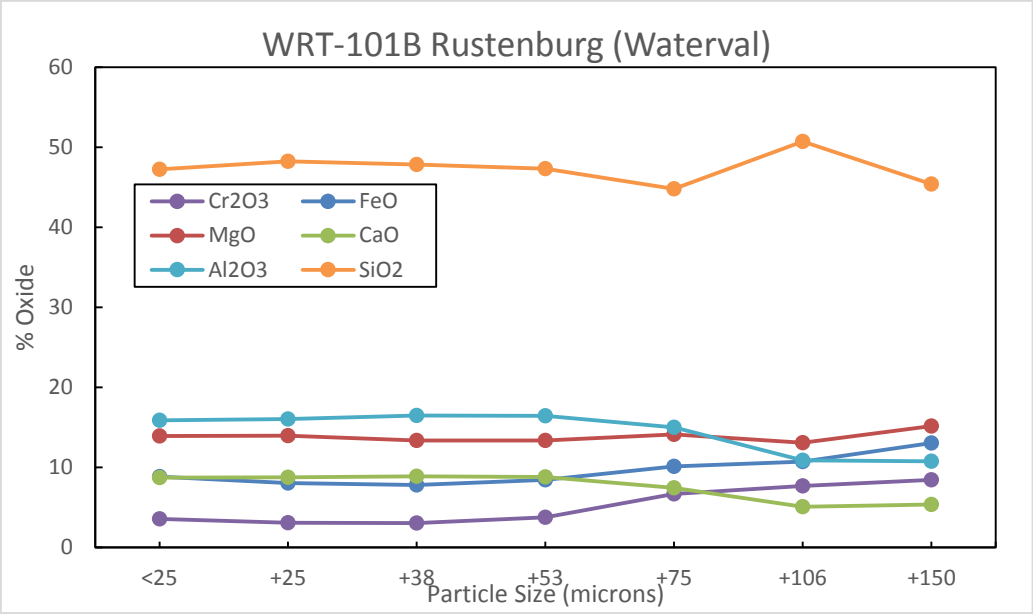

Figure 4. 43: Major oxide composition of size fractions in WRT/101.

The relationship between the measured and calculated bulk for the Rustenburg sample was determined. A very strong correlation was observed between the two bilk samples (Figure 4.44).

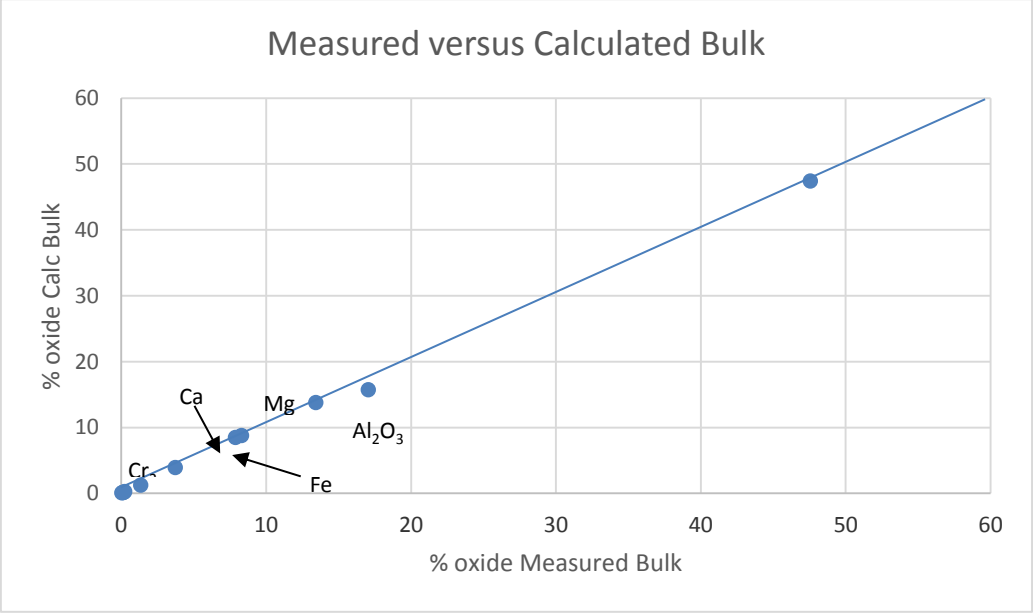

Figure 4. 44: Relationship between measured and calculated bulk for WRT/101.

4.3. Characterization of Nkomati nickel tailings

The two plant tails samples for MMZ and PCMZ from the Nkomati operations were examined for the purpose of this study. A total of six samples were chosen for sieving analysis. Sieving analysis and particle size measurement by Malvern was focused on the samples, NK-PCMZ/PT and NK-MMZ/PT. One sample was chosen for surface area analysis. This depended on results from the Malvern particle size analysis where the overall finest bulk sample further scrutinized for its specific surface area. Numerous mineralogical examinations were executed on the two plant tailings.

4.3.1. Particle size analysis

The notably fine nature of the Nkomati PCMZ plant tailings have been laid out in Table 4.18. With over 60 % of material reporting below 25 µm and less than 10 % identified above 106 µm, it was concluded that the Nkomati sample was distinctively fine in nature.

Table 4. 18:

	MMZ-PT A	MMZ-PT B	MMZ-PT C	MMZ-PT (avg)	PCMZ-PT A	PCMZ-PT B	PCMZ-PT C	PCMZ-PT (avg)
Sieve (µm)	wt%							
<25	40.89	37.26	41.10	39.75	69.71	66.34	65.84	67.30
25	8.64	8.54	8.71	8.63	7.45	8.65	10.67	8.93
38	11.59	13.79	11.75	12.38	7.39	9.50	7.54	8.14
53	12.86	13.06	11.94	12.62	5.16	5.38	5.27	5.27
75	12.33	12.59	12.51	12.47	5.44	5.68	5.57	5.56
106	9.17	9.39	9.34	9.30	4.84	4.45	5.11	4.80
150	4.53	5.37	4.65	4.85	0.00	0.00	0.00	0.00
TOTAL	100	100	100	100	100	100	100	100

As demonstrated in Figure 4.45, no crucial differences were noticed in the three screening tests. All tests followed the same trend and retained similar amounts in all size fractions.

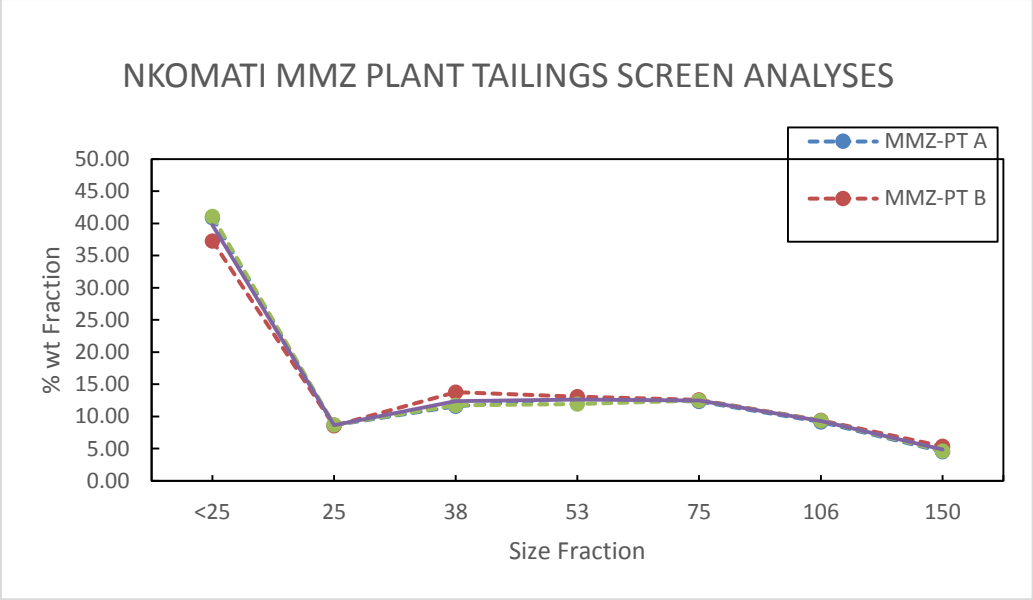

Figure 4. 45: NK-MMZ/PT plant tail screening results including the calculated average.

NK-MMZ/PT on average, had about 40 % of material reporting below 25 µm. The rest of the sample is fairly distributed across the other size fractions as shown in Table 4.18.

Tests A and C are similar throughout all size fractions. Test B on the other hand, slightly differs from test A and C. Results for test B, it was observed that the 38 µm fraction had more sample retained than in the other tests, but the lowest in material for the finest size fraction (Figure 4.46).

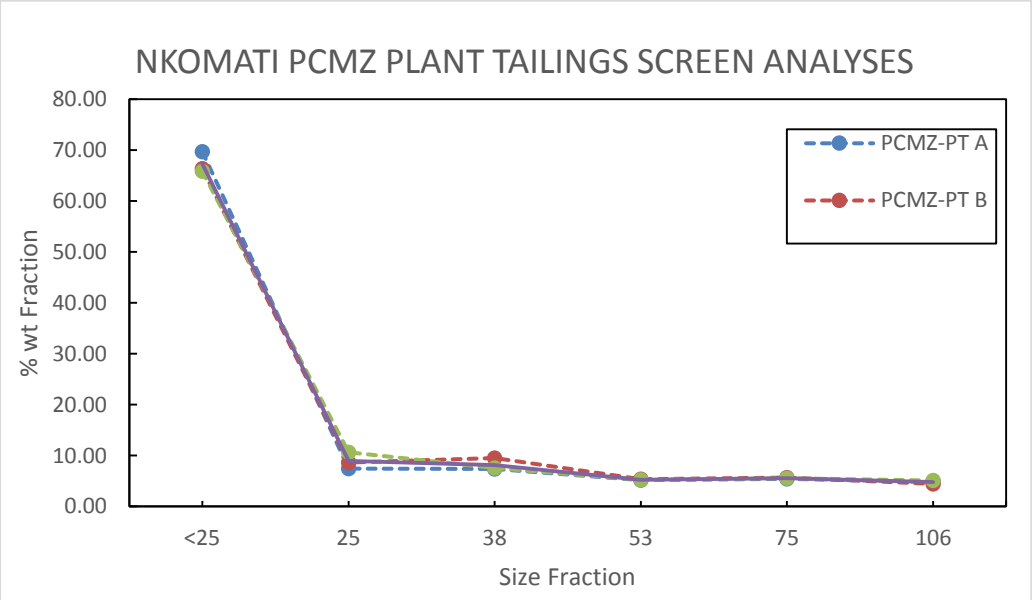

Figure 4. 46: NK-PCMZ/PT screening results including the calculated average.

From Figure 4.47, it was observed that NK-PCMZ/PT retained the highest amount of material, where close to 70 % was recorded in the finest size fraction. NK-MMZ/PT however retained a mass of 40 % within the same fraction. Both samples recorded equal amounts of material retained within the 25 µm size fraction.

A change was noticed with size fractions greater than 25 µm. NK-MMZ/PT amounts were higher than NK-PCMZ/PT for material greater than 25 µm. The similarity between the two samples was that they followed same pattern as they gradually reduced in mass at material got coarser (Figure 4.47).

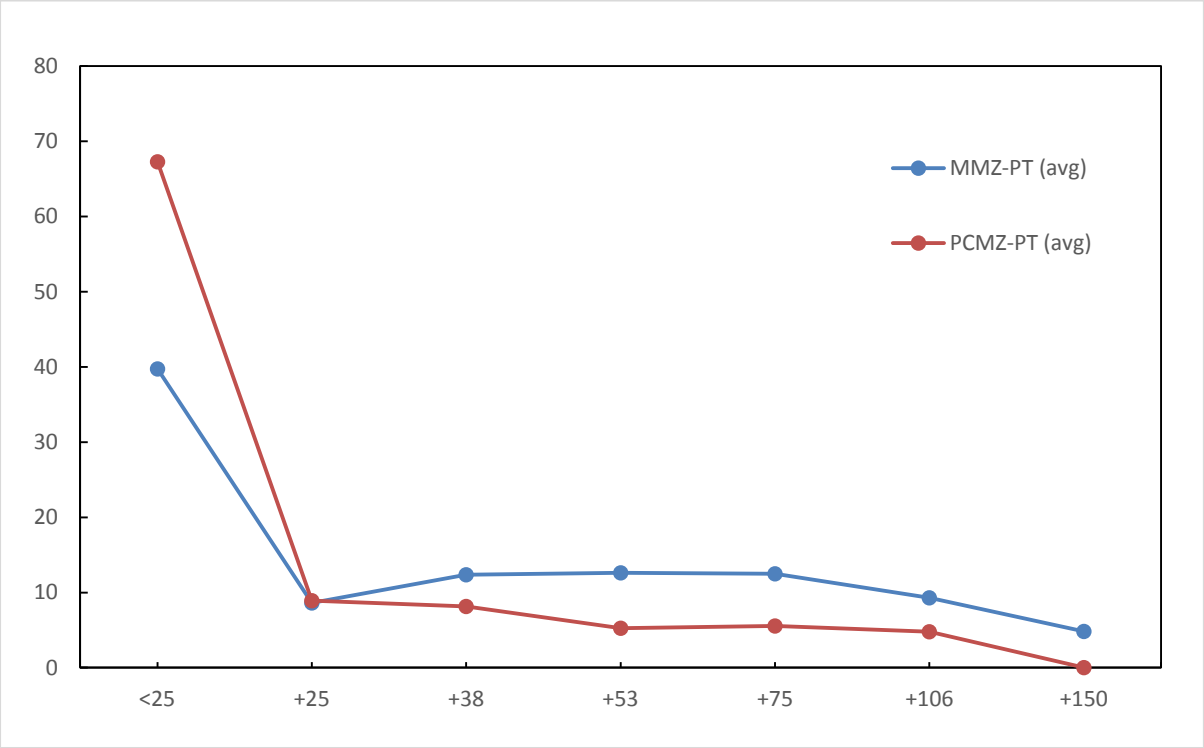

Figure 4. 47: A graph comparing the averages of the two Nkomati samples.

Cumulative values were derived from the averages of the replicates of the two Nkomati samples and plotted against the size fractions as shown in Fig. 4.48. This was used to determine any similarities in Malvern results. A full sieve analysis can be found in Appendix A1.6.

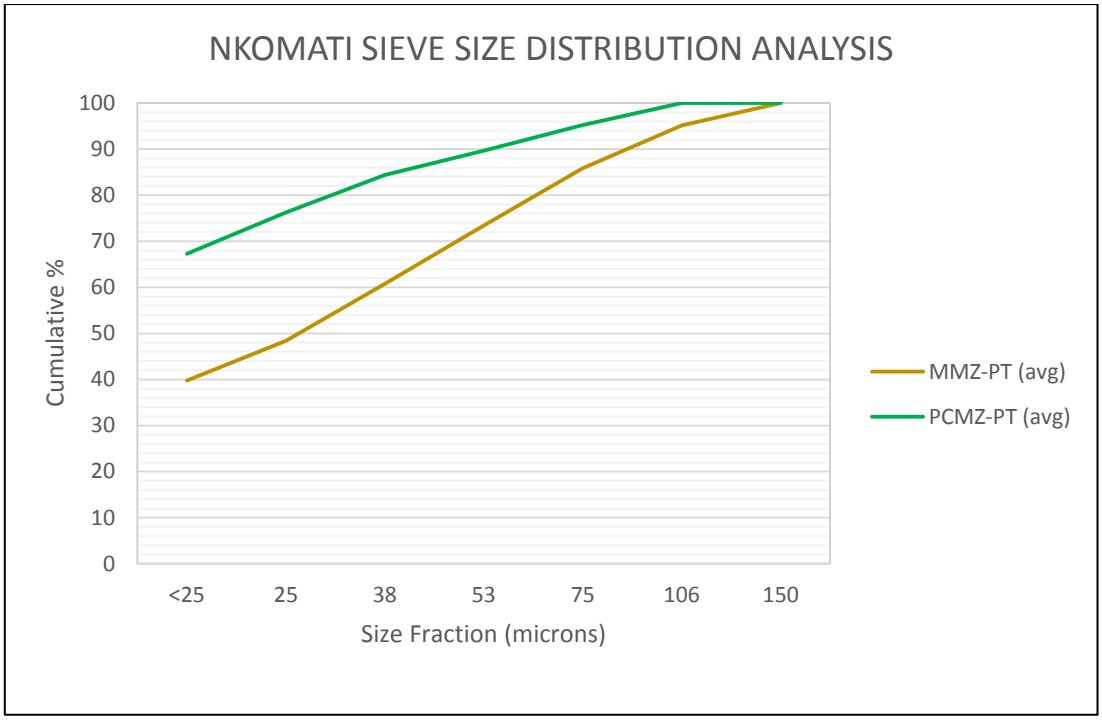

Figure 4. 48: Average sieving results plotted against cumulative percentage for Nkomati.

Malvern analysis was undertaken to obtain accurate particle size distribution curves for the Nkomati samples. The two main Nkomati plant tailings were examined (Figure 4.49). The finest in particle size was observed to be the NK-PCMZ/PT sample with its Dv(0.9) =130.443 µm as revealed in Table 4.19.

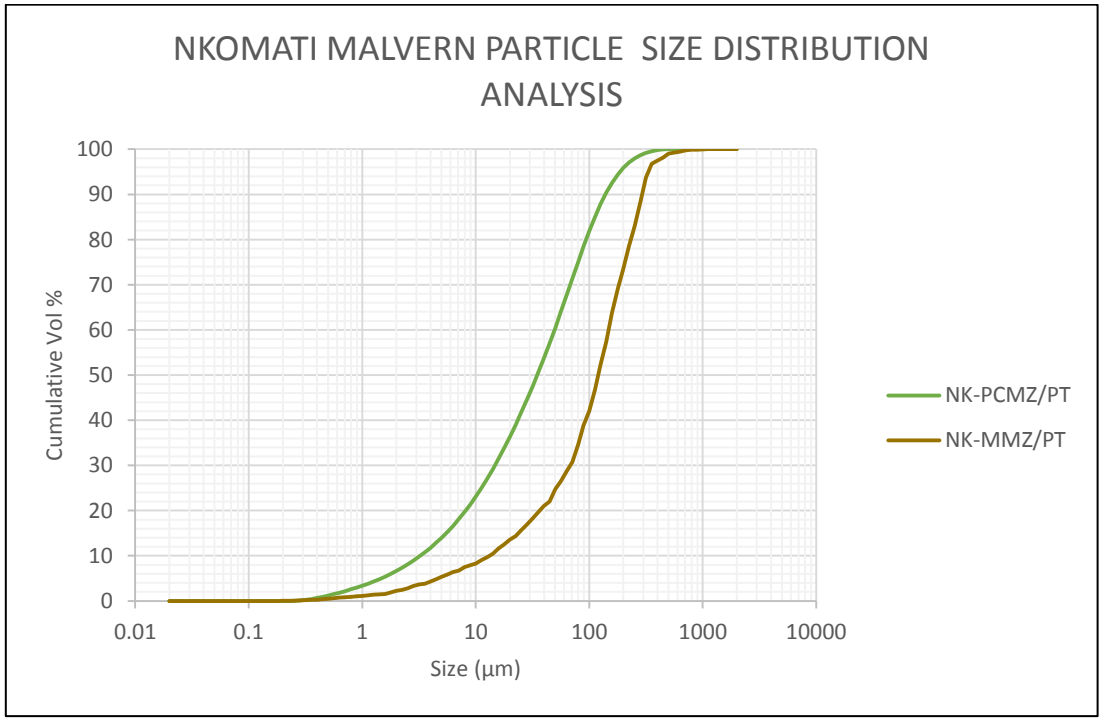

Figure 4. 49: Malvern size distribution curve results the two Nkomati samples.

Table 4. 19: Nkomati plant tailings Malvern data.

Tailings Sample	Dv (0.1)(µm)	Dv (0.5)(µm)	Dv(0.9)(µm)
NK-MMZ/PT	17.327	99.801	312.029
NK-PCMZ/PT	3.938	33.767	130.443

From Figure 4.49, as it was observed that the NK-PCMZ/PT sample was finer in particle size than NK-MMZ/PT, it was selected for BET analysis. Automatic results from the BET device indicated that the specific surface area was given as 5.888 m^2/g as displayed in Figure 4.50.

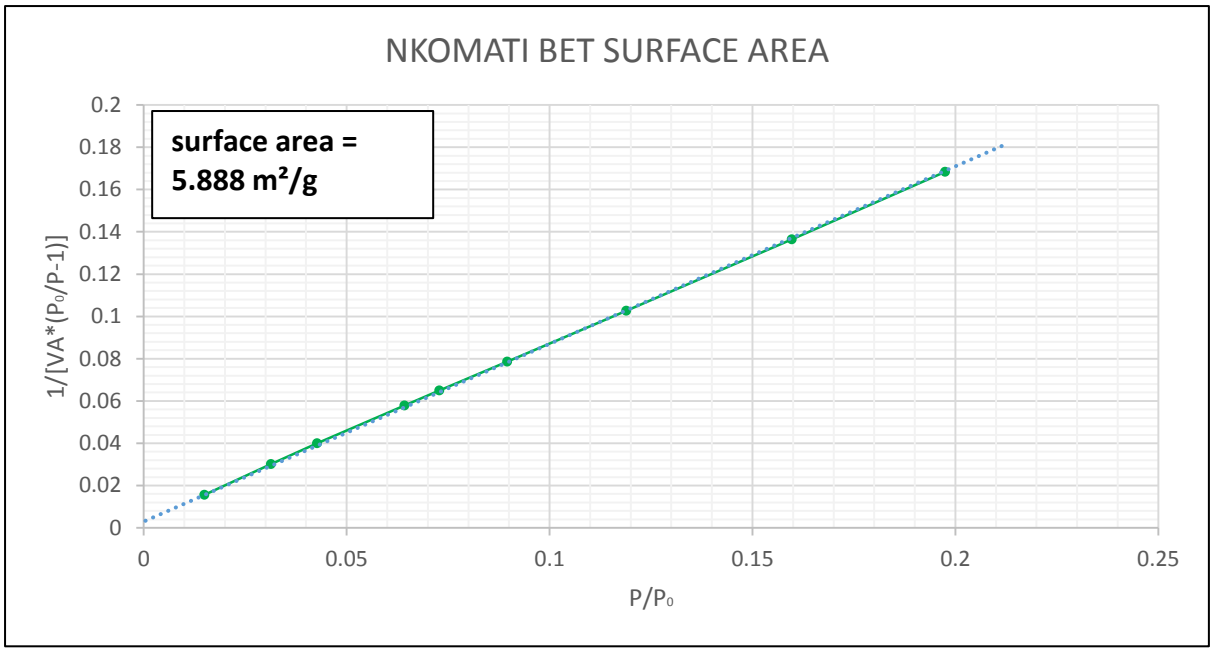

Figure 4. 50: Multi-point BET plot to determine the specific surface area for NK-PCMZ/PT.

4.3.2. QXRD and QEMSCAN mineralogy

Minerals species were investigated for both MMZ and PCMZ samples with the aid of QXRD. Table 4.20 and Figure 4.51 show QXRD results for bulk MMZ plant tailings sample (NK- MMZ/PT). Typically, enstatite, a member of the orthopyroxene group and diopside a clinopyroxene seems to dominate the MMZ sample with concentrations of 19 % and 20 % respectively. Lizardite, a member of the serpentine group was also identified in amounts of close to 15 %. An interesting observation from the results is the relatively high amount of talc (11 %), which is an alteration mineral (Figure 4.51).

A combination of all mafic material in the MMZ sample added up to about 68 %. A moderate amount base metal sulphides summed up to around 7.6 %. There was a

relatively volume of alteration minerals in the region of 24.5 % was detected by QXRD (Table 4.20).

Table 4. 20: QXRD results for Nkomati, with the sum of primary igneous, sulphide and alterations mineral highlighted.

	Chemical Composition	NK-MMZ/PT	NK-PCMZ/PT
Lithology		%	%
Chromite	$(Fe, Mg)Cr_2O_4$	9.45	17.06
Enstatite*	$MgSiO_3$	19.22	25.45
Hornblende*	$Ca_2(Mg, Fe, Al)_5 (Al, Si)_8O_{22}(OH)_2$	14.01	18.57
Biotite*	$K(Mg, Fe)_3 (AlSi_3O_{10})(F,OH)_2$	4.80	3.20
Diopside*	$MgCaSi_2O_6$	20.37	16.60
Sum: Primary Igneous		**67.85**	**80.88**
Chalcopyrite	$CuFeS_2$	1.03	0.99
Pentlandite	$(Fe, Ni)_9S_8$	1.74	0.28
Pyrrhotite	$Fe_{1-x}S$ (x = 0 to 0.2)	3.63	1.48
Pyrite	FeS_2	1.18	0.86
Sum: Sulphide		**7.58**	**3.61**
Talc*	$Mg_3Si_4O_{10}(OH)_2$	11.30	8.80
Lizardite*	$Ni_3(Si_2O_5)(OH)_4$	13.27	6.71
Sum: Alteration		**24.57**	**15.51**
*Carbonatable		82.96	79.33
Non Carbonatable		17.04	20.67

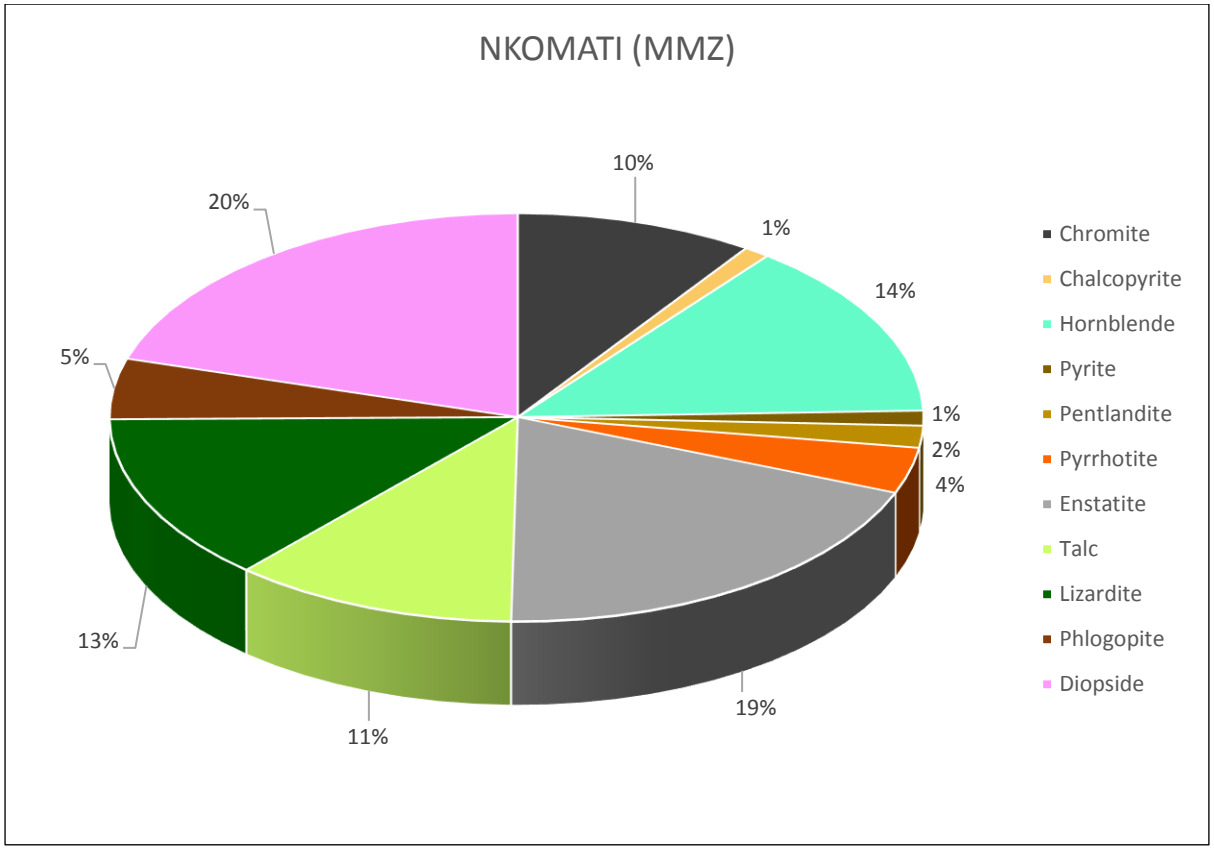

Figure 4. 51: QXRD results for Nkomati MMZ sample.

further proven by QXRD (NK-PCMZ/PT) results illustrated in Figure 4.52. Chromite was as high as 17 % compared the 10 % found in the MMZ sample in Figure 4.51. Very high amount, great than 15 % were reported for enstatite, diopside and hornblende in the PCMZ sample. The relatively high concentration in talc (9 % in PCMZ) as shown in Figure 4.52, appears to be a general characteristic of Nkomati samples.

The sum of base metal sulphide was reported to be in the region of 4 %. This amount was lower what was detected in the MMZ sample. From Table 4.20, a combined value of alteration minerals was estimated at 15.5 %, whereas the mineral group under mafic made up 81 % of the sample. The mafic category of the PCMZ sample was therefore higher than the MMZ.

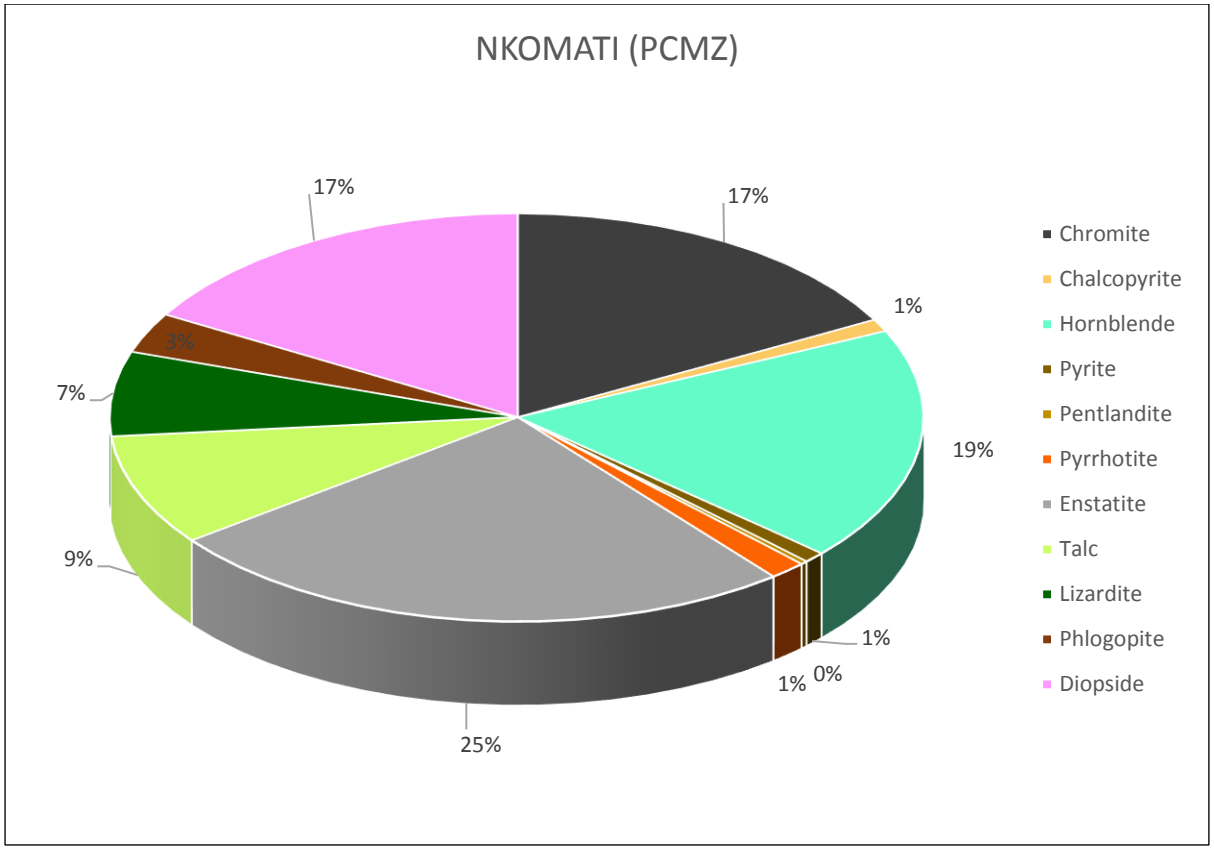

Figure 4. 52: QXRD results for Nkomati PCMZ sample.

Table 4. 21: QEMSCAN results for Nkomati PCMZ and MMZ samples.

Nkomati			
Lithology	Chemical Composition	NK-MMZ/PT(%)	NK-PCMZ/PT (%)
Chromite	$(Fe, Mg)Cr_2O_4$	3.72	14.36
Orthopyroxene*	$Mg_2Si_2O_6$	21.09	33.54
Clinopyroxene*	CaMgSi2O6	25.18	1.09
Hornblende*	$Ca_2(Mg, Fe, Al)_5 (Al, Si)_8O_{22}(OH)_2$	16.32	16.34
Biotite*	$K(Mg, Fe)_3 (AlSi_3O_{10})(F,OH)_2$	2.84	3.97
Olivine*	(Mg, Fe)2SiO4	3.52	0.92
Plagioclase*	$(Na,Ca)(Si,Al)_4O_8$	4.59	4.26
Sum: Primary Igneous		**77.26**	**74.48**
Pyrrhotite	$Fe_{1-x}S$ (x = 0 to 0.2)	5.02	1.76
Pentlandite	$(Fe, Ni)_9S_8$	0.15	0.53
Chalcopyrite	$CuFeS_2$	0.08	0.11
Pyrite	FeS_2	1.01	1.19
Sum: Base Metal Sulphide		**6.26**	**3.59**
Talc*	$Mg_3Si_4O_{10}(OH)_2$	0.27	1.13
Chlorite*	$(Mg, Fe)_3(Si, Al)_4O_{10}(OH)_2 \cdot (Mg, Fe)_3(OH)_6$	7.03	13.73
Calcite	$CaCO_3$	0.73	1.23
Serpentine*	$Mg_3(Si_2O_5)(OH)_5$	5.22	5.04
Epidote*	$Ca_2Fe_{3+2.25}Al_{0.75}(SiO_4)_3(OH)$	1.73	0.25
Quartz	SiO_2	1.50	0.55
Sum: Secondary Alteration		**16.48**	**21.93**
*Carbonatable		87.79	80.27
Non carbonatable		12.21	19.73

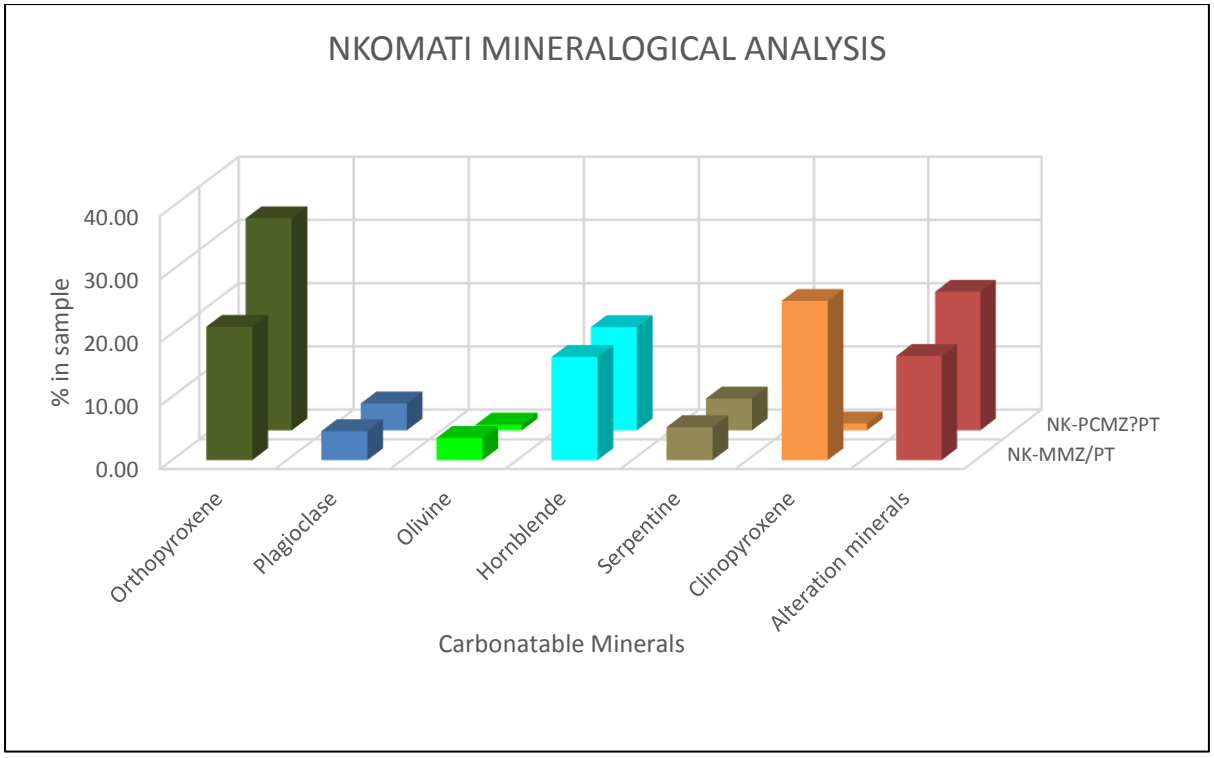

Figure 4. 53: Nkomati mineralogical analysis determined by QEMSCAN.

QEMSCAN detected more mineral species shown in Table 4.21 and Figure 4.53. The two plant tailings results were compared. Similarities in levels for plagioclase, serpentine and hornblende were noted (Figure 4.53). Chromite is predictably higher in the PCMZ (~10 %) than MMZ (Table 4.21). Moreover alteration mineral content in the PCMZ was rather higher than MMZ mainly due to the chlorite. Orthopyroxene was fairly high in both samples, especially in the PCMZ, which reported about 30 %.

Olivine was detected in the MMZ sample, with the PCMZ showing trace amounts. One crucial different noticed was that of clinopyroxene. Amounts of clinopyroxene were higher than 25 % in MMZ but lower than 5 % in the PCMZ sample (Figure 4.53).

Less than 10 % of base metal sulphides were reported for both MMZ and PCMZ. The alteration mineral content was relative high in both samples but the value detected in the PCMZ sample (22 %) is the highest encountered in the study. Fairly similar values in the primary igneous categories were detected and presented in table 4.21

Chromite is estimated higher in QXRD as compared to QEMSCAN. However, NK-PCMZ/PT contains more chromite than NK-MMZ/PT from both QXRD and QEMSCAN results (Table 4.20 and 4.21). Alteration minerals such as lizardite and talc were also estimated higher in QXRD than in QEMSCAN for both sets of Nkomati samples (MMZ

and PCMZ). The sum of carbonatable minerals were higher in NK-MMZ/PT than in sample NK-PCMZ/PT based on calculations from both QXRD and QEMSCAN analysis (Table 4.20 and 4.21). Feldspar was interestingly absence during QXRD analysis but present in QEMSCAN results for both Nkomati samples. This discrepancy could possibly have been as a result of the different sample specifications used in the respective analytical techniques. Using a bulk fraction for QXRD produced broad results whereas the size-specific QEMSCAN analysis produced considerably precise mineralogical estimates.

4.3.3. XRF major oxide geochemistry

SiO_2 values generally did not exceed 50 %. The finest size fraction had about 47 % SiO_2, gradually increasing and remained steady at 50 % in fractions greater than 75 µm. Results from XRF analysis detected an average amount of 20 % in all size fractions for MgO. Observations from Figure 4.54 also confirmed that FeO values were as high as 14 % in the smaller size groupings but reduced to as low as 8 % in the coarse 150 µm fraction. CaO on the other hand was low in all size fractions. On the average CaO values were recorded as approximately 10 % (Figure 4.54).

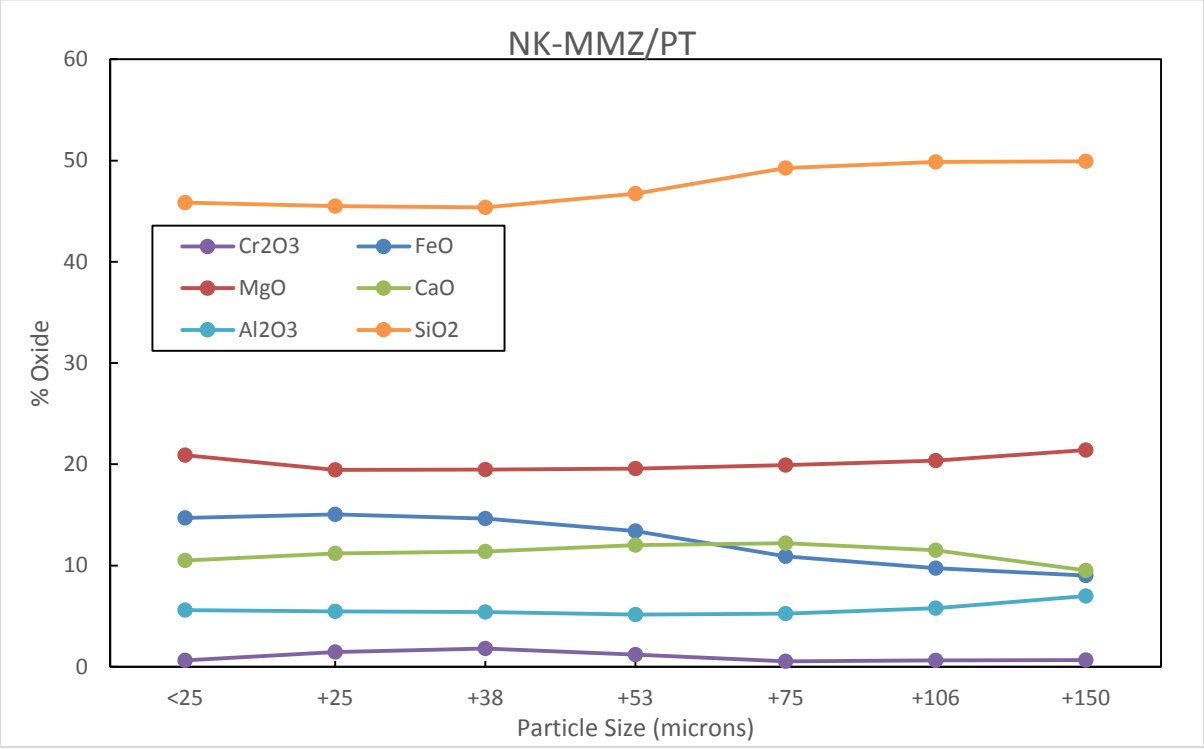

Figure 4. 54: Major oxide composition of size fractions in NK-MMZ/PT.

As displayed in Figure 4.55, SiO_2 is slightly higher in the larger fractions. The MgO values for NK-PCMZ/PT with concentrations ranging between 20 % and close to 30 % in coarser fractions (Figure 4.55). FeO concentrations decrease in coarser fractions to as low as 7 % as confirmed by QEMSCAN results in Figure 4.53.

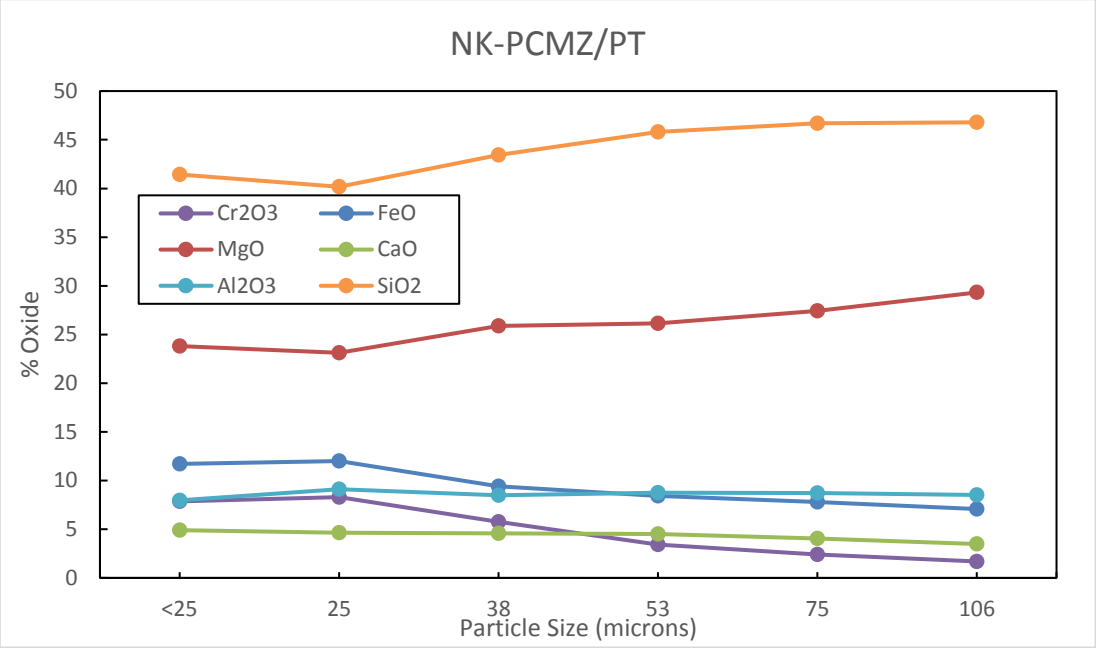

Figure 4. 55: Major oxide composition of size fractions in NK-PCMZ/PT.

A strong correlation was observed between the measured and calculated bulks for both the MMZ and PCMZ sample (Figure 4.56).

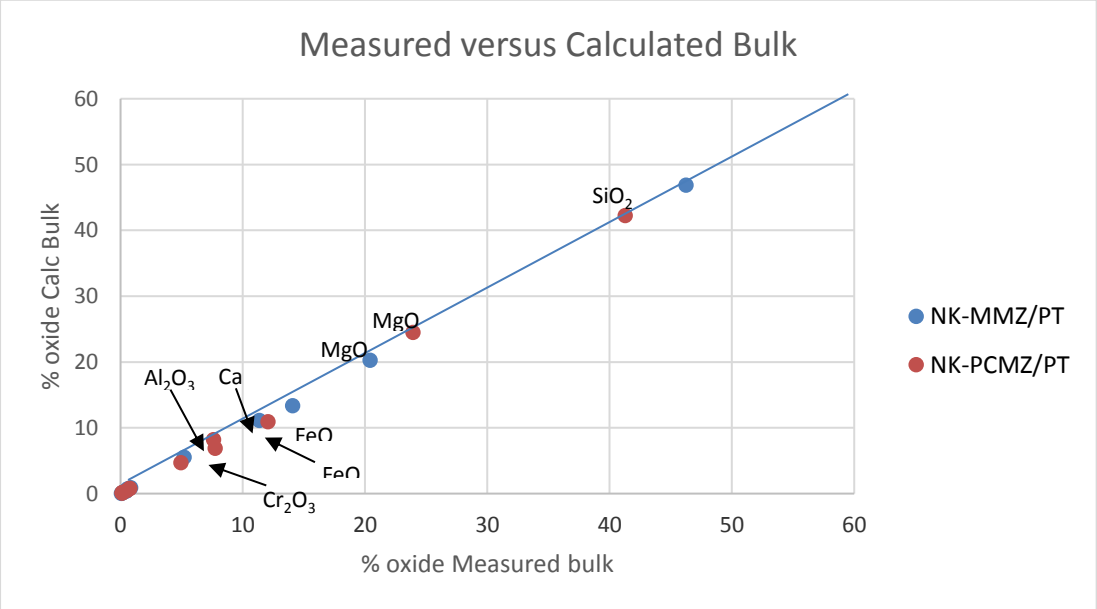

Figure 4. 56: Relationship between the measured and calculated bulk for both Nkomati plant tail samples.

4.4. Characterization of O'okiep tailings

There were two sample (OKP-1 and OKP-2) from O'okiep analysed for particle size, surface area and mineral species.

4.4.1. Particle size analysis

Sample OKP-1 is generally coarse as indicated by results provided in Table 4.22. Observations for the screening tests brought to light the coarse nature of OKP-1 as compared to OKP-2. From Table 4.22, more than 50 % of material were reported in size fractions greater than 75 µm. The finer size fractions retained lesser material.

Table 4. 22: As demonstrated in Figure 4.57, test B looked to have retained more sample than tests A and C for fractions 38, 53 and 75 µm. Tests A and C produced fairly similar results.

	OKP-1A	OKP-1B	OKP-1C	OKP-1 (avg)	OKP-2A	OKP-2B	OKP-2C	OKP-2 (avg)
Sieve (µm)	wt%							
<25	1.55	0.68	3.14	1.79	3.08	1.04	2.86	2.33
25	4.15	1.92	5.57	3.88	5.59	3.73	4.85	4.73
38	9.75	11.56	10.22	10.51	10.29	11.59	9.94	10.61
53	15.55	17.38	15.58	16.17	7.02	7.72	7.85	7.53
75	23.91	25.47	22.50	23.96	20.07	21.78	21.13	20.99
106	15.72	14.89	14.47	15.02	28.69	28.23	28.43	28.45
150	29.37	28.11	28.53	28.67	25.25	25.90	24.94	25.36
TOTAL	100	100	100	100	100	100	100	100

As demonstrated in Figure 4.57, test B looked to have retained more sample than tests A and C for fractions 38, 53 and 75 µm. Tests A and C produced fairly similar results.

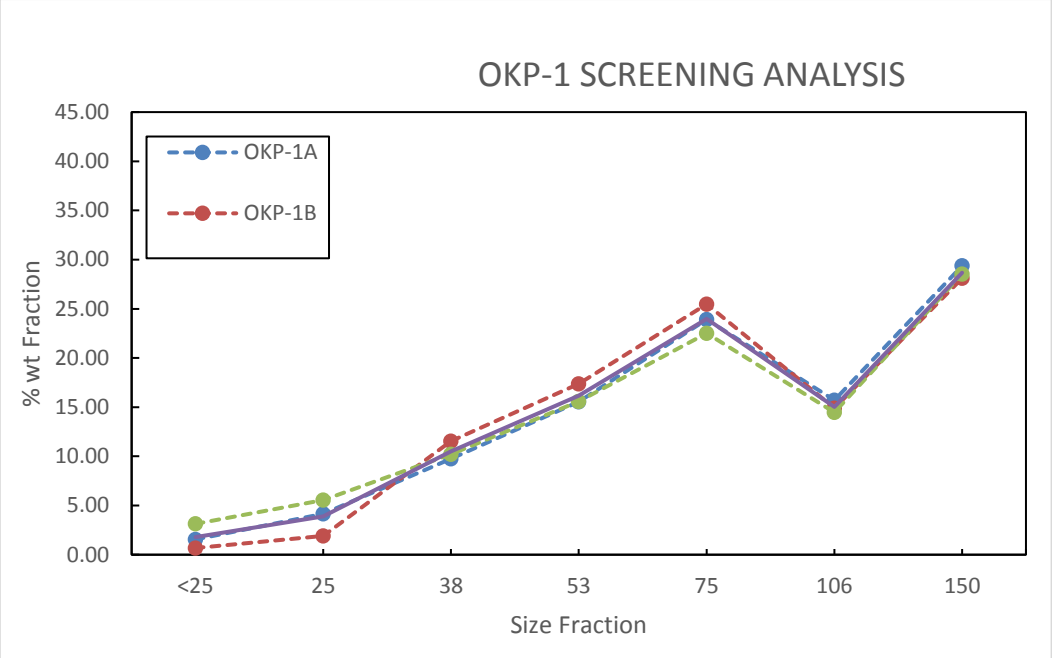

Figure 4. 57: O'okiep (OKP-1) screening test results.

OKP-2 was similar to OKP-1 in having the majority of material retained in the larger size fractions (Table 4.22). Over 60 % material was identified within size fractions greater than 75 µm.

There were no significant variation in the three test results and this has been demonstrated in Figure 4.58.

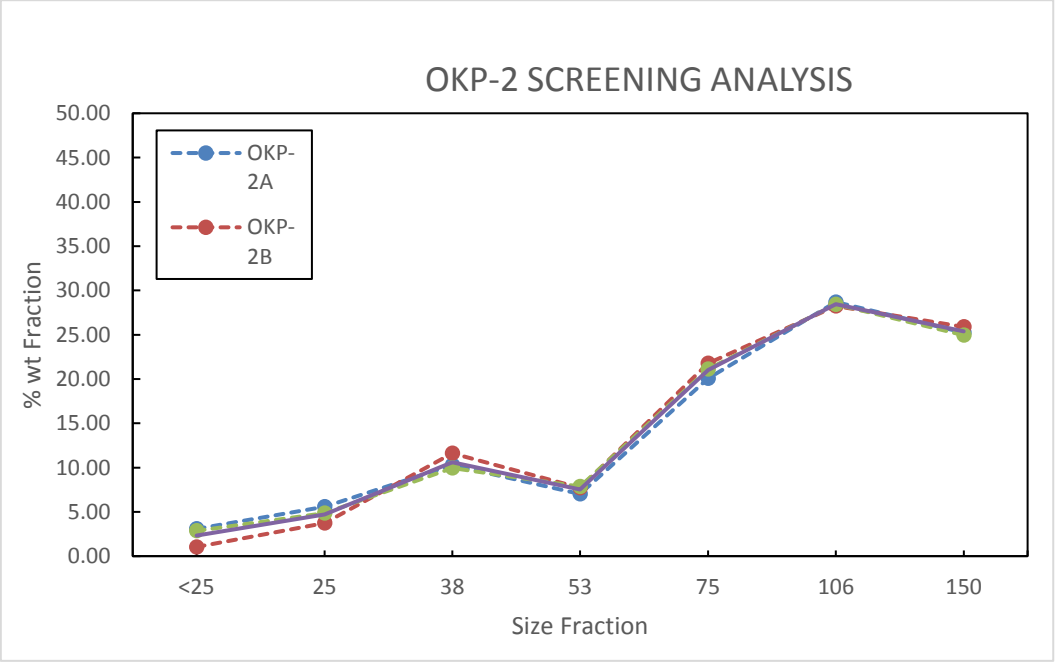

Figure 4. 58: O'okiep (OKP-2) screening test results.

Average values for OKP-1 and OKP-2 were compared and presented in Figure 4.59. Both samples retained similar amounts in fractions lesser than 38 µm. A high amount of OKP-1 material was retained in fractions between 38 and 75 µm and subsequently lower in fractions larger than 75 µm (Figure 4.59).

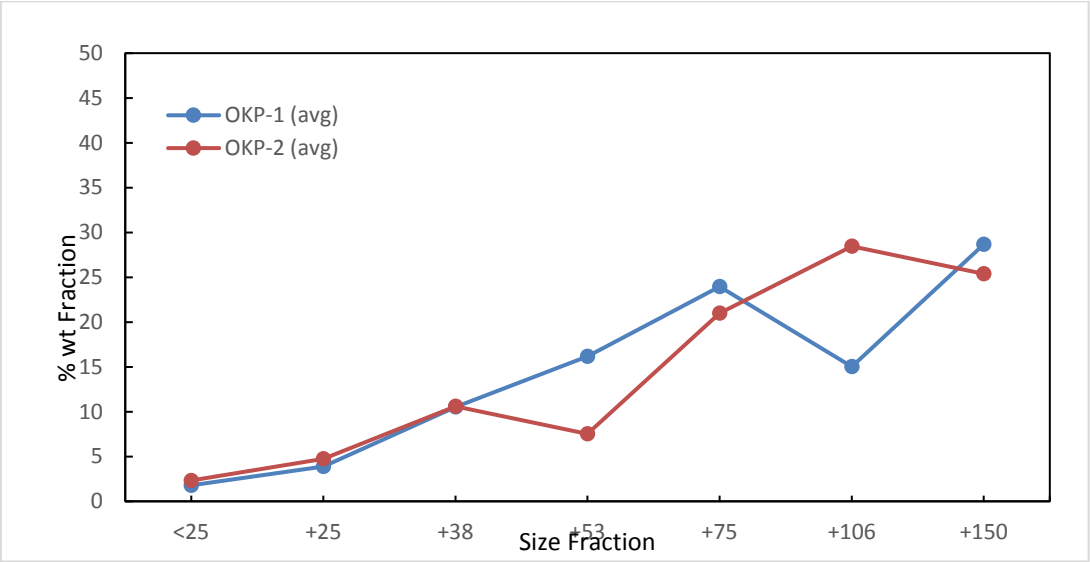

Figure 4. 59: A graph comparing the averages of the two O'okiep samples.

Cumulative values were derived from the averages of the replicates of O'okiep samples and plotted against the size fractions as shown in Fig. 4.60. This was used to determine any similarities in Malvern results. A full sieve analysis can be found in Appendix A1.7.

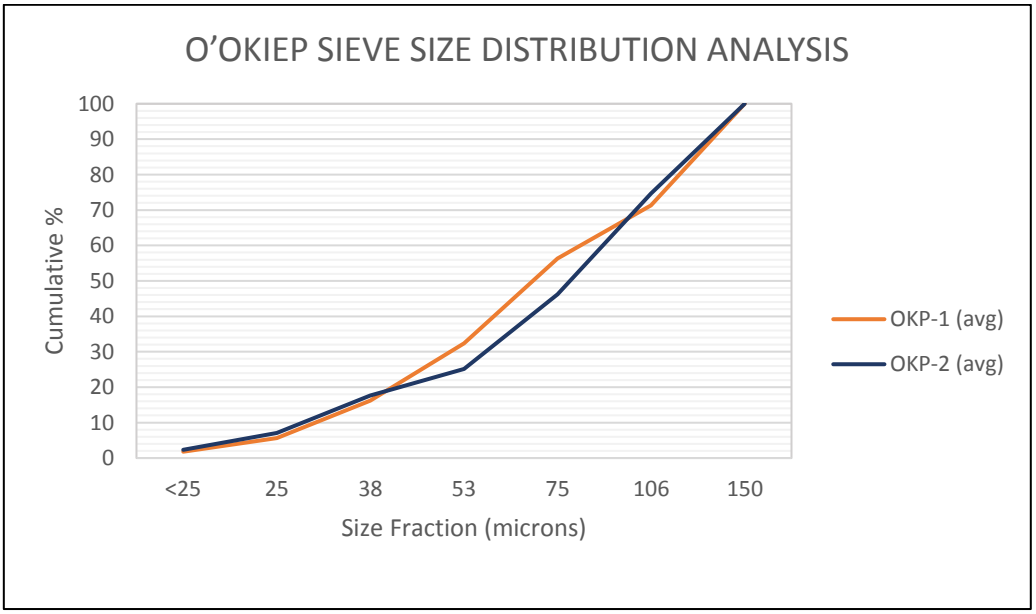

Figure 4. 60: Average sieving results plotted against cumulative percentage for O'okiep.

Malvern was used to determine the particle size distribution for both OKP-1 (grey) and OKP-2 (dark blue) as exhibited in Figure 4.61. OKP-2 was considered to the finest particles [Dv (0.9) = 214.693 µm] while OKP-2 was coarser [Dv (0.9) = 396.213 µm) as shown in Table 4.23.

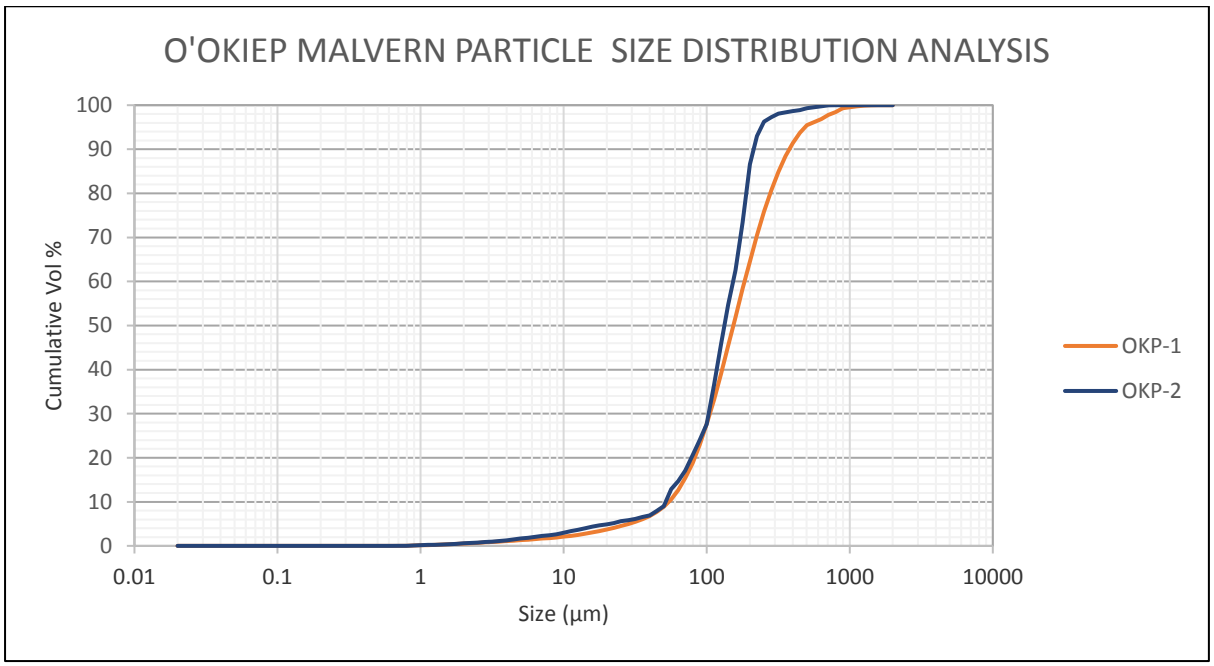

Figure 4. 61: Malvern particle size distribution analysis for O'okiep.

Table 4. 23: Particle size distribution analysis indicating average particle size for O'okiep samples at percentiles 10, 50 and 90.

Tailings Sample	Dv (0.1)(µm)	Dv (0.5)(µm)	Dv(0.9)(µm)
OKP-1	59.713	173.394	396.213
OKP-2	53.398	152.001	214.693

The OKP-2 sample was selected for BET analysis as it was considered to be finer in particle size (Figure 4.62). The sample OKP-2 had a specific surface area of 1.596 m^2/g as displayed in Figure 4.62.

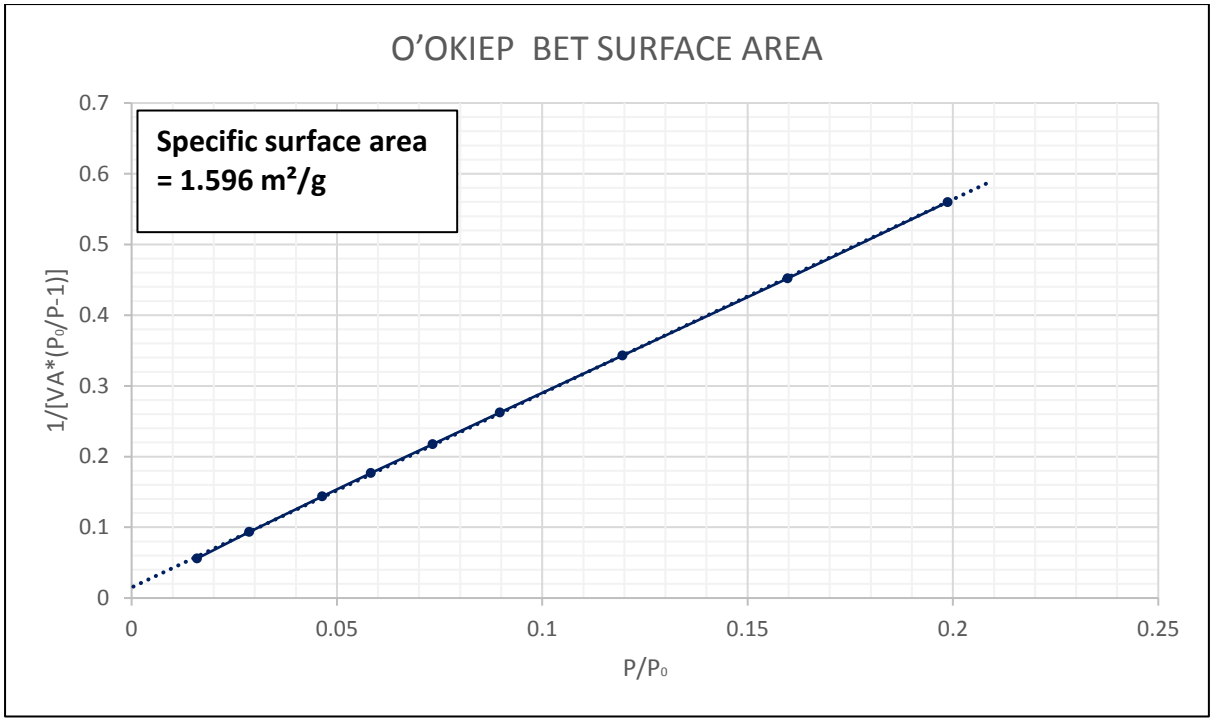

Figure 4. 62: Multi-point BET plot used to determine the specific surface area for O'okiep (OKP-2).

4.4.2. QXRD and QEMSCAN mineralogy

Labradorite, a mineral of the plagioclase feldspar group, made up 50 % of the OKP-2 sample. Quartz was also present and made up 15 %. Other minerals included hypersthene (9%), hornblende (2 %), magnetite (5 %), talc (4 %) and chlorite (5 %) as presented in Figure 4.63.

As presented in Table 4.24, the sum of mafic and alterations were fairly equal with very little significance between them. Mafic minerals made up 23 %, while alteration minerals amounted to 25 %. The base metal sulphide category was as low as 2.4 %.

Table 4. 24: QXRD results for O'okiep (OKP-2), with the sum of mafic, sulphide and alterations mineral highlighted.

O'OKIEP		
Lithology	Chemical Composition	%
Magnetite	$Fe^{2+}Fe^{3+}{}_2O_4$	5.93
Hornblende*	$Ca_2(Mg, Fe, Al)_5 (Al, Si)_8O_{22}(OH)_2$	2.28
Hypersthene*	$(Mg,Fe)SiO_3$	9.13
Biotite*	$K(Mg, Fe)_3 (AlSi_3O_{10})(F,OH)_2$	5.98
Labradiorite*	$(Ca,Na)(Al,Si)_4O_8$	49.75
Sum: Primary Igneous		**73.07**
Chalcopyrite	$CuFeS_2$	1.96
Pyrite	FeS_2	0.39
Sum: Sulphide		**2.35**
Talc*	$Mg_3Si_4O_{10}(OH)_2$	3.88
Lizardite*	$Ni_3(Si_2O_5)(OH)_4$	0.53
Chlorite*	$(Mg, Fe)_3(Si, Al)_4O_{10}(OH)_2 \cdot (Mg, Fe)_3(OH)_6$	5.42
Epidote*	$\{Ca_2\}\{Al_2Fe^{3+}\}[O\|OH\|SiO_4\|Si_2O_7]$	0.00
Quartz	SiO_2	15.06
Sum: Alteration		**24.89**
*Carbonatable		76.97
Non carbonatable		23.03

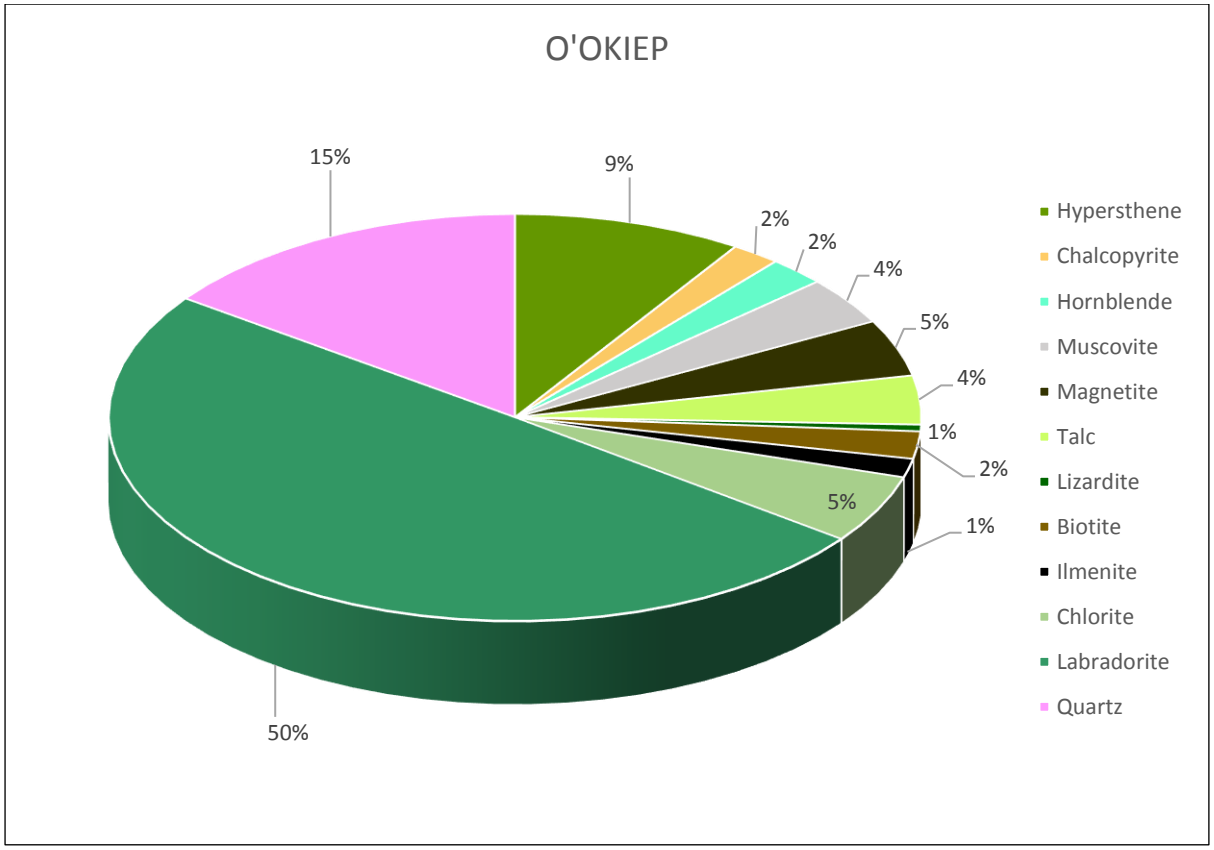

Figure 4. 63: O'okiep (OKP-2) QXRD results.

QEMSCAN was used to examine mineralogy in both samples OKP-1 and OKP-2. Results presented in Table 4.25 and Figure 4.64, shows that plagioclase is the most dominant in both samples, with about 45 % recorded in OKP-1 and 39 % in OKP-2. Quartz was also detected by QEMSCAN and was as low as 8 % in OKP-1 and more than 30 % in OKP-2.

Orthopyroxene (enstatite and hypersthene) was observed to have made up about 20 % in OKP-1 and nearly 10 % in OKP-2 (Figure 4.64). A simple calculation for the total carbonatable minerals was determined for both samples. It was discovered that OKP-1 had about 86.5 % and was higher in carbonatable minerals than OKP-2, which totalled 53.5 %.

As presented in Table 4.25, the sum of alteration minerals between OKP-1 and OKP-2 vastly differed. QEMSCAN detected 13 % of alteration minerals OKP-1 and 37 % for OKP-2. Nearly 83 % of mafic minerals was detected in OKP-1 and was in high amounts compared to OKP-2's 62 %. Base metal sulphides were traditionally lower compared to the other mineral groupings. OKP-1 however had about 4 % base metal sulphide with bornite being the dominant mineral with a concentration of about 2 %.

Quartz had to be included in the O'okiep alteration section for consistency with the other mining operations. The presence of quartz in the O'okiep tailings has a different status than all PGE mine tailings as the orebody may be noritic but the run of mine could contain granites, gneisses and metasediments.

Table 4. 25: QEMSCAN results for O'okiep tailings samples.

O'OKIEP			
Lithology	Chemical Composition	OKP-1	OKP-2
Chromite	$(Fe, Mg)Cr_2O_4$	0.37	0.21
Orthopyroxene	$Mg_2Si_2O_6$	23.91	10.13
Clinopyroxene	CaMgSi2O6	0.65	0.11
Hornblende	$Ca_2(Mg, Fe, Al)_5 (Al, Si)_8O_{22}(OH)_2$	3.80	0.53
Biotite	$K(Mg, Fe)_3 (AlSi_3O_{10})(F,OH)_2$	5.11	8.43
Magnetite	$Fe^{2+}Fe^{3+}{}_2O_4$	4.61	4.49
Plagioclase	$(Na,Ca)(Si,Al)_4O_8$	44.20	38.45
Sum: Primary Igneous		**82.65**	**62.35**
Pyrrhotite	$Fe_{1-x}S$ (x = 0 to 0.2)	0.18	0.01
Pentlandite	$(Fe, Ni)_9S_8$	0.11	0.01
Chalcopyrite	$CuFeS_2$	1.26	0.06
Pyrite	FeS_2	0.33	0
Bornite	Cu_5FeS_4	2.13	0.19
Chalcocite	Cu_2S	0.08	0
Covellite	CuS	0.33	0
Sum: Base Metal Sulphide		**4.42**	**0.27**
Talc	$Mg_3Si_4O_{10}(OH)_2$	0.47	0.16
Chlorite	$(Mg, Fe)_3(Si, Al)_4O_{10}(OH)_2 \cdot (Mg, Fe)_3(OH)_6$	2.13	2.24
Calcite	$CaCO_3$	0.32	0.57
Epidote	$Ca_2Fe_{3+2.25}Al_{0.75}(SiO_4)_3(OH)$	1.69	1.31
Quartz	SiO_2	8.32	33.1
Sum: Secondary Alteration		**12.93**	**37.38**
Carbonatable		86.49	53.50
Non carbonatable		21.83	46.50

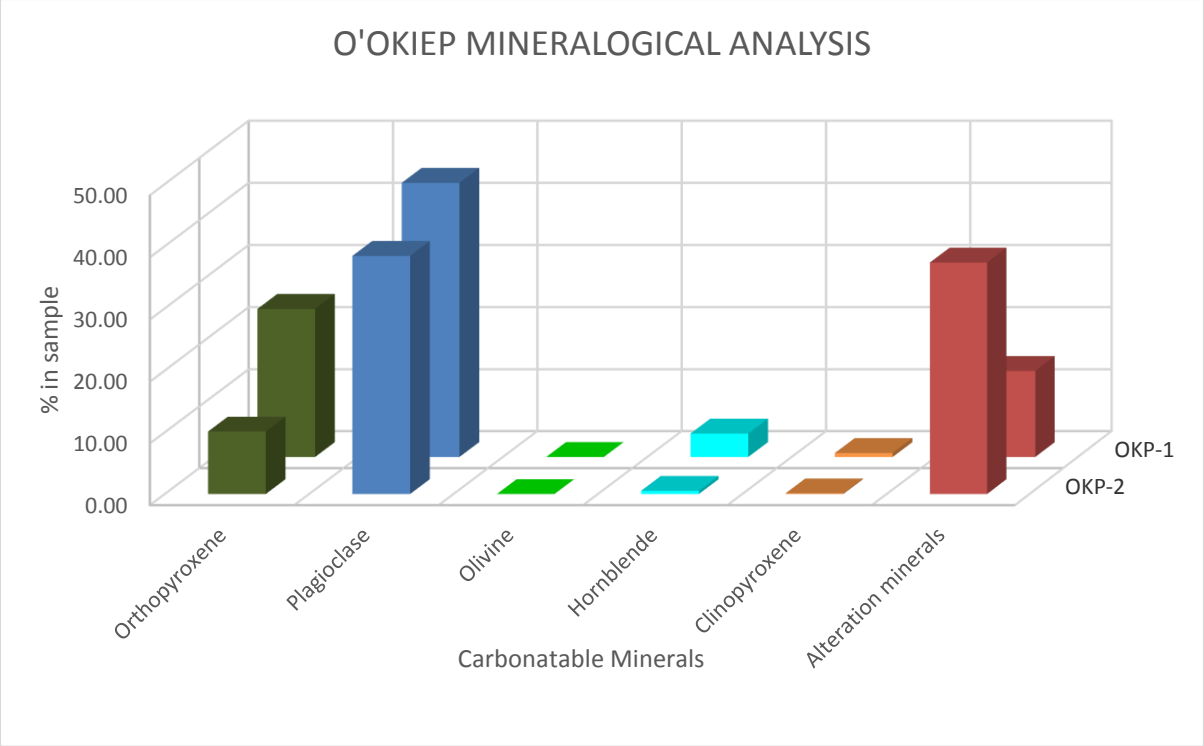

Figure 4. 64: QEMSCAN results for OKP-1 and OKP-2.

4.4.3. XRF major oxide geochemistry

OKP-1 results obtained from XRF analysis confirmed that SiO_2 values were below 50 % in size fractions less than 53 µm and gradually increased in coarser fractions but still remained below 60 % in the coarsest size fraction. FeO levels on average were as high as 25 % in smaller size fractions and gradually reduced as size particles got coarser, where about 10 % was recorded in the 150 µm size fraction (Figure 4.65).

Both CaO and MgO were relatively low in OKP-1. CaO (5 %) values were steady throughout the size groupings. MgO values were below 5 % (Figure 4.65).

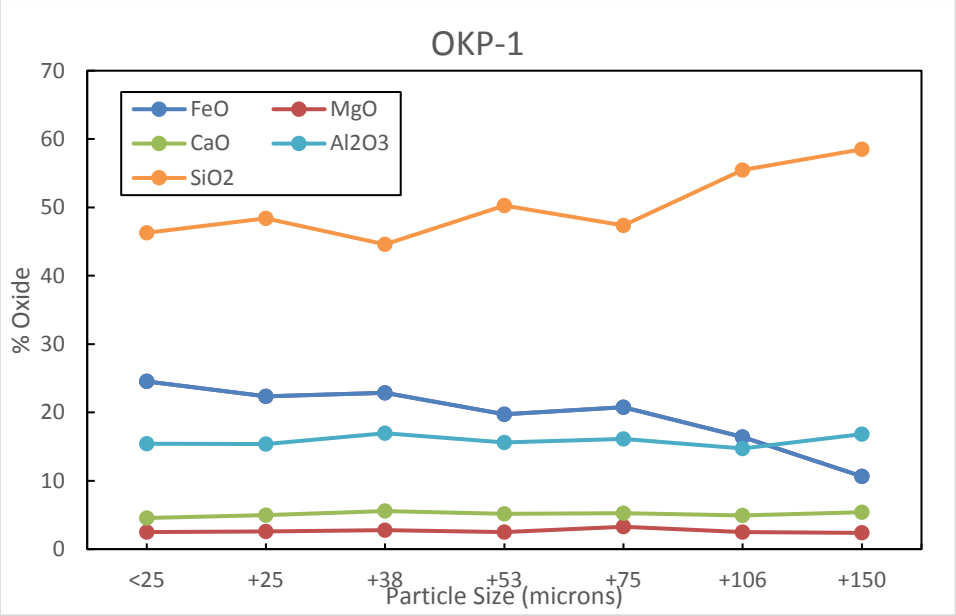

Figure 4. 65: Major oxide composition of size fractions in OKP-1.

XRF analysis results for OKP-2 were quite different from sample OKP-1 shown in Figure 4.59. The SiO_2 concentration in OKP-2 was higher than OKP-2. About 60 % was recorded in finer size fractions and gently increased in coarser fraction where a value of 70 % was reported for the 150 µm size fraction. FeO values were as high as nearly 15 % in the smallest fraction (<25 µm) but gradually decreased as the sample coarsened to as low as 4 % in the 150 µm. MgO and CaO amounts were very low at about 2 % (Figure 4.66).

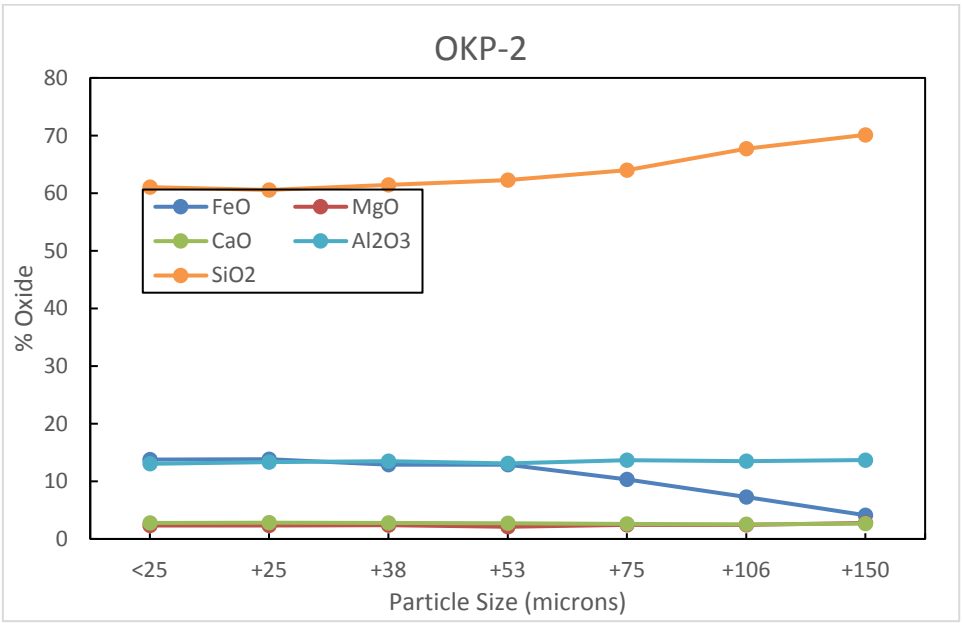

Figure 4. 66: Major oxide composition of size fractions in OKP-2.

The calculated and measured bulk for OKP-1 and OKP-2 were plotted in Figure 4.67. From the graph, a very strong positive correlations between the measure and calculated bulk was established for both samples OKP-1 and OKP-2.

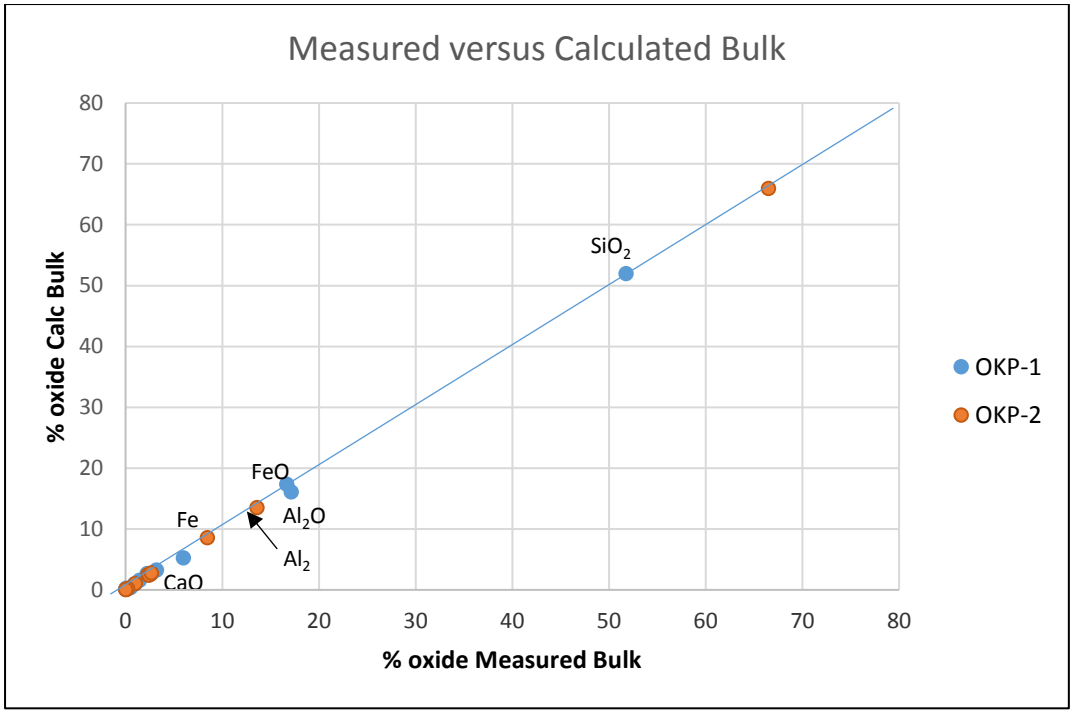

Figure 4. 67: Relationship between measured and calculated bulk for O'okiep.

CHAPTER 5

DISCUSSION

5.1. Introduction

This chapter discusses the significance of results from particle size, surface area and mineralogical analysis presented in the previous chapter. Theoretical CO_2 specific sequestration capacities for the seven South African operations within this study were estimated using mineralogical data reported in the results chapter. This discussion chapter is devoted to a summary and discussion of the main objective; to improve the existing ranking scheme for mineral carbonation. Comparisons in carbonation capacities, mineralogy, particle size distribution, surface area and proximity from the CO_2 supply will serve towards the identification of the most suitable tailings facility for the purpose of mineral carbonation. An investigation into the viability of newly assessed Nkomati and O'okiep facilities for the purpose mineral carbonation will be carried out as knowledge regarding these two operations is scarce.

Consideration should certainly be given to cost and energy factors as these are of utmost importance to a project of this nature. However, the scope of this project was limited to tailings characterization and idealized CO_2 distance estimation. A more comprehensive study regarding critical factors such as overall costing and energetics would prove highly beneficial in the near future.

5.2. Authenticity and Reliability of Sieve Analysis.

To ensure optimal sieve analysis, the extraction of a representative sub-sample from the bulk is a basic requirement. Harris (1971) lays emphasis on the essence of effective splitting of representative samples using various splitting techniques to obtain a homogenous aliquot as a prime necessity for precision sieve analysis. A wide range of splitting exercises were employed in this study and have been presented in Chapter 3.

A report by Retsch (2009), the world's leading manufacturer of sieves revealed splitting with a rotatory divider had the lowest qualitative splitting error (standard deviation) as compared to other sample splitters. Therefore, the use of the rotary divider (Chapter 3.4.1) for the purpose of this study was an attempt to eliminate any significant error hinted by Retsch.

Further studies conducted by Retsch (2009) illustrated a 20% variation in sieve results using the same initial material. This occurrence was noticed among fractions below 2 mm. This implies that two or more identical samples from the same material may not produce the same results irrespective of the precision exercised during splitting. Thus splitting leads to varying results which are not reproducible although samples would originate from the same initial material. Evidently, as presenting in Chapter 4, the three sets of identical aliquots for each tailings facility in this is study produced varying results irrespective of the type of sieving technique applied.

The primary function of precision sieve analysis is to obtain quantitative data about size distribution of particles in the sample (Bernhardt, 1994). Bernhardt (1994) further specifies that sieve analysis is suggested for aggregate material of particles size less than 100 000 µm and a highly recommended method for particles finer than 75 µm, referred as being in the “sub-sieve” range by Bernhardt (1994). Samples considered in this study were obviously less the 100 000 µm in terms of particle size with majority of material finer than 75 µm, falling within Bernhardt’s classification of sub-sieve range and making sieve analysis a favourable method of particle size analysis.

Conventionally, during sieve analysis, the degree of fineness of the sample or material determines the appropriate sieving method to be employed. In pursuit of high quality particle size analysis, Retsch performed numerous tests and presented findings in their 2009 sieve guide regarding dry sieving as the most appropriate method for aggregate size ranging between 40 µm and 125 mm. However, the measurement range according to Retsch, could be limited by properties of the material being tested such as a tendency to agglomerate, density or electrostatic charging. Wet sieving extends the measurement range to 20 µm.

As explained in the methodology chapter, three sieving tests (dry, wet, dry-wet) were performed on each sample. A notable trend observed in the sieving data with respect to this study was the minimal but crucial variation in wet and dry sieving results for fractions below 53 µm. It was observed that dry sieving data marginally differed from the other results as lower amounts were recorded within fractions below 53 µm. An explanation for such an incident would be a suspected blockage caused by the presence of finer material on sieves sizes below 53 µm. A similar condition

encountered by Retsch (2009), concluded that dry sieving of samples with particle size below 40 µm would lead to blockage of the sieve.

Most sieve analyses are traditionally carried out with dry material for the fear of water altering the sample causing either swelling or agglomeration of material. Generally, with regards to tailings materials, which have fortunately been thoroughly tested throughout this study, concerns relating to the alteration of samples by water during sieve analysis should be neglected. Following several sieve analyses performed in this project, one can confidently endorse wet sieving as the appropriate method for tailings material as water used in the sieving exercise serves as an undisruptive medium of liberating clustered particles. The only striking limitation is the excessive use of clean water during the analysis which raises environmental concerns but does not affect the validity of results.

Reaction kinetics in Mineral Carbonation requires the finest fraction of grain sizes to accelerate the reaction. As this work emphasizes on the evaluation of mineral properties for purposes of Mineral Carbonation, a vital revelation from the sieve analysis was uncovered. Data for the finest fraction (<25 µm) for the different mining companies in this study were pulled out from the sieve analysis data in Appendix A.1 and tabulated in Table 5.1.

Table 5. 1: Sieving data of the finest size fraction (<25 µm) for samples in this study.

Tailings	Amount of material in <25 µm fraction (wt%)
Impala	0.25
Amandelbult	1.30
Mogalakwena	31.08
Union Section	3.16
Rustenburg (Waterval)	44.15
Nkomati	67.30
O'okiep	2.33

Individual fractions were nominated from mines that presented more than one sample. For instance, one of the two Impala samples had to be chosen based on the mass retained in the fraction. In this case, sample IMP/001 was selected as it has more material in the <25 µm fraction as compared to IMP/003. In the same manner OKP-2 and NK-PCMZ/PT were chosen for O'okiep and Nkomati respectively.

A visual representation (Figure 5.1) clearly showed Nkomati having the highest amount of material recorded in the finest fraction with 67.30 wt% indicated to have been retained (Table 5.1). Rustenburg (Waterval) and Mogalakwena operations reported fairly high amounts and followed Nkomati in that sequence with 44.15 wt% and 31.08 wt% respectively. Not enough information could be deduced from Impala as it had the lowest amount (0.25 wt%) in the finest fraction (Table 5.1).

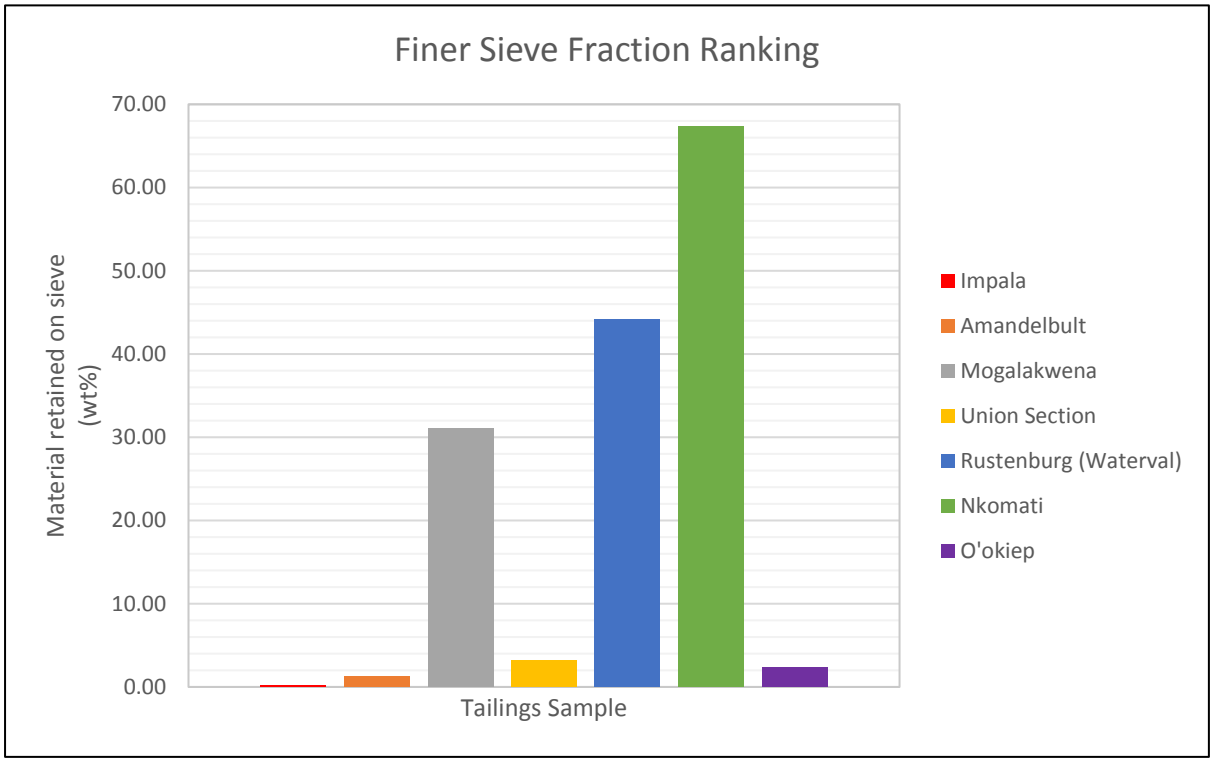

Figure 5. 1 A bar graph representing the average quantity of material retained on the finest size fraction <25 µm for the various tailings samples.

In terms of reaction kinetics, the fine nature of particle sizes from Nkomati, Rustenburg (Waterval) and Mogalakwena operations, render them potential candidates for Mineral Carbonation.

5.3. Relationship between Particle Size Distribution and Surface Area.

Researchers (e.g. Brandt et al., 2003) claim specific surface area captures the combined effects of particle size in a measurement that is independent and complementary to grain-size distribution. Hypothetically, there is a connection between specific surface area and particle size. This correlation shows that specific surface is controlled by the smallest dimension of a particle. Particle size has an effect

on specific surface: as the particle size decreases, specific surface area increases not only due to the inverse relationship between specific surface and size, but also because the shape of small particles tends towards platy and rod-like geometries.

A combined assessment of particle size distribution and specific area was conducted on mines relating to the study. From Figure 5.1, Nkomati undoubtedly displayed the finest grain size orientation. Mogalakwena, Rustenburg (Waterval) and Union Section follow in numerical order. Impala was definitely the coarsest of all samples with greater part of the sample confined in coarser fraction (Table 5.1).

Table 5. 2: A complication of specific surface area for respective mine tailings samples.

Sample	BET Surface Area (m2/g)
Impala (IMP/001)	1.810
Amandelbult (S/4-TD44)	1.450
Mogalakwena (MPL/101)	4.625
Union Section (UST/201)	2.572
Rustenburg (WRT/101)	2.603
Nkomati (NK-PCMZ/PT)	5.888
O'okiep (OKP-2)	1.596

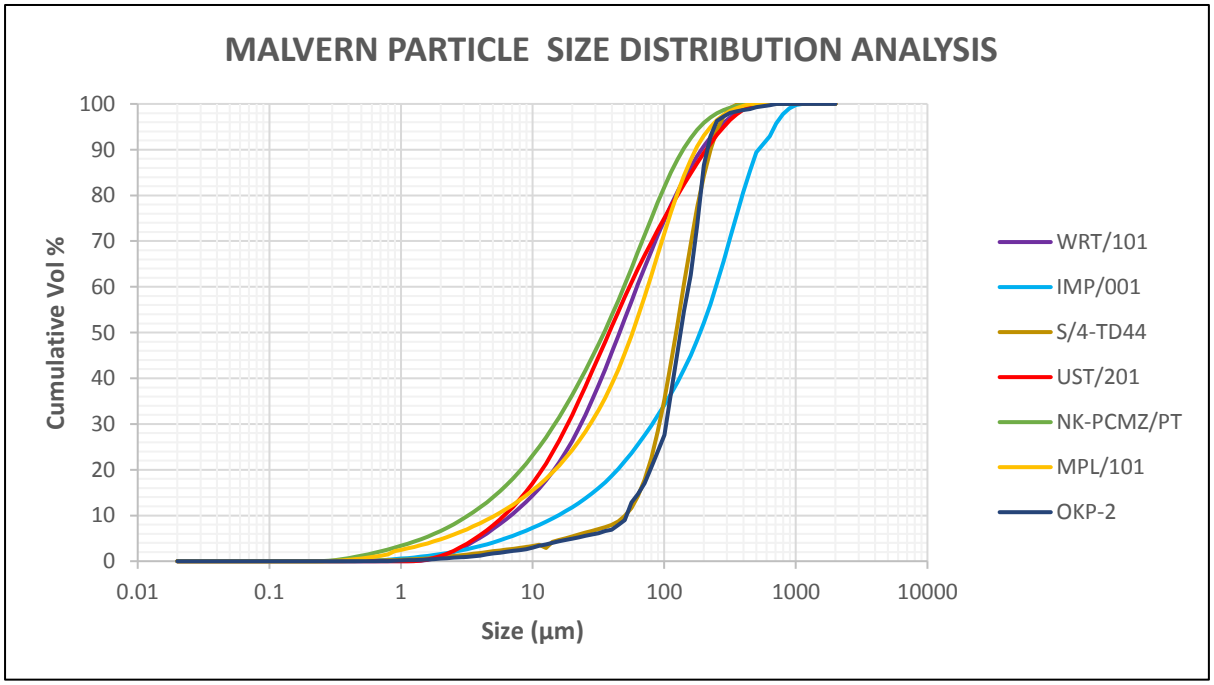

Figure 5. 2: A combined particle size distribution of the seven mines in this study.

The specific surface area for the respective mines have been illustrated in Figure 5.3 and tabulated in Table 5.2. As predicted, Nkomati had the largest specific surface area (5.888 m^2/g). Samples from Mogalakwena, Rustenburg (Waterval) and Union Section

also demonstrated large specific surface area. Amandelbult (1.450 m^2/g) however displayed the smallest specific surface area as shown in Table 5.2 and Figure 5.3.

Table 5. 3: Particle size distribution analysis indicating average particle size at 10, 50 and 90 volume % for the seven mining operations.

Sample	Dv(0.1)(µm)	Dv(0.5)(µm)	Dv(0.9)(µm)
Impala (IMP/001)	17.542	231.45	591.095
Amandelbult (S/4-TD44)	56.831	138.178	251.095
Mogalakwena (MPL/101)	5.406	61.028	197.392
Union Section (UST/201)	6.840	42.788	233.523
Rustenburg (WRT/101)	7.664	51.376	251.182
Nkomati (NK/PCMZ-PT)	3.938	33.767	130.443
O'okiep (OKP-2)	53.398	152.001	214.693

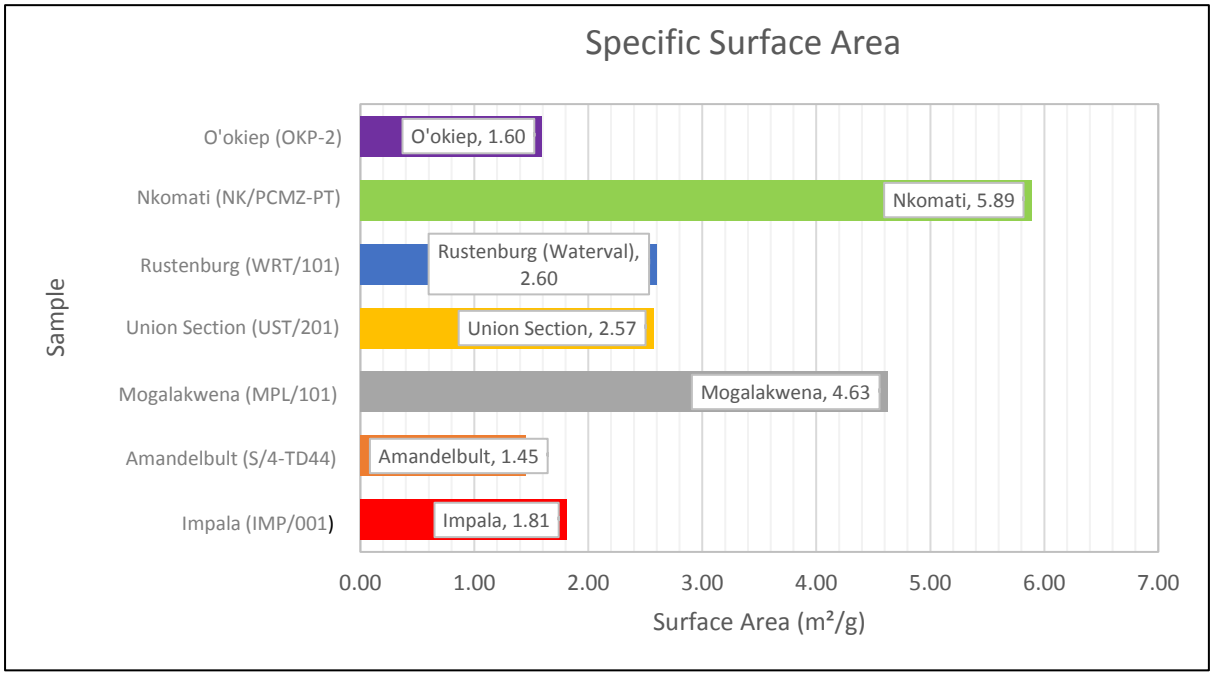

Figure 5. 3: The specific surface area for samples in the study.

Figure 5.4: The specific surface area for samples in the study.

For the purpose of this study, the determination of particle size distribution and specific surface area were collectively used to examine mineral reaction capacities. An inverse proportionality between surface area and particle size is normally assumed based on geometry (Brandt et al., 2003). Vogeli (2012) conducted a similar particle size distribution (Table 5.4 and Figure 5.4) and surface area analysis (Table 5.5) on four South African PGM tailings namely; Impala, Northam, Bafokeng Rasimone Platinum Mine (BRPM) and Lonmin. It was established from his research that BRPM was in fact

the finest sample with regards to particle size. Northam and Lonmin followed numerically with Impala having the coarsest sample (Table 5.4 and Figure 5.4).

Table 5. 4: Particle size distribution analysis indicating average particle size at 10, 50 and 90 volume % (from Vogeli, 2012).

Sample	Dv(0.1)(µm)	Dv(0.5)(µm)	Dv(0.9)(µm)
Northam	7.3	72.1	237.5
BRPM	2.3	25.1	137.5
Impala	18.0	126.3	363.6
Lonmin	7.4	87.4	293

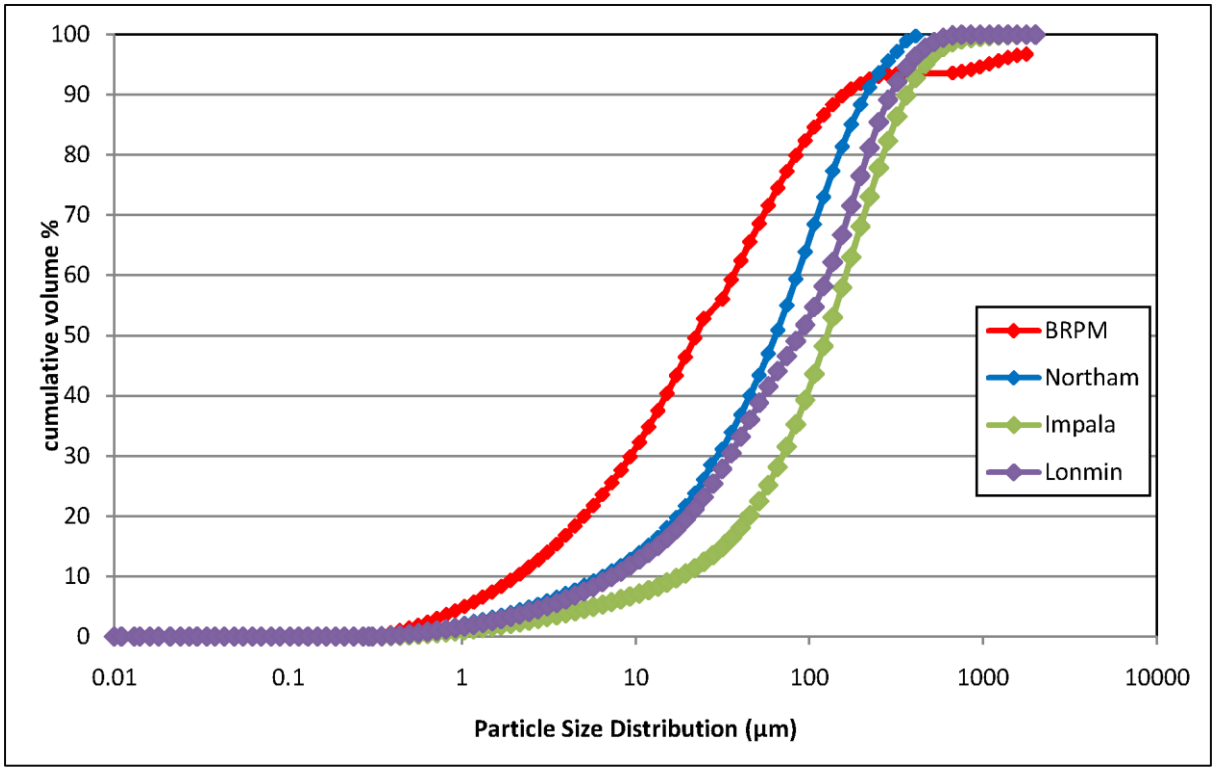

Figure 5. 5: Particle size distribution of the BRPM, Northam, Impala and Lonmin Merensky PGM mine tailings (Vogeli, 2012).

On the contrary, advance findings by Vogeli (2012) on the specific surface area of the four tailings with the aid of the BET method, previously discussed in Chapter 3.8, indicates that BRPM has the largest surface area (1.488 m^2/g). Northam and Lonmin follow in descending order leaving Impala with the smallest surface area as listed in Table 5.5.

Table 5. 5: BET Surface area analysis of tailings samples (Vogeli, 2012).

Sample	BET Surface Area (m2/g)
Northam	1.301
BRPM	1.488
Lonmin	1.211
Impala	0.917

Vogeli's work perfectly validates the theory crafted by Brandt et al., (2003). Particle size and surface area had a flawless correlation as an inverse proportionality was established.

Primarily, a logical relationship is noticed between the sieve analysis presenting in Figure 5.1 and particle size distribution analysis (Figure 5.2) in the present study. There is a numerical sequence in which tailings are ranked in Figure 5.1, is similarly portrayed in the particle size distribution analysis in Figure 5.2. In both cases, Nkomati spearheads the other tailings by possessing finest particle size while O'okiep, Amandelbult and Impala display the coarsest samples.

In comparing Figure 5.2 and 5.3, the desired correlation between particle size and surface area advocated by Brandt et al., (2003) only applies to four tailings (Nkomati, Mogalakwena, Rustenburg (Waterval) and Union Section). However a delicate relationship is observed within the remaining three tailings. The coarsest tailings sample (Impala) does not have the smallest surface area as anticipated. Amandelbult registered the smallest surface area whereas Impala is the third smallest. This setback does not satisfy the assumption that there is an inverse proportionality between surface area and particle size (Brandt et al., 2003). However the proportionality between surface reactivity and specific surface area has always been subject of debate (Hodson 1999, 2006). A detailed investigation into the grain shape and orientation is strongly recommended.

Further comparisons made between Vogeli's work and the current study showed differences in specific surface areas obtained and particle size distribution results for Impala. For instance Vogeli's Impala surface area was 0.917 m^2/g while the current study recorded Impala's surface area at 1.810 m^2/g.

As established in the previous section, identical samples from the same material will not produce the exact results irrespective of the precision exercised. Moreover, Vogeli only sampled the Merensky plant tail while the current research looked into a UG-2-Merensky blend taken from the dam sample. It is predicted that the difference in ore types could have resulted in the dissimilar particle size and surface area results. Furthermore, ever-changing milling specifications (e.g. Rudashevsky et al., 2002; Cabri et al., 2008) where a previous prescribed grind of 80% passing 75 µm was upgraded to 90% passing 25 µm, could have been the result of the contradictory Impala particle size and surface area results.

5.4. Theoretical CO_2 Specific Sequestration Capacity.

To date the parameter widely used to estimate the mineral carbonation potential of an ultramafic deposit is R_{CO2}. This measure was first proposed by Lackner et al., (1995) with the first R_{CO2} estimations illustrated in Table 5.6, and used by Goff and Lackner (1998) and Goff et al., (2000) to estimate the carbonation potential of the major ultramafic complexes in North America.

Table 5. 6: Minerals and their R_{CO2} values. Modified from (Lackner et al., 1995).

Rock		MgO (wt%)	CaO (wt%)	RCO2
Peridotites	Dunite	49.5	0.3	1.8
	Harzburgite	45.4	0.7	2.0
	Lherzolite	28.1	7.3	2.7
Serpentine		~40	~0	~2.3
Gabbro		~10	~13	~4.3
Basalt	Continental Theoleiite	6.2	9.4	7.1

R_{CO2} is defined as the mass of ore necessary to convert a ton of CO_2 to a carbonate. By this definition, a low R_{CO2} is preferable to a high R_{CO2} as a lower mass of material sequestering one tonne of CO_2 would give a logical interpretation to the mineral carbonation concept.

The initial measure was defined by the molar concentration of magnesium and calcium (Lackner et al., 1995; Goff and Lackner, 1998; Goff et al., 2000), but was later modified to include ferric iron in the calculation (Equation 5.1). This modification was made due to iron potentially being able to form stable carbonates. This permitted the calculation

of the carbonation potential for alternative feedstock such as fly-ash and steel slag (Penner et al., 2004).

$$R_{CO2} = \frac{100}{(\sum Ca^{2+} + Fe^{2+} + Mg^{2+})MW_{CO2}} \ldots\ldots\ldots\ldots\ldots\ldots Equation\ 5.1$$

Where

$\sum Ca^{2+} + Fe^{2+} + Mg^{2+}$ are the sum of the molar concentrations for the specified cations and;

MW_{CO2} is the molecular weight of CO_2.

In a study conducted by Gerdemann et al., (2007), The Twin Sisters deposit in northwest Washington State was estimated to contain over 2 billion tons of unaltered dunite (> 90% olivine) enough to carbonate 100% of the CO_2 emissions from 8 to10 1 gigawatt coal fired power plants for approximately 15 years. Theoretical R_{CO2} values from the work done by Gerdemann's team calculated serpentine, olivine and wollastonite as 2.5, 1.8 and 2.8 respectively (Table 5.7), not significantly deviating from Lackner's findings in Table 5.6. From both studies, olivine rich material ((R_{CO2} = 1.8) emerged first priority to sequester extremely large volumes of CO_2.

Table 5. 7: Mineral deposits and their R_{CO2} values modified from (Gerdemann et al., 2007).

Mining District/ Deposit	Mineral	R_{co2}
Twin Sisters, WA	Olivine (Dunite)	1.8
Trinity-Siskyou Mtn, CA-OR	Serpentine (Lizardite)	2.5
Coastal Range, Southern CA	Serpentine (Lizardite)	2.5
Llano Uplift, TX	Serpentine (Lizardite)	2.5
Asheville, NC	Olivine	1.8
State Line, MD-PA	Serpentine (Antigorite)	2.1
Willsboro, NY	Wollastonite	2.8

Table 5. 8: The carbonation potential (R_{co2}) for the mining operations in this study.

Mining Operation	Host Rock	Major Oxides	Chemical Assay (wt%)*	Cation Conversion	Cation Assay (wt%)*	Molar Concentration	Rco_2
Impala	Pyroxenitic	MgO	14.739	Mg	8.891	0.366	3.50
		CaO	6.736	Ca	4.817	0.120	
		FeO	11.464	Fe	8.908	0.160	
		Total	**32.939**	**Total**	**22.616**	**0.646**	
Amandelbult (plant)	Harzburgitic	MgO	16.737	Mg	12.015	0.415	3.27
		CaO	4.840	Ca	3.459	0.086	
		FeO	13.897	Fe	10.804	0.194	
		Total	**35.474**	**Total**	**26.278**	**0.695**	
Mogalakwena	Feldspathic Pyroxenite	MgO	19.983	Mg	12.015	0.494	3.04
		CaO	7.801	Ca	5.575	0.139	
		FeO	10.069	Fe	7.826	0.140	
		Total	**37.853**	**Total**	**25.416**	**0.773**	
Union Section	Noritic	MgO	15.650	Mg	9.440	0.388	3.39
		CaO	2.365	Ca	1.694	0.042	
		FeO	18.330	Fe	14.248	0.256	
		Total	**36.346**	**Total**	**25.382**	**0.686**	
Rustenburg (Waterval)	Noritic	MgO	13.423	Mg	8.095	0.353	3.94
		CaO	7.881	Ca	5.632	0.197	
		FeO	8.301	Fe	6.374	0.114	
		Total	**29.605**	**Total**	**20.101**	**0.664**	
O'okiep	Anorthositic	MgO	2.215	Mg	1.339	0.055	6.31
		CaO	2.557	Ca	1.830	0.064	
		FeO	8.156	Fe	6.343	0.114	
		Total	**12.928**	**Total**	**9.512**	**0.233**	
Nkomati (PCMZ)	Pyroxenitic	MgO	21.987	Mg	13.264	0.546	2.91
		CaO	4.542	Ca	3.245	0.081	
		FeO	11.088	Fe	8.620	0.154	
		Total	**37.617**	**Total**	**25.129**	**0.781**	
Nkomati (MMZ)	Pyroxenitic	MgO	19.139	Mg	11.544	0.475	2.61
		CaO	10.642	Ca	7.606	0.190	
		FeO	13.195	Fe	10.256	0.207	
		Total	**42.976**	**Total**	**29.406**	**0.872**	
Amandelbult (dam)	Harzburgitic	MgO	16.747	Mg	10.102	0.416	3.09
		CaO	3.301	Ca	2.360	0.059	
		FeO	18.974	Fe	14.503	0.260	

The R_{CO2} values for the respective mining operations in the current study were calculated and have been presented in Table 5.8. The full R_{CO2} calculations can be found in Appendix C.

The carbonation potential for Impala was estimated at 3.50 calculated from MgO, CaO and FeO values at 14.74, 6.74 and 11.47 wt% respectively. R_{CO2} value for Impala estimated for Impala by Vogeli (2012) was 3.11, from MgO, CaO and FeO values at 15.74, 6.85 and 12.29 wt% respectively. In comparing Vogeli's work with the present study, there was not an enormous deviation between the two Impala results.

From Table 5.8, it was observed that Nkomati emerged to have the lowest R_{CO2} among other sampling sites in this project with a value of 2.91. Nkomati had the highest concentration of MgO (21.99 wt %) than any other sample in this study. It was also seen to be the sample with a fairly uniform representation of the main oxides (MgO, CaO and FeO) from Table 5.8. Amandelbult, Union Section and Mogalakwena followed in sequential order with R_{CO2} values of 3.27, 3.39, and 3.04 respectively. The R_{CO2} value for O'okiep (6.31) was exceptionally larger than all other samples as it prematurely renders O'okiep the least considered for a mineral carbonation project in South Africa.

5.5. Ranking Scheme Revision

Although all tailings samples in this study are mineralogically suitable for purpose of mineral carbonation other factors have to be considered to classify a carbonation project's feasibility. Three main factors come to mind namely; (1) carbonation **Capacity**, (2) relative **Reactivity** and (3) the **Distance** (or proximity) from the CO_2 source. A ranking scheme for the theoretical mineral carbonation potential was developed by Vogeli et al., (2011). He assessed four PGM operations (Impala, BRPM, Lonmin and Northam) using the above-mentioned factors. It is also important to note that the factors are independent of each other, containing criteria whose definition and measurement are completely separate.

According to Surridge and Cloete (2009), 32 mega metric tons (Mt) of 95% pure CO_2 stream is available annually at Secunda, located within the Mpumalanga Province in South Africa. The 95% purity of the CO_2 makes it readily available for large-scale mineral carbonation projects. Estimations based on the distance from Secunda to the tailings sites have been illustrated in Figure 5.5. The most practical approach in terms

of logistics would be by transporting the CO_2 towards the respective tailings facilities through pipelines as this would prove cost effective. It should be noted that distances presented in Figure 5.5 are idealised direct line distances and do not take into account any deviations that may occur.

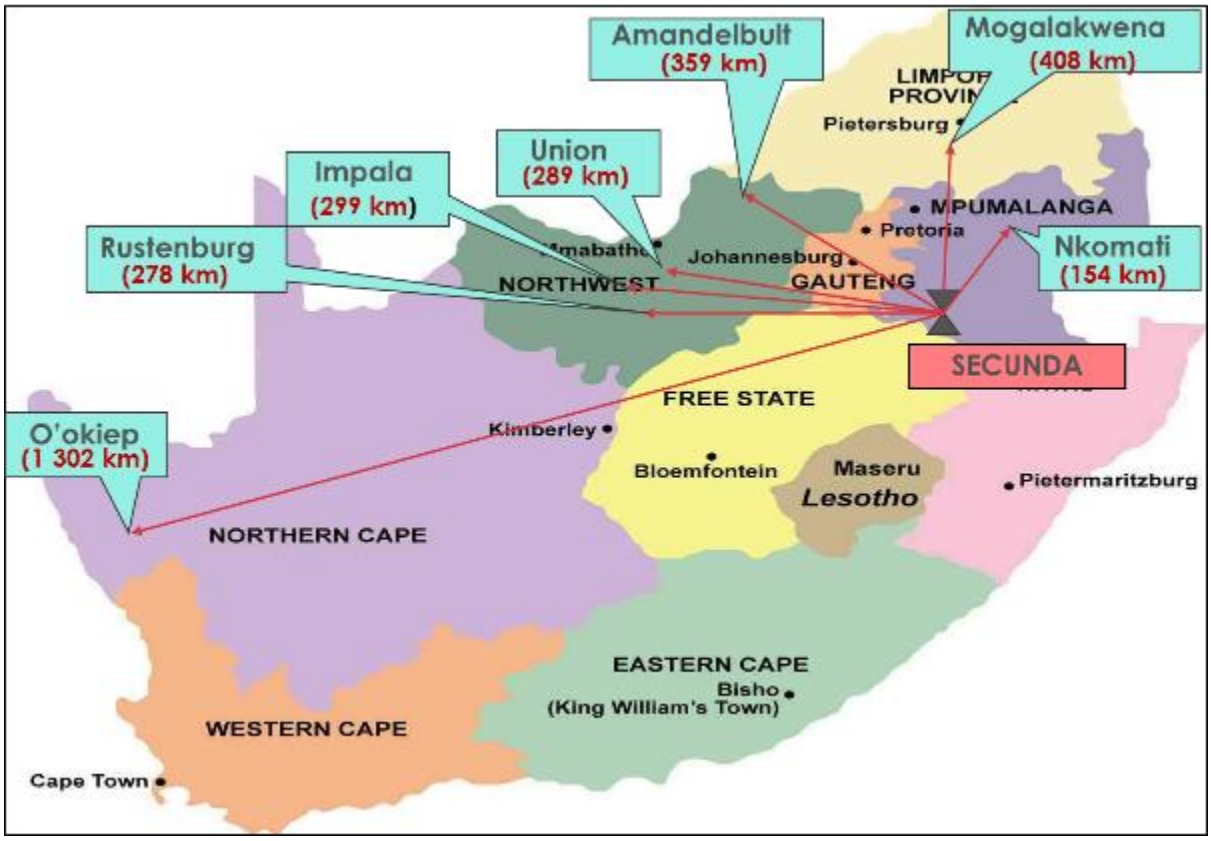

Figure 5. 6: A map showing the distance from Secunda to the tailings sites.

5.5.1. Carbonation Capacity

The carbonation capacity is made up of the annual tonnage, R-value and amount CO_2 taken up by the respective tailings material. Annual tonnage values were obtained from 2012 performance reports of the respective mines in the current study, with the exception of O'okiep which was derived from 2003 reports as it closed down in 2006. Previous tonnage output assessed by Vogeli was derived from 2010 (Table 5.9).

Two samples Impala (plant) and Impala dam had different tonnage outputs (5 385 and 10 654 kt/year respectively). Apart from the fact that they were examined during different years, there were differences in ore types assessed. Impala (plant) tailings was made up of only the Merensky Reef type ore while the Impala (dam) examined in 2012 was a blend of UG-2 and Merensky.

Table 5. 9: Annual tonnage of ore milled for the respective mining operations (Anglo American Plc Report, 2013; Cockburn. G, 2013; Impala Annual Report, 2013; Metorex limited Annual Report, 2003; Vogeli et al., 2011; Vogeli 2012).

Mining Operation	Ore milled (kt/year)
Impala (dam)	10 654
Amandelbult[2]	5 149
Mogalakwena	10 480
Union Section[2]	3 919
Rustenburg (Waterval)[2]	4 834
O'okiep**	360**
Nkomati (PCMZ)	3 600
Nkomati (MMZ)	4 200
BRPM[1,2]	1 039
Lonmin[1,2]	2 636
Northam[1,2]	1 002
Impala (plant)[1,2]	5 385

**O'okiep mine has been dormant since 2006; [1] Samples studied by Vogeli; [2] Merensky tailings.

Calculation of the CO_2 absorbed is a function of both Tonnage and R-value and thus they counteract each other. For the same tonnage, a range in R-value between 2.61 and 3.9 (Table 5.10) can result in a 50% change in CO_2 take up. Nevertheless, the tailings capacity to take up CO2 can be regarded as an important means by which to rank each mine.

5.5.2. Relative Reactivity

This factor is made up of the particle size and surface area. Relative reactivity with respect to particle size and surface area theoretically favoured mining operations with the current study as the cost of pre-crushing and grinding process during mineral carbonation is eliminated due to the fine nature of the tailings. Particle size as determined by the Malvern method (optical diffraction) is a measure of the diameter of a sphere with equivalent volume of the particle. Since most mineral particles produced by the milling process will not approximate spheres, it follows that a surface area calculated from Malvern data will be close to a minimum value. In contrast, the BET gas adsorption method takes cognisance of the surface irregularities that typify mineral particles that are produced by milling breakage. It follows that the Surface Area data is a better basis upon which to predict Reactivity. There is however, a rough anti-correlation between Malvern particle size and BET surface area, but in this assessment the latter will be adopted as the sole measure of Reactivity.

Table 5. 10: A layout of values for the respective variables of the ranking scheme.

Mining Operation	Capacity			Reactivity		Proximity
	Tonnage	R-value	CO_2	Particle Size	Surface Area	Distance
	kt/year	t/ton CO_2	kt/year	Dv (0.9) µm	m²/g	km
Nkomati (PCMZ)	3600	2.91	1237	130.44	5.888	154
Nkomati (MMZ)	4200	2.61	1609	312.03	1.163	154
Mogalakwena (plant)	10480	3.04	3447	197.39	4.625	408
Impala (plant)	5385	3.11	1732	363.60	0.917	292
Amandelbult (plant)	5149	3.27	1575	251.10	1.450	359
Amandelbult (dam)	5149	3.09	1666	303.62	1.226	359
Waterval (plant)	4834	3.94	1227	251.18	2.603	278
Union (plant)	3919	3.39	1156	233.52	2.572	289
Lonmin (plant)	2636	2.72	969	293.00	1.211	215
Northam(plant)	1002	2.61	384	237.50	1.301	300
BRPM (plant)	1039	3.24	321	275.09	1.488	280
Impala (dam)	10654	3.5	3044	248.54	1.810	292
O'okiep (dam)	360	6.31	57	214.69	1.596	1302

5.5.3. Distance from CO_2 source

It has been assumed that the cost and energetics of producing 95% pure CO_2 in a liquefied form at Secunda is essentially the same for all mines. Moreover, transport of the liquefied CO_2 is assumed to be a direct pipeline and thus would not be subject to variability in alternative vehicular transport routes (existing road or rail networks). Consequently the direct line length in km has been adopted as a measure of the Distance factor in the ranking scheme.

Table 5. 11: A series of rankings based on individual factors of the theoretical carbonation ranking scheme.

Ranking	Mining Operation	CO_2 (kt/year)	Ranking	Mining Operation	Surface Area (m^2/g)	Ranking	Mining Operation	Distance (km)
1	Mogalakwena (plant)	3447.368	1	Nkomati (PCMZ)	5.888	1	Nkomati (PCMZ)	154
2	Impala (dam)	3044.000	2	Mogalakwena (plant)	4.625	1	Nkomati (MMZ)	154
3	Impala (plant)	1731.511	3	Waterval (plant)	2.603	3	Lonmin (plant)	215
4	Amandelbult (dam)	1666.343	4	Union (plant)	2.572	4	Waterval (plant)	278
5	Nkomati (MMZ)	1609.195	5	Impala (dam)	1.81	5	BRPM (plant)	280
6	Amandelbult (plant)	1574.618	6	O'okiep (dam)	1.596	6	Union (plant)	289
7	Nkomati (PCMZ)	1237.113	7	BRPM (plant)	1.488	7	Impala (dam)	292
8	Waterval (plant)	1226.904	8	Amandelbult (plant)	1.45	7	Impala (plant)	292
9	Union (plant)	1156.047	9	Northam (plant)	1.301	9	Northam (plant)	300
10	Lonmin (plant)	969.118	10	Amandelbult (dam)	1.226	10	Amandelbult (plant)	359
11	Northam (plant)	383.908	11	Lonmin (plant)	1.211	10	Amandelbult (dam)	359
12	BRPM (plant)	320.679	12	Nkomati (MMZ)	1.163	12	Mogalakwena (plant)	408
13	O'okiep (dam)	57.052	13	Impala (plant)	0.917	13	O'okiep (dam)	1302

Table 5.11 summarises the three ranking lists obtained from using the three different categories. Predictably the high tonnage mines (eg. Mogalakwena) figure prominently in the Capacity ranking factor. Inconsistencies are evident due to the variable reporting of Tonnage (Table 5.10), such as the case of Impala; the Plant sample from Vogeli (2011) represent the tailings produced from the Merensky Reef ore type only, while that for the Dam sample includes a mixture of both UG2 and Merensky tailings. The main differences in the two tailing types is the abundance of chromite in the former, which was shown earlier to negatively influence the R-value, since the inert nature of this mineral reduces the capacity to absorb CO_2. UG2 tailings also tend to be finer grained than those of the Merensky, due to advance milling to liberate the PGM. Amandelbult suffers from the same problem of Plant and Dam samples representing different bulk mineral assemblages as well.

With respect to Reactivity, the ranking list is essentially controlled by Surface Area, so the mines with the finer grain size tailings are prominent. The PCMZ plant tailings of Nkomati score above Mogalakwena, while the other operations shuffle about in the lower order. Most notable is the position of the other Nkomati ore type, the MMZ, which ranks very poorly based on Reactivity, although is produced in greater quantities.

Distance is the third factor that can control rankings. The close proximity of Nkomati mine to Secunda, compared to Mogalakwena for example, results in another high score. The poor score of the coarser-grained Nkomati MMZ tailings is overcome in this alternative ranking. Certain mines in the Rustenburg region also score higher with Distance, and the big production, finer-grain Mogalakwena mine really suffers in this context. However, one argument that could be raised is that the Distance factor being based only on direct line km does not take into account the actual route. Those routes from Secunda to the western Bushveld platinum mines would need to traverse major metropolitan areas such as Johannesburg and Pretoria, whereas the route to Nkomati and beyond to Mogalakwena (Figure 5.5) might pose less problems.

It is therefore apparent from the approach to ranking described above that taking Capacity, Reactivity and Distance separately leads to quite disparate results. Some combination is demanded and it was decided to utilise the three ranking lists to calculate an overall placement that is simply the average (Table 5.12)

Table 5. 12: A overall ranking order based on the average of the rankings from Table 5.11.

Ranking Order	Mining operation	Average
1	Nkomati (PCMZ)	4.500
	Nkomati (MMZ)	
2	Impala (dam)	4.667
3	Mogalakwena (plant)	5.000
3	Waterval (plant)	5.000
5	Union (plant)	6.333
6	Impala (plant)	7.667
7	Amandelbult (plant)	8.000
7	BRPM (plant)	8.000
7	Lonmin(plant)	8.000
7	Amandelbult (dam)	8.000
11	Northam (plant)	9.667
12	O'okiep (dam)	10.667

The final ranking is therefore based on a combination of the three totally independent factors was required to successfully identify the top priority mine tailings. Nkomati is ranked first above Impala and Mogalakwena. Since the Impala sample is from a historic deposit and not an active plant output, it has to be disregarded and thus Waterval gets ranked third.

A further alternative to simple ranking list manipulation, is a mathematical combination of the five criteria can also be devised, which perhaps represents a more elegant approach. Each criteria can be quantified and combined in an equation that is designed to produce a numerical ranking value, with following constraints:

1. The higher the ranking value the better. It follows that certain criteria, such as R-value, Particle Size and Distance need to be reciprocated in the equation.

2. To overcome the different units of measure used in the different criteria. This allows the numerical values of each criteria to be expressed in similar orders of magnitude.

3. To provide different weightings (= magnitude of the coefficients) so that each criteria can exert influences that are appropriate. This allows for different scenarios that emphasise Capacity, Reactivity and Proximity, as demonstrated previously.

To devise a justifiable decision-making process, an algorithm had to be employed. The formula given in Equation 5.2 was used for such an exercise.

$$Rank = (tonnage/1000) + (100/R\ value) + (100/particle\ size) + (surface\ area)^2 + (100/distance) \ldots\ldots\ldots\ldots\ldots\ldots\ldots\ldots\ldots\ldots\ldots\ldots\ldots\ldots\ldots\ldots Equation\ 5.2$$

From the algorithm, the Ranking factor is defined by the largest value. The larger the value, the better. Two variables, Tonnage and Surface Area are considered better when higher. Three variables (Particle Size, R-value and Distance) need to be reciprocated in the ranking algorithm (Equation 5.2) as the variables need to have individual weighting to overcome the widely varying units of measure, to produce values that have the same order of magnitude.

Table 5. 13: A full updated ranking scheme comparing the two ranking methods used in the study (where T = Tonnage; R = R-value; P = Particle Size; S = Surface Area and D = Distance from CO_2).

Factor	T/1000 1000	100/R 100	100/P 100	S^2	100/D 1000	Sum	Rank (equation)	Rank (Order)
Nkomati (PCMZ)	3.600	34.364	0.767	34.669	6.494	130.574	1	1
Nkomati (MMZ)	4.200	38.314	0.320	1.353	6.494			
Mogalakwena (plant)	10.480	32.895	0.507	21.391	2.451	67.723	2	3
Impala (dam)	10.654	28.571	0.402	3.276	3.425	46.329	3	2
Lonmin (plant)	2.636	36.765	0.341	1.467	4.651	45.860	4	7
Northam (plant)	1.002	38.314	0.421	1.693	3.333	44.763	5	11
Union (plant)	3.919	29.499	0.428	6.615	3.460	43.921	6	5
Amandelbult (dam)	5.149	32.362	0.329	1.503	2.786	42.129	7	7
Impala (plant)	5.385	32.154	0.275	0.841	3.425	42.080	8	6
Amandelbult (plant)	5.149	30.581	0.398	2.103	2.786	41.016	9	7
Waterval (plant)	4.834	25.381	0.398	6.776	3.597	40.986	10	3
BRPM (plant)	1.039	30.864	0.364	2.214	3.571	38.052	11	7
O'okiep (dam)	0.360	15.848	0.466	2.547	0.768	19.989	12	12

From the updated ranking scheme (Table 5.13), Nkomati (PCMZ and MMZ) is undoubtedly first preference for mineral carbonation in South Africa when employing both types of ranking exercises. This could possibly be as a result of its close proximity to Secunda, fairly reasonable tonnage, lowest R_{CO2} compared to the other operations, and its high reactivity. O'okiep on the other hand, would be least favourable due to its distance from Secunda and very low tonnage in tailings. Its carbonation potential compared to the other mining operations is another factor that would hinder O'okiep's potential of being mineral carbonation candidate, having the lowest ranking factor in both ranking experiments (Table 5.13).

Mogalakwena ranks second in the algorithmic ranking but third in the combined average ranking exercise. Conversely, the Impala (dam) sample treated in the current study ranks third in the algorithmic exercise and second in the preceding ranking exercise. A characteristic discovery emerging from both ranking exercises is the dominance of Nkomati, Mogalakwena and the Impala (dam) as the top three tailings

(not in any specific order) to consider for the purpose of mineral carbonation projects in South Africa.

CHAPTER 6

CONCLUSIONS AND RECOMMENDATIONS

This is the closing chapter of the study. The outcomes and main research findings will be assessed in this chapter. Significant discoveries and their respective feasibilities will be evaluated. Any distinctive observation as well as suggestions regarding future research on South African tailings characterization for the purpose of mineral carbonation will be presented in the forthcoming sections.

6.1. Conclusions

Prior to the commencement of this study, there was an initial concern in the feasibility of UG-2 tailings to be carbonated, as the presence of high concentrations in chromite would render the tailings unfavourable for mineral carbonation. Although mining companies processing UG-2 ore like Impala have a chromite scavenger plant tailings channelled to the dam comprise of a Merensky - UG-2 blend. The capacity ranking bias is cause by this UG-2 factor.

A preliminary ranking scheme adopted from Vogeli et al., (2011), fused three key factors namely; carbonation capacity, relative reactivity and distance from the CO_2 source. This project was a pilot study and its main aim was to evaluate the potential of the South African PGM, nickel and copper industry to sequester CO_2 through mineral carbonation. Seven mining operations comprising of five PGM, one nickel and a dormant copper company were considered for the study with the idea of rating their potential for large-scale mineral carbonation projects using an updated ranking scheme.

The carbonation capacity was influence by the tonnage output of each mining operation in the ranking process. Annual values presented in the study were over-estimates of tonnage. Capacity was bias due to the uncertainty of Merensky and UG-2 specific tonnage outputs as in the case of Impala (dam), Lonmin, BRPM and Amandelbult (plant). Most annual production reports presented overall tonnage outputs rather than ore tonnage outputs. This could be the possible cause of the discrepancy observed in the second and third spots of both rankings.

Relative reactivity was influenced by BET surface area and particle size results. Recent mineral carbonation studies have focused on ways to speed up reaction kinetics.

It should be noted that the three main factors are totally independent of each other. A change in capacity for instance would not affect reactivity or distance. Similarly, any disparity in reactivity would not necessarily influence capacity and distance.

6.2. Recommendations

The present study was initially aimed at a combined trace metal recovery and mineralogical characterization of historic tailings, in order to evaluate their potential for mineral carbonation. Unfortunately, the sampling of certain historic PGM tailings facilities was temporarily prohibited by law as these dams were believed to have fairly good ore grade accumulated at the base over a long period of time.

Primarily, future research should target historic tailings with the aim of incorporating tailings retreatment and mineral carbonation assessment. There are other suggestions for future studies and these are provided below.

6.2.1. Kudu Gas Project

As Namibia is planning towards boosting its energy sector by ensuring the security of reliable power supply in the near future, a proposed 800 MW Kudu Power Project near Oranjemund in south-west Namibia would undoubtedly emit extremely high levels CO_2, making it a reliable source. Location of Kudu Power Station is 25 km outside Oranjemund and about 280 km from O'okiep. The Kudu Gas power station is expected to be up and running by 2018, potentially making Namibia a net exporter, rather than an importer of electricity (Namibia Press Agency, 2013). Historic MgO – rich (generally >15%) Kimberlite tailings as estimated by Nixon (1995) and the dormant O'okiep mine waste situated within fairly reasonable proximities to the proposed power project, could serve as first-choice candidates to sequester CO_2 in the near future.

6.2.2. Onsite CO_2 Emission

Over the past years, mining companies have accounted for their CO_2 emissions. These figures are presented in annual reports. Although CO_2 emission rates from mining operations do not come close to that produced at Secunda, some consideration should be given to such CO_2 sources in order to mitigate climate change. Further

investigations regarding the incorporation of onsite (direct and indirect) sources of CO_2 emission from respective mining operations into mineral carbonation projects would prove valuable.

6.2.3. Phytomining through Metal Hyper-accumulation

A combined trace metal recovery and mineral carbonation can be experimented. This is a concept first suggested by Chaney (1983). The Nkomati operation could benefit from Nickel Hyper-accumulation. A similar study was conducted by Netty et al., (2012), who used twenty-three plant species from three post-mining sites in South Sulawesi, Indonesia.

About 300 Ni-hyper-accumulator species were reported by Chaney (1983). A phytomining operation would entail planting a hyperaccumulator crop over a low-grade ore body or mineralized soil, followed by harvesting and incineration of the biomass to produce a commercial *bio-ore*. The first field trials on Ni phytomining in 1994 were based at the US Bureau of Mines, Reno, Nevada (Nicks and Chambers, 1998).

CHAPTER 7

REFERENCES

Akai, M., Nishio, N., Iijima, M., Ozaki, M., Minamiura, J., and Tanaka, T. (2004). Performance and Economic Evaluation of CO_2 Capture and Sequestration Technologies. Proceedings of the Seventh International Conference on Greenhouse Gas Control Technologies. 5th September 2004, Vancouver, Canada.

Anglo American Platinum Limited Annual Report. (2012). Retrieved from: http://www.angloamerican.com/files/reports/angloamericamplc/2012 [Accessed: 04 August 2014].

Anglo American PLC Annual Report. (2013). Retrieved from: http://www.angloamerican.com/files/reports/angloamerican/2013 [Accessed: 04 August 2014].

ARM Operational Review. (2012). Retrieved from: http://www.arm.integrated-report.com/2013/operational/arm-platinum [Accessed: 04 August 2014].

Assima, G. P., Larachi, F., Molson, J., and Beaudoin, G. (2014). Impact of temperature and oxygen availability on the dynamics of ambient CO_2 mineral sequestration by nickel mining residues. Chemical Engineering Journal. 2014, 240, 394–403.

Bachu, S. and Shaw, J.C., (2005). CO_2 storage in oil and gas reservoirs in western Canada: Effect of aquifers, potential for CO_2-flood enhanced oil recovery and practical capacity. Proceedings of the 7th International Conference on Greenhouse Gas Control Technologies (GHGT-7), September 5–9, 2004, Vancouver, Canada, v.I, 361-370.

Baciocchi, R., Costa, G., Polettini, A., Pomi, R., and Prigiobbe, V. (2009a). Comparison of different reaction routes for carbonation of APC residues. Energy Procedia 1, 4851-4858.

Baciocchi, R., Costa G., Polettini, A., and Pomi, R. (2009b). Influence of particle size on the carbonation of stainless steel slag for CO_2 storage. Energy Procedia 1, 4859-4866.

Back, M., Kuehn, M., Stanjek, H., Peiffer, S. (2008). Reactivity of alkaline lignite fly ashes towards CO_2 in water. Environmental Science & Technology 42, 4520-4526.

3rd International Conference on Accelerated Carbonation for Environmental and Materials Engineering, Turku, Finland, pp 193-202.

Baer, P., 2003: An issue of scenarios: carbon sequestration as an investment and the distribution of risk. An editorial comment. Climate Change, 59, 283–291.

Baldyga, J., Henczka, M., and Sokolnicka, k. (2010). Utilization of carbon dioxide by chemically accelerated mineral carbonation. Materials letters. 64(6):702.

Barry, J.P., Buck, K.R., Lovera, C.F., Kuhnz, L., Whaling, P.J., Peltzer, E.T., Walz, P., and Brewer, P.G. (2004). Effects of direct ocean CO_2 injection on deep-sea meiofauna. Journal of Oceanography, 60(4), 759-766.

Beck, R. D., and Chamart, J. J. (1980). The Broken Hill concentrator of Black Mountain Mineral Development Co (Pty) Limited South Africa, The South African Institute of Mining and Metallurgy, Conference on Complex Sulphide ores. October 1980. pp 88-99.

Benedict, P. C., Wiid, D. de N., Cornelissen, A. K and Staff (1964). Progress report on the geology of the O'okiep copper district. In: Haughton, S. H. (ed.) The Geology of some Ore Deposits in Southern Africa. Geological Society of South Africa II. 239-302.

Bernhardt, C. (1994). Particle Size Analysis: Classification and Sedimentation Techniques. Vol.5. Chapman and Hall, London.

Bernstein, L., Bosch, P., Canziani, O., Chen, Z., Christ, R., and Davidson, O. (2007). Climate Change 2007. Synthesis report: An Assessment of the Intergovernmental Panel on Climate Change. An adopted section at IPCC Plenary XXVII (Valencia - Spain, November 2007).

Blencoe, J.G., Palmer, D. A., Anovitz, l. M. L., and Beard, J. S. (2004). Carbonation of metal silicates for long term CO_2 sequestration. WO 2004/094043.

Bodenan, F., Bourgeois, F., Petiot, C., Auge, T., Bonfils, B., Julcour-Lebigue, C., Guyot, F., Boukary, A., Tremosa, J., Lassin, A., Gaucher, E., and Chiquet, P. (2014). Ex situ mineral carbonation for CO_2 mitigation: Evaluation of mining waste resources, aqueous carbonation processability and life cycle assessment (Carmex project). Mineral Engineering. 2014, 59, 52–63.

Brandriss, M.E., Cawthorn, R.G. (1996). Formation of anorthosite and leucotonalite during magma hybridization in the Koperberg Suite of Namaqualand, South Africa. South African Journal of Geology. 99, 135–152.

Brandt, F., Bosbach, D., Krawczyk-Bärsch, E., Arnold, T. and Bernhard, G. (2003). Chlorite dissolution in the acid pH-range: a combined microscopic and macroscopic approach. Geochimica et Cosmochimica Acta. Vol 67, Issue 8, April 2003, pp 1451–1461.

British Petroleum (BP). (2004). Statistical Review of World Energy. http:\www.bp.com. [Accessed: 23 May 2012].

Britz, J. (2008). High level review on the mineralogical variability of the Main Mineralized Zone at Nkomati Mine. Internal Memorandum, Norilsk Nickel Africa, 18 July 2008.

Bulatovic, S. M (2010). Handbook of Flotation Reagents. Chemistry, theory and practice. Flotation of gold, PGM and other oxides. Vol.2.pp 1-17.

Cabri, L.J., Rudashevsky, N.S. and Rudashevsky, V.N. (2008). Current approaches for the process mineralogy of platinum-group element ores and tailings; in Ninth International Congress for Applied Mineralogy ICAM 2008, The Australasian Institute of Mining and Metallurgy, Publication Series No 8/2008, pp 9-17.

Cairncross, B. (2004). History of the Okiep Copper District, Namaqualand, Northern Cape Province, South Africa. Mineral Rec 35:289–317

Canadell, J.G., Le Quere, C., Raupach, M.R., Field, C.B., Buitenhuis, E. T., Ciais, P., Conway, T.J., Gillet, N. P., Houghton, R.A., and Marland, G. (2007).Contributions to accelerating atmospheric CO_2 growth from economic activity, carbon intensity, and efficiency of natural sinks. Proceedings of the National Academy of Sciences of the United States (PNAS). In 104(47)-18866-70.

Cawthorn, R.G., Meyer, F.M. (1993). Petrochemistry of the Okiep Copper District basic intrusive bodies, North-western Cape Province, Southern African Economic Geology 88, 590–605.

Cawthorn, R.G (1999a). Geological models for platinum-group metal mineralization in the Bushveld Complex. South African Journal of Science. 95(11-12):490-498.

Cawthorn, R.G., (1999b). Platinum in South Africa – the platinum and palladium resources of the Bushveld Complex. South African Journal of Science 95, 481–489.

Cawthorn, R.G., (2006). Centenary of the discovery of platinum in the BushveldComplex. Platinum Metals Review 50 (3), 130–133.

Cawthorn, R.G. (2010). The Platinum Group Element Deposits of the Bushveld Complex in South Africa. Platinum metals review. 54(4):205-215.

Chaney, R. L. (1983). Plant uptake of inorganic waste constituents. Pp 50-76. In James F. Parr, Paul B. Marsh and Joanne M. Kla (eds.) Land Treatment of Hazardous Wastes. Noyes Data Corp., Park Ridge, NJ.

Clifford, T. N., Stumpfl, E. F., Burger, A. J., McCarthy, T. S., and Rex, D. C. (1981). Mineral–chemical and isotopic studies of Namaqualand granulites, South Africa: a Grenville analogue. Contrib Mineral Petrol 77:225–250.

Clifford, T.N., Barton, E.S., Stern, R.A., and Duchesne, J. –C. (2004). U–Pb zircon calendar for Namaquan (Grenville) crustal events in the granulite facies terrane of the O'okiep Copper District of South Africa. J Petrol 45:669–691

Clifford, T. N., and Barton, E. S. (2012). The O'okiep Copper District, Namaqualand, South Africa: A review of the geology with emphasis on the petrogenesis of the cupriferous Koperberg Suite. Miner Deposita (2012) 47:837–857 DOI 10.1007/s00126-012-0403-x

Cockburn, G. (2013). Challenges and successes at the Nkomati Nickel JV: pit-to-product process improvements. (The Southern African Institute of Mining and Metallurgy Base Metals Conference 2013).

Cole, S and Ferron, J. C. (2002). A Review of the Beneficiation and Extractive Metallurgy of the Platinum Group Elements, Highlighting recent process innovations. Technical paper 2002. SGS Mineral Serves. In L. J. Cabri (Ed.), The geology, geochemistry, mineralogu and mineral beneficiation of platinum-group elements (pp. 811-844). CIM.

Conradie, J. A., and Schoch, A. E.(1986). Petrographical characteristics of the Koperberg suite, South Africa – an analogy to massif-type anorthosites? In

Precambrian Research 31(2): 157-188. March 1986. DOI: 10.1016/0301-9268(86)90072-0.

Cook, P.J. (1999) Sustainability and non-renewable resources. Environmental Geosciences, 6(4), 185–190.

Cooney, C. (2012). Managing the Risks Extreme Weather: IPCC Special Report. Climate Change Environmental health perspectives. 120(2):A58.

Cornelissen, A. K. (1959). A comparative study of barren and mineralized diorites. Unpublished report, O'okiep Copper Company 9, p 32.

Dahlin, D.C., O'Connor, W.K., Nilsen, D.N., Rush, G.E., Walters, R.P., and Turner, P.C. (2000), A Method for Permanent CO_2 Sequestration: Supercritical CO_2 Mineral Carbonation. Proceedings of the 17th Annual International Pittsburgh Coal Conference, Pittsburgh, PA, September 11-15, 14 pp.

de Figueiredo, M.A., Herzog, H.J., Joskow, P.L., Oye, K.A., Reiner, D.M. (2007). Regulating carbon dioxide capture and storage. CEEPR WP-2007-003, MIT Centre for Energy and Environmental Policy Research, Massachusetts Institute of Technology.

De Waal, S. A., and Gauert, C. D. K. (1997). The Basal Gabbro Unit and the identity of the Parental Magma of the Uitkomst Complex, Badplaas, South Africa. Journal of African Earth Sciences. v100, no.4 pp 349-361.

De Waal, S. A., Maier, W. D., Armstrong, R. A., and Gauert, C. D. K. (2001). Parental magma and emplacement of the stratiform Uitkomst Complex, South Africa. The Canadian Mineralogist 39 (2), 557–571.

Delgado, T. M., (2010). Assessing the Mineral Carbonation Science and Technology, MSc (Eng.) Thesis. ETH Zürich, Switzerland. 51.

Dooley, J.J. and Wise, M.A. (2003). Retention of CO_2 in Geologic Sequestration Formations: Desirable Levels, Economic Considerations, and the Implications for Sequestration R&D. Proceedings of the 6th International Conference on Greenhouse Gas Control Technologies. J. Gale and Y. Kaya (eds). Elsevier Science, Amsterdam pp. 273–278.

Dooley, J.J., Davidson, C.L. and Dahowski, R.T. (2009). An assessment of the commercial availability of carbon dioxide capture and storage technologies as of June 2009. Richland, WA: Pacific north-west national laboratory, United States Department of Energy.

Doucet, F. J. (2011). Carbonate mineralization technologies: A for-profit approach to CO2 management. In: Carbon Mitigation. Nova Science Publishers, Inc., New-York, USA (in preparation).

du Plessis, J. (2008). Petrochemical characterization of dolerites and their influence on coal in the Witbank Highveld coalfield, South Africa. Thesis. Degree of Master of Science, Natural Science, University of the Free State.

Du Toit, A.L. (1954). The Geology of South Africa. Third Edition ed. Edinburgh: Tweedale Court. London: 98 Great Russell Street, W.C.: Oliver and Boyd.

Dunsmore, H.E. (1992). A geological perspective on global warming and the possibility of carbon dioxide removal as calcium carbonate mineral, Energy Conversion and Management. (33), pp. 565-572.

Eales, H.V. (2001). A first introduction to the geology of the Busveld Complex and those aspects of South African geology related to it. First Edition ed. 208 Pretoria Street, Silverton 0184. : The Council for Geoscience.

Eikeland, E., Blichfeld, A. B., Tyrsted, C., Jensen, A and Iversen, B. B. (2015). Optimised carbonation of magnesium silicate minerals for CO_2 storage. 7 (9):5258-64. ACS Applied Material Interfaces.

Engelbrecth A., Golding A., Hietkamp S. and R Scholes, (2004). The Potential for Sequestration of Carbon Dioxide in South Africa. Contract Report 86DD / HT339, Process Technology Centre, CSIR, Pretoria, South Africa, (available on the Department of Minerals and Energy website – www.dme.gov.za). [Accessed: 13 March, 2012].

Evans, W. C., Kling, G. W., Tuttle, M. L., Tanyileke, G. and White, L. D. (1993) Gas buildup in Lake Nyos, Cameroon: The recharge process and its consequences. Appl. Geochem. 8, 207–221.

Flannery, T. (2005). The Gaseous Greenhouse. In The Weather Makers: The history and future impact of climate change. Austrailia: Text Publishing Company. pp 27-35.

Fourie, N. K. (2008). Maximizing value through Isa Mill Grinding Technology. Smart Idea Conference, Anglo American, Johannesburg, South Africa. 2008. pp 186.

Gain, S. B., and Mostert, A. B. (1982). The geological setting of the platinoid and base metal sulphide mineralization in the Platreef of the Bushveld Complex in Drenthe, North of Potgietersrus, Economic Geology 77, 1395-1404.

Gauert, C.D.K., De Waal, S.A., and Wallmach, T. (1995). Geology of the ultrabasic to basic Uitkomst complex, eastern Transvaal, South Africa: An overview. Journal of African Earth Sciences 21 (4), 553–570.

Gauert, C. (2001) Sulfide and oxide mineralization in the Uitkomst Complex, South Africa: Origin in a magma conduit. Journal of African Earth Sciences, 32(2), 149-161.

Gerdemann, S.J. O'Connor, W. K. Dahlin, D.C., Penner, L. R., and Rush, H. (2007). Ex situ aqueous mineral carbonation. Environmental science and technology. 41:2587-93.

Gibbins, J., Crane, R. I., Lambropoulos, D., Booth, D., Roberts, C.A., and Lord, M. (2005). Maximising the effectiveness of post-combustion CO_2 capture systems. Proceedings of the 7th International Conference on Greenhouse Gas Control Technologies. Volume I: Peer Reviewed Papers and Overviews, E.S. Rubin, D.W. Keith, and C.F. Gilboy (eds.), Elsevier Science, Oxford, UK, 139-146.

Gibson, R.L, and Walmach, T. (1992). Metamorphism in the Okiep District: geological investigations into the genesis of the Koperberg Suite, Namaqualand. Unpublished report, Economic Geology Res Unit, University of the Witwatersrand, Johannesburg, pp 25–40

Gibson, R.L., Robb, L.J., Kisters, A.F.M., and Cawthorn, R.G. (1996). Regional setting and geological evolution of the O'okiep Copper District, Namaqualand, South Africa. . South African Journal of Geology, (99):107-120.

Gislason S.R., Wolff-Boenish D., Stefansson A., Oelkers E.H., Gunnlaugsson E., Sigurdardottir H., Sigfusson B., Broecker W.S., Matter J.M., Stute M., Axelsson G., Fridriksson T. (2010) Mineral sequestration of carbon dioxide in basalt: A pre-injection

overview of the CarbFix project. International Journal of Greenhouse Gas Control 4, 537-545.

Glaister, B. J., and Mudd, G. M. (2010). The environmental costs of platinum–PGM mining and sustainability: Is the glass half-full or half-empty? Environmental Engineering, Department of Civil Engineering, Monash University, Clayton 3800, Melbourne, Australia. Minerals Engineering 23 (2010) 438–450.

Goff, F., Guthrie, G., Counce, D., Kluk, E., Bergfeld, D., and Snow, M. (1997). "Preliminary Investigations on the Carbon Dioxide Sequestering Potential of Ultramafic Rocks." Los Alamos, NM: Los Alamos National Laboratory; LA-13328-MS.

Goff, F., and Lackner, K.S. (1998). Carbon dioxide sequestering using ultramafic rocks, Environmental Geosciences. (5), pp. 89-101.

Goff, F., Guthrie, G., Counce, D., Kluk, E., Bergfeld, D., and Snow, M. (2000). Evaluation of Ultramafic Deposits in the Eastern United States and Puerto Rico as sources of Magnesium for Carbon Dioxide Sequestration. LA-13694-Ms. Los Alamo, New Mexico, USA – Los Alamos National Laboratory.

Google Earth. (2012).https://earth.google.com [accessed: 14th August, 2012].

Google Earth. (2014). https://earth.google.com [accessed: 10th March, 2014]

Govender, V. and Vukea, N. A. (2007). Mineralogical characterisation of the Wesizwe Merensky feed and UG-2 rougher tailings. Mintek Internal Report, 12pp.

Green. A.N., and Smith A. M. (2012). Can ancient shelf sand ridges be mistaken for Gilbert-type deltas? Examples from the Vryheid Formation, Ecca Group, KwaZulu-Natal, South Africa. Journal of African Earth Sciences. Vol 76:27-33.

Gunter, W.D., Perkins, E.H., and McCann, T. J. (1993) Aquifer disposal of CO_2 - rich gases: reaction design for added capacity. Energy Conversion and Management, 34, 941–948.

Ha-Duong, M., and Keith, D. W. (2003). Carbon storage: The economic efficiency of storing CO_2 in leaky reservoirs. Clean Technologies and Environmental Policy, 5, 181–189.

Halbwachs, M., Sabroux, J.-C., Grangeon, J., Kayser, G., Tochon-Danguy, J.-C., Felix, A., Beard, J.-C., Villevieille, A., Vitter, G., Richon, B., Wuest, A. and Hell. J. (2004) Degassing the “Killer Lakes” Nyos and Monoun, Cameroon. EOS 85, No. 30, 27 July 2004, 281–288.

Hamman, J.N., Rozendaal, A. and Jordaan, W., (1996). Gabbro norite hosted Ni-Cu-(Co) sulphide mineralization in southern Namaqualand and its relationship to the cupriferous Koperberg Suite of the O’okiep Copper District, South Africa. . South African journal of geology, (99,):153-167.

Harris, C. C., (1971). Graphical presentation of size distribution data: an assessment of current practice, Trans. IMM Sect. C, 80, (Sept.) 133pp.

Hattenbach, R.P., Wilson, M., Brown, K. (1999). Capture of carbon dioxide from coal combustion and its utilization for enhanced oil recovery. In: Eliasson, B., Riemer, P.W.F., Wokaun, A. (Eds.), Greenhouse Gas Control Technologies. Elsevier Science, Amsterdam, pp. 217–221.

Heinrich, J.J., Herzog, H.J., Reiner, D.M. (2004). Environmental assessment of geologic storage of CO_2. MIT LFEE 2003-002 RP, revised, Massachusetts Institute of Technology. Presented at the Second National Conference on Carbon Sequestration, Washington, DC, May 5-8 (2003).

Herzog, H.J. (2010). Scaling up Carbon Dioxide Capture and Storage: From megatons to gigatons. Energy Economics. MIT Energy Institute, Cambridge, MA, USA.

Hill, C., Bognion, V., Follows, M., and Marshall, J. (2004). Evaluating carbon sequestration efficiency in an ocean model using adjoint sensitivity analysis. Journal of Geophysical Research-Oceans, 109, C11005, doi: 10.1029/2002JC001598.

Hodson, M.E. (1999). Micropore surface area variation with grain size in unweathered alkali feldspars: Implications for surface roughness and dissolution studies. Geochimica et Cosmochimica Acta 62(21/22): 3429–3435.

Hodson, M.E. (2006). Does reactive surface area depend on grain size? Results from pH3, 25°C far-from equilibrium flow-through dissolution experiments on anorthite and biotite. Geochimica et Cosmochimica Acta 70(7): 1655–1667.

Holloway, S., (1997). Safety of the underground disposal of carbon dioxide. Energy Conversion and Management, 38(Suppl.), S241–S245.

Holwell, D.A. (2011). Precious metal enrichment in the Platreef, Bushveld Complex, South Africa: evidence from homogenized magmatic sulfide melt inclusions. Contributions to mineralogy and petrology. 161(6):1011-1026.

Houghton, J.T., Ding, Y., Griggs, D.J., Noguer, N., van der Linden, P.J., Xiaosu, D., Maskell, K., and Johnson, C.A. (2001) . Climate Change 2001: The Scientific Basis. Contribution of working group I to the third assessment report of the Intergovernmental Panel on Climate Change. Cambridge, UK and New York, USA: Cambridge University Press.

Energy Economics 33 (2011) 597–604Huijgen, W.J.J., and Coman, R.N.J. (2005). Carbon dioxide sequestration by mineral carbonation: Literature review update 2003-2004, ECN-C--05-022, Energy Research Centre of The Netherlands, Petten, and The Netherlands.

Huijgen, W. 2006. Energy consumption and net CO_2 sequestration of aqueous mineral carbonation. Industrial engineering chemistry research. 45(26):9184-9194.

Humphries, G., Rule, C., and Wolmarans, E. (2006). The development of a process flowsheet for the new Anglo Platinum, PPRust north concentrator, incorporation HPGR technology. International Platinum Conference 'Platinum Surges Ahead'. The Southern African Institute of Mining and Metallurgy, 2006.

Huntzinger, D.N., Gierke, J.S., Sutter, L.L., Kawatra, S.K., and Eisele, T.C. (2009). Mineral carbonation for carbon sequestration in cement kiln dust from waste piles. Journal of Hazardous Materials 168, 31-37.

IEA CCC. (2005). IEA CCC (IEA Clean Coal Centre). The World Coal fired Power Plants Database, Gemini House, Putney, London, United Kingdom.

IEA WEO (2004). IEA World Energy Outlook 2004, International Energy Agency, Paris France.

IISD Reporting Services, (2009). Carbon Capture and storage Bulletin. A Summary of the high level Conference on Fighting Climate Change with Carbon Capture and Storage. Available at: http://www.iisd.ca/ymb/climate/ccs/ [Accessed: June 7, 2015].

Impala Platinum Annual Report (2013). Retrieved from: http://www.implats.co.za/implats_integrated_report_2013.asp [Accessed: 04 March 2014].

International Energy Agency. (2011). CO_2 emissions from fuel consumption highlights [internet]. [Online]. Available: http://www.iea.org/co2highlights/co2highlights.pdf [Accessed: May 9, 2012].

International Panel on Climate Change (IPCC), (2002). Workshop on Carbon Dioxide Capture and Storage. Proceedings published by ECN, the Netherlands.

Jacobs, A.D. (2011). Experimental mineral carbonation: Approaches to accelerate CO_2 sequestration in mine waste materials. International Journal of Mining, Reclamation and Environment. 25(4):321-331.

Jacobs, A.D. (2014). Quantifying the mineral carbonation potential of mine waste material: a new parameter for geospatial estimation. A thesis submitted in partial fulfilment of the requirement for the degree of Doctor of Philosophy in Mining Engineering. The University of British Columbia, Vancouver.

Kelemen P.B., Matter J.R. (2008) In situ carbonation of peridotite for CO_2 storage. Proceedings of the National Academy of Sciences 105, 17295-17300.

Kenyon, A.K., Attridge, R. L., and Coetzee, G. L. (1986). The Uitkomst Nickel-Copper Deposit, Eastern Transvaal. Anhaeusser. C. R., Maske, S., (eds), Mineral Deposits of Southern Africa. Geological Society of South Africa, Johannesburg. Vv2 pp 1009-1017.

Kinnaird, J. A., Hutchinson, L., Schurmann, Nex P. A. M., and de Lange, R. (2005). Petrology and mineralization of the southern Platreef: northern limb of the Bushveld Complex, South Africa. Mineralium Deposita 40, 576–597.

Kisters, A. F. M., Potgieter, J. E., Charlesworth, E. G., Anhaeusser, C. R., Gibson, R. L. and Watkeys, M. K. (1994) Emplacement feature of cupriferous noritoids in the Okiep Copper District, Namaqualand, South Africa. Exploration and Mining Geology 3(3), 297-310.

Kleyn, E.G., and Bergh, A. O. (2008). Some aspects regarding the handling of dolerite for base and sub-base construction. Proceedings of the 27th South African Transport Conference (SATC 2008), 98-107.

Kohl, A. L. and Nielsen, R. (1997). Gas Purification, Fifth Edition. Gulf Professional Publishing, 1997.

Korbol, R. and Kaddour, A. (1994). Sleipner West CO_2 disposal: injection of removed CO_2 into the Utsira formation. Energy Conversion and Management, 36(6–9), 509–512.

Kusakabe, M., and Sano, Y. (1992). Origin of gases in Lake Nyos, Cameroon. Natural Hazards in West and Central Africa, International Monograph Series on Interdisciplinary Earth Science Research and Applications (Freeth, S. J., Ofoegb, C. O. and Onohua, K. M., eds.), 83–95, Friedrich Viewegand Sohn Verlag, Braunschweig, Wiesbaden.

Kwak, J.H., Hu, J.Z., Hoyt, D.W., Sears, J.A., Wang, C. Rosso, K.M., Felmy, A.R. (2010). Metal carbonation of forsterite in supercritical CO_2 and H_2O using solid state 29Si, 13C NMR spectroscopy. The Journal of Physical Chemistry C 114, 4126-4134.

Lackner, K.S., Wendt, C.H., Butt, D.P., Joyce, E.L. Jr., and Sharp, D.H., (1995). Carbon dioxide disposal in carbonate minerals. Energy 20: 1153-1170.

Lackner, K. S. (2003). Climate change: A guide to CO_2 sequestration. Science. 300(1677):8.

Lebowa Platinum Limited Technical Report. (2006). Retrieved from: http://www.sec.gov/Archives/edgar/data/1028277/000119312511020420/dex994.htm [Accessed: 04 March 2014].

Lekgau, S. (2012). Mineralogical characterization of Amandelbult Section Dam 1 mine tailings for Mineral Carbonation. An unpublished dissertation submitted as part of requirements for the award of a Bachelor of Science Honours degree by the University of Cape Town.

Li, C., Ripley, E. M., Maier, W. D. and Gomwe, T. E. S. (2002). Olivine and sulfur isotopic compositions of the Uitkomst Ni-Cu sulphide ore-bearing complex, South

Africa: evidence of sulfur contamination and multiple magma emplacements. Chemical Geology. 1 September 2002, Vol.188 (3): 149-159.

Lim, M., Han, G-C., Ahn, J-W., and You, K-S. (2010). Environmental Remediation and Conversion of Carbon Dioxide (CO_2) into Useful Green Products by Accelerated Carbonation Technology. International Journal of Environmental Research and Public Health. 7(1):203-228.

Liu Z., and Zhao J. (1999). Contribution of carbonate rock weathering to the atmospheric CO_2 sink. Environmental Geology 39, 1053-1058.

Lombaard, A. F., and Schreuder, F. J. G. (1978). The distribution patterns and general geological features of steep structures, megabreccias and basic rocks in the Okiep Copper District. Spec Publication. Geological Society South Africa 4:269–295.

Lombaard, A. F. (1986). The copper deposits of the Okiep Copper District, Namaqualand. In: Anhaeusser CR, Maske S (eds) Mineral deposits of southern Africa. Geological Society South Africa II, pp 1421-1445.

Lossin, A. (2001). Copper. Ullmann's Encyclopaedia of Industrial Chemistry. DOI: 10.1002/14356007.a07_471.

Mani, D., Nirmal Charan, S. and Kumar, B. (2008). Assessment of carbon dioxide sequestration potential of ultramafic rocks in the greenstone belts of southern India. Current Science, 1, 94pp.

Manyeruke, T.D. (2003). The petrography and geochemistry of the Platreef on the farm Townlands, near Potgietersrus northern Bushveld Complex. A thesis submitted for the degree of Master of Science at the University of Pretoria.

Marais, J. A. N., Agenbacht, A. L. D., Prinsloo, M., and Basson, W.A (2001). The Geology of the Springbok Area. Council for Geosciences, South Africa. : pp 3-7.

Maroto-Valer, M.M., Fauth, D. J., Kuchta, M.E., Zhang, Y., and Andresen, J. M. (2005). Activation of magnesium rich minerals as carbonation feedstock materials for CO_2 sequestration. Fuel processing technology. 86(1627):45.

Matter, J.M., and Kelemen, P. B. (2009). Permanent storage of carbon dioxide in geological reservoirs by mineral carbonation. Nature geoscience. 2(12):837-841.

Mathivha, R. (2010). Carbonation of dolerite dykes intruding into coal seams: Natural sequestration during fossil fuel combustion. Thesis. Department of Geological Sciences. University of Cape Town.

McDonald, I., Holwell, D.A. and Armitage, P. E. B. (2005). Geochemistry and mineralogy of the Platreef and "Critical Zone" of the northern lobe of the Bushveld Complex, South Africa: implications for Bushveld stratigraphy and the development of PGE mineralization. Mineralium deposita. 40(5):526-549.

Merkle, R. K.W., and McKenzie, A.D. (2002). The Mining and Beneficiation of South African PGE ores - An Overview, The Geology, Geochemistry, Mineralogy and Mineral Beneficiation of Platinum-Group Elements. Edited by L.J. Cabri. Canadian Institute of Mining, Metallurgy and Petroleum, Special volume 54, pp 793-810.

Metorex limited Annual Report (2003). www.shreadata.co.za/metorex_ar_03 [Accessed: 05 March 2014].

Metz, B., Davidson, O., de Coninck, H., Loos, M., and Meyer, L. (2005). Intergovernmental Panel on Climate Change (IPCC) special report on carbon dioxide capture and storage. Prepared by working group III. Cambridge, UK and New York, USA: Cambridge University Press.

Meyer, N. (2011). Naturally Carbonated Dolerite Dykes in the Karoo Coal Measures, South Africa. A mini-dissertation submitted for an Honours degree at the Department of Geological Sciences, University of Cape Town.

Meyer, N. (2014). An investigation into the dissolution of pyroxene: A precursor to mineral carbonation of PGM tailings in South Africa. A thesis submitted for the degree of Master of Science at the University of Cape Town, Cape Town, South Africa.

Mishra, G., Viljoen K, S. and Mouri, H. (2013). Influence of mineralogy and ore texture on pentlandite flotation at the Nkomati nickel mine, South Africa. Minerals Engineering. December 2013, Vol.54:63-78, doi:10.1016/j.mineng.2013.04.009.

Naldrett, A. J. (1989). Magmatic sulfide deposits. New York: New York: Clarendon Press Oxford University Press. Oxford monographs on geology and geophysics no. 14. pp 159-177.

Naldrett, A.J., Wilson, A., Kinnaird, J., Yudovskaya, M., and Chunnett, G. (2012). The origin of chromitites and related PGE mineralization in the Bushveld Complex: New mineralogical and petrological constraints. (Report). Mineralium deposita. 47(3):209-232.

Namibia Press Agency (2013). ManPower to Import one million LED bulbs – The Namibian. Business Issue. 15 October 2013. Retrieved from: http://www.namibian.com.na/print.php?id=11596&type=2 [Accessed: 09 June 2014].

Netty, S., Wardiyati, T., Handayanto, E. and Maghfoer, M. D. (2012). Nickel accumulating plants in the post-mining land of Sorowako, South Sulawesi, Indonesia. Journal of tropical agriculture. 50(1):45-48.

Ngwagwe, M. (2009). The impact of alteration on the detectability of dolerite dykes by Aeromagnetics. Thesis. Department of Geological Sciences. University of Cape Town.

Nicks, L. and Chambers, M. F. (1998). A pioneer study of the potential of phytomining for nickel. In: brooks, R. R.(ed.), Plants that hyperaccumulate heavy metals, pp. 313-326. CAB, Wallingford, UK.

NITG (2006). Netherlands Institute of Applied Geoscience, TNO. Retireved from: http://www.nitg.tno.nl /eng /projects /6_stor /index.shtml [accessed: 5th August, 2012].

Nixon, P. H., (1995). The morphology and nature of primary diamondiferous occurrences. Journal of Geochemical Exploration, 53:41-71.

Norisor, M., Badea, A., and Dinca, D. (2012). Economical and Technical Analysis of CO_2 Transport Ways. U.P.B. Sci. Bull., Series C, Vol. 74 (1), 303-308.

Oelkers E.H., Gislason S.R., Matter J. (2008). Mineral carbonation of CO_2. Elements 4, 331-335.

Ougougdal, M. A., Robb, L. J., Lespinasse, M., Cathelineau, M., and Boiron, M. C. (1996). The nature of fluids associated with granulite facies metamorphism in the Okiep Copper District, Namaqualand, South Africa. South African Journal Geology 99:197–208.

Penner, J. E., Zhang, S. and Ito, A. (2004). Estimates of black carbon emissions from open biomass burning, Eos Trans. AGU, 84(47), Fall Meet. Suppl., Abstract A 12B-01.

Perez-Lopez, R., Montes-Hernandez, G., Nieto, J.M., Renard, F., and Charlet, L. (2008). Carbonation of alkaline paper mill waste to reduce CO_2 greenhouse gas emissions into the atmosphere. Applied Geochemistry 23, 2292-2300.

Phadi, T., T. (2012). Titanium oxide- carbon spheres composite for use as supports in Cobalt Fischer-Tropsch synthesis. A thesis submitted to the Faculty of Science at the University of Witwatersrand, Johannesburg, in fulfilment of the requirement for the degree of Doctor of Philosophy.

Power, I. M., Wilson, S. A., Small, D. P., Dipple, G. M. Wan, W., and Southam, G. (2011). Bioleaching of ultramafic tailings by Acidithiobacillus spp. for CO_2 sequestration. Environmental Science and Technology. 45 (20), 9061–9068.

Praetorius, B. and Schumacher, K. (2009). Greenhouse gas mitigation in a carbon constrained world: the role of carbon capture and storage. Energy policy. 37(50):81-93.

Priestnall, M. (2013). Mineral Carbonation- an industrial perspective on a commercial route to negative CO_2 emission. Conference Proceedings, Cambridge Carbon Capture. 13th March 2013, RAE, London.

Pronost, J., Beaudoin, G., Tremblay, G., Larachi, F., Duchesne, J., Hebert, R., and Constantin, M. (2011). Carbon Sequestration Kinetic and Storage Capacity of Ultramafic Mining Waste. Environmental science technology. 45(21):9413-9420.

Raith, J. G., and Harley, S. L. (1998). Low-P/high-T metamorphism in the Okiep Copper District, western Namaqualand, South Africa. Journal of Metamorphic Geology 16:281–305.

Raza, Y. (2009). Uncertainty analysis of capacity estimates and leakage potential for geologic storage of carbon dioxide in saline aquifers. Master's thesis, Massachusetts Institute of Technology.

Renforth, P., Washbourne, C. –L, Taylder, J., and Manning D. A. C. (2011). Silicate Production and Availability for Mineral Carbonation. Environmental science & technology. 45(6):2035-2041.

Retsch (2009). Sieve Analysis: Taking a close look at quality.

Riemer, P., Eliasson, B., and Wokaun, A. (Eds.) (1999). Greenhouse gas control technologies. Amsterdam: Elsevier.1999.

Ringane, B. (2003). Impact of alteration on the detectability of dolerite dykes by aeromagnetics, New Denmark Colliery, Mpumalanga. Thesis. Department of Geological Sciences. University of Cape Town.

Robb, L. J., Armstrong, R. A., and Waters, D. J. (1999). The history of granulite facies metamorphism and crustal growth from single zircon U–Pb geochronology, Namaqualand, South Africa. J Petrol 40:1747–1770.

Rose, D. (2011). Detailed assessment of platinum-group mineral associated with chromitite stringers in the Eastern Bushveld Complex, South Africa. Canadian mineralogist. 49(6):1385-1396.

Rubin, E.S. and Rao, A.B. (2003). Uncertainties in CO_2 capture and sequestration costs, Greenhouse Gas Control Technologies, Proceedings of the 6th International Conference on Greenhouse Gas Control Technologies (GHGT-6), 1-4 Oct. 2002, Kyoto, Japan, J. Gale and Y. Kaya (eds.), Elsevier Science Ltd, Oxford, UK.

Rudashevsky, N, s., Garuti, G., Andersen, J. and Zaccarini, F. (2002). Separation of accessory minerals from rocks and ores by hydroseparation (HS) technology: Method and application to CHR-2 chromitite, Niquelandia intrusion, Brazil. In: Applied Earth Science. IMM Transactions section B 111(1): 87-94. April 2002. DOI: 10.1179/aes.2002.111.1.87.

Rule, C.M. (2009). Energy consideration in the current PGM processing flowsheet utilizing new technologies. The journal of the South African Institute of Mining and Metallurgy. 108:39-46.

Sarkar, A., Ripley, E.M., Li, C. and Maier, W.D. (2008) Stable isotope, fluid inclusion, and mineral chemistry constraints on contamination and hydrothermal alteration in the Uitkomst Complex, South Africa. Chemical Geology, 257, 129-138.

Sarv, H. (2001). Large-scale CO_2 transportation and deep ocean sequestration - Phase II final report. McDermott Technology Inc., Ohio. Technology Report DE-AC26-98FT40412, 2001.

Schouwstra, R. P., Kinloch, E. D., and Lee, C. A. (2000). A Short Geological Review of the Bushveld Complex. Platinum Metal REV., 2000, 44, (1). 33-39.

Scoates, J.S., and Friedman, R.M. (2008). Precise age of the platiniferous Merensky Reef, Bushveld complex, South Africa by the U–Pb zircon chemical abrasion ID-TIMS technique. Economic Geology 103 (3), 465–471.

Seiersten, M. (2001). Material selection for separation, transportation and disposal of CO_2. Proceedings Corrosion 2001, National Association of Corrosion Engineers, paper 01042.

Seifritz, W. (1990). CO_2 disposal by means of silicates, Nature. (345), 486–486.

Shakun, J., Clark, P. U., He, F., Marcott,S. A., Mix, A. C., Liu,Z., Otto-Bliesner, B., Schmittner, A. and Bard, E. (2012). Global warming preceded by increasing carbon dioxide concentrations during the last deglaciation. Nature. 484(7392): 49–54.

Sharman, E.R., Penniston-Dorland, S.C., Kinnaird, J.A., Nex, P.A.M., Brown, M., Wing, B.A., (2013). Primary origin of marginal Ni-Cu-PGE mineralization in layered intrusions: $\Delta^{33}S$ evidence from the Platreef, Bushveld, South Africa. Economic Geology. : 365-377.

Sigurdsson, H., Devine, J. D., Tchoua, F. M., Presser, T. S., Pringle, M. K. W. and Evans W. C. (1987) Origin of the lethal gas burst from Lake Monoun, Cameroon. J. Volc. Geotherm. Res. 31, 1-16.

Sipilä, J., Teir, S., and Zevenhoven, R. (2008). Carbon dioxide sequestration by mineral carbonation Literature review update 2005–2007. Åbo Akademi University Faculty of Technology Heat Engineering Laboratory. Report VT 2008-1.

Solomon, S., Qin, D., Manning, M., Chen, Z., Marquis, K.B., Averyt, M., and Miller, H.L. (2007). Climate change 2007: The Physical Science Basis. Contribution of working group I to the fourth assessment report of the Intergovernmental Panel on Climate Change. Cambridge, UK and New York, USA: Cambridge University Press.

Strauss, C. A. (1941). The geology, copper-ore deposits and ground water hydrology of the area around Springbok and O'okiep, Namaqualand. Unpublished DSc thesis, University of Stellenbosch, p 166.

Stumpfl, E.F., Clifford, T.N., Burger, A.J., and Zyl, V. (1976). The copper deposits of the O'Okiep district. South Africa: new data and concepts: Mineral Deposita 11:46–70.

Surridge, A.D and Cloete, M. (2009). Carbon capture and storage in South Africa. Energy procedia. 1:2741-2744.

Svensson, R., Odenberger, M., Johnsson, F., and Stromberg, L. (2004). Transportation systems for CO_2 - application to carbon capture and storage. Energy conservation and management. 45(23):43-53.

Theart, H.F.J. and de Nooy, C.D. (2001). The Platinum Group Minerals in two parts of the Massive Sulfide Body of the Uitkomst Complex, Mpumalanga, South Africa. South African Journal of Geology, 104, 287-300.

Thompson, M. Y. (1991). Copper. Metals and Minerals Annual Review 43: 83 – 92.

True, W.R., (1990). U.S. gas pipelines improve operations, want to expand. Oil & Gas Journal 88 (48), 41–63.

United States Environmental Protection Agency (USEPA). (1994). Technical Report. Design and Evaluation of tailings dams. Office of Solid Waste. Special Waste Branch. 401 m Street, SW. Washington, DC 20460.

van Alphen, K., Hekkert, M.P., and Turkenburg, W.C. (2010). Accelerating the deployment of carbon capture and storage technologies by strengthening the innovation system. International Journal of Greenhouse Gas Control. 4(2):396-409.

van der Merwe, M.J. (2008). The geology and structure of the Rustenburg Layered Suite in the Potgietersrus/Mokopane area of the Bushveld Complex, South Africa. Mineralium deposita. 43(4):405-419.

Van der Merwe, K. (2012). Primary crusher report dd12Jul2012. Report, IME, 12 July 2012.

Van Zwieten (1996). A petrogenetic model of the Koperberg Suite: Evidence from the Jubilee Mine, Namaqualand, South Africa. South African Journal of Geology. 99(2):121-134. June 1996.

Van Zyl D. (1978). A petrological approach towards the ore-bearing potentialities of the Okiep basic rocks in Namaqualand. Spec Pub. Geological Society South Africa 4:323–329.

Vermaak, C.F. (1995). The Platinum Group Metals: A Global Perspective. Mintek, Randburg, 1995,247 pp.

Vermaak, C. F and van der Merwe, M.J (1999). The Platinum Mines and Deposits of the Bushveld Complex, South Africa. Randburg, South Africa.

Vogeli, J., Reid, D. L., Becker, M., Broadhurst, J., and Franzidis, J-P. (2011). Investigation of the potential for mineral carbonation of PGM tailings in South Africa. Minerals engineering. 24(12):1348-1356.

Vogeli, J. (2012). Investigation of the potential for mineral carbonation of South African PGM tailings. A dissertation in fulfilment of Masters in Chemical Engineering at the University of Cape Town.

Voordouw, R. J., Gutzmer, J., and Beukkes, N. J. (2010) and others. Zoning of platinum group mineral assemblages in the UG-2 chromitite determined through in situ SEM-EDS-based image analysis. Mineralium deposita. 45(2):147-159.

Wills, B. A., and Atkinson, K. (1991). The development of minerals engineering in the 20th century. Mineral Engineering 4 (7-11) 643.

Wills, B. A. (1997). Mineral Processing Technology. An introduction to the practical aspects of ore treatment and mineral recovery. Sixth edition. Butterworth-Heinemann. Linacre House, Jordan Hill, Oxford OX2 8DP.

Yamasaki, A. (2003). An overview of CO_2 mitigation options for global warming emphasizing CO_2 sequestration options. Journal of Chemical Engineering of Japan. 38(4):361-75.

Yuan D. (1997). The carbon cycle in karst. Zeitschrift fur Geomorph Suppl-Bd.108, 91-102.

Zevenhoven, R., Eloneva, S., Teir, S. (2006). Chemical fixation of CO_2 in carbonates: Routes to valuable products and long-term storage, Catalysis Today. (115), pp. 73-79.

Zevenhoven, R., Fagerlund, J., and Songok, J.K., (2011). Review: CO_2 mineral sequestration: developments towards large scale application. Greenhouse Gas Science Technology. 1:48–57.

Zhao, L., Sang, L., Chen, J., Ji, J., and Teng, H.H. (2010). Aqueous carbonation of natural brucite: Relevance to CO_2 sequestration. Environmental Science and Technology 44, 406-411.

APPENDICES

A. Particle Size Analysis

A 1 Screening Exercise

A1.1. Impala

Table A. 1: Wet screening analysis results for IMP/001.

Sample No.	Size Fraction (µm)	Weight(g)	wt%	cumulative %
IMP/001A	Bulk (unsized)	102.15		
IMP/001A	150	34.02	33.95	33.95
	106	22.61	22.56	56.51
	75	19.65	19.61	76.11
	53	16.27	16.23	92.35
	38	6.24	6.23	98.57
	25	1.23	1.23	99.80
	<25	0.20	0.20	100.00
Total		100.22	100.00	

Table A. 2: Dry screening analysis results for IMP/001.

Sample No.	Size Fraction (µm)	Weight(g)	wt%	cumulative %
IMP/001B	Bulk (unsized)	101.79		
IMP/001B	150	35.02	34.62	34.62
	106	23.13	22.87	57.49
	75	24.82	24.54	82.03
	53	11.4	11.27	93.30
	38	4.6	4.55	97.84
	25	2.15	2.13	99.97
	<25	0.03	0.03	100.00
Total		101.15	100.00	

Table A. 3: IMP/001 results for screening analysis which involves dry screening following a wet screening exercise.

Sample No.	Size Fraction (µm)	Weight(g)	wt%	cumulative %
IMP/001C	Bulk (unsized)	101.3		
IMP/001C	150	34.84	34.53	34.53
	106	21.06	20.87	55.40
	75	23.19	22.98	78.38
	53	13.1	12.98	91.36
	38	6.21	6.15	97.51
	25	2	1.98	99.49
	<25	0.51	0.51	100.00
Total		100.91	100.00	

Table A. 4: Wet screening results for Impala sample IMP/003

Sample No.	Size Fraction (µm)	Weight(g)	wt%	cumulative %
IMP/003A	Bulk (unsized)	100		
IMP/003A	150	30.41	31.27	31.27
	106	16.45	16.92	48.19
	75	16.4	16.87	65.06
	53	10.98	11.29	76.35
	38	19.31	19.86	96.21
	25	3.69	3.79	100.00
	<25	0	0	100.00
Total		97.24	100.00	

Table A. 5: IMP/003 dry screening results.

Sample No.	Size Fraction (µm)	Weight(g)	wt%	cumulative %
IMP/003B	Bulk (unsized)	103.33		
IMP/003B	150	31.41	30.46	30.46
	106	18.23	17.68	48.13
	75	17.2	16.68	64.81
	53	18.34	17.78	82.59
	38	17.03	16.51	99.11
	25	0.92	0.89	100.00
	<25	0	0	100.00
Total		103.13	100.00	

Table A. 6: A combined wet and dry screen test results for IMP/003.

Sample No.	Size Fraction (µm)	Weight(g)	wt%	cumulative %
IMP/003C	Bulk (unsized)	102.32		
IMP/003C	150	29.46	29.08	29.08
	106	17.33	17.11	46.19
	75	16.68	16.47	62.66
	53	13.71	13.54	76.20
	38	22.01	21.73	97.93
	25	2.1	2.07	100.00
	<25	0	0	100.00
Total		101.29	100.00	

A1.2. Amandelbult

Table A. 7: Wet screening analysis results for AMB/101.

Sample No.	Size Fraction (µm)	Weight(g)	wt%	cumulative %
AMB/101A	Bulk (unsized)	98.88		
AMB/101A	150	13.5	14.29	14.29
	106	21.39	22.64	36.93
	75	20.81	22.03	58.96
	53	21.3	22.55	81.51
	38	8.46	8.96	90.47
	25	7.32	7.75	98.22
	<25	1.68	1.78	100.00
Total		94.46	100.00	

Table A. 8: Dry screening results for Amandelbult sample, AMB/101.

Sample No.	Size Fraction (µm)	Weight(g)	wt%	cumulative %
AMB/101B	Bulk (unsized)	101.32		
AMB/101B	150	13.85	14.29	14.29
	106	21.44	22.12	36.41
	75	19.57	20.19	56.60
	53	23.61	24.36	80.96
	38	11.4	11.76	92.72
	25	6.04	6.23	98.95
	<25	1.02	1.05	100.00
Total		96.93	100.00	

Table A. 9: Combined wet and dry screening test results for AMB/101.

Sample No.	Size Fraction (µm)	Weight(g)	wt%	cumulative %
AMB/101C	Bulk (unsized)	103.3		
AMB/101C	150	13.47	14.29	14.29
	106	21.1	22.39	36.68
	75	20.3	21.54	58.23
	53	20	21.22	79.45
	38	11.04	11.72	91.17
	25	7.3	7.75	98.91
	<25	1.02	1.08	100.00
Total		94.23	100.00	

Table A. 10: Amandelbult (S/4-TD44) wet screening results.

Sample No.	Size Fraction (µm)	Weight(g)	wt%	cumulative %
S/4-TD44 (A)	Bulk (unsized)	107.72		
S/4-TD44 (A)	150	15.94	15.74	15.74
	106	14.63	14.45	30.20
	75	13.79	13.62	43.82
	53	11.93	11.78	55.60
	38	7.21	7.12	62.72
	25	10.34	10.21	72.94
	<25	27.4	27.06	100.00
Total		101.24	100.00	

Table A. 11: Dry screening results for S/4-TD44.

Sample No.	Size Fraction (µm)	Weight(g)	wt%	cumulative %
S/4-TD44 (B)	Bulk (unsized)	103.47		
S/4-TD44 (B)	150	13.5	13.92	13.92
	106	11.64	12.00	25.93
	75	10.54	10.87	36.79
	53	9.61	9.91	46.71
	38	8.61	8.88	55.58
	25	13.64	14.07	69.65
	<25	29.43	30.35	100.00
Total		96.97	100.00	

Table A. 12: Results for a combined screening exercise for S/4-TD44.

Sample No.	Size Fraction (µm)	Weight(g)	wt%	cumulative %
S/4-TD44 (C)	Bulk (unsized)	102.17		
S/4-TD44 (C)	150	12.23	12.53	12.53
	106	11.12	11.39	23.92
	75	10.1	10.35	34.27
	53	9.5	9.73	44.01
	38	8	8.20	52.20
	25	16.21	16.61	68.81
	<25	30.44	31.19	100.00
Total		97.6	100.00	

Table A. 13: Results for S/4-TD83 wet screening analysis.

Sample No.	Size Fraction (µm)	Weight(g)	wt%	cumulative %
S/4-TD83 (A)	Bulk (unsized)	101.57		
S/4-TD83 (A)	150	16.29	16.41	16.41
	106	14.55	14.66	31.06
	75	12.75	12.84	43.91
	53	13.75	13.85	57.76
	38	11.96	12.05	69.80
	25	8.96	9.02	78.83
	<25	21.02	21.17	100.00
Total		99.28	100.00	

Table A. 14: S/4-TD83 dry screening results.

Sample No.	Size Fraction (µm)	Weight(g)	wt%	cumulative %
S/4-TD83 (B)	Bulk (unsized)	102.53		
S/4-TD83 (B)	150	15.91	16.21	16.21
	106	15.1	15.38	31.59
	75	12.97	13.21	44.80
	53	15.35	15.64	60.44
	38	16.27	16.57	77.02
	25	10.65	10.85	87.87
	<25	11.91	12.13	100.00
Total		98.16	100.00	

Table A. 15: S/4-TD83 combined screening analysis results.

Sample No.	Size Fraction (µm)	Weight(g)	wt%	cumulative %
S/4-TD83 (C)	Bulk (unsized)	104.84		
S/4-TD83 (C)	150	15.65	15.42	15.42
	106	15.14	14.92	30.35
	75	13.03	12.84	43.19
	53	16.79	16.55	59.74
	38	11.84	11.67	71.41
	25	8.99	8.86	80.27
	<25	20.02	19.73	100.00
Total		101.46	100.00	

Table A. 16: Wet screening results for S3/TD43.

Sample No.	Size Fraction (µm)	Weight(g)	wt%	cumulative %
S3-TD43(A)	Bulk (unsized)	103.71		
S3-TD43(A)	150	14.66	14.95	14.95
	106	13.91	14.19	29.14
	75	11.83	12.07	41.21
	53	14.93	15.23	56.44
	38	10.4	10.61	67.04
	25	11.33	11.56	78.60
	<25	20.98	21.40	100.00
Total		98.04	100.00	

Table A. 17: Results for S3/TD43 dry screening analysis.

Sample No.	Size Fraction (µm)	Weight(g)	wt%	cumulative %
S3-TD43(B)	Bulk (unsized)	99.45		
S3-TD43(B)	150	13.29	14.47	14.47
	106	11.94	13.00	27.47
	75	10.83	11.79	39.27
	53	8.85	9.64	48.91
	38	7.59	8.27	57.17
	25	14.86	16.18	73.35
	<25	24.47	26.65	100.00
Total		91.83	100.00	

Table A. 18: Combined screening results for S3/TD43.

Sample No.	Size Fraction (µm)	Weight(g)	wt%	cumulative %
S3-TD43(C)	Bulk (unsized)	101.97		
S3-TD43(C)	150	13.94	14.70	14.70
	106	12.2	12.86	27.56
	75	11.28	11.89	39.45
	53	14.96	15.77	55.22
	38	11.11	11.71	66.94
	25	9.1	9.59	76.53
	<25	22.26	23.47	100.00
Total		94.85	100.00	

A1.3. Mogalakwena

Table A. 19: MPL/101 wet screening results.

Sample No.	Size Fraction (µm)	Weight(g)	wt%	cumulative %
MPL/101A	Bulk (unsized)	102.44		
MPL/101A	150	3.86	3.99	3.99
	106	4.35	4.50	8.50
	75	10.59	10.96	19.46
	53	15.34	15.87	35.33
	38	13.93	14.42	49.75
	25	11.6	12.00	61.75
	<25	36.96	38.25	100.00
Total		96.63	100	

Table A. 20: Dry screening results for MPL/101.

Sample No.	Size Fraction (µm)	Weight(g)	wt%	cumulative %
MPL/101B	Bulk (unsized)	102.51		
MPL/101B	150	4.34	4.29	4.29
	106	6.94	6.87	11.16
	75	10.82	10.70	21.86
	53	17.49	17.30	39.16
	38	16.16	15.99	55.15
	25	23.64	23.39	78.53
	<25	21.7	21.47	100.00
Total		101.09	100	

Table A. 21: MPL/101 combined wet and dry screening results.

Sample No.	Size Fraction (µm)	Weight(g)	wt%	cumulative %
MPL/101C	Bulk (unsized)	101.75		
MPL/101C	150	3.4	3.68	3.68
	106	4.37	4.73	8.41
	75	9.68	10.48	18.89
	53	15.8	17.11	36.00
	38	14.01	15.17	51.16
	25	14.15	15.32	66.48
	<25	30.96	33.52	100.00
Total		92.37	100	

A1.4. Union Section

Table A. 22: Union Section (UST/201) wet screening results.

Sample No.	Size Fraction (µm)	Weight(g)	wt%	cumulative %
UST/201A	Bulk (unsized)	98.07		
UST/201A	150	2.81	2.99	2.99
	106	5.69	6.04	9.03
	75	11.86	12.60	21.63
	53	14.27	15.16	36.79
	38	13.24	14.07	50.86
	25	7.99	8.49	59.34
	<25	38.27	40.66	100.00
Total		94.13	100.00	

Table A. 23: Dry screening results for UST/201.

Sample No.	Size Fraction (µm)	Weight(g)	wt%	cumulative %
UST/201B	Bulk (unsized)	104.35		
UST/201B	150	3.64	3.66	3.66
	106	6.84	6.88	10.53
	75	13.21	13.28	23.81
	53	15.44	15.52	39.33
	38	17.31	17.40	56.74
	25	11.34	11.40	68.13
	<25	31.7	31.87	100.00
Total		99.48	100.00	

Table A. 24: Combined wet-dry screening results for UST/201.

Sample No.	Size Fraction (µm)	Weight(g)	wt%	cumulative %
UST/201C	Bulk (unsized)	100.79		
UST/201C	150	2.67	2.84	2.84
	106	5.73	6.09	8.93
	75	12.02	12.78	21.72
	53	14.98	15.93	37.65
	38	13.12	13.95	51.61
	25	8.84	9.40	61.01
	<25	36.66	38.99	100.00
Total		94.02	100.00	

A1.5. Rustenburg

Table A. 25: WRT/101 wet screening results.

Sample No.	Size Fraction (µm)	Weight(g)	wt%	cumulative %
WRT/101A	Bulk (unsized)	101.44		
WRT/101A	150	1.33	1.42	1.42
	106	2.5	2.68	4.10
	75	6.61	7.08	11.18
	53	11.54	12.35	23.53
	38	12.58	13.47	36.99
	25	13.39	14.33	51.33
	<25	45.47	48.67	100.00
Total		93.42	100.00	

Table A. 26: Dry screening results for WRT/101.

Sample No.	Size Fraction (µm)	Weight(g)	wt%	cumulative %
WRT/101B	Bulk (unsized)	105.58		
WRT/101B	150	3.64	3.64	3.64
	106	4.3	4.30	7.95
	75	5.37	5.38	13.32
	53	14.84	14.86	28.18
	38	13.62	13.63	41.82
	25	18.58	18.60	60.42
	<25	39.54	39.58	100.00
Total		99.89	100.00	

Table A. 27: A combined wet-dry screening result for WRT/101.

Sample No.	Size Fraction (µm)	Weight(g)	wt%	cumulative %
WRT/101C	Bulk (unsized)	102.06		
WRT/101C	150	1.57	1.64	1.64
	106	3.02	3.16	4.81
	75	7.14	7.48	12.29
	53	12.32	12.91	25.19
	38	13.68	14.33	39.52
	25	15.54	16.28	55.80
	<25	42.19	44.20	100.00
Total		95.46	100.00	

A1.6. O'okiep

Table A. 28: Wet screening results for OKP-1.

Sample No.	Size Fraction (µm)	Weight(g)	wt%	cumulative %
OKP-1A	Bulk (unsized)	98.07		
	150	27.61	29.37	29.37
	106	14.78	15.72	45.09
	75	22.48	23.91	69.00
	53	14.62	15.55	84.55
	38	9.17	9.75	94.30
	25	3.9	4.15	98.45
	<25	1.46	1.55	100.00
Total		94.02	100.00	

Table A. 29: OKP-1 dry screening results.

Sample No.	Size Fraction (µm)	Weight(g)	wt%	cumulative %
OKP-1B	Bulk (unsized)	101.84		
	150	28.19	28.11	28.11
	106	14.93	14.89	42.99
	75	25.55	25.47	68.46
	53	17.43	17.38	85.84
	38	11.59	11.56	97.40
	25	1.93	1.92	99.32
	<25	0.68	0.68	100.00
Total		100.3	100.00	

Table A. 30: Table A 30: Combined screening results for OKP-1.

Sample No.	Size Fraction (µm)	Weight(g)	wt%	cumulative %
OKP-1C	Bulk (unsized)	101.61		
	150	28.02	28.53	28.53
	106	14.21	14.47	43.00
	75	22.1	22.50	65.50
	53	15.3	15.58	81.07
	38	10.04	10.22	91.30
	25	5.47	5.57	96.86
	<25	3.08	3.14	100.00
Total		98.22	100.00	

Table A. 31: OKP-2 wet screening results.

Sample No.	Size Fraction (µm)	Weight(g)	wt%	cumulative %
OKP-2A	Bulk (unsized)	102.33		
	150	25.06	25.25	25.25
	106	28.47	28.69	53.94
	75	19.92	20.07	74.01
	53	6.97	7.02	81.04
	38	10.21	10.29	91.32
	25	5.55	5.59	96.92
	<25	3.06	3.08	100.00
Total		99.24	100.00	

Table A. 32: A 32: Dry screening results for OKP-2.

Sample No.	Size Fraction (µm)	Weight(g)	wt%	cumulative %
OKP-2B	Bulk (unsized)	101.51		
	150	25.67	25.90	25.90
	106	27.98	28.23	54.14
	75	21.58	21.78	75.91
	53	7.65	7.72	83.63
	38	11.49	11.59	95.23
	25	3.7	3.73	98.96
	<25	1.03	1.04	100.00
Total		99.1	100.00	

Table A. 33: A combined screening analysis results for OKP-2.

Sample No.	Size Fraction (µm)	Weight(g)	wt%	cumulative %
OKP-2C	Bulk (unsized)	104.2		
	150	25.33	24.94	24.94
	106	28.88	28.43	53.37
	75	21.46	21.13	74.50
	53	7.97	7.85	82.35
	38	10.1	9.94	92.29
	25	4.93	4.85	97.14
	<25	2.9	2.86	100.00
Total		101.57	100.00	

A1.7. Nkomati

Table A. 34: Wet screening results for NK-PCMZ/PT.

Sample No.	Size Fraction (µm)	Weight(g)	wt%	cumulative %
NK-PCMZ/PT (A)	Bulk (unsized)	106.09		
	150	1.66	1.69	1.69
	106	3.09	3.15	4.84
	75	5.34	5.44	10.29
	53	5.06	5.16	15.45
	38	7.25	7.39	22.84
	25	7.31	7.45	30.29
	<25	68.37	69.71	100.00
Total		98.08	100.00	

Table A. 35: Dry screening results for NK-PCMZ/PT.

Sample No.	Size Fraction (µm)	Weight(g)	wt%	cumulative %
NK-PCMZ/PT (B)	Bulk (unsized)	101.84		
	150	1.11	1.15	1.15
	106	3.17	3.29	4.45
	75	5.47	5.68	10.13
	53	5.18	5.38	15.51
	38	9.14	9.50	25.01
	25	8.33	8.65	33.66
	<25	63.85	66.34	100.00
Total		96.25	100.00	

Table A. 36: Combined screening results for NK-PCMZ/PT.

Sample No.	Size Fraction (μm)	Weight(g)	wt%	cumulative %
NK-PCMZ/PT (C)	Bulk (unsized)	104.01		
	150	1.84	1.89	1.89
	106	3.14	3.22	5.11
	75	5.43	5.57	10.67
	53	5.14	5.27	15.94
	38	7.36	7.54	23.49
	25	10.41	10.67	34.16
	<25	64.23	65.84	100.00
Total		97.55	100.00	

Table A. 37: Wet screening results for NK-MMZ/PT.

Sample No.	Size Fraction (μm)	Weight(g)	wt%	cumulative %
NK-MMZ/PT (A)	Bulk (unsized)	102.8		
	150	4.30	4.53	4.53
	106	8.70	9.17	13.70
	75	11.70	12.33	26.03
	53	12.20	12.86	38.88
	38	11.00	11.59	50.47
	25	8.20	8.64	59.11
	<25	38.80	40.89	100.00
Total		94.90	100.00	

Table A. 38: Dry screening results for NK-MMZ/PT.

Sample No.	Size Fraction (μm)	Weight(g)	wt%	cumulative %
NK-MMZ/PT (B)	Bulk (unsized)	103.7		
	150	5.19	5.37	5.37
	106	9.08	9.39	14.76
	75	12.17	12.59	27.35
	53	12.62	13.06	40.41
	38	13.33	13.79	54.20
	25	8.25	8.54	62.74
	<25	36.02	37.26	100.00
Total		96.66	100.00	

Table A. 39: NK-MMZ/PT combined wet-dry screening results.

Sample No.	Size Fraction (μm)	Weight(g)	wt%	cumulative %
NK-MMZ/PT (C)	Bulk (unsized)	101.4		
	150	4.55	4.65	4.65
	106	9.14	9.34	13.99
	75	12.24	12.51	26.49
	53	11.69	11.94	38.43
	38	11.50	11.75	50.18
	25	8.53	8.71	58.90
	<25	40.23	41.10	100.00
Total		97.88	100.00	

Table A. 40: Wet screening results for NK-CNF.

Sample No.	Size Fraction (μm)	Weight(g)	wt%	cumulative %
NK-CNF (A)	Bulk (unsized)	103.85		
	150	1.80	1.77	1.77
	106	4.00	3.93	5.70
	75	5.75	5.65	11.34
	53	11.55	11.34	22.69
	38	14.75	14.49	37.18
	25	10.25	10.07	47.24
	<25	53.71	52.76	100.00
Total		101.81	100.00	

Table A. 41: Dry screening results for NK-CNF.

Sample No.	Size Fraction (μm)	Weight(g)	wt%	cumulative %
NK-CNF (B)	Bulk (unsized)	105.77		
	150	2.03	2.01	2.01
	106	5.63	5.57	7.58
	75	5.75	5.69	13.26
	53	13.19	13.05	26.31
	38	17.35	17.16	43.47
	25	8.00	7.91	51.38
	<25	49.16	48.62	100.00
Total		101.11	100.00	

Table A. 42: NK-CNF results for a combined wet-dry screening.

Sample No.	Size Fraction (µm)	Weight(g)	wt%	cumulative %
NK-CNF (C)	Bulk (unsized)	104.70		
	150	1.87	1.85	1.85
	106	4.06	4.01	5.85
	75	6.64	6.55	12.41
	53	9.23	9.11	21.52
	38	14.00	13.82	35.34
	25	11.16	11.02	46.35
	<25	54.35	53.65	100.00
Total		101.31	100.00	

Table A. 43: Wet screening results for NK-CNC.

Sample No.	Size Fraction (µm)	Weight(g)	wt%	cumulative %
NK-CNC (A)	Bulk (unsized)	104.25		
	150	15.15	15.52	15.52
	106	18.25	18.69	34.21
	75	21.45	21.97	56.19
	53	16.32	16.72	72.91
	38	11.35	11.63	84.53
	25	4.85	4.97	89.50
	<25	10.25	10.50	100.00
Total		97.62	100.00	

Table A. 44: Dry screening results for NK-CNC.

Sample No.	Size Fraction (µm)	Weight(g)	wt%	cumulative %
NK-CNC (B)	Bulk (unsized)	102.64		
	150	16.25	16.33	16.33
	106	21.97	22.07	38.40
	75	18.69	18.78	57.18
	53	15.52	15.59	72.77
	38	10.50	10.55	83.32
	25	4.97	4.99	88.32
	<25	11.63	11.68	100.00
Total		99.53	100.00	

Table A. 45: NK-CNC results for combined wet-dry screening.

Sample No.	Size Fraction (µm)	Weight(g)	wt%	cumulative %
NK-CNC (C)	Bulk (unsized)	101.84		
	150	15.33	15.39	15.39
	106	19.67	19.75	35.14
	75	21.62	21.70	56.84
	53	16.42	16.48	73.33
	38	11.41	11.45	84.78
	25	4.87	4.89	89.67
	<25	10.29	10.33	100.00
Total		99.61	100.00	

Table A. 46: NK-PCMZ/CDF wet screening results.

Sample No.	Size Fraction (µm)	Weight(g)	wt%	cumulative %
NK-PCMZ/CDF (A)	Bulk (unsized)	106.15		
	150	6.75	6.48	6.48
	106	5.55	5.33	11.81
	75	8.05	7.73	19.54
	53	9.15	8.79	28.32
	38	9.65	9.27	37.59
	25	8.65	8.31	45.90
	<25	56.35	54.10	100.00
Total		104.15	100.00	

Table A. 47: NK-PCMZ/CDF dry screening results.

Sample No.	Size Fraction (µm)	Weight(g)	wt%	cumulative %
NK-PCMZ/CDF (B)	Bulk (unsized)	99.88		
	150	7.64	7.84	7.84
	106	4.09	4.20	12.04
	75	7.20	7.39	19.43
	53	9.81	10.07	29.50
	38	10.70	10.98	40.48
	25	9.78	10.04	50.51
	<25	48.22	49.49	100.00
Total		97.44	100.00	

Table A. 48: Combined wet-dry screening results for NK-PCMZ/CDF.

Sample No.	Size Fraction (µm)	Weight(g)	wt%	cumulative %
NK-PCMZ/CDF (C)	Bulk (unsized)	102.31		
	150	7.02	7.05	7.05
	106	5.64	5.67	12.72
	75	8.17	8.21	20.93
	53	10.30	10.35	31.27
	38	9.91	9.96	41.23
	25	9.01	9.05	50.28
	<25	49.49	49.72	100.00
Total		99.54	100.00	

Table A. 49: Wet screening results for NK-PCMZ/CDC.

Sample No.	Size Fraction (µm)	Weight(g)	wt%	cumulative %
NK-PCMZ/CDC (A)	Bulk (unsized)	98.07		
	150	8.46	9.20	9.20
	106	9.05	9.84	19.03
	75	10.44	11.35	30.38
	53	12.36	13.44	43.82
	38	11.46	12.46	56.28
	25	6.55	7.12	63.40
	<25	33.67	36.60	100.00
Total		91.99	100.00	

Table A. 50: Dry screening results for NK-PCMZ/CNC.

Sample No.	Size Fraction (µm)	Weight(g)	wt%	cumulative %
NK-PCMZ/CDC (B)	Bulk (unsized)	103.87		
	150	10.35	10.64	10.64
	106	9.20	9.46	20.09
	75	11.35	11.67	31.76
	53	13.57	13.95	45.71
	38	10.17	10.45	56.16
	25	7.51	7.72	63.88
	<25	35.14	36.12	100.00
Total		97.29	100.00	

Table A. 51: NK-PCMZ/CNC results for combined wet-dry screening analysis.

Sample No.	Size Fraction (µm)	Weight(g)	wt%	cumulative %
NK-PCMZ/CDC (C)	Bulk (unsized)	105.3		
	150	9.84	10.09	10.09
	106	9.69	9.93	20.02
	75	11.11	11.39	31.41
	53	13.05	13.38	44.79
	38	12.02	12.32	57.12
	25	6.83	7.00	64.12
	<25	35.00	35.88	100.00
Total		97.54	100.00	

A2 Particle Size Distribution

A2.1. Impala

Table A. 52: Malvern particle size distribution results for Impala.

IMPALA				
	IMP/001		IMP/003	
Size (µm)	Volume in %	Cumulative Vol %	Volume in %	Cumulative Vol %
0.02	0	0	0	0
0.022	0	0	0	0
0.025	0	0	0	0
0.028	0	0	0	0
0.032	0	0	0	0
0.036	0	0	0	0
0.04	0	0	0	0
0.045	0	0	0	0
0.05	0	0	0	0
0.056	0	0	0	0
0.063	0	0	0	0
0.071	0	0	0	0
0.08	0	0	0	0
0.089	0	0	0	0
0.1	0	0	0	0
0.112	0	0	0	0
0.126	0	0	0	0
0.142	0	0	0	0
0.159	0	0	0	0
0.178	0	0	0	0
0.2	0	0	0	0
0.224	0	0	0	0
0.252	0	0	0	0
0.283	0	0	0	0
0.317	0	0	0	0
0.356	0	0	0	0
0.399	0	0	0.01	0.01
0.448	0	0	0.04	0.05
0.502	0.03	0.03	0.07	0.12
0.564	0.06	0.09	0.08	0.2
0.632	0.07	0.16	0.09	0.29
0.71	0.08	0.24	0.1	0.39
0.796	0.09	0.33	0.11	0.5
0.893	0.1	0.43	0.12	0.62
1.002	0.12	0.55	0.13	0.75
1.125	0.13	0.68	0.15	0.9

Table A 52: Malvern particle size distribution results for Impala (continued).

1.262	0.14	0.82	0.16	1.06
1.416	0.16	0.98	0.17	1.23
1.589	0.17	1.15	0.18	1.41
1.783	0.19	1.34	0.2	1.61
2	0.21	1.55	0.21	1.62
2.244	0.23	1.78	0.23	1.85
2.518	0.25	2.03	0.24	2.09
2.825	0.28	2.31	0.26	2.35
3.17	0.3	2.61	0.28	2.63
3.557	0.33	2.94	0.3	2.93
3.991	0.36	3.3	0.33	3.26
4.477	0.39	3.69	0.35	3.61
5.024	0.42	4.11	0.38	3.99
5.637	0.45	4.56	0.41	4.4
6.325	0.48	5.04	0.44	4.84
7.096	0.51	5.55	0.47	5.31
7.962	0.54	6.09	0.51	5.82
8.934	0.58	6.67	0.55	6.37
10.024	0.61	7.28	0.63	7
11.247	0.65	7.93	0.68	7.68
12.619	0.69	8.62	0.73	8.41
14.159	0.73	9.35	0.78	9.19
15.887	0.77	10.12	0.84	10.03
17.825	0.81	10.93	0.91	10.94
20	0.87	11.8	0.98	11.92
22.44	0.93	12.73	1.06	12.98
25.179	1	13.73	1.16	14.14
28.251	1.08	14.81	1.26	15.4
31.698	1.18	15.99	1.36	16.76
35.566	1.28	17.27	1.47	18.23
39.905	1.4	18.67	1.58	19.81
44.774	1.53	20.2	1.68	21.49
50.238	1.66	21.86	1.77	23.26
56.368	1.78	23.64	1.84	25.1
63.246	1.9	25.54	1.9	27
70.963	2.01	27.55	1.93	28.93
79.621	2.11	29.66	1.96	30.89
89.337	2.2	31.86	1.99	32.88
100.237	2.3	34.16	2.05	34.93
112.468	2.42	36.58	2.15	37.08
126.191	2.57	39.15	2.32	39.4
141.589	2.78	41.93	2.15	41.55
158.866	3.04	44.97	2.32	43.87

Table A 52: Malvern particle size distribution results for Impala (continued).

178.25	3.38	48.35	2.57	46.44
200	3.76	52.11	2.91	49.35
224.404	4.15	56.26	3.33	52.68
251.785	4.53	60.79	3.8	56.48
282.508	4.84	65.63	4.3	60.78
316.979	5.04	70.67	4.77	65.55
355.656	5.08	75.75	5.17	70.72
399.052	4.95	80.7	5.42	76.14
447.744	4.63	85.33	5.48	81.62
502.377	4.13	89.46	5.31	86.93
632.456	3.5	92.96	4.89	91.82
709.627	2.78	95.74	4.22	96.04
796.214	2.02	97.76	3.35	99.39
893.367	1.29	99.05	2.33	99.4
1002.374	0.72	99.77	1.31	99.4
1124.683	0.23	100	0.54	99.89
1261.915	0.02	100	0.1	100
1415.892	0	100	0	100
1588.656	0	100	0	100
1782.502	0	100	0	100
2000	0	100	0	100

A2.2. Amandelbult

Table A. 53: Malvern particle size distribution results for Amandelbult.

AMANDELBULT				
	AMB/101		S/4-TD44	
Size (µm)	Volume in %	Cumulative Vol %	Volume in %	Cumulative Vol %
0.02	0	0	0	0
0.022	0	0	0	0
0.025	0	0	0	0
0.028	0	0	0	0
0.032	0	0	0	0
0.036	0	0	0	0
0.04	0	0	0	0
0.045	0	0	0	0
0.05	0	0	0	0
0.056	0	0	0	0
0.063	0	0	0	0
0.071	0	0	0	0
0.08	0	0	0	0
0.089	0	0	0	0
0.1	0	0	0	0
0.112	0	0	0	0
0.126	0	0	0	0
0.142	0	0	0	0
0.159	0	0	0	0
0.178	0	0	0	0
0.2	0	0	0	0
0.224	0	0	0	0
0.252	0	0	0	0
0.283	0	0	0	0
0.317	0	0	0	0
0.356	0	0	0	0
0.399	0	0	0.01	0.01
0.448	0	0	0.03	0.04
0.502	0	0	0.03	0.07
0.564	0.01	0.01	0.03	0.1
0.632	0.03	0.04	0.03	0.13
0.71	0.02	0.06	0.04	0.17
0.796	0.03	0.09	0.04	0.21
0.893	0.03	0.12	0.04	0.25
1.002	0.03	0.15	0.05	0.3
1.125	0.03	0.18	0.05	0.35
1.262	0.06	0.24	0.06	0.41
1.416	0.06	0.3	0.09	0.5

Table A 53: Malvern particle size distribution results for Amandelbult (continued).

1.589	0.06	0.36	0.1	0.6
1.783	0.02	0.38	0.11	0.71
2	0.01	0.39	0.13	0.84
2.244	0.13	0.52	0.14	0.98
2.518	0.11	0.63	0.15	1.13
2.825	0.05	0.68	0.16	1.29
3.17	0.04	0.72	0.16	1.45
3.557	0.04	0.76	0.17	1.65
3.991	0.06	0.82	0.18	1.8
4.477	0.14	0.96	0.18	1.98
5.024	0.33	1.29	0.18	2.16
5.637	0.13	1.42	0.18	2.34
6.325	0.06	1.48	0.18	2.52
7.096	0.04	1.52	0.18	2.7
7.962	0.06	1.58	0.19	2.89
8.934	0.06	1.64	0.21	3.1
10.024	0.12	1.76	0.23	3.33
11.247	0.16	1.92	0.26	3.59
12.619	0.47	2.39	0.3	2.89
14.159	0.1	2.49	0.34	4.23
15.887	0.24	2.73	0.38	4.61
17.825	0.32	3.05	0.41	5.02
20	0.27	3.32	0.42	5.44
22.44	0.42	3.74	0.42	5.86
25.179	0.58	4.32	0.4	6.26
28.251	0.21	4.53	0.38	6.64
31.698	0.41	4.94	0.37	7.01
35.566	0.5	5.44	0.41	7.42
39.905	0.61	6.05	0.53	7.95
44.774	0.65	6.7	0.77	8.72
50.238	0.96	7.66	1.18	9.9
56.368	0.77	8.43	1.78	11.68
63.246	2.08	10.51	2.58	14.26
70.963	2.17	12.68	3.57	17.83
79.621	2.59	15.27	4.69	22.52
89.337	2.52	17.79	5.87	28.39
100.237	5.05	22.84	6.98	35.37
112.468	4.8	27.64	7.93	43.3
126.191	4.92	32.56	8.56	51.86
141.589	6.11	38.67	8.81	60.67
158.866	4.44	43.11	8.62	69.29

Table A 53: Malvern particle size distribution results for Amandelbult (continued).

178.25	6.57	49.68	7.99	77.28
200	8.21	57.89	6.98	84.26
224.404	5.45	63.34	5.73	89.99
251.785	7.51	70.85	4.34	94.33
282.508	5.64	76.49	2.99	97.32
316.979	2.85	79.34	1.77	99.09
355.656	5.18	84.52	0.79	99.88
399.052	4.85	89.37	0.14	100
447.744	3.08	92.45	0	100
502.377	2.44	94.89	0	100
632.456	1.83	96.72	0	100
709.627	0.76	97.48	0	100
796.214	0.86	98.34	0	100
893.367	0.78	99.12	0	100
1002.374	0.44	99.56	0	100
1124.683	0.22	99.78	0	100
1261.915	0.06	99.84	0	100
1415.892	0.14	99.98	0	100
1588.656	0.01	99.99	0	100
1782.502	0.01	100	0	100
2000	0	100	0	100

A2.3. Mogalakwena

Table A. 54: Table A 54: Malvern results for Mogalakwena.

Mogalakwena		
Size (µm)	**Volume %**	**Cumulative Vol %**
0.02	0	0
0.022	0	0
0.025	0	0
0.028	0	0
0.032	0	0
0.036	0	0
0.04	0	0
0.045	0	0
0.05	0	0
0.056	0	0
0.063	0	0
0.071	0	0
0.08	0	0
0.089	0	0
0.1	0	0
0.112	0	0
0.126	0	0
0.142	0	0
0.159	0	0
0.178	0	0
0.2	0	0
0.224	0	0
0.252	0	0
0.283	0	0
0.317	0	0
0.356	0	0
0.399	0.01	0.01
0.448	0.03	0.04
0.502	0.03	0.07
0.564	0.03	0.1
0.632	0.03	0.13
0.71	0.04	0.17
0.796	0.04	0.21
0.893	0.04	0.25
1.002	0.05	0.3
1.125	0.05	0.35
1.262	0.06	0.41
1.416	0.09	0.5
1.589	0.1	0.6
1.783	0.11	0.71

Table A 54: Malvern results for Mogalakwena (continued).

2	0.13	0.84
2.244	0.14	0.98
2.518	0.15	1.13
2.825	0.16	1.29
3.17	0.16	1.45
3.557	0.17	1.65
3.991	0.18	1.8
4.477	0.18	1.98
5.024	0.18	2.16
5.637	0.18	2.34
6.325	0.18	2.52
7.096	0.18	2.7
7.962	0.19	2.89
8.934	0.21	3.1
10.024	0.23	3.33
11.247	0.26	3.59
12.619	0.3	2.89
14.159	0.34	4.23
15.887	0.38	4.61
17.825	0.41	5.02
20	0.42	5.44
22.44	0.42	5.86
25.179	0.4	6.26
28.251	0.38	6.64
31.698	0.37	7.01
35.566	0.41	7.42
39.905	0.53	7.95
44.774	0.77	8.72
50.238	1.18	9.9
56.368	1.78	11.68
63.246	2.58	14.26
70.963	3.57	17.83
79.621	4.69	22.52
89.337	5.87	28.39
100.237	6.98	35.37
112.468	7.93	43.3
126.191	8.56	51.86
141.589	8.81	60.67
158.866	8.62	69.29
178.25	7.99	77.28
200	6.98	84.26
224.404	5.73	89.99
251.785	4.34	94.33

Table A 54: Malvern results for Mogalakwena (continued).

282.508	2.99	97.32
316.979	1.77	99.09
355.656	0.79	99.88
399.052	0.14	100
447.744	0	100
502.377	0	100
632.456	0	100
709.627	0	100
796.214	0	100
893.367	0	100
1002.374	0	100
1124.683	0	100
1261.915	0	100
1415.892	0	100
1588.656	0	100
1782.502	0	100
2000	0	100

A2.4. Union Section

Table A. 55: Union Section Malvern particle size distribution results.

Union Section		
Size (µm)	**Volume %**	**Cumulative Vol %**
0.02	0	0
0.022	0	0
0.025	0	0
0.028	0	0
0.032	0	0
0.036	0	0
0.04	0	0
0.045	0	0
0.05	0	0
0.056	0	0
0.063	0	0
0.071	0	0
0.08	0	0
0.089	0	0
0.1	0	0
0.112	0	0
0.126	0	0
0.142	0	0
0.159	0	0
0.178	0	0
0.2	0	0
0.224	0	0
0.252	0.03	0.03
0.283	0.08	0.11
0.317	0.14	0.25
0.356	0.18	0.43
0.399	0.22	0.65
0.448	0.26	0.91
0.502	0.29	1.2
0.564	0.31	1.51
0.632	0.33	1.84
0.71	0.35	2.19
0.796	0.37	2.56
0.893	0.39	2.95
1.002	0.41	3.36
1.125	0.44	3.8
1.262	0.48	4.28
1.416	0.52	4.8
1.589	0.56	5.36
1.783	0.61	5.97

Table A 55: Union Section Malvern particle size distribution results (continued).

2	0.66	6.63
2.244	0.71	7.34
2.518	0.77	8.11
2.825	0.82	8.93
3.17	0.88	9.81
3.557	0.94	10.75
3.991	1.01	11.76
4.477	1.09	12.85
5.024	1.17	14.02
5.637	1.26	15.28
6.325	1.35	16.63
7.096	1.45	18.08
7.962	1.56	19.64
8.934	1.67	21.31
10.024	1.79	23.1
11.247	1.91	25.01
12.619	2.03	27.04
14.159	2.15	29.19
15.887	2.27	31.46
17.825	2.38	33.84
20	2.49	36.33
22.44	2.6	38.93
25.179	2.7	41.7
28.251	2.81	44.51
31.698	2.93	47.44
35.566	3.06	50.5
39.905	3.19	53.69
44.774	3.32	57.01
50.238	3.44	60.45
56.368	3.55	64
63.246	3.63	67.63
70.963	3.67	71.3
79.621	3.64	74.94
89.337	3.55	78.49
100.237	3.38	81.87
112.468	3.14	85.01
126.191	2.85	87.86
141.589	2.51	90.37
158.866	2.17	92.54
178.25	1.82	94.36
200	1.49	95.85
224.404	1.2	97.05
251.785	0.93	97.98

Table A 55: Union Section Malvern particle size distribution results (continued).

282.508	0.7	98.68
316.979	0.51	99.19
355.656	0.36	99.55
399.052	0.25	99.8
447.744	0.15	99.95
502.377	0.05	100
632.456	0.01	100
709.627	0	100
796.214	0	100
893.367	0	100
1002.374	0	100
1124.683	0	100
1261.915	0	100
1415.892	0	100
1588.656	0	100
1782.502	0	100
2000	0	100

A2.5. Rustenburg

Table A. 56: Malvern data for Rustenburg tailings sample.

Rustenburg-Waterval		
Size (µm)	**Volume %**	**Cumulative Vol %**
0.02	0	0
0.022	0	0
0.025	0	0
0.028	0	0
0.032	0	0
0.036	0	0
0.04	0	0
0.045	0	0
0.05	0	0
0.056	0	0
0.063	0	0
0.071	0	0
0.08	0	0
0.089	0	0
0.1	0	0
0.112	0	0
0.126	0	0
0.142	0	0
0.159	0	0
0.178	0	0
0.2	0	0
0.224	0	0
0.252	0	0
0.283	0	0
0.317	0	0
0.356	0	0
0.399	0	0
0.448	0	0
0.502	0	0
0.564	0	0
0.632	0	0
0.71	0	0
0.796	0	0
0.893	0	0
1.002	0	0
1.125	0	0
1.262	0.01	0.01
1.416	0.14	0.15
1.589	0.22	0.37
1.783	0.33	0.7

Table A 56: Malvern data for Rustenburg tailings sample (continued).

2	0.43	1.13
2.244	0.53	1.66
2.518	0.63	2.29
2.825	0.72	3.01
3.17	0.8	3.81
3.557	0.89	4.7
3.991	0.97	5.67
4.477	1.05	6.72
5.024	1.14	7.86
5.637	1.24	9.1
6.325	1.34	10.44
7.096	1.45	11.89
7.962	1.58	13.47
8.934	1.72	15.19
10.024	1.88	17.07
11.247	2.05	19.12
12.619	2.22	21.34
14.159	2.4	23.74
15.887	2.58	26.32
17.825	2.75	29.07
20	2.9	31.97
22.44	3.04	35.01
25.179	3.15	38.16
28.251	3.23	41.39
31.698	3.29	44.68
35.566	3.31	47.99
39.905	3.3	51.29
44.774	3.27	54.56
50.238	3.21	57.77
56.368	3.13	60.9
63.246	3.04	63.94
70.963	2.93	66.87
79.621	2.83	69.7
89.337	2.72	72.42
100.237	2.62	75.04
112.468	2.54	77.58
126.191	2.47	80.05
141.589	2.4	82.45
158.866	2.34	84.79
178.25	2.28	87.07
200	2.19	89.26
224.404	2.07	91.33
251.785	1.92	93.25

Table A 56: Malvern data for Rustenburg tailings sample (continued).

282.508	1.73	94.98
316.979	1.5	96.48
355.656	1.26	97.74
399.052	0.99	98.73
447.744	0.72	99.45
502.377	0.47	99.92
632.456	0.08	100
709.627	0	100
796.214	0	100
893.367	0	100
1002.374	0	100
1124.683	0	100
1261.915	0	100
1415.892	0	100
1588.656	0	100
1782.502	0	100
2000	0	100

A2.6. O'okiep

Table A. 57: Malvern results for O'okiep.

O'OKIEP				
	OKP-1		OKP-2	
Size (µm)	Volume in %	Cumulative Vol %	Volume in %	Cumulative Vol %
0.02	0	0	0	0
0.022	0	0	0	0
0.025	0	0	0	0
0.028	0	0	0	0
0.032	0	0	0	0
0.036	0	0	0	0
0.04	0	0	0	0
0.045	0	0	0	0
0.05	0	0	0	0
0.056	0	0	0	0
0.063	0	0	0	0
0.071	0	0	0	0
0.08	0	0	0	0
0.089	0	0	0	0
0.1	0	0	0	0
0.112	0	0	0	0
0.126	0	0	0	0
0.142	0	0	0	0
0.159	0	0	0	0
0.178	0	0	0	0
0.2	0	0	0	0
0.224	0	0	0	0
0.252	0	0	0	0
0.283	0	0	0	0
0.317	0	0	0	0
0.356	0	0	0	0
0.399	0	0	0	0
0.448	0	0	0	0
0.502	0	0	0	0
0.564	0	0	0	0
0.632	0	0	0	0
0.71	0	0	0.01	0.01
0.796	0.03	0.03	0.02	0.03
0.893	0.05	0.08	0.06	0.09
1.002	0.05	0.13	0.06	0.15
1.125	0.06	0.19	0.05	0.2
1.262	0.06	0.25	0.03	0.23
1.416	0.06	0.31	0.1	0.33

Table A 57: Malvern results for O'okiep (continued).

1.589	0.07	0.38	0.01	0.34
1.783	0.07	0.45	0.12	0.46
2	0.08	0.53	0.12	0.58
2.244	0.08	0.61	0.06	0.64
2.518	0.09	0.7	0.12	0.76
2.825	0.09	0.79	0.09	0.85
3.17	0.09	0.88	0.08	0.93
3.557	0.1	0.98	0.16	1.09
3.991	0.1	1.08	0.14	1.23
4.477	0.11	1.19	0.25	1.48
5.024	0.11	1.3	0.21	1.69
5.637	0.11	1.41	0.13	1.82
6.325	0.12	1.53	0.21	2.03
7.096	0.12	1.65	0.21	2.24
7.962	0.13	1.78	0.18	2.42
8.934	0.15	1.93	0.19	2.61
10.024	0.17	2.1	0.36	2.97
11.247	0.19	2.29	0.39	3.36
12.619	0.22	2.51	0.31	3.67
14.159	0.25	2.76	0.31	3.98
15.887	0.29	3.05	0.37	4.35
17.825	0.32	3.37	0.28	4.63
20	0.35	3.72	0.28	4.91
22.44	0.38	4.1	0.29	5.2
25.179	0.41	4.51	0.37	5.57
28.251	0.45	4.96	0.24	5.81
31.698	0.5	5.46	0.29	6.1
35.566	0.58	6.04	0.48	6.58
39.905	0.72	6.76	0.32	6.9
44.774	0.92	7.68	1.05	7.95
50.238	1.22	8.9	1.04	8.99
56.368	1.62	10.52	3.85	12.84
63.246	2.13	12.65	1.81	14.65
70.963	2.73	15.38	2.4	17.05
79.621	3.41	18.79	3.49	20.54
89.337	4.12	22.91	3.44	23.98
100.237	4.81	27.72	3.6	27.58
112.468	5.44	33.16	8.96	36.54
126.191	5.95	39.11	9.3	45.84
141.589	6.31	45.42	8.86	54.7
158.866	6.47	51.89	7.84	62.54
178.25	6.45	58.34	10.78	73.32
200	6.2	64.54	13.26	86.58

Table A 57: Malvern results for O'okiep (continued).

224.404	5.9	70.44	6.44	93.02
251.785	5.41	75.85	3.28	96.3
282.508	4.84	80.69	0.96	97.26
316.979	4.2	84.89	0.8	98.06
355.656	3.56	88.45	0.32	98.38
399.052	2.92	91.37	0.29	98.67
447.744	2.32	93.69	0.24	98.91
502.377	1.79	95.48	0.4	99.31
632.456	1.33	96.81	0.43	99.74
709.627	0.96	97.77	0.24	99.98
796.214	0.68	98.45	0.02	100
893.367	0.9	99.35	0	100
1002.374	0.2	99.55	0	100
1124.683	0.17	99.72	0	100
1261.915	0.14	99.86	0	100
1415.892	0.12	99.98	0	100
1588.656	0.02	100	0	100
1782.502	0	100	0	100
2000	0	100	0	100

A2.7. Nkomati

Table A. 58: Nkomati Malvern particle size data.

NKOMATI				
	NK-MMZ/PT		NK-PCMZ/PT	
Size (µm)	Volume in %	Cumulative Vol %	Volume in %	Cumulative Vol %
0.02	0	0	0	0
0.022	0	0	0	0
0.025	0	0	0	0
0.028	0	0	0	0
0.032	0	0	0	0
0.036	0	0	0	0
0.04	0	0	0	0
0.045	0	0	0	0
0.05	0	0	0	0
0.056	0	0	0	0
0.063	0	0	0	0
0.071	0	0	0	0
0.08	0	0	0	0
0.089	0	0	0	0
0.1	0	0	0	0
0.112	0	0	0	0
0.126	0	0	0	0
0.142	0	0	0	0
0.159	0	0	0	0
0.178	0	0	0	0
0.2	0.01	0.01	0	0
0.224	0.01	0.02	0	0
0.252	0.02	0.04	0.03	0.03
0.283	0.04	0.08	0.08	0.11
0.317	0.08	0.16	0.14	0.25
0.356	0.07	0.23	0.18	0.43
0.399	0.03	0.26	0.22	0.65
0.448	0.1	0.36	0.26	0.91
0.502	0.09	0.45	0.29	1.2
0.564	0.15	0.6	0.31	1.51
0.632	0.14	0.74	0.33	1.84
0.71	0.09	0.83	0.35	2.19
0.796	0.09	0.92	0.37	2.56
0.893	0.12	1.04	0.39	2.95
1.002	0.07	1.11	0.41	3.36
1.125	0.12	1.23	0.44	3.8
1.262	0.13	1.36	0.48	4.28
1.416	0.12	1.48	0.52	4.8

Table A 58: Nkomati Malvern particle size data (continued).

1.589	0.05	1.53	0.56	5.36
1.783	0.36	1.89	0.61	5.97
2	0.37	2.26	0.66	6.63
2.244	0.2	2.46	0.71	7.34
2.518	0.35	2.81	0.77	8.11
2.825	0.49	3.3	0.82	8.93
3.17	0.32	3.62	0.88	9.81
3.557	0.18	3.8	0.94	10.75
3.991	0.51	4.31	1.01	11.76
4.477	0.48	4.79	1.09	12.85
5.024	0.53	5.32	1.17	14.02
5.637	0.52	5.84	1.26	15.28
6.325	0.61	6.45	1.35	16.63
7.096	0.28	6.73	1.45	18.08
7.962	0.72	7.45	1.56	19.64
8.934	0.44	7.89	1.67	21.31
10.024	0.4	8.29	1.79	23.1
11.247	0.73	9.02	1.91	25.01
12.619	0.69	9.71	2.03	27.04
14.159	0.72	10.43	2.15	29.19
15.887	1.18	11.61	2.27	31.46
17.825	0.87	12.48	2.38	33.84
20	1.1	13.58	2.49	36.33
22.44	0.76	14.34	2.6	38.93
25.179	1.3	15.64	2.7	41.7
28.251	1.24	16.88	2.81	44.51
31.698	1.36	18.24	2.93	47.44
35.566	1.39	19.63	3.06	50.5
39.905	1.36	20.99	3.19	53.69
44.774	1.01	22	3.32	57.01
50.238	2.74	24.74	3.44	60.45
56.368	1.72	26.46	3.55	64
63.246	2.2	28.66	3.63	67.63
70.963	2.06	30.72	3.67	71.3
79.621	3.8	34.52	3.64	74.94
89.337	4.34	38.86	3.55	78.49
100.237	3.2	42.06	3.38	81.87
112.468	4.72	46.78	3.14	85.01
126.191	5.47	52.25	2.85	87.86
141.589	5.15	57.4	2.51	90.37
158.866	6.39	63.79	2.17	92.54
178.25	5.29	69.08	1.82	94.36
200	4.39	73.47	1.49	95.85

Table A 58: Nkomati Malvern particle size data (continued).

224.404	5.1	78.57	1.2	97.05
251.785	4.48	83.05	0.93	97.98
282.508	5.38	88.43	0.7	98.68
316.979	5.31	93.74	0.51	99.19
355.656	3.05	96.79	0.36	99.55
399.052	0.66	97.45	0.25	99.8
447.744	0.7	98.15	0.15	99.95
502.377	0.88	99.03	0.05	100
632.456	0.45	99.48	0.01	100
709.627	0.24	99.72	0	100
796.214	0.14	99.86	0	100
893.367	0.06	99.92	0	100
1002.374	0.05	99.97	0	100
1124.683	0.03	100	0	100
1261.915	0	100	0	100
1415.892	0	100	0	100
1588.656	0	100	0	100
1782.502	0	100	0	100
2000	0	100	0	100

A3. BET Surface Area

A3.1. Impala

Table A. 59: Impala BET surface area data.

BET Surface Area Report		
Sample:	IMP-001	
BET Surface Area ± 0.0067 m²/g	1.3506	
Slope:	3.21599 ± 0.15795	
Y-Intercept:	0.021490 ± 0.1663	
C:	149.979618	
VM:	0.310261 cm³/g STP	
Correlation Coefficient:	9.999148E-01	
Molecular Cross-section:	0.1620 nm²	
Sample Weight:	5.946 g	
Relative Pressure	Vol Adsorbed (cm³/g STP)	1/ [VA *(Po/P - 1)]
0.014922493	0.237	0.063912
0.029847556	0.2642	0.116443
0.0482185	0.2848	0.177863
0.05846799	0.2942	0.21109
0.073707887	0.3061	0.259917
0.089798101	0.3175	0.310764
0.119578064	0.3358	0.404503
0.159742899	0.3578	0.531265
0.198980963	0.3779	0.65737

A3.2. Amandelbult

Table A. 60: Amandelbult BET surface area data.

BET Surface Area Report		
Sample:	S/4-TD44	
	BET Surface Area 1.5015 ± 0.0082 m²/g	
Slope:	2.879401 ± 0.015812	
Y-Intercept:	0.19806 ± 0.001665	
C:	146.382025	
VM:	0.344922 cm³/g STP	
Correlation Coefficient:	9.998945E-01	
Molecular Cross-section:	0.1620 nm²	
Sample Weight:	7.810 g	
Relative Pressure	Vol Adsorbed (cm³/g STP)	1/ [VA *(Po/P - 1)]
0.01432456	0.2619	0.055498
0.03293462	0.2973	0.114538
0.04780271	0.3154	0.159195
0.058525685	0.3263	0.190514
0.07337483	0.3393	0.233376
0.089741599	0.352	0.280053
0.119472285	0.3725	0.364276
0.159746631	0.3974	0.478358
0.198783326	0.42	0.590719

A3.3. Mogalakwena

Table A. 61: Mogalakwena BET surface area data.

BET Surface Area Report		
Sample:	MPL-101	
	BET Surface Area 4.0760 ± 0.0062 m^2/g	
Slope:	1.17582 ± 0.001489	
Y-Intercept:	0.09899 ± 0.000188	
C:	103.799327	
VM:	0.973254 cm^3/g STP	
Correlation Coefficient:	9.999957E-01	
Molecular Cross-section:	0.1620 nm^2	
Sample Weight:	5.902 g	
Relative Pressure	Vol Adsorbed (cm^3/g STP)	1/ [VA *(Po/P - 1)]
0.05988977	0.9023	0.070599
0.072243314	0.9332	0.08344
0.0895272	0.9717	0.101195
0.119081532	1.0301	0.131224
0.1589231	1.1015	0.171537
0.199163535	1.1703	0.212512

A3.4. Union Section

Table A. 62: Union Section BET surface area data.

BET Surface Area Report		
Sample:	UST-201	
	BET Surface Area 2.1272 ± 0.0020 m^2/g	
Slope:	2.29502 ± 0.00195	
Y-Intercept:	0.16937 ± 0.000248	
C:	120.829467	
VM:	0.488654 cm^3/g STP	
Correlation Coefficient:	9.999982E-01	
Molecular Cross-section:	0.1620 nm^2	
Sample Weight:	5.496 g	
Relative Pressure	Vol Adsorbed (cm^3/g STP)	1/ [VA *(Po/P - 1)]
0.065604204	0.4683	0.149923
0.074062257	0.4783	0.167237
0.089797911	0.4947	0.199429
0.119125473	0.5226	0.258796
0.159288695	0.5574	0.339902
0.199412938	0.5906	0.421781

A3.5. Rustenburg (Waterval)

Table A. 63: Rustenburg (Waterval) BET surface area data.

BET Surface Area Report		
Sample:	WRT-101	
	BET Surface Area 2.1307 ± 0.0152 m^2/g	
Slope:	2.26801 ± 0.014464	
Y-Intercept:	0.16239 ± 0.001518	
C:	125.812359	
VM:	0.489467 cm^3/g STP	
Correlation Coefficient:	9.998218E-01	
Molecular Cross-section:	0.1620 nm^2	
Sample Weight:	6.981 g	
Relative Pressure	Vol Adsorbed (cm^3/g STP)	1/ [VA *(Po/P - 1)]
0.014570679	0.3606	0.041001
0.032062006	0.411	0.080603
0.046512672	0.4372	0.111584
0.058314526	0.4546	0.136228
0.072832563	0.4731	0.166032
0.089641931	0.4923	0.200025
0.119298114	0.5226	0.259181
0.159495774	0.5601	0.338808
0.198251837	0.5946	0.415847

A3.6. O'okiep

Table A. 64: O'okiep BET surface area data.

BET Surface Area Report		
Sample:	OKP-2	
	BET Surface Area 1.5791 ± 0.0055 m^2/g	
Slope:	2.741388 ± 0.009622	
Y-Intercept:	0.15304 ± 0.001011	
C:	180.134545	
VM:	0.362754 cm^3/g STP	
Correlation Coefficient:	9.999569E-01	
Molecular Cross-section:	0.1620 nm^2	
Sample Weight	7.940 g	
Relative Pressure	Vol Adsorbed (cm^3/g STP)	1/ [VA *(Po/P - 1)]
0.015919878	0.29	0.055786
0.028652965	0.3155	0.093494
0.046394994	0.3384	0.143786
0.058297856	0.3503	0.176747
0.073288234	0.3633	0.217668
0.089690159	0.3759	0.262084
0.119527049	0.396	0.342803
0.159747339	0.4208	0.451829
0.198723606	0.443	0.559894

A3.7. Nkomati

Table A. 65: Nkomati BET surface area data.

BET Surface Area Report		
Sample:	NK-PCMZ/PT	
	BET Surface Area 5.2080 ± 0.0156 m^2/g	
Slope:	0.831846 ± 0.002489	
Y-Intercept:	0.04018 ± 0.000261	
C:	208.8882	
VM:	1.196366 cm^3/g STP	
Correlation Coefficient:	9.999687E-01	
Molecular Cross-section:	0.1620 nm^2	
Sample Weight:	6.782 g	
Relative Pressure	Vol Adsorbed (cm^3/g STP)	1/ [VA *(Po/P - 1)]
0.014952979	0.9692	0.015662
0.031365921	1.0718	0.030211
0.042761372	1.118	0.039955
0.064290806	1.1867	0.0579
0.072842628	1.2102	0.064919
0.089614625	1.2512	0.078675
0.118915873	1.3137	0.102733
0.159722603	1.3929	0.136464
0.197487022	1.4611	0.16843

B. Mineralogical Analysis

B1. XRF Data

B1.1. Impala

Table B. 1: XRF data for Impala tailings.

Sample	IMP-001	IMP-001	IMP-001	IMP-001	IMP-001	IMP-001	IMP-001	IMP-003	IMP-003	IMP-003	IMP-003	IMP-003	IMP-003
Sieve size (µm)	<25	+25	+38	+53	+75	+106	+150	+25	+38	+53	+75	+106	+150
Oxides	(wt%)												
SiO_2	38.170	39.205	41.069	44.495	47.453	49.594	47.561	34.118	34.329	33.162	34.624	34.323	34.051
TiO_2	0.517	0.465	0.404	0.323	0.238	0.183	0.222	0.561	0.553	0.551	0.517	0.517	0.503
$Al2O_3$	13.661	13.116	13.147	13.459	14.091	16.674	19.275	12.862	12.681	12.300	11.988	11.922	11.860
Fe_2O_3	14.868	14.850	13.708	12.041	9.789	7.720	6.786	18.349	18.311	18.926	18.176	18.366	18.719
MnO	0.228	0.231	0.212	0.190	0.156	0.122	0.104	0.190	0.194	0.199	0.199	0.202	0.191
MgO	14.544	15.399	15.503	15.619	15.282	13.212	10.467	14.789	14.933	15.186	15.663	15.512	14.773
CaO	6.153	5.930	6.241	6.901	7.692	9.095	9.814	4.404	4.244	4.007	4.133	4.054	4.052
Na_2O	0.895	0.854	0.921	1.008	1.145	1.414	1.614	0.723	0.698	0.622	0.650	0.616	0.585
K_2O	0.161	0.134	0.142	0.159	0.190	0.250	0.371	0.093	0.096	0.074	0.080	0.069	0.087
P_2O_5	0.040	0.026	0.028	0.025	0.028	0.024	0.027	0.044	0.043	0.039	0.039	0.034	0.036
SO_3	0.237	0.251	0.206	0.112	0.219	0.189	0.208	0.069	0.057	0.043	0.056	0.060	0.082
Cr_2O_3	9.542	9.616	8.035	5.417	2.589	0.910	1.443	13.926	14.105	14.789	14.065	14.730	15.284
NiO	0.090	0.089	0.080	0.074	0.067	0.057	0.153	0.121	0.120	0.122	0.119	0.123	0.140
H_2O^-	0.149	0.024	0.020	0.028	0.032	0.052	0.163	0.034	0.004	0.012	0.007	0.002	0.025
LOI	0.473	-0.370	-0.261	0.100	0.229	0.386	0.995	-0.431	-0.635	-0.391	-0.510	-0.533	-0.706
Total	99.728	99.822	99.455	99.951	99.200	99.883	99.202	99.853	99.733	99.641	99.808	99.998	99.683

B1.2. Amandelbult

Table B. 2: Amandelbult XRF data.

Sample	AMB/101B	AMB/101B	AMB/101B	AMB/101B	AMB/101B	AMB/101B	AMB/101B	S/4-TD44	S/4-TD44	S/4-TD44	S/4-TD44	S/4-TD44	S/4-TD44	S/4-TD44
Sieve size (μm)	<25	+25	+38	+53	+75	+106	+150	<25	25	+38	+53	+75	+106	+150
Oxides	(wt%)													
SiO_2	34.049	34.468	35.593	36.471	37.367	38.159	42.038	27.247	27.781	26.478	23.552	19.981	16.026	17.558
TiO_2	0.477	0.456	0.428	0.407	0.389	0.383	0.405	0.631	0.633	0.619	0.644	0.671	0.696	0.670
$Al2O_3$	12.290	12.206	12.098	12.319	12.257	12.033	11.866	12.871	12.303	12.615	12.848	13.438	14.179	13.688
Fe_2O_3	17.541	17.671	17.068	16.719	15.459	15.078	14.396	20.571	21.954	21.838	23.674	25.865	27.164	26.965
MnO	0.190	0.196	0.193	0.193	0.181	0.179	0.182	0.203	0.220	0.209	0.219	0.233	0.236	0.234
MgO	15.860	16.553	16.865	16.793	16.860	16.685	17.274	15.656	14.903	14.801	14.373	13.862	13.464	14.050
CaO	4.619	4.429	4.511	4.660	4.720	4.844	5.196	3.452	3.220	3.077	2.429	1.723	1.310	1.383
Na_2O	0.830	0.791	0.795	0.832	0.900	0.901	0.963	0.688	0.495	0.702	0.526	0.291	0.281	0.214
K_2O	0.118	0.111	0.115	0.127	0.166	0.153	0.155	0.111	0.103	0.145	0.160	0.066	0.053	0.050
P_2O_5	0.049	0.044	0.044	0.045	0.041	0.039	0.039	0.042	0.040	0.040	0.039	0.033	0.030	0.035
SO_3	0.167	0.118	0.093	0.039	0.083	0.060	0.035	0.093	0.049	0.039	0.002	0.010	0.002	0.010
Cr_2O_3	12.627	12.547	11.924	11.276	10.665	10.107	5.705	18.100	18.456	18.788	21.677	24.458	27.623	25.701
NiO	0.144	0.131	0.125	0.120	0.115	0.118	0.126	0.130	0.146	0.137	0.173	0.153	0.172	0.166
H_2O^-	0.125	0.100	0.150	0.065	0.150	0.199	0.250	0.026	0.047	0.025	0.148	0.138	0.099	0.066
LOI	0.113	-0.210	-0.070	0.019	0.130	0.319	0.715	-0.391	-0.589	-0.353	-0.686	-1.182	-1.382	-1.394
Total	99.200	99.611	99.934	100.084	99.484	99.256	99.347	99.431	99.762	99.161	99.777	99.741	99.952	99.393

B1.3. Mogalakwena

Table B. 3: Mogalakwena XRF data.

Sample	MPL/101B	MPL/101B	MPL/101B	MPL/101B	MPL/101B	MPL/101B	MPL/101B
Sieve size (μm)	<25	+25	+38	+53	+75	+106	+150
Oxides	(wt%)						
SiO_2	47.427	50.351	50.631	50.688	50.862	50.347	49.894
TiO_2	0.217	0.219	0.210	0.197	0.188	0.178	0.188
$Al2O_3$	8.616	8.008	8.157	8.567	9.557	9.660	9.330
Fe_2O_3	11.837	11.105	10.971	10.490	9.816	9.557	9.861
MnO	0.216	0.216	0.215	0.215	0.200	0.201	0.205
MgO	19.554	19.518	19.560	19.561	19.103	18.985	19.958
CaO	7.459	7.611	7.608	7.532	7.582	7.556	7.471
Na_2O	1.556	1.255	1.246	1.306	1.481	1.487	1.408
K_2O	0.344	0.293	0.318	0.339	0.407	0.440	0.442
P_2O_5	0.055	0.047	0.046	0.043	0.044	0.040	0.049
SO_3	0.263	0.141	0.065	0.058	0.065	0.060	0.083
Cr_2O_3	0.446	0.533	0.492	0.406	0.352	0.324	0.448
NiO	0.226	0.124	0.122	0.113	0.109	0.115	0.097
H_2O^-	1.212	0.227	0.237	0.354	0.324	0.343	0.423
LOI	-0.103	0.015	-0.015	-0.010	-0.060	-0.067	-0.037
Total	99.324	99.662	99.862	99.857	100.031	99.228	99.822

B1.4. Union Section

Table B. 4: Union Section XRF data.

Sample	UST/201B	UST/201B	UST/201B	UST/201B	UST/201B	UST/201B	UST/201B
Sieve size (μm)	<25	+25	+38	+53	+75	+106	+150
Oxides	(wt%)						
SiO_2	22.185	22.662	21.352	24.139	29.306	42.324	49.161
TiO_2	0.615	0.591	0.593	0.553	0.466	0.413	0.485
$Al2O_3$	12.071	12.109	11.771	10.966	10.193	8.398	8.578
Fe_2O_3	23.758	22.313	23.672	21.291	19.507	14.395	11.357
MnO	0.220	0.211	0.213	0.206	0.199	0.173	0.150
MgO	15.982	15.492	16.188	15.911	17.782	16.717	14.826
CaO	2.533	2.213	2.102	2.182	2.689	3.373	4.666
Na_2O	0.487	0.497	0.395	0.446	0.461	0.576	0.704
K_2O	0.082	0.062	0.047	0.046	0.076	0.096	0.156
P_2O_5	0.051	0.047	0.040	0.044	0.042	0.049	0.089
SO_3	0.109	0.021	0.038	0.048	0.051	0.076	0.163
Cr_2O_3	21.827	24.231	23.598	24.261	19.182	12.205	7.454
NiO	0.149	0.135	0.145	0.136	0.128	0.125	0.122
H_2O^-	0.026	0.050	0.022	0.008	0.032	0.027	0.055
LOI	-0.621	-0.876	-0.713	-0.553	-0.199	0.270	1.267
Total	99.475	99.757	99.463	99.683	99.917	99.216	99.234

B1.5. Rustenburg (Waterval)

Table B. 5: Rustenburg (Waterval) XRF data.

Sample	WRT/101B	WRT/101B	WRT/101B	WRT/101B	WRT/101B	WRT/101B	WRT/101B
Sieve size (μm)	<25	+25	+38	+53	+75	+106	+150
Oxides	(wt%)						
SiO_2	46.157	47.415	46.879	46.196	43.664	49.744	44.098
TiO_2	0.267	0.220	0.220	0.246	0.305	0.501	0.537
$Al2O_3$	15.487	15.782	16.134	16.044	14.627	10.669	10.432
Fe_2O_3	9.571	8.772	8.475	9.150	10.970	11.695	14.063
MnO	0.136	0.131	0.120	0.127	0.139	0.144	0.164
MgO	13.578	13.702	13.070	13.037	13.758	12.803	14.712
CaO	8.525	8.617	8.708	8.601	7.241	4.974	5.202
Na_2O	1.103	1.260	1.900	1.174	1.037	0.748	0.763
K_2O	0.171	0.167	0.203	0.195	0.180	0.171	0.114
P_2O_5	0.052	0.049	0.053	0.050	0.044	0.064	0.079
SO_3	0.083	0.054	0.055	0.021	0.087	0.164	0.078
Cr_2O_3	3.485	3.000	2.982	3.668	6.492	7.535	8.205
NiO	0.109	0.080	0.083	0.092	0.095	0.221	0.219
H_2O^-	0.028	0.029	0.033	0.058	0.064	0.101	0.089
LOI	0.791	0.558	0.719	0.965	0.613	0.304	0.962
Total	99.543	99.835	99.633	99.624	99.317	99.837	99.718

B1.6. O'okiep

Table B. 6: O'okiep XRF data.

Sample	OKP-01	OKP-01	OKP-01	OKP-01	OKP-01	OKP-01	OKP-01	OKP-02	OKP-02	OKP-02	OKP-02	OKP-02	OKP-02	OKP-02
Sieve size (μm)	<25	+25	+38	+53	+75	+106	+150	<25	25	+38	+53	+75	+106	+150
Oxides	(wt%)													
SiO_2	41.524	43.814	40.456	46.360	43.353	52.123	55.376	59.224	58.428	58.350	60.407	61.920	65.726	67.415
TiO_2	1.066	0.960	1.004	0.977	1.044	0.983	0.605	1.243	1.279	1.182	1.206	1.109	0.953	0.799
$Al2O_3$	13.820	13.931	15.384	14.415	14.748	13.834	15.934	12.656	12.886	12.825	12.694	13.245	13.082	13.162
Fe_2O_3	24.453	22.465	23.043	20.229	21.110	17.114	11.196	14.836	14.835	13.592	13.862	11.136	7.860	4.398
MnO	0.124	0.121	0.134	0.120	0.138	0.124	0.089	0.100	0.100	0.096	0.094	0.091	0.081	0.069
MgO	2.217	2.325	2.516	2.322	2.996	2.322	2.252	2.238	2.248	2.257	2.052	2.351	2.377	2.668
CaO	4.086	4.493	5.050	4.754	4.823	4.633	5.116	2.717	2.726	2.619	2.639	2.519	2.460	2.549
Na_2O	2.722	2.573	2.998	3.008	2.938	2.855	3.368	2.282	2.278	2.238	2.312	2.308	2.346	2.404
K_2O	1.541	1.416	1.663	1.491	1.498	1.208	1.407	2.454	2.433	2.496	2.479	2.671	2.646	2.959
P_2O_5	0.426	0.425	0.497	0.459	0.466	0.327	0.190	0.327	0.308	0.290	0.324	0.267	0.190	0.081
SO_3	0.257	0.191	0.136	0.175	0.174	0.150	0.247	0.269	0.176	0.204	0.177	0.170	0.152	0.669
Cr_2O_3	0.115	0.140	0.244	0.093	0.511	0.095	0.228	0.402	0.364	0.328	0.274	0.211	0.128	0.040
NiO	0.040	0.107	0.054	0.029	0.041	0.034	0.027	0.034	0.085	0.034	0.031	0.031	0.035	0.030
H_2O^-	0.255	0.257	0.204	0.208	0.318	0.169	0.197	0.032	0.060	0.115	0.045	0.060	0.046	0.293
LOI	6.945	5.905	5.759	4.878	5.392	3.326	3.140	1.171	1.313	2.739	1.166	1.448	1.417	1.642
Total	99.590	99.123	99.142	99.518	99.551	99.297	99.371	99.985	99.517	99.364	99.763	99.539	99.500	99.178

B1.7. Nkomati

Table B. 7: Nkomati XRF data.

Sample	NK-MMZ/PT	NK-MMZ/PT	NK-MMZ/PT	NK-MMZ/PT	NK-MMZ/PT	NK-MMZ/PT	NK-MMZ/PT	NK-PCMZ/PT	NK-PCMZ/PT	NK-PCMZ/PT	NK-PCMZ/PT	NK-PCMZ/PT	NK-PCMZ/PT
Sieve size (μm)	<25	+25	+38	+53	+75	+106	+150	<25	25	+38	+53	+75	+106
Oxides	(wt%)												
SiO_2	42.593	42.878	42.943	43.886	47.052	47.397	46.689	37.553	37.212	40.423	42.051	42.708	42.180
TiO_2	0.414	0.424	0.438	0.419	0.392	0.377	0.370	0.455	0.478	0.395	0.407	0.431	0.446
$Al2O_3$	5.187	5.151	5.107	4.852	5.009	5.499	6.525	7.224	8.438	7.907	8.042	7.965	7.693
Fe_2O_3	15.173	15.761	15.399	14.001	11.562	10.278	9.378	11.805	12.354	9.739	8.606	7.910	7.086
MnO	0.193	0.206	0.217	0.219	0.212	0.202	0.182	0.182	0.188	0.155	0.119	0.099	0.085
MgO	19.416	18.340	18.454	18.367	19.037	19.356	20.010	21.576	21.416	24.080	24.010	25.084	26.426
CaO	9.755	10.547	10.789	11.296	11.662	10.941	8.897	4.445	4.305	4.255	4.129	3.691	3.138
Na_2O	0.609	0.684	0.667	0.614	0.715	0.763	0.954	0.728	0.879	0.673	0.999	0.847	0.739
K_2O	0.307	0.326	0.342	0.362	0.387	0.443	0.636	0.507	0.748	0.980	1.034	1.205	1.396
P_2O_5	0.056	0.052	0.046	0.040	0.033	0.036	0.041	0.109	0.089	0.066	0.056	0.043	0.045
SO_3	1.900	1.003	0.946	0.897	0.498	0.424	0.653	1.563	0.910	0.514	0.837	0.664	0.568
Cr_2O_3	0.589	1.366	1.719	1.141	0.518	0.614	0.626	7.119	7.686	5.347	3.148	2.201	1.525
NiO	0.140	0.110	0.103	0.104	0.091	0.165	0.156	0.119	0.071	0.037	0.076	0.088	0.091
H_2O^-	0.248	0.107	0.081	0.300	0.194	0.234	0.275	0.382	0.241	0.250	0.255	0.436	0.429
LOI	3.011	3.004	2.571	2.625	2.449	3.004	3.882	5.471	4.562	5.000	5.954	6.628	7.376
Total	99.592	99.957	99.823	99.122	99.812	99.736	99.274	99.237	99.577	99.820	99.723	99.999	99.225

C. Calculations

C 1 BET Surface Area Calculations

The BET equation is given as:

$$\frac{1}{W[\left(\frac{P}{P_o}\right)-1} = \frac{1}{W_m C} + \frac{C-1}{W_m C}(\frac{P}{P_o})$$

Where:

W = weight of gas absorbed

$\frac{P}{P_o}$ = relative pressure

W_m= weight of absorbate as monolayer

C = BET constant

Other variables required for to determine the BET specific surface area include:

N = Avogadro's number (6.022 x 10^{23})

M = molecular weight of absorbant (28.0134 g/mol for Nitrogen)

A_{cs} = absorbate cross-sectional area (16.2 $Å^2$ for nitrogen)

s = slope

i = intercept

S_t = total surface area

S_{spec} = specific surface area

w = sample weight

The equation requires a linear plot of

$\frac{1}{[W\left(\frac{P}{P_o}\right)-1]}$ vs $\frac{P}{P_o}$

Slope(s):

$s = \frac{C-1}{W_m C}$

Intercept(i):

$i = \frac{1}{W_m C}$

Weight of monolayer:

$W_m = \frac{1}{s+i}$

Total surface area:

$S_t = \frac{W_m\, N\, A_{cs}}{M}$

Specific surface area:

$S_{spec} = \frac{S_t}{w}$

C1.1. Impala

From Table A 59, given that:

s = 3.21599

i = 0.021490

c = 149.979618

w = 5.946 g

$W_m = \frac{1}{s+i} = \frac{1}{3.21599+0.021490}$ $\therefore \boldsymbol{W_m = 0.309\ g}$

$S_t = \frac{W_m\ N\ A_{cs}}{M} = \frac{(0.3088)(6.02 \times 10^{23})\ (16.2)}{28.0134} \times\ 10^{-20}$ $\therefore \boldsymbol{S_t = 10.761\ m^2/g}$

$S_{spec} = \frac{S_t}{w} = \frac{10.761}{5.946}$

$\therefore (\boldsymbol{Impala})\ \boldsymbol{S_{spec} = 1.810\ m^2/g}$

C1.2. Amandelbult

C1.2. Amandelbult

From Table A 60, given that:

s = 2.879401

i = 0.19806

c = 146.382025

w = 7.810 g

$W_m = \frac{1}{s+i} = \frac{1}{2.879401 +0.19806}$ $\therefore \boldsymbol{W_m = 0.325\ g}$

$S_t = \frac{W_m\ N\ A_{cs}}{M} = \frac{(0.325)(6.02 \times 10^{23})\ (16.2)}{28.0134} \times\ 10^{-20}$ $\therefore \boldsymbol{S_t = 11.312\ m^2/g}$

$$S_{spec} = \frac{S_t}{w} = \frac{11.312}{7.810}$$

$$\therefore (\boldsymbol{Amandelbult})\ \boldsymbol{S_{spec} = 1.450\ m^2/g}$$

C1.3. Mogalakwena

From Table A 61, given that:

s = 1.17582

i = 0.09899

c = 103.799327

w = 5.902 g

$$W_m = \frac{1}{s+i} = \frac{1}{1.17582 + 0.09899} \qquad \therefore \boldsymbol{W_m = 0.784\ g}$$

$$S_t = \frac{W_m\ N\ A_{cs}}{M} = \frac{(0.784)\left(6.02 \times 10^{23}\right)(16.2)}{28.0134} \times 10^{-20} \quad \therefore \boldsymbol{S_t = 27.304\ m^2/g}$$

$$S_{spec} = \frac{S_t}{w} = \frac{27.304}{5.902}$$

$$\therefore (\boldsymbol{Mogalakwena})\ \boldsymbol{S_{spec} = 4.625\ m^2/g}$$

C1.4. Union Section

From Table A 62, given that:

s = 2.29502

i = 0.16937

c = 120.829467

w = 5.496 g

$$W_m = \frac{1}{s+i} = \frac{1}{2.29502 + 0.16937} \quad \therefore \boldsymbol{W_m = 0.406\ g}$$

$$S_t = \frac{W_m\, N\, A_{cs}}{M} = \frac{(0.406)\left(6.02 \times 10^{23}\right)(16.2)}{28.0134} \times 10^{-20} \quad \therefore \boldsymbol{S_t = 14.134\ m^2/g}$$

$$S_{spec} = \frac{S_t}{w} = \frac{14.134}{5.496}$$

$$\therefore (\boldsymbol{Union\ Section})\ \boldsymbol{S_{spec} = 2.572\ m^2/g}$$

C1.5. Rustenburg (Waterval)

From Table A 63, given that:

s = 2.26801

i = 0.16239

c = 125.812259

w = 6.981g

$$W_m = \frac{1}{s+i} = \frac{1}{2.26801 + 0.16239} \quad \therefore \boldsymbol{W_m = 0.411\ g}$$

$$S_t = \frac{W_m\, N\, A_{cs}}{M} = \frac{(0.411)\left(6.02 \times 10^{23}\right)(16.2)}{28.0134} \times 10^{-20} \quad \therefore \boldsymbol{S_t = 14.308\ m^2/g}$$

$$S_{spec} = \frac{S_t}{w} = \frac{14.308}{5.496}$$

$$\therefore (\boldsymbol{Rustenburg\ (Waterval)})\ \boldsymbol{S_{spec} = 2.603\ m^2/g}$$

C1.6. O'okiep

From Table A 64, given that:

s = 2.741388

i = 0.009622

c = 180.134545

w = 7.940g

$$W_m = \frac{1}{s+i} = \frac{1}{2.741388 + 0.009622} \quad \therefore \boldsymbol{W_m = 0.364\ g}$$

$$S_t = \frac{W_m\ N\ A_{cs}}{M} = \frac{(0.364)(6.02 \times 10^{23})\ (16.2)}{28.0134} \times\ 10^{-20} \quad \therefore \boldsymbol{S_t = 12.674\ m^2/g}$$

$$S_{spec} = \frac{S_t}{w} = \frac{12.674}{7.940}$$

$$\therefore (\boldsymbol{O'okiep})\ \boldsymbol{S_{spec} = 1.596\ m^2/g}$$

C1.7. Nkomati

From Table A 65, given that:

s = 0.831846

i = 0.04018

c = 208.8882

w = 6.782 g

$$W_m = \frac{1}{s+i} = \frac{1}{0.831846 + 0.04018} \quad \therefore \boldsymbol{W_m = 1.147\ g}$$

$$S_t = \frac{W_m\ N\ A_{cs}}{M} = \frac{(1.147)(6.02 \times 10^{23})\ (16.2)}{28.0134} \times\ 10^{-20} \quad \therefore \boldsymbol{S_t = 39.930\ m^2/g}$$

$$S_{spec} = \frac{S_t}{w} = \frac{39.930}{6.782} \quad \therefore (\boldsymbol{Nkomati})\ \boldsymbol{S_{spec} = 5.888\ m^2}$$